The Dynamics of Spatial Elastic Mechanisms with Clearances and Support Structures

by

Joseph Francis Deck
B.S. Mechanical Engineering and German
Carnegie-Mellon University 1980

Submitted to the
Department of Mechanical Engineering
in partial fulfillment of the requirements for the degree of
Doctor of Philosophy
at
The Massachusetts Institute of Technology

November 19, 1992

Author
Joseph Francis Deck
November 19, 1992

Certified by
Professor Steven Dubowsky
Department of Mechanical Engineering
Chair, Thesis Committee

Accepted by
Professor Ain Ants Sonin
Department of Mechanical Engineering
Chair, Department Graduate Committee

The Dynamics of Spatial Elastic Mechanisms with Clearances and Support Structures

by Joseph F. Deck

Submitted to the Department of Mechanical Engineering
on November 19, 1992, in partial fulfillment of the requirements
for the degree of Doctor of Philosophy

Abstract

This thesis is an experimental and analytical study of the effects of clearances in machine systems. A finite element-based modeling technique for spatial machine systems with flexible links, nonlinear kinematics and control systems is extended to include support structures and enclosures, and analytical models of machine system joints. These nonlinear joint models predict internal contact forces as functions of the joint geometry and construction, and the motions of the machine's links, and include nonlinear joint clearance, compliance and friction. This new modeling technique is applied to several systems, including a SCARA robotic manipulator, an impact beam, and a spatial slider-crank.

Experimental versions of the impact beam system (IBS) and the spatial slider-crank (SSC) are constructed, including instrumented, adjustable clearance joints that permit measurement of internal contact forces practically at the point of contact. The clearances in the joints of these machine systems cause unexpected dynamic behavior, including non-periodic response to steady periodic inputs and high sensitivity to small variations in operating parameters. Predictions of contact forces using the modeling technique exhibit similar sensitivities. Particularly for large joint clearances and high speeds, the physical systems exhibit such large variability and sensitivity in their response that the numerical predictions must be used with caution. Limitations on the ability of numerical models to predict the behavior of such systems may be fundamental, not related to finite computer power.

Implications of these results for designing machine systems with clearances are discussed. These include non-repeatability and uncertainty in machine response due to unavoidable manufacturing tolerances; reluctance of the machine to settle into steady-state behavior; and the difficulty of predicting machine response accurately using computer-based methods.

Thesis Supervisor: Dr. Steven Dubowsky
Title: Professor of Mechanical Engineering

Table of Contents

Nomenclature

Nomenclature in this thesis uses the following conventions:

- Bold letters are used for matrices and vectors, and normal weight letters are used for scalars. An uppercase letter indicates a matrix, and a lowercase letter, a vector. Subscripts on a matrix or vector name indicate the link number that the matrix or vector is associated with. Subscripts on a scalar name indicate that it is a component of a matrix or vector. Examples: "The mass matrix for link i" is written $\mathbf{M}_i$; "the α,β element of mass matrix $\mathbf{M}_i$" is written $M_{i,\alpha\beta}$. "The position vector of grid point g on link i" is written $\mathbf{r}_{i,g}$, and "element 3 of position vector $\mathbf{r}_{i,g}$" is written $r_{i,g,3}$.

- Coordinate frames are identified by uppercase italic letters, with a subscript to identify the link. Thus, G_i is a coordinate frame associated with link i. The inertial frame is O.

- A vector name enclosed in parentheses and with a subscripted link number means that the components of the vector are referenced to the nominal reference frame of the link. Thus, $(\mathbf{r}_{i,g})_k$ means "the vector $\mathbf{r}_{i,g}$, with its components referenced to coordinate frame N_k." A zero or an italic O indicates the inertial frame. A zero as part of the vector name means that the vector is based in the inertial reference frame.

- An matrix name with an underline indicates a 3x3 matrix, and a vector name with an underline indicates a 3x1 column vector. Thus, $\underline{\mathbf{T}}_j^i$ is a 3x3 submatrix of matrix $\mathbf{T}_j^i$.

The symbols used in this thesis, and their definitions, follow. This

nomenclature is based on, but somewhat expanded from, that used in reference [100].

(KINEMATICS AND NOMINAL MOTION)

$\mathbf{b}_{i,g}$.....undeformed position of grid point g on link i, measured from frame N_i.

G.....interface-node-fixed reference frame

H_i.....Denavit - Hartenberg joint variable if joint i is prismatic.

N_i.....nominal motion reference frame for link i.

O.....inertial reference frame.

$\mathbf{Q}^H, \mathbf{Q}^\Theta, \underline{\mathbf{Q}}^H, \underline{\mathbf{Q}}^\Theta,$
$\mathbf{q}^H, \mathbf{q}^\Theta$.....4x4, 3x3 and 3x1 differentiation matrices and vectors for prismatic (H) or revolute (Θ) joints.

$\mathbf{Q}_i, \underline{\mathbf{Q}}_i, \mathbf{q}_i$.....4x4, 3x3 and 3x1 differentiation matrices and vector for link i.

$\mathbf{r}_{i,g}$.....location of grid point g on link i, measured from frame N_i.

$\mathbf{r}_{0i,g}$.....inertial location of grid point g on link i.

$\mathbf{T}_j^i$.....4x4 dynamic transformation matrix between link coordinate frames N_i and N_j.

$\underline{\mathbf{T}}_j^i$.....Lower-right 3x3 submatrix of $\mathbf{T}_j^i$.

$\mathbf{t}_j^i$.....Lower-left 3x1 column vector of $\mathbf{T}_j^i$.

$\mathbf{U}_{i,j}, \mathbf{U}_{i,j,k}$.....first and second partial derivatives of $\mathbf{T}_0^i$ transformation matrix with respect to θ_j and θ_k.

$\mathbf{v}_{0i,g}$.....inertial velocity of grid point g on link i.

X_i.....General D-H joint variable; evaluated as θ_i or H_i.

θ_i.....Denavit - Hartenberg joint variable if joint i is revolute.

$\sigma_{g\alpha}$.....4x1 degree of freedom selector vector for degree of freedom α at finite element grid point g.

$\sigma_{g\alpha}$ .....lower 3x1 subvector of $\sigma_{g\alpha}$.

(LINK PROPERTIES AND GLOBAL EQUATIONS)

$\mathbf{A}_i$, $\mathbf{a}_i$, $\dot{\mathbf{a}}_i$, $\ddot{\mathbf{a}}_i$ .....Component Mode Synthesis transformation matrix, reduced coordinates perturbation vector, and its time derivatives.

$\mathbf{B}_i$.....global compatibility matrix for link i.

$\mathbf{B}_{i,j}$, $\mathbf{B}_{i,j,k}$ .....first and second partial derivatives of $\mathbf{B}_i$ with respect to θ_j and θ_k.

$\mathbf{f}_{e,i}$ .....externally applied forces for link i.

$\mathbf{f}_{e,i}^{I}$, $\mathbf{f}_{e,i}^{F}$.....subvectors of $\mathbf{f}_{e,i}$.

$\mathbf{f}_{g,i}$ .....gravity force vector for link i.

$\mathbf{f}_i$, $\mathbf{f}_i^{I}$ .....applied force vector for link i and its interface partition.

$\mathbf{G}_i^{damp}$ .....viscous damping matrix for link i.

g.....gravity vector.

I, F .....superscript I: interface partition; superscripf F: internal partition

$KE_{i,g}$, KE_i.....kinetic energy associated with grid point g of link i, and total kinetic energy of link i.

M, G, K.....global mass, damping and stiffness matrices.

$\mathbf{M}_i$, $\mathbf{K}_i$ .....finite element mass and stiffness matrices for link i.

$\overline{\mathbf{M}}_i$, $\overline{\mathbf{G}}_i$, $\overline{\mathbf{K}}_i$, $\overline{\mathbf{K}}_{2i}$
$\overline{\mathbf{K}}_{3i}$, $\overline{\mathbf{f}}_{2i}$, $\overline{\mathbf{f}}_{3i}$, $\overline{\mathbf{f}}_{gi}$ .....CMS reduced finite element and dynamic matrices and vectors, corresponding to $\mathbf{M}_i$, $\mathbf{K}_i$, etc.

$\mathbf{M}_i^{dyn}$, $\mathbf{G}_i^{dyn}$, $\mathbf{K}_i^{dyn}$,
$\mathbf{f}_i^{dyn}$, $\mathbf{G}_i$, $\mathbf{K}_{2i}$, $\mathbf{K}_{3i}$,
$\mathbf{f}_{2i}$, $\mathbf{f}_{3i}$.....dynamic matrices and dynamic force vectors for link i.

$\mathbf{M}_i^{II}$,$\mathbf{M}_i^{IF}$,$\mathbf{M}_i^{FI}$,$\mathbf{M}_i^{FF}$ ...submatrices of the partitioned F.E. mass matrix, $\mathbf{M}_i$.

$\mathbf{K}_i^{II}$,$\mathbf{K}_i^{IF}$,$\mathbf{K}_i^{FI}$,$\mathbf{K}_i^{FF}$ .....submatrices of the partitioned F.E. stiffness matrix, $\mathbf{K}_i$.

$NDOF_i$ .....number of degrees of freedom on link i.

NG_i.....number of finite element grid points on link i.

NL.....number of links in the system.

$NMOD_i$.....number of mode shapes preserved in Component Mode Synthesis for link i.

$NRED_i$.....reduced number of degrees of freedom defined for link i after CMS.

$PE_{i,grav}$, $PE_{i,elastic}$..potential energy of link i due to displacements in a gravitational field and to elastic deformations.

$\mathbf{p}_i$, $\dot{\mathbf{p}}_i$, $\ddot{\mathbf{p}}_i$ .....perturbation displacement, velocity and acceleration vectors for all node points on link i, defined in link reference frame N_i.

$\mathbf{p}_i^I$, $\mathbf{p}_i^F$, $\dot{\mathbf{p}}_i^I$, $\dot{\mathbf{p}}_i^F$, $\ddot{\mathbf{p}}_i^I$, $\ddot{\mathbf{p}}_i^F$ subvectors of $\mathbf{p}_i$, and its derivatives.

q.....vector of system independent coordinates.

w .....global force vector.

(CLEARANCE CONNECTION MODELS)

c.....friction force ramping function

$\mathbf{d}$, $\mathbf{d}_i$, $\mathbf{d}_{cen}$, $\mathbf{d}_{rad}$, $\mathbf{d}_{ax}$, $\mathbf{d}_p$ .....contact point location vectors for different connection models

$f_{nor,p}$.....normal contact force at a contact point p

$\mathbf{f}_{rad}$, $\mathbf{f}_{fric}$, $\mathbf{f}_{slid}$.....force at a contact point due to normal or sliding motion.

k,b .....contact stiffness and damping

L, L_g .....pin length, axial clearance

$\mathbf{p}_{i,g}$ .....perturbation displacement vector for node g on link i.

$p_{i,\alpha}$.....the α^{th} degree of freedom in the link i perturbation vector.

R_a, R_b, r_c.....ball radius, socket radius, radial clearance

r_p, r_g.....pin radius, radial clearance

$s, \dot{s}$ .....interference and interference rate of change between joint parts.

$\Gamma_{rad}, \Gamma_{slid}$.....torque applied to interface node, due to contact force

$\Delta \mathbf{p}, \Delta\phi$.....relative translation/rotation of the parts of a clearance joint.

$\Phi_{a,2}$.....rotation matrix corresponding to perturbation rotations at node (a,2)

$\phi_{i,g}$.....perturbation rotation vector for node g on link i.

μ .....coefficient of sliding friction

Chapter 1. Introduction

A. Motivation and Goals

The motivation behind this dissertation is the desire to improve our understanding of the behavior of complex machine systems. Machine systems are important: the national and global economies depend on them, simple and complex, from a home sewing machine to a block–long printing press, to do work, to enhance life, and to multiply the efforts of our hands and minds. Sometimes, though, machines perform in unexpected ways. The consequences of unexpected behavior may be expensive, such as poor assembly quality in high speed automated factories, or unexpected downtime due to component failures. Worker safety may be affected too, both by chronic poor performance such as excessive noise or high control efforts and by acute problems such as machine failure. If we could know more about complex machine systems, these kinds of poor performance could be anticipated, and there would be fewer surprises.

A desirable goal would be to enable the designer of a complex machine such as that shown in Figure 1.1 to generate a computer model that would rapidly yield accurate, reliable predictions of all desired performance characteristics of the machine, including items such as its vibration levels, its noise radiation, its power consumption, the expected lifetimes of its components, the dynamic stresses and strains in its moving and stationary parts, and whatever other information might be needed to arrive at a design that would meet market demands for quality, performance and cost, while simultaneously optimizing the machine's manufacturability and minimizing its use of scarce resources. Impressive progress has been made, but we remain far from such a goal. The

results of this thesis suggest some strategies for coming closer to that goal, but they also reveal some unexpected areas of difficulty.

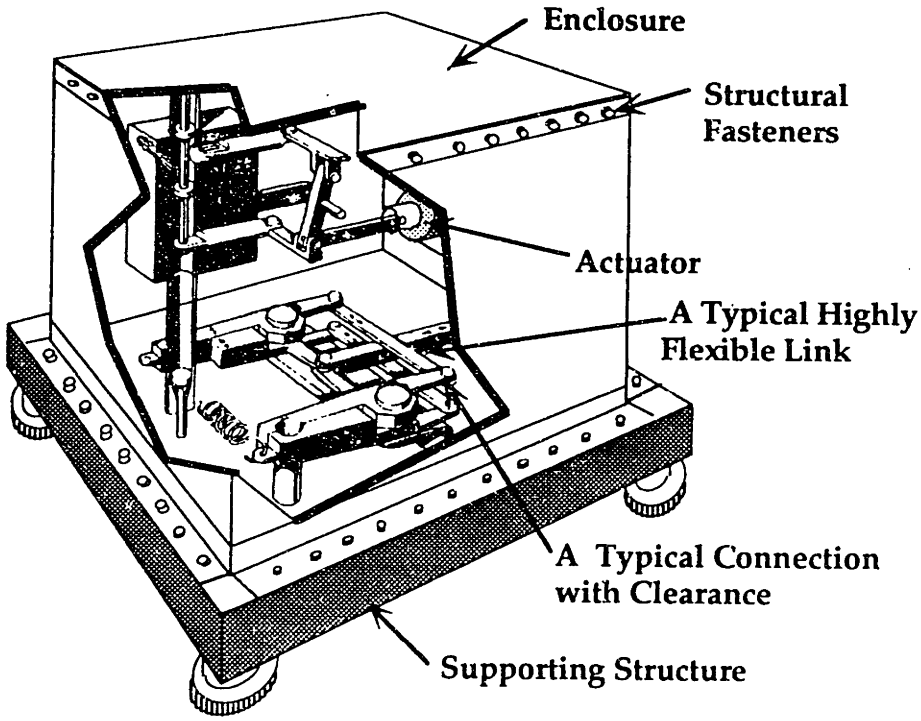

Figure 1.1. A complex machine system. (Matsushita Electrical Industries)

The machine systems dealt with in this thesis are those in which the following effects are important: distributed mass and flexibility in the components; nonlinear kinematic motion of the links; dynamic influence of the mounting base or other support structure and enclosures; and, especially, internal impacts in the clearance joints between the moving parts. The goals of this research are, first, to explore and characterize the behavior of some examples of such machine systems; second, to attempt to improve computer modeling methods for such systems; and, third, to assess the performance of these new modeling techniques by comparing their predictions against experimental measurements of real systems.

Most of the comparisons in this thesis are between the predicted and measured contact forces generated by impacts between two components of a machine system. Such impact forces are important design information in themselves. For example, they affect the service life of the bearings that connect two rotating links. In addition, internal impact forces are a major source of excitation of the vibrations of many machine systems with moving parts. Thus, an attempt to model other machine system characteristics, such as vibration and noise, can start by examining the internal contact forces.

B. Principle Contributions of the Research

The major contribution of this work is an analytical and experimental exploration of some of the nonlinear dynamic properties of joint clearances, and their relevance for the design of machine systems. Mathematical models for some types of clearance connections are proposed. A computer program including those models is used to generate numerical predictions of machine system behavior, which are then compared with experimentally measured behavior. A hypothesis is presented for a coupling mechanism between machine vibration and impact forces.

C. Overview and Summary of the Thesis

The remaining chapters of this thesis are:

- Chapter 2. Previous Work in Machine System Modeling
- Chapter 3. The Analytical Method
- Chapter 4. The Impact Beam System
- Chapter 5. The Spatial Slider Crank System

- Chapter 6. Conclusion
- Bibliography
- Appendix A. Perturbation Coordinates
- Appendix B. 4x4 Matrix Notation; Hartenberg-Denavit Notation
- Appendix C. Dynamic Equations
- Appendix D. Component Mode Synthesis, Ideal Joint Compatibility, and Global System Equations
- Appendix E. Nominal Motion Equations for the Spatial Slider Crank
- Appendix F. Details of the ASSET models for the IBS and SSC

Chapter 2 reviews some of the previous work in modeling flexible spatial machine systems, including several techniques to incorporate clearance connections into the models. A review of experimental work is also given. Finally, the problems addressed in this thesis are discussed.

Chapter 3 shows how an existing technique for modeling spatial machine systems that included component flexibility and nonlinear kinematics was extended to include compliance/clearance connections between its links. The resulting program, called ASSET (Advanced Spatial Systems Emulation Technique), is capable of modeling a wide variety of spatial machine systems that have these effects. Chapter 3 discusses in detail two numerical models that were developed to represent spherical and revolute joints with clearances in ASSET. Finally, as an example, the ASSET software is used to model a SCARA robotic manipulator.

Chapter 4 presents the results from numerical and experimental studies of a very simple machine system called the impact beam system (IBS). The IBS

contains no nonlinear elements except a one–dimensional clearance gap, and has only planar motion. The studies show the very strong influence that a clearance connection can have on a machine system's performance. Both the numerical and experimental models confirm, as has been reported in the past [30, 34, 36], that a clearance can have a strong amplifying effect on the contact forces between two components of a machine. The experiments also reveal two unexpected effects of a clearance connection: its ability to cause the response of a system to vary even when the system's inputs are stable, and the very high degree of sensitivity to slight variations in the inputs that it can cause in the response of a system. The numerical simulation was able to provide useful predictions of the peak impact force seen in the experiments. However, the simulation revealed neither the real system's varying response with stable inputs nor the full degree of its sensitivity to small variations in the inputs.

Chapter 5 presents analytical and experimental studies of a more complex system with spatial, large–rotation nonlinear kinematics and two spatial clearance joints, called the spatial slider crank system (SSC). The much greater complexity of the SSC does not permit as tidy an analysis as does the IBS. Nonetheless, lessons learned from the IBS were found to be applicable to the SSC. Clearance impact forces in this experimental system also exhibit a great deal of non-periodic variability when the machine is operating at a constant speed. The numerical model of the SSC exhibits highly nonlinear behavior, where extremely small variations in the model's parameters may lead to dramatically different results. This behavior illustrates the difficulty of modeling systems with impacts: both the physical system and the

numerical model can show exaggerated sensitivity to small parameter variations, making detailed agreement between them very unlikely.

Chapter 6 summarizes the results of these experimental and numerical studies. The experimental systems exhibit behavior that appears to be similar to that associated with chaotic systems. Thus, attempts to predict such behavior with high accuracy may be fundamentally impossible. Nonetheless, the numerical models can provide useful predictions. Predictions at any one set of operating conditions are very likely to be inaccurate, so a numerical model must be exercised over a band of the machine's operating parameters that includes the design conditions. Partly, this effect is due to the variability and sensitivity observed experimentally in these systems: when the *actual* response is not stable, an accurate *prediction* is impossible unless the simulation is run for a length of time that is impractical with today's workstation computers. Partly, the effect is due to the inability of the numerical model to predict the full degree of sensitivity seen in the real systems; this inability may be due to fundamental physical limitations, rather than finite computing resources. As a rule of thumb, the numerical predictions are also more reliable and accurate for low operating speeds and small clearances.

Appendices A-D give some details of the modeling method for spatial systems with ideal non-clearance joints, flexible links and nonlinear kinematics, due to Sunada [100], that was extended to include clearance joints in this thesis. The ideal joint technique is synopsized here because of a new implementation and some new notations required by the extension to clearance joints.

Appendix E gives the equations used to describe the nominal motion of the spatial slider crank system.

Appendix F gives detailed information regarding the ASSET simulations of the IBS and SSC systems.

Chapter 2. Previous Work in Machine System Modeling

A. Non-Ideal Effects

Engineers have known for a long time that non-ideal machine properties such as clearance, backlash, the impacts they cause, and link flexibility often significantly degrade machine dynamic performance [44, 49, 57]. Eliminating these effects is almost always expensive, and often impossible. Models of these and other machine system dynamic effects can anticipate their performance consequences during the design process. Constructing such models of machine system performance, usually computer based, has long been a major activity of the machine design research community.

Broadly speaking, two fields of research have developed that are relevant to this topic. One is research into methods for modeling the distributed link mass and flexibility, control systems and actuators, and the nonlinear kinematics of a machine system. The other is research into the clearance, compliance, friction, impacts and other non-ideal effects present in the system's connections. More recently, widely available computers have gained sufficient power to permit sophisticated models that merge the results from these fields.

B. Machine Dynamics Modeling Techniques

The first machine system dynamic performance models did not consider link flexibility, but were concerned with analyzing the forces and torques generated under the assumption of rigid body behavior for all links of the system, [4, 88, 109]. Such rigid body dynamic models have been implemented

in commercial software packages such as ADAMS, DRAM, IMP, and others [18, 82, 94, 114]. These useful programs can model the nominal forces produced by the machine's gross motion and external loading in a wide variety of planar and spatial mechanisms, but cannot predict machine behavior that is due to effects such as flexibility and clearance impacts. Nonetheless, such rigid body models are appropriate for many applications, and are attractive because they are relatively quick and inexpensive to use.

To address the limitations of these methods, numerous flexible link modeling techniques have been developed. The literature in this field is voluminous and only a sample is given here. Some techniques for planar [5, 13, 55] and spatial systems [33] represent the links using analytically tractable models with a limited number of dynamic degrees of freedom, for example, Euler-Bernoulli beams. This approach is limited to simply shaped links. Finite element methods that could model generally shaped links were formulated, for planar [9] and spatial systems [14, 15, 58, 69, 70, 89, 92, 101, 102, 105]. These techniques, too, have been used in commercial software such as DISCOS [77] and, with a preprocessor, the DADS dynamic analysis package [119]. Work appeared that used finite element models for the links and also accommodated intermittent motion [61]. A review paper in the field was published in 1986 [73].

Methods that model the distributed mass and flexibility of machine elements generally assume them to be constructed of continuous, homogeneous metallic materials. There are some exceptions, for example [104, 106].

Because machine system dynamic models tend to be highly computationally intensive, methods to reduce the computational effort are important. Many

of these techniques employ some form of Component Mode Synthesis [2, 16, 54, 66, 86, 91] to reduce the size of the dynamic model while maintaining accuracy. Symbolic manipulation of the equations of motion has also been employed [17].

Techniques have also been suggested to model the nonlinear effects that occur due to coupling of large deformations and the gross motion of the links [10, 21, 60]. However, these techniques are not relevant to machine systems because the deformations that occur in machine systems are generally small. Methods that accommodate inertia-variant systems [90] may be particularly useful with systems such as high speed robots performing pick and place maneuvers.

C. Models of Connection Clearances

The machine dynamic analysis methods discussed above generally model a machine's joints in the form of simple or time varying kinematic constraints between links. Research developing more realistic models for clearance joints has been done. Several approaches have evolved for modeling the impact and contact behavior of clearance connections.

The first approach, the momentum transfer model [53, 83, 108], models an impact between links as an infinitesimally short event, characterized by conservation of momentum and energy dissipation controlled by a restitution coefficient. It does not consider the time history of an impact. This type of model cannot predict the forces developed between links, an important issue in the design of real systems.

The second approach, the compliance/friction model [56, 87, 96] assumes the connection to be described in terms of compliance, friction, and viscous damping between the two links. This type of model can predict some internal connection forces that result from joint parts in contact. However, it does not predict the large forces associated with impacts, which occur when joint parts change from an out-of-contact to an in-contact condition.

Finally, the clearance force model [29] predicts contact force as a function of the relative motion, internal geometry, and material properties of a connection. This model is capable of predicting the forces generated between links when an impact occurs. Several approaches have been suggested to estimate the force/displacement relationship at the point of contact, including Hertzian contact analysis [29, 76, 78] and finite element based techniques [6, 20]. One interesting technique applies finite element substructuring techniques to the region around an impact site as part of a link's finite element model [115].

Researchers have developed simple conceptual and experimental models of machine connections in order to understand their behavior [67]. The impact pair model [29] is an example that includes the clearance force model described above. The impact beam [30] and impact ring [36] models were simple experimental and analytical models that provided insight into the behavior of clearance connections. The impact beam included link flexibility as well as joint clearance. The inclined impact pair model [52] investigated the behavior of an impact pair at various angles of inclination in a gravity field. A few experimental studies of journal bearing impacts have also appeared [38, 48].

The static constitutive relationships of spatial revolute joints [75] and revolutes as well as other joints [112] have been treated. These models may be used to analyze kinematic effects such as tip errors in a robot arm [113], but predicting internal forces is outside their scope. Stochastic models aimed at applications such as producing a statistical description of position errors at the end effector of a robot due to the kinematic effects of clearance have been developed [117, 118]. Such models are poorly adapted for use in deterministic dynamic models.

D. Combined Machine Dynamics and Clearance Models

The connection models described above have been combined with rigid and flexible body link models in order to model the dynamics of an integrated machine system. A survey paper on the field of planar machine systems with clearance was published in 1980 [47]. Reference [73], although primarily concerned with flexible mechanisms, also included some citations of work on clearance connections.

One basic approach to modeling clearance connections in a machine system is to treat them as constraints between links. The number and direction of the constraints may be permitted to vary with time and mechanism configuration to model contact / no contact conditions and varying constrained directions, as at a revolute joint. This general approach is followed in, for example, [41, 42]. A model was developed for a spatial 4-bar mechanism with rigid bodies and kinematic models of its spherical clearance joints [24]. A variant of this idea called the "continuous contact" model has also been employed [116]. Such techniques do not attempt to model the nature of the interactions at the point of contact, such as compliance or

friction, and therefore may not provide adequate modeling detail if information about impact forces is needed.

The momentum transfer model for impacts is particularly well suited to an intermittent motion dynamics model [65] and has been used with flexible body models for planar [62] and spatial systems [63, 64] with both internal and external impacts, and changing system mass, as might be caused, for example, by a robot arm grasping or releasing a payload [93]. This connection model has also been combined with a geometrically nonlinear flexible link technique [11]. The effect of a constant speed drive vs. a constant torque drive on impulse due to impacts was explored for a 4-bar mechanism, using rigid link models and a restitution coefficient impact model [110].

Planar, rigid body systems with a clearance force model were analyzed [27]. Planar, flexible body machine systems were analyzed analytically with clearance force models [31, 103]. One of these models was experimentally verified [34].

The compliance/friction connection model has been applied to spatial systems with rigid bodies [50, 51, 95]. A technique using a compliance/viscous friction/Coulomb friction model was combined with a rigid link dynamics model for planar [7] and spatial [8] systems. A study was done using lumped parameter models for the link mass and flexibility of an industrial robot, combined with Coulomb friction in the joints [1].

One more approach to the integrated treatment of machine dynamics and connection clearances should be mentioned. In this technique, mechanism parameters and operating conditions are chosen to avoid loss of contact, thereby preventing impacts and the consequent high impact forces [36, 37, 39,

46, 84, 120]. However, the design choices and operating limits required in order to maintain internal joint contact at all times may be impractical.

E. Experimental Studies

Designers need reliable methods that are capable of modeling realistic, complex machine systems. More complete methods result from theoretical and analytical work. However, the reliability of new methods can be demonstrated only through experimental verification.

Several reported experimental studies have been concerned primarily with flexibility effects. One group has reported on design methods and experimental verification in studies of machines containing links fabricated with composites [104, 106]. The strains and accelerations of flexible links operating at high speed have been measured using a photographic technique [72] and using strain gauges [71, 74]. In [71], results that differed qualitatively from theoretical expectations were observed, emphasizing the importance of verifying numerical models with physical measurements. Indirect measurement of bearing loads was achieved in [22], using a load cell to mount the bearing to the link. The ability of a simple numerical model to predict the behavior of a slider mechanism with stiff links whose slider rode on a flexible cantilevered beam was investigated [23]. Experimental results and predictions obtained from a finite element model were compared for a cantilevered beam undergoing transient rotational acceleration due to a spring [40].

Among studies where impacts were a focus, most of the emphasis has been on measuring link strains and accelerations due to impacts, rather than on the impact forces themselves. Experimental measurement of the deflections

of a nominally stationary cantilevered arm experiencing a single external impact have been reported [19]. Noise radiation from machine links has been measured [35] and noise reduction via thin compliant layers in the bearings investigated [3]. This study also measured bearing contact forces near the point of contact, using a load cell. Link deformations and accelerations due to bearing clearance impacts have been addressed [97, 98]. In [97], large amplification factors of link acceleration when impacts were present relative to link accelerations without impacts were observed. In [98], aperiodic behavior was noted in a system operating in a nominally cyclic motion. Impacts were measured in an impact pair [38], a Scotch yoke [34] and in an impact ring model, a planar clearance joint [36]. All of these measurements have been performed in planar or co-planar systems.

F. Current Issues

What is lacking so far is an analytical method that combines a flexible body, spatial dynamic model of a machine system with a clearance force model for its connections, accompanied by experimental verification. That is the objective of this thesis. Some of the work appearing in this thesis has appeared in the literature already, including a general outline of the technique combined with a planar machine system analytical model [28] and an analytical study of a spatial robotic manipulator [59]. The method has been used by others to simulate a co-planar manipulator [68]. Extensions by others to the basic technique have been demonstrated to consider a stationary, flexible support structure and enclosures [80] and a mobile support structure [32]. A thesis currently being completed in our laboratory integrates the basic method described here with a technique to allow noise prediction [81]. Some

of the experimental results reported in this thesis have appeared in a recent paper [25].

A fundamental assumption behind virtually all numerical techniques for dynamic structural modeling is that the accuracy of the model is limited by its level of detail. In terms of finite element modeling, widely used in present-day techniques, "detail" means the size of the finite element mesh, and the time step used for numerical integration. Present-day computers reach limits of capacity and reasonable job time long before the theoretical limits of the finite element mesh are approached[1] [12]. Thus, under this assumption, modeling accuracy is limited by computer power, and disagreements between the predictions of modeling techniques and experimental measurements should continue to be reduced as computers become more powerful. However, some recent studies have suggested the existence of different limits on accuracy, much more constraining than these computational limits [111]. Briefly put, the problem is due to the sensitivity of high order structural modes to physical parameters of a structure, such as its size, mass and mass distribution. When the modes are so sensitive that they are strongly affected by parameter variations of the same order as unavoidable manufacturing tolerances, it becomes impossible to construct a numerical model that accurately represents any particular physical example of a structure.

Clearance impact forces contain substantial high frequency energy that can excite the high-order modes of a structure. Furthermore, the nonlinear

---

[1]Since finite element methods are based on an assumption of continuum material behavior, they become invalid when the elements become so small that continuum material models no longer apply.

spatial mechanism analysis technique described in this thesis is adapted from structural finite element models, and shares many of the characteristics of these models. Thus, the physical modeling limits just described may contribute to and partly explain the difficulty of accurately predicting clearance impact forces excited by repetitive high speed motion, as noted in Chapter 4 of this thesis and in [25].

Finally, some of the results discussed in this thesis suggest the possibility of chaotic behavior in systems with clearance impacts. Such behavior has been seen experimentally in a slider-crank system with stiff links connected by soft springs [85]. An exploration of this topic is beyond the scope of this thesis. However, work underway in our laboratory is expected to address some issues of chaotic behavior, using the mechanical systems discussed in Chapters 4 and 5 of this thesis [45].

Chapter 3. The Analytical Method

A. Introduction

The purpose of this chapter is to describe an analytical FE (Finite Element) -based technique, developed for complex machine systems to provide design information about their performance. It models the distributed mass and flexibility of their components and attached support structures such as baseplates and enclosures. It includes their nonlinear, large motion kinematics. The technique can consider realistic control system and actuator effects such as frequency response and saturation. It can also model nonlinear connections between the components of the system, including effects such as compliance and clearance.

This chapter begins with a synopsis of the modeling method as applied to systems with ideal connections. Next, an extension necessary to model clearance connections is introduced. Then, connection models developed for two types of joints with clearance are presented. Finally, an analytical study of a SCARA robotic manipulator including two revolute joints with clearance and compliance is presented as an example.

A numerical simulation package called ASSET (Advanced Spatial Systems Emulation Technique) has been written that implements this method. ASSET offers automatic equation assembly and time integration for modeling the dynamics of complex machine systems. It also supplies a library of subroutines that describe the properties of some common machine system clearance connections.

In this thesis, the terms "clearance connection," "non-ideal joint" and "clearance joint" refer to a machine system joint that has internal compliance and clearance, and may also have internal friction and other effects. The terms "ideal joint" and "ideal connection" mean a machine system joint modeled as in reference [100], without any internal clearance or compliance, though it can have internal friction. The clearance joint model presented here is more general than non-ideal joint models such as those in references [8, 87, 56]. These methods can treat a joint's compliance and friction effects, but do not model a clearance zone. It is also different from models such as that in reference [39], where a clearance is modeled as a rigid link with variable length and orientation. Such methods do not include a joint's internal compliance. Certain types of joints, such as preloaded ball bearings, normally operate with zero internal clearance. The method presented here can model the internal compliance and friction of such a joint, its normal operation with zero clearance, and the clearance that might appear if it were severely overloaded.

B. The Modeling Technique

B.1. The Dynamic Modeling Method

In reference [100], a FE-based modeling technique for flexible, spatial machine systems with ideal joints was developed. The block diagram in Figure 3.1 is a schematic of this method, except for the blocks labeled "Support Structure," "Enclosure," and "Bearing Force Model." These extensions will be discussed after describing the ideal joint method.

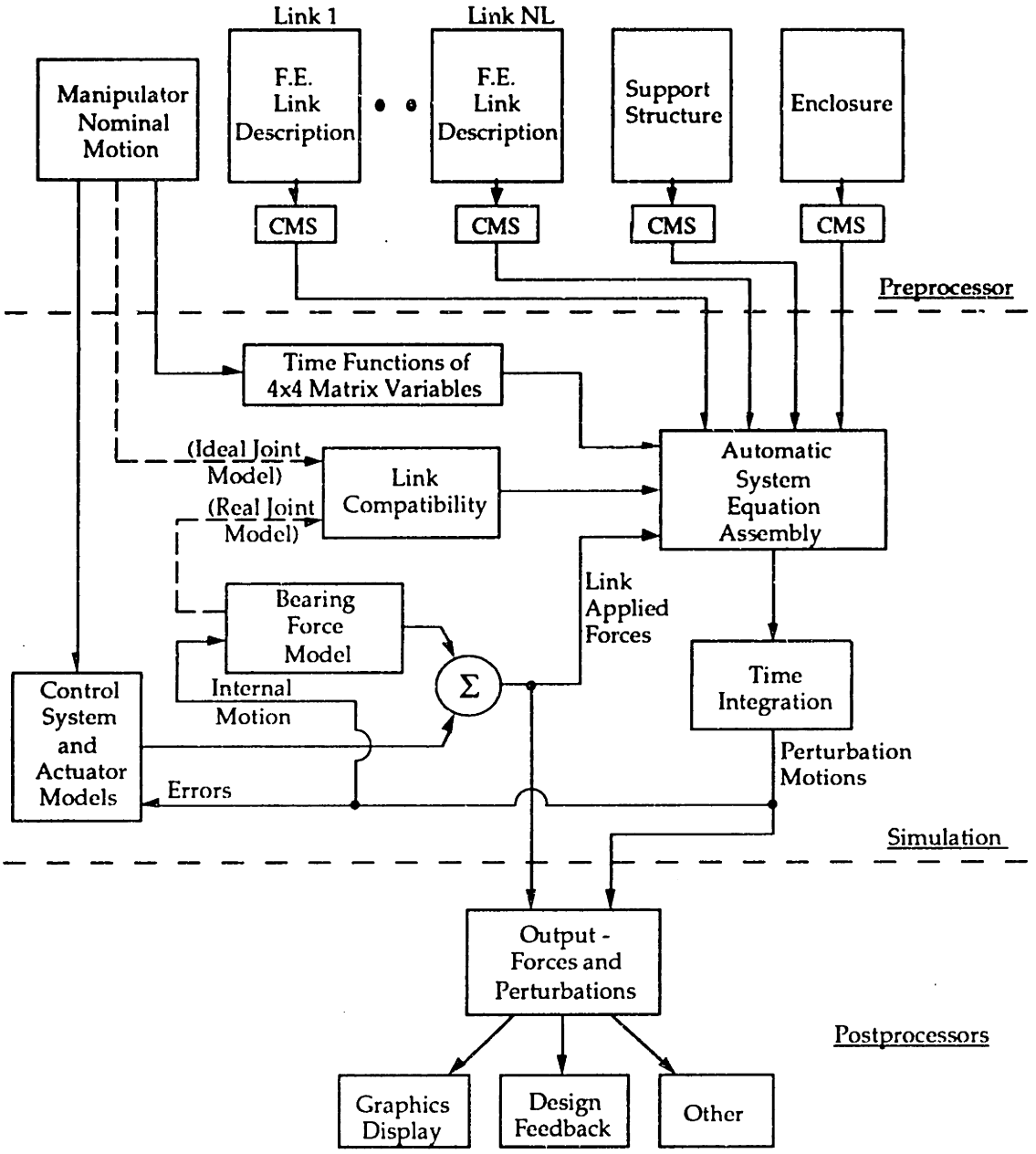

Figure 3.1. ASSET block diagram. [59]

The machine system is first separated into individual components, called links, numbered 1 ... NL. Each link's distributed mass and flexibility are described using a finite element model. In many machine systems, the links rotate and translate as the machine operates, subjecting them to large accelerations that are different for each link. Conventional finite element

structural methods can not be used when a structure consists of many parts that have different rigid body accelerations. To overcome this limitation, reference [100] showed, for systems with ideal joints, how to combine standard finite element structural models of the machine's links with Hartenberg-Denavit descriptions of their nominal motions to arrive at equations of motion that include the effects of large scale motions and accelerations on the elastic deformations of the links. These equations of motion for a given link i are derived using Lagrange's equation, with perturbation coordinates as generalized displacements. They may be stated in the familiar form:

$$\mathbf{M}_i^{dyn}\,\ddot{\mathbf{p}}_i + \mathbf{G}_i^{dyn}\,\dot{\mathbf{p}}_i + \mathbf{K}_i^{dyn}\,\mathbf{p}_i = \mathbf{f}_i^{dyn} \tag{3.1}$$

The perturbation coordinates are the elements of the vector $\mathbf{p}_i$. As generalized displacement variables, they describe the motions of the FE node points of link i with respect to a coordinate frame that follows the link's nominal motion. The vectors $\dot{\mathbf{p}}_i$ and $\ddot{\mathbf{p}}_i$ are the perturbation velocities and accelerations. Perturbation coordinates and Hartenberg-Denavit methods are described briefly in Appendices A and B. The matrices $\mathbf{M}_i^{dyn}$, $\mathbf{G}_i^{dyn}$ and $\mathbf{K}_i^{dyn}$ are the mass, damping and stiffness terms of the equations of motions. The vector $\mathbf{f}_i^{dyn}$ contains the forces applied to link i. The elements of the matrices $\mathbf{M}_i^{dyn}$, $\mathbf{G}_i^{dyn}$ and $\mathbf{K}_i^{dyn}$, and the vector $\mathbf{f}_i^{dyn}$, are in general nonlinear functions of the motions of the machine. Following reference [100], these matrix elements can be approximated by time varying functions of the known nominal motions of the machine. These functions express the nonlinear kinematics of the machine system, including configuration-dependent mass and stiffness properties and corrections for the accelerated motions of the link reference frames. The elements of these matrices are defined in Appendix C,

Equations C.25 to C.27. The elements of the force vector $\mathbf{f}_i^{dyn}$ are defined in Equation C.28, and include nonlinear equations that represent the forces applied to link i by gravity, the link's nominal motion accelerations and rotations, and external devices, such as actuators and clearance connections.

Each link's equations of motion are reduced by Component Mode Synthesis (CMS) to improve numerical efficiency [54]. After CMS, a vector of state variables, $\mathbf{a}_i$, called the link's reduced perturbation coordinate vector, can be written. The CMS transformation is expressed by a constant matrix, $\mathbf{A}_i$. The relationship between the reduced perturbation coordinates, $\mathbf{a}_i$, and original perturbation coordinates, $\mathbf{p}_i$, is:

$$\mathbf{p}_i = \mathbf{A}_i \, \mathbf{a}_i \tag{3.2}$$

A reduced equation of motion is produced for each link by substituting Equation 3.2 and its derivatives into 3.1 as the value of the link index, i, ranges from 1 to NL. The reduced link equations of motion are combined with information about the connections between the links to create a global system of equations of the form:

$$\mathbf{M}\ddot{\mathbf{q}} + \mathbf{G}\dot{\mathbf{q}} + \mathbf{K}\mathbf{q} = \mathbf{w} \tag{3.3}$$

in which the matrices **M**, **G** and **K** describe the mass, damping and stiffness properties of the system and, in general, are time varying. The vector $\mathbf{q}$, and its derivatives $\dot{\mathbf{q}}$ and $\ddot{\mathbf{q}}$ are the global independent generalized displacement coordinates, velocities and accelerations. The vector **w** describes the generalized forces applied to the system, including actuator forces and torques, internal bearing forces and torques at clearance joints, and external loads, including gravity.

Geometric compatibility information, needed to form Equation 3.3 from the individual link equations, is supplied by the compatibility matrices, $\mathbf{B}_i$. In

general, the compatibility matrices are nonlinear functions of the nominal motion vector θ and its derivatives. Each link's compatibility matrix defines the link's reduced coordinate vector, $\mathbf{a}_i$, in terms of the global coordinate vector, $\mathbf{q}$:

$$\mathbf{a}_i = \mathbf{B}_i \mathbf{q} \qquad (3.4)$$

Altering the construction of the $\mathbf{B}_i$ compatibility matrices is the key to incorporating clearance joint models into the ideal joint modeling method. Compatibility will be discussed in Section B.2, later in this chapter.

The global matrices $\mathbf{M}$, $\mathbf{G}$ and $\mathbf{K}$ in Equation 3.3 are defined in terms of the links' configuration dependent mass, damping and stiffness matrices, $\mathbf{M}_i^{dyn}$, $\mathbf{G}_i^{dyn}$ and $\mathbf{K}_i^{dyn}$ of Equation 3.1. These matrices also depend on the CMS transformation matrices, $\mathbf{A}_i$, the compatibility matrices $\mathbf{B}_i$ and their derivatives, and derivatives of the link nominal motion joint variables, θ_i. See reference [100] for a complete derivation, and see Appendices C and D of this thesis for a brief derivation. The global matrices $\mathbf{M}$, $\mathbf{G}$ and $\mathbf{K}$ are defined in Appendix D, Equations D.20 to D.27. For example:

$$\mathbf{K} = \sum_{i=1}^{NL} \mathbf{B}_i^T \mathbf{A}_i^T \mathbf{K}_i^{dyn} \mathbf{A}_i \mathbf{B}_i + \sum_{i=1}^{NL}\sum_{j=1}^{NL} \mathbf{B}_i^T \mathbf{A}_i^T \mathbf{G}_i^{dyn} \mathbf{A}_i \mathbf{B}_{ij} \dot{\theta}_j + \sum_{i=1}^{NL}\sum_{j=1}^{NL} \mathbf{B}_i^T \mathbf{A}_i^T \mathbf{M}_i^{dyn} \mathbf{A}_i \left[\sum_{k=1}^{NL} \mathbf{B}_{ijk}\dot{\theta}_j\dot{\theta}_k + \mathbf{B}_{ij}\ddot{\theta}_j\right] \qquad (3.5)$$

where NL is the number of links in the system, $\mathbf{B}_{ij}$ is defined as $\frac{\partial \mathbf{B}_i}{\partial \theta_j}$, and $\mathbf{B}_{ijk}$ is defined as $\frac{\partial^2 \mathbf{B}_i}{\partial \theta_j \partial \theta_k}$.

Before CMS, the nodes of each flexible link's finite element mode are classified as "interface" or "free" nodes. FE nodes at which forces are applied to the link by contact with other parts of the system are the "interface" nodes, and all other nodes are "free." Figure 3.2 illustrates interface and free FE

nodes. The CMS procedure, see reference [54], is explained briefly in Appendix D as it is used in ASSET. After CMS, the perturbation coordinates of the interface nodes are retained as elements in each link's a vector. However, the perturbation coordinates at all of the free nodes are replaced in the a vector by distributed coordinates called modal amplitudes.

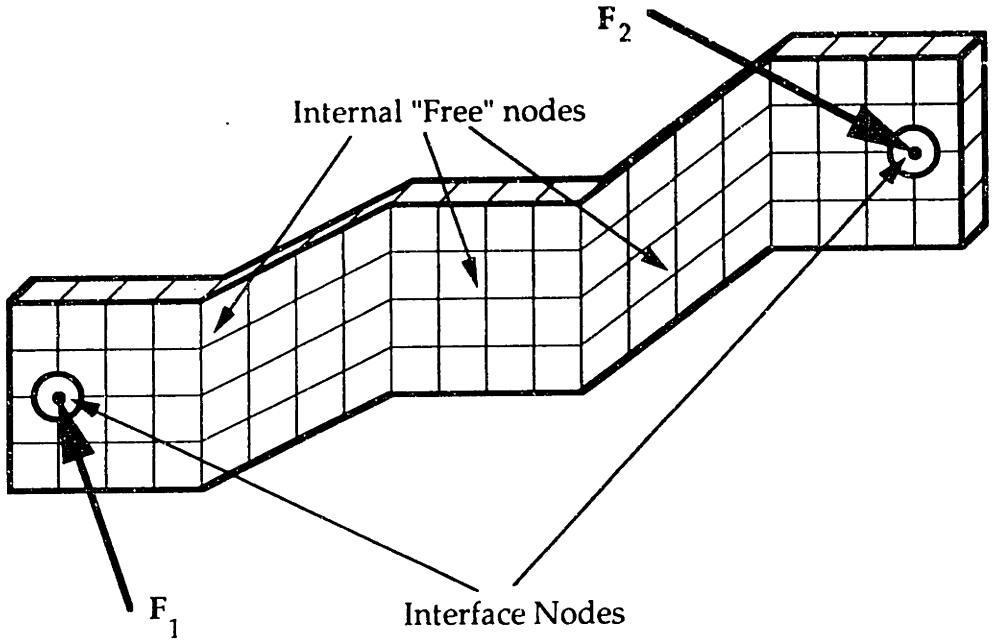

Figure 3.2. Flexible link FE model, showing interface nodes and external forces.

The vector of generalized forces applied to the interface nodes of link i is called the link's external force vector and is denoted $f_{e,i}$. Equation C.28 shows how $f_{e,i,\alpha}$, which is the α^{th} element of $f_{e,i}$, is added with other terms to form $f_{i,\alpha}^{dyn}$, the α^{th} element of the vector f_i^{dyn}, the link's dynamic force vector in Equation 3.1. Each vector element $f_{e,i,\alpha}$ may partly be determined by clearance joint forces on link i in the direction of its α^{th} degree of freedom. The other terms in Equation C.28 handle body forces due to gravity and rigid body acceleration, which act at both interface and free nodes.

B.2. Ideal Joints and Kinematic Constraints

"Compatibility" refers to the method used to express dynamic coupling between the links of a machine system. The essence of kinematic compatibility is that certain motions of one machine system element are made to match the motions of another. The mathematical statement of this condition is a *kinematic constraint.*

In traditional finite element methods, time-invariant kinematic constraints arise from the fixed joints between elements, made by methods such as bolting or welding that permit no relative motion. These kinematic constraints can be stated in time-invariant compatibility matrices, for structures in which the flexible elements are nominally at rest with respect to each other.

In the method developed in [100] and outlined above, machine systems can be modeled whose flexible parts may have large relative motions, and are connected by, for instance, revolute, spherical or prismatic joints. The method permits this by introducing time varying kinematic constraints, in which certain motions of a link are made to match those of another, but the relationship changes over time. In addition, the kinematic constraints are relaxed for motions that are permitted by the joint. For example, an ideal ball joint between two links permits the links to rotate but not translate with respect to each other. The kinematic constraint for a solid joint would constrain both translations and rotations and would not be time-varying, but that for a ball joint does not constrain rotations, and the constraints on translations are time varying.

Mathematically, kinematic constraints cause some generalized displacement perturbations of the links joined by a connection to become dependent degrees of freedom. When the global state vector, $\mathbf{q}$, is constructed for a model with kinematic constraints, the dimension of $\mathbf{q}$ is strictly less than the sum of dimensions of the links' reduced perturbation vectors:

$$\begin{pmatrix}\text{condition with one or}\\ \text{more kinematic constraints}\end{pmatrix} \dim(\mathbf{q}) < \sum_{i=1}^{NL} \dim(\mathbf{a}_i) \tag{3.6}$$

Figure 3.3a shows pictorially how the reduced perturbation vectors of two links, $\mathbf{a}_i$ and $\mathbf{a}_j$, depend on some of the same elements of the global state vector $\mathbf{q}$, when the links are joined by a kinematic constraint. Appendix D gives details for a simple example. In general, the elements of the $\mathbf{B}_i$ matrix are nonlinear functions.

Note that the presence of a kinematic constraint removes the joint's internal forces and torques in the constrained directions from the dynamic equations of the system. Since the constraint causes these generalized forces to act through zero displacement, their virtual work can be shown to be zero [100].

When kinematic constraints are relaxed, the links become free dynamic subsystems, not influenced by any other parts of the machine system. The connections between links are then expressed by force constraints, discussed in the next section.

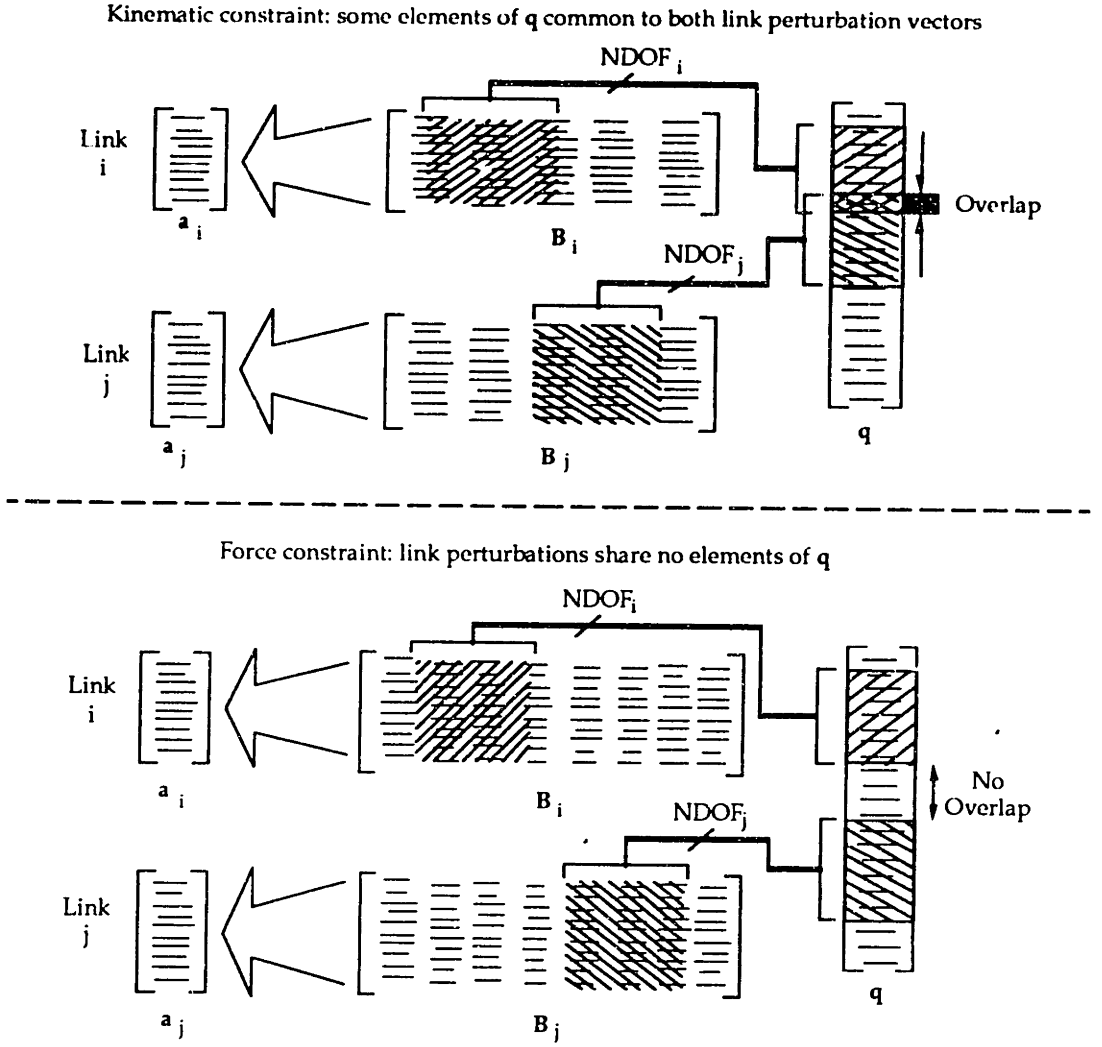

Figure 3.3. Computation of the **a** vectors using the **B** matrices.
a) Kinematic constraint. (top)
b) Force constraint. (bottom)

B.3. Clearance Joints and Force Constraints

A clearance joint model, in the sense defined at the beginning of this chapter, is a nonlinear *force constraint*. A force constraint is really just a statement of Newton's Third Law, and its concept is a simple one: two links are connected through a device that defines forces and torques as a function of the relative

motion between the links, and these generalized forces are applied as reactions to both of the links. The device can be linear or nonlinear. The forces are applied to the interface nodes through each link's external force vector, $\mathbf{f}_{e,i}$. As explained at the end of Section B.1, this vector is included in the $\mathbf{f}_i^{dyn}$ vector in the link's equation of motion, Equation 3.1. After the CMS and compatibility transformations of Equations D.9 and D.23, the forces appear in the system's global force vector **w** in Equation 3.3.

Inserting a force constraint into a global system model is accomplished by formulating the system's compatibility matrices, $\mathbf{B}_i$ in Equation 3.4, so that the interface perturbation elements of the $\mathbf{a}_i$ vectors at the force constraint become globally independent. Then, all relative translations and rotations of the links at the force constraint are permitted, and forces can be computed as functions of these motions and applied to the link's interface nodes. Figure 3.3b shows how the reduced perturbation vectors of two links, $\mathbf{a}_i$ and $\mathbf{a}_j$, depend on all different elements of the global state vector **q** when the links are joined by a force constraint, in contrast to the situation with a kinematic constraint. If *every* link in a machine system is connected by force constraints, then all the elements of all the **a** vectors are independent, the **q** vector is simply a concatenation of the $\mathbf{a}_i$ vectors, and Equation 3.6 becomes:

$$\begin{pmatrix}\text{condition with no}\\ \text{kinematic constraints}\end{pmatrix} \qquad \dim(\mathbf{q}) = \sum_{i=1}^{NL} \dim(\mathbf{a}_i) \tag{3.7}$$

The elements of the $\mathbf{B}_i$ matrix in the rows that define the interface elements of the $\mathbf{a}_i$ vector are constant, either zero or one, for force constraints.

A link may have a clearance joint or other force constraint at one interface node, and an ideal joint with kinematic constraints at another interface node. In this case, its **B** matrix may have both constant and nonlinear terms, and its

a vector may have globally dependent elements associated with the kinematic constraint of the ideal joint, and independent elements associated with the force constraint. Note also that even an ideal joint model, in the sense used in reference [100], uses a partial force constraint, for the motions that are not kinematically constrained. For example, an ideal revolute joint model does not constrain the relative rotations of the links about the axis of the joint. Thus, it is possible to model an actuator and its control system by computing a torque as a function of the relative angle between two links, and applying that torque to the $\mathbf{f}_{e,i}$ vectors of the links.

C. Clearance Connection Models

This thesis develops clearance connection force models for spherical, revolute and prismatic joints that connect two links at interface nodes. All three models are based on the same principles, but their details are different. In this section, a general description of the models is presented. Sections D and E present equations that can model spherical and revolute clearance joints. One model for a prismatic joint is discussed briefly in Section F of this chapter, and a slightly different one is presented in detail in Chapter 5.

C.1. Descriptive Overview of Clearance Connection Modeling

A clearance joint is assumed to consist of two parts that fit together with a clearance that is small compared with the overall dimensions of the joint. Each joint part is connected to a link of the machine. When the machine is set into motion, its links move, often causing impacts between the joint parts and producing contact forces that may be quite large. These contact forces react on the links attached to the joint, accelerating and deforming them. The

resulting link motions may further change the contact forces. The contact forces are defined by the relative position, orientation and velocity of the joint parts, but they also depend in complex ways on the joint's geometry and materials.

A clearance connection force model is a set of equations that predicts the internal joint contact forces for a particular type of clearance joint. The block titled "Bearing Force Model" in Figure 3.1 suggests how such a model generates forces depending on the links' relative motions, and then feeds those forces back into the dynamic equations to affect the system's motion.

Note that force transmission through a clearance joint is inherently nonlinear. As long as the two parts of the joint are not touching, they are in free flight, and they can move and accelerate freely, with no reaction forces. (Although in a real joint air drag and lubricant effects may exist, in this thesis they are not considered.) When the parts come "into contact," the joint changes nonlinearly from an element that presents practically zero resistance to relative motions of its parts, into one that presents a stiffness that may be of the same order or even larger than the end-to-end stiffness of the links attached to the joint. This fundamental nonlinearity must be considered in clearance connection models. After the joint parts touch, their force vs. displacement and force vs. velocity characteristics may also be nonlinear.

C.2. Common Features of the Joint Models

Each clearance joint model depicts the parts of the joint as geometric shapes. Shapes that can be used to model spherical, revolute and prismatic joints are shown in Figures 3.4 to 3.6, with typical clearances greatly exaggerated for

illustration. In every case, one shape is hollowed out, and the other shape is a solid that fits closely within that cavity. With knowledge of the position and velocity of the shapes, it is possible to determine whether the shapes interfere, and, if so, the location of the interference, the depth of interference, the speed with which that depth is changing, and the speed and direction with which the interference region slides across the surface of the hollowed-out part. When interference between the shapes occurs, it is interpreted as contact in the joint. The interference between shapes can be used as an indicator of the deformations that the real joint parts would experience, and a contact force can be calculated based on the deformations.

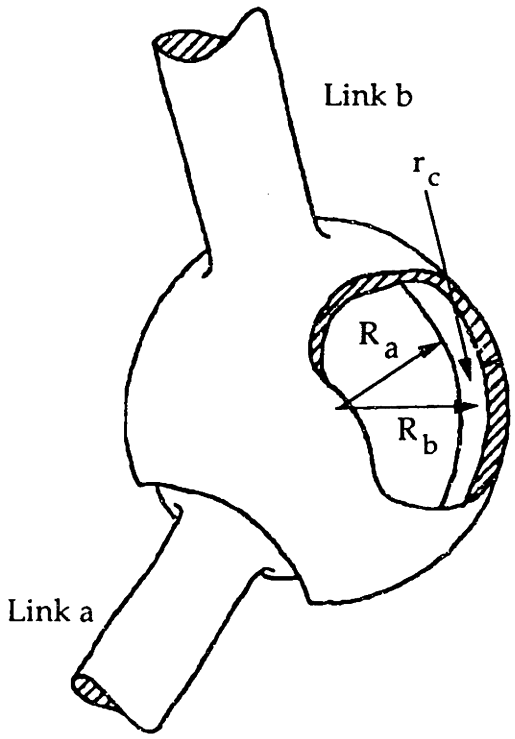

Figure 3.4. Spherical Clearance Connection Model. [28]

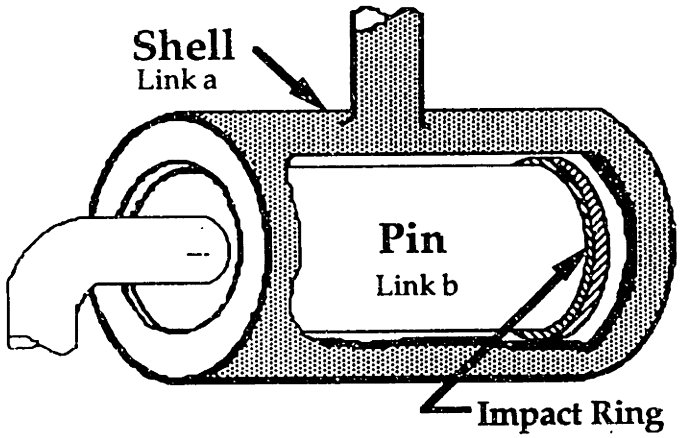

Figure 3.5. Spatial Revolute Clearance Connection Model. [59]

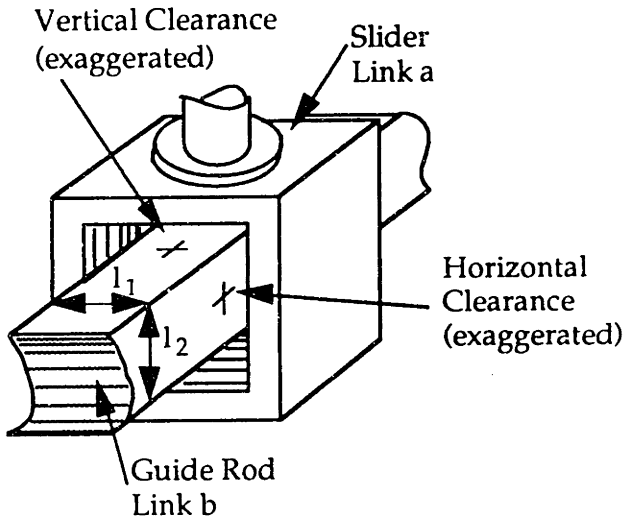

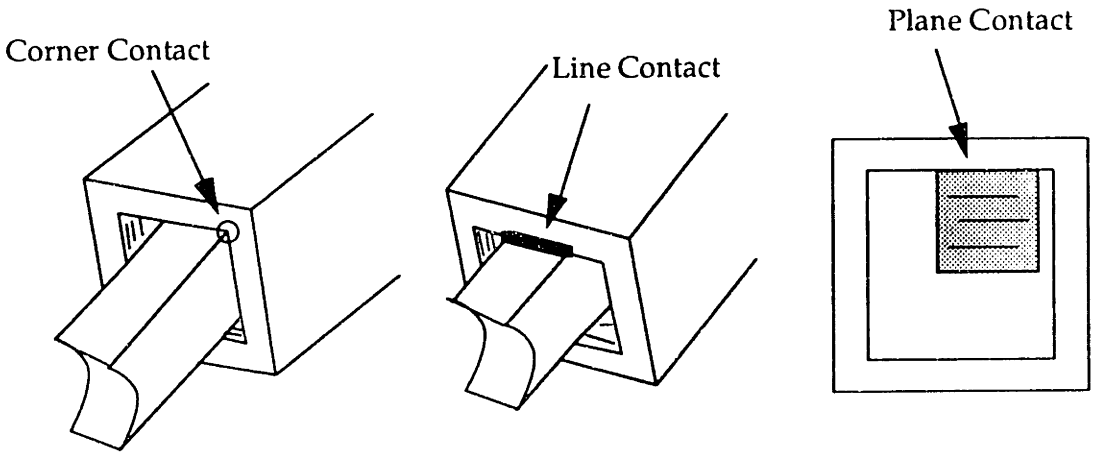

Figure 3.6. Spatial Prismatic Clearance Connection Model.

To include a clearance connection model as part of a larger machine system model, a link interface node must be associated with each joint part. These nodes will be assumed to be at the geometric centers of the joint parts, but this assumption is a useful convention, not a requirement.[1] The $\mathbf{B}_i$ matrix for a link, Equation 3.4, causes the link's interface node perturbations to appear as independent elements of $\mathbf{q}$ when force constraints are present. In a simulation using ASSET, the correspondence between elements of the $\mathbf{q}$ vector and elements of the link $\mathbf{a}$ vectors is controlled by the user, because the user supplies a subroutine to generate the $\mathbf{B}$ matrices.

The relative motions of the links joined by a clearance connection determine its internal forces. These motions fall into two categories: "ideal" and "non-ideal" motions. The ideal motions of a clearance joint are those that would be permitted by the joint's ideal model, and are always associated with symmetry in the parts of the joint. All other motions are non-ideal, associated with clearance in the joint and deformation of its parts. For example, the ideal motion of a revolute clearance joint is rotation of the joint parts about the joint axis. These categories are useful because the configuration and contact modes of a clearance joint are determined solely by its non-ideal motions. Because of symmetry, a joint's ideal motions do not affect its contact modes and can be ignored when determining the joint's internal configuration.

---

[1]The relative motion of the joint parts is analyzed using rigid-body mechanics. Thus, knowledge of the displacement and rotation of any point on the body, not necessarily the center, is sufficient.

Figure 3.7 shows the quantities that enter into the computation of relative motion at a joint. This figure first appeared in reference [28]. Two links, a and b, meet at a joint. They are shown in their nominal and perturbed positions. Their interface nodes (a,2) and (b,1), and vectors of interface perturbation coordinates, are shown. Figure 3.7 is general and applies to spherical, revolute and prismatic connections. The notation "(a,2)" is interpreted as "node number 2 on link a." The ASSET software assumes that the interface nodes of a link are nodes number 1 and 2.

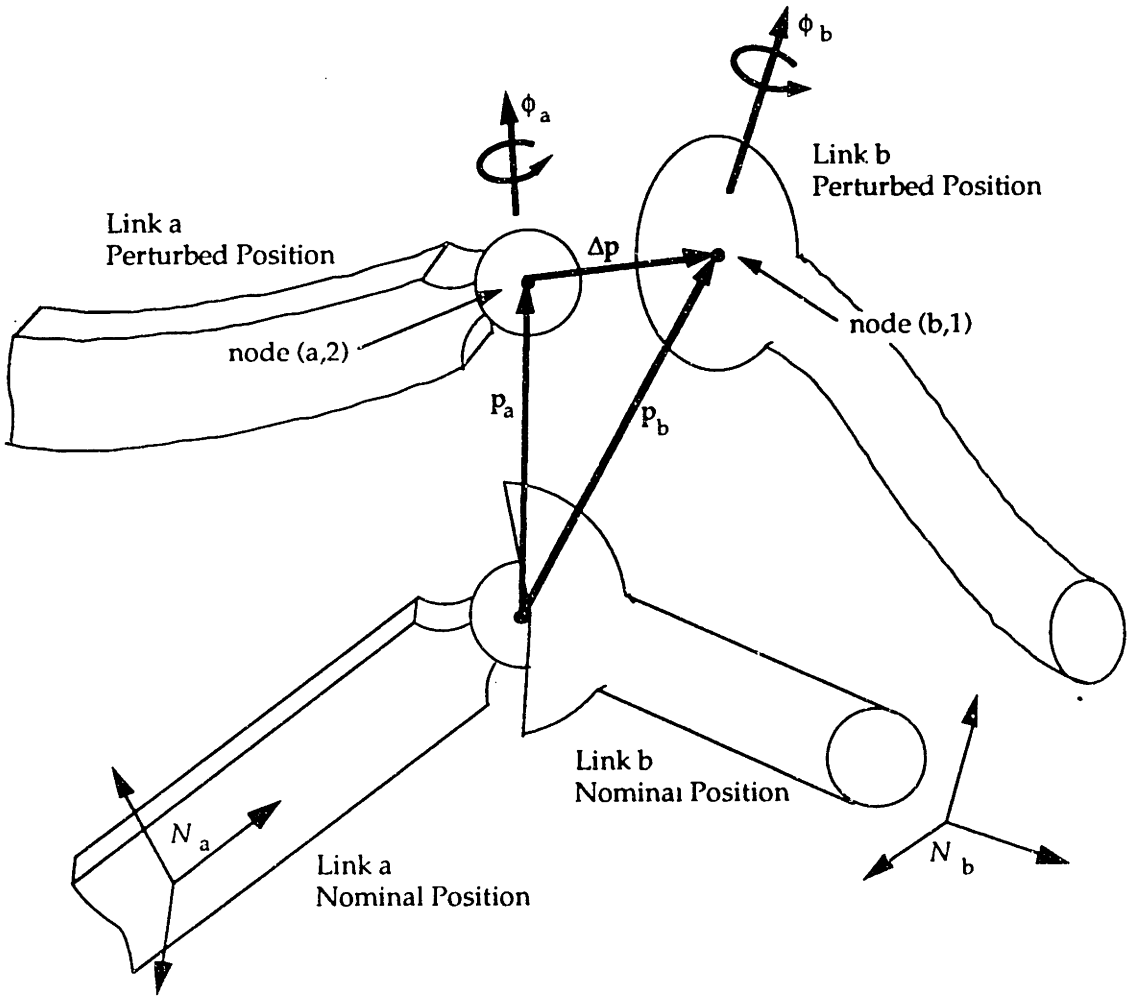

Figure 3.7. General clearance connection variables. [28]

The joint perturbations are the relative motions of node (b,1) with respect to (a,2), obtained by subtracting the perturbations of interface node (a,2) from those of (b,1). The relative translation perturbation, $\Delta\mathbf{p}$ in Figure 3.7, locates node (b,1) with respect to (a,2). The relative rotation perturbation, $\Delta\phi$, not shown in Figure 3.7, is the rotation at (b,1) relative to (a,2). The perturbations of the interface nodes are elements of the reduced link perturbation vectors, $\mathbf{a}_a$ and $\mathbf{a}_b$, obtained from the global $\mathbf{q}$ vector by using Equation 3.4 with the link index, i, set to a and b. The nodal perturbation vectors must be expressed in a common reference frame before they can be subtracted. The necessary transformation is given by the lower right 3x3 rotation submatrix of the 4x4 Hartenberg-Denavit transformation matrix that relates nominal motion frames N_b and N_a. The 4x4 matrix is $\mathbf{T}_a^b$ and its 3x3 rotation submatrix is denoted $\underline{\mathbf{T}}_a^b$. Hartenberg-Denavit methods are explained further in Appendix B. To express the vector $\mathbf{p}_{b,1}$ in the N_a coordinate frame, it is multiplied by $\underline{\mathbf{T}}_a^b$. Therefore, the joint perturbation vectors are:

$$\Delta\mathbf{p} = \underline{\mathbf{T}}_a^b \mathbf{p}_{b,1} - \mathbf{p}_{a,2} \tag{3.8}$$

for the translation perturbations, and:

$$\Delta\phi = \underline{\mathbf{T}}_a^b \phi_{b,1} - \phi_{a,2} \tag{3.9}$$

for the rotation perturbations. Equation 3.9 assumes implicitly that the rotation perturbations are small; direct vector subtraction of rotations is valid only for small rotations. Note that when the perturbation motions of the two nodes are the same, then $\Delta\mathbf{p}$ and $\Delta\phi$ are zero and the joint is in its "nominal" position, i.e., the mating parts remain coincident and aligned.

The perturbation velocities of the joint parts are the derivatives of Equations 3.8 and 3.9:

$$\Delta\dot{\mathbf{p}} = \dot{\underline{T}}_a^b \mathbf{p}_{b,1} + \underline{T}_a^b \dot{\mathbf{p}}_{b,1} - \dot{\mathbf{p}}_{a,2} \tag{3.10}$$

$$\Delta\dot{\phi} = \dot{\underline{T}}_a^b \phi_{b,1} + \underline{T}_a^b \dot{\phi}_{b,1} - \dot{\phi}_{a,2} \tag{3.11}$$

The time derivative of the Hartenberg-Denavit transformation matrix, $\dot{\underline{T}}_a^b$, is defined in Appendix B. In general, $\dot{\underline{T}}_a^b$ is a function of the nominal motion of the machine system. The perturbation velocities $\dot{\mathbf{p}}_{a,2}$, $\dot{\phi}_{a,2}$, etc., are derived by differentiating Equation 3.4.

Once the perturbation generalized displacements and velocities have been calculated, the contact configuration can be analyzed and contact forces, if any, computed. If contact exists, say that the point of contact between joint parts a and b is located with respect to (a,2) by a vector **d**. The analysis of contact configuration and evaluation of **d** depend on the joint geometry, and will be discussed in the following sections. Using rigid body mechanics, the velocity of joint part b with respect to joint part a at the point of contact is:

$$\mathbf{v}_{cont} = \Delta\dot{\mathbf{p}} + \mathbf{V}_{nom} + (\Omega_{nom} + \Delta\dot{\phi}) \times \mathbf{d} \tag{3.12}$$

where $\mathbf{V}_{nom}$ and Ω_{nom} are the nominal motion translational and angular velocities. The expression assumes that $\mathbf{V}_{nom}$ and Ω_{nom} are defined in the N_a frame; if they are not, the appropriate transformations must be applied first. Strictly speaking, the angular velocities Ω_{nom} and $\Delta\dot{\phi}$ need not have the same center of rotation, and Equation 3.12 is therefore not quite correct. Ω_{nom} is a rotation about the nominal location of the centers of the joint parts, and $\Delta\dot{\phi}$ is the joint's relative rotation about the (a,2) interface node. Therefore, an exact expression for the contribution of these angular velocities to the linear velocity at the contact point would be:

$$\mathbf{v}_{cont}^{ang} = \Omega_{nom} \times (\mathbf{d} - \mathbf{p}_{a,2}) + \Delta\dot{\phi} \times \mathbf{d} \tag{3.13}$$

This expression would replace the last term in Equation 3.12. However, since **d** is of the order of the dimensions of the joint while $\mathbf{p}_{a,2}$ is of the order of the joint clearance, and therefore much smaller than **d**, Equation 3.12 was used in practice.

The clearance connection models in this thesis use Equations 3.8 to 3.12 to compute a generalized contact force vector with 6 elements, representing the x-y-z force and x-y-z torque components of the contact force acting on link a in the N_a frame. These joint forces and torques are applied to the equation of motion of link a by adding them to the link's external force vector, $\mathbf{f}_{e,a}$. As discussed at the end of Section B.1 and in Appendix C, Equation C.28, the external force vector expresses the generalized forces applied at the interface nodes of a link and is part of the dynamic force vector, denoted $\mathbf{f}_a^{dyn}$ for link a, on the right hand side of Equation 3.1. To satisfy Newton's Third Law and the force constraint between links a and b, the computed contact force vector is then negated, multiplied by $\left(\underline{T}_a^b\right)^{-1}$ to transform it into the N_b reference frame, and added to $\mathbf{f}_{e,b}$, the external force vector for link b.

D. Spherical Clearance Connection Model

The clearance connection model for spherical joints is simple because of this joint's spherical symmetry. The clearance model consists of a ball that fits inside a socket, as suggested by Figure 3.4. The clearance model assumes that the socket is completely closed, without the access hole for the inner ball shown in the figure. Some of the modeling details and figures in this section first appeared in reference [28].

In the following, assume that the ball is attached to link a in Figure 3.4, and the socket to link b. The difference in radii of the ball and the socket is the amount of clearance, r_c, as shown in Figure 3.4. There can be at most one point of contact between the ball and socket at any given time. This condition arises from the geometry of a spherical ball contacting the inner surface of a socket of slightly larger diameter. If the amount of joint displacement, $|\Delta \mathbf{p}|$, calculated from Equation 3.8, is at least r_c, then the ball is in contact with the socket. Relative to the center of the ball, the point of contact is located on the circumference of the ball in the direction opposite to the displacement $\Delta \mathbf{p}$, so its location vector is $\mathbf{d}$, with direction $-\mathbf{u}_r$:

$$\left.\begin{aligned} \mathbf{d} &= -R_a \mathbf{u}_r \\ \mathbf{u}_r &= \frac{\Delta \mathbf{p}}{|\Delta \mathbf{p}|} \end{aligned}\right\} \text{ only if } |\Delta \mathbf{p}| \geq r_c \tag{3.14}$$

where R_a is the radius of the ball and $\mathbf{u}_r$ is a unit vector in the direction of $\Delta \mathbf{p}$.

D.1. Radial Component of Contact Force

The unit vector $\mathbf{u}_r$, defined in Equation 3.14, lies along a radius of the ball, and is a vector normal to the ball's surface at the point of contact. Since the ball and inner surface of the socket are tangent at the point of contact, $\mathbf{u}_r$ is also a normal to the socket's surface. Define the amount of radial interference between the ball and socket, s, and the rate of change of the radial interference, $\dot{s}$:

$$\left.\begin{aligned} s &= |\Delta \mathbf{p}| - r_c \\ \dot{s} &= \Delta \dot{\mathbf{p}} \cdot \mathbf{u}_r \end{aligned}\right\} \text{ only if } |\Delta \mathbf{p}| \geq r_c \tag{3.15}$$

where $\Delta \dot{\mathbf{p}}$ is defined in Equation 3.10 and $\cdot$ indicates the vector dot product. An equivalent definition for $\dot{s}$ is $\dot{s} = \frac{d}{dt}|\Delta \mathbf{p}|$.

A compressive contact force normal to the surfaces of the ball and socket is directed along $\mathbf{u}_r$. Thus, assuming linear contact stiffness and damping, the radial contact force vector can be expressed:

$$\mathbf{f}_{rad} = \begin{cases} 0; & (k*s + b*\dot{s}) < 0 \\ (k*s + b*\dot{s})\,\mathbf{u}_r; & (k*s + b*\dot{s}) \geq 0 \end{cases} \tag{3.16}$$

Negative values of $(k*s + b*\dot{s})$ are ignored because they indicate a tensile contact force, which is physically impossible. Note that the contact force could be modeled as any function of s, $\dot{s}$ and time, including nonlinear functions, by changing the right hand side of Equation 3.16. For the examples in this thesis, the linear stiffness and damping model of Equation 3.16 was used. A value for the effective stiffness, k, was determined by linearization of a Hertzian contact problem. A damping coefficient was then derived using the familiar equation $b = 2\zeta\sqrt{km}$, where m was an estimate of the effective mass seen by motions of the ball and socket and ζ was the desired damping ratio.

The contact force $\mathbf{f}_{rad}$ is added to the link's external force vector, $\mathbf{f}_{e,a}$, as explained at the end of Section C. Also as explained at the end of Section C, the contact force is then negated, transformed by multiplication with $\left(\underline{T}_a^b\right)^{-1}$, and added to $\mathbf{f}_{e,b}$ to satisfy the force constraint. Since the line of action of $\mathbf{f}_{rad}$ passes through the node (a,2) at the center of the ball, it produces no net torque on the ball.

D.2. Friction Component of Contact Force

If sliding friction forces are important, they may be added to the radial contact forces modeled by Equations 3.15 to 3.16. These forces could be modeled by a variety of linear and nonlinear force models, such as linear viscous friction or nonlinear Coulomb friction. Coulomb friction is chosen here.

The total velocity of the socket relative to the ball at the point of contact is given by Equation 3.12. For a spherical joint, $\mathbf{V}_{nom}$ in Equation 3.12 is always zero since ideal spherical joints constrain translational motion. In Hartenberg-Denavit notation [26], the kinematics of a spherical joint are expressed by three coincident revolute joints. The nominal angular velocity of the spherical joint, Ω_{nom} in Equation 3.12, is the sum of the angular velocity vectors of these three revolute joints, with appropriate transformations applied so that the result is referenced to the N_a frame. In most cases the expression is:

$$\Omega_{nom} = \Omega_{a+1}\mathbf{z}_a + \underline{\mathbf{T}}_a^{a+1}\,\Omega_{a+2}\,\mathbf{z}_{a+1} + \underline{\mathbf{T}}_a^{a+2}\,\Omega_{a+3}\,\mathbf{z}_{a+2} \tag{3.17}$$

in which Ω_{a+1}, etc., are the nominal angular velocities of the revolute joints and $\mathbf{z}_a$, etc., are the z-direction unit vectors of the N_a, etc., reference frames. These velocities are determined by a kinematic analysis of the machine system.

The sliding velocity at the point of contact in a spherical joint is the tangential component of the relative velocity vector. It may be calculated by subtracting the radial component of velocity from the total relative velocity, Equation 3.12. The magnitude of the radial velocity is $\dot{s}$ in Equation 3.15, and its direction is $\mathbf{u}_r$, Equation 3.14. Thus the sliding velocity is $\mathbf{v}_{tang}$:

$$\mathbf{v}_{tang} = \mathbf{v}_{cont} - \dot{s}\,\mathbf{u}_r \tag{3.18}$$

and a unit vector in the direction of the sliding velocity is $\mathbf{u}_t$:

$$\mathbf{u}_t = \frac{\mathbf{v}_{tang}}{|\mathbf{v}_{tang}|} \tag{3.19}$$

Since $\mathbf{v}_{tang}$ is the velocity of the socket relative to the ball, the friction force acting on the ball is in the same direction as the velocity, and its magnitude is

the product of the coefficient of friction and the normal force, when contact exists:

$$\mathbf{f}_{fric} = \begin{cases} \mu\,|\mathbf{f}_{rad}|\,\mathbf{u}_t; & |\mathbf{f}_{rad}| > 0 \\ 0; & |\mathbf{f}_{rad}| \le 0 \end{cases} \tag{3.20}$$

This model causes the friction force to change discontinuously when the tangential velocity passes through zero. For improved performance of numerical integration techniques, it may be necessary to modify this model so that the force changes continuously when the velocity passes through zero. One way to do this is to add a ramping function to Equation 3.20 such as:

$$c = \begin{cases} \dfrac{|\mathbf{v}_{tang}|}{v_{tol}}; & |\mathbf{v}_{tang}| \le v_{tol} \\ 1; & |\mathbf{v}_{tang}| > v_{tol} \end{cases} \tag{3.21}$$

where v_{tol} is chosen to be a small fraction of the maximum expected value of $\mathbf{v}_{tang}$. Thus, the definition of th friction component of contact force used is:

$$\mathbf{f}_{fric} = \begin{cases} c\,\mu\,|\mathbf{f}_{rad}|\,\mathbf{u}_t; & |\mathbf{f}_{rad}| > 0 \\ 0; & |\mathbf{f}_{rad}| \le 0 \end{cases} \tag{3.22}$$

Equations 3.21 and 3.22 could be replaced by other models, including time varying models of sliding contact force.

The vector $\mathbf{f}_{fric}$ is added to link a's external force vector $\mathbf{f}_{e,a}$, as explained at the end of Section C. Unlike $\mathbf{f}_{rad}$, $\mathbf{f}_{fric}$ produces a torque, Γ_{fric}, computed as:

$$\Gamma_{fric} = \mathbf{d} \times \mathbf{f}_{fric} \tag{3.23}$$

which must also be added to the appropriate elements of $\mathbf{f}_{e,a}$. The contact location vector $\mathbf{d}$ is defined in Equation 3.14. The forces and torques added to $\mathbf{f}_{e,a}$ are then negated, transformed by multiplication with $\left(\underline{T}_a^b\right)^{-1}$ and added to $\mathbf{f}_{e,b}$.

Equations 3.14 to 3.23 comprise a contact force model for spherical clearance connections, including the effects of sliding friction. Note that if the test $|\Delta \mathbf{p}|$ greater than or equal to r_c is not met after computing Equation 3.8, then computation of Equations 3.14 to 3.23 can be skipped because all contact forces are zero.

E. Revolute Clearance Connection Model

The geometric model for a revolute joint is a solid pin inside a cylindrical shell, Figure 3.5. The "impact ring" is shaded and exaggerated to call attention to the edges of the pin where point contact may occur, but in fact the pin is modeled as a simple cylinder with constant diameter. Some possible contact modes for this joint model are shown in Figure 3.8. Three types of contact can occur: point contact, between points on the impact ring of the pin and either the cylindrical inner surface of the shell or its end planes; line contact, between the cylindrical surfaces of the pin and the shell; and plane contact, between the end planes of the pin and the shell. Note that a plane or line contact mode requires perfect parallel alignment between the cylinder axes of the pin and shell. These modes will not be considered further.

The essential geometric features of this model first appeared in reference [75]. Some of the modeling details and figures in this section have appeared in reference [59]. A few details and figures appeared before that, in reference [28].

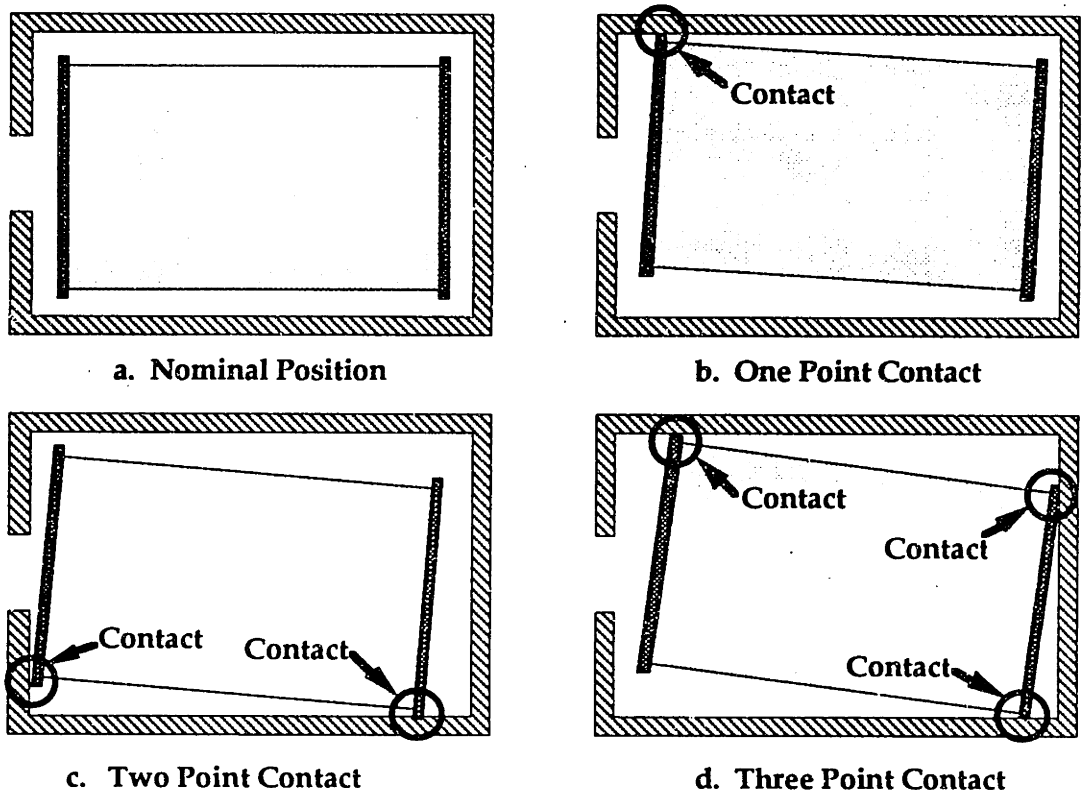

a. Nominal Position **b. One Point Contact**

c. Two Point Contact **d. Three Point Contact**

Figure 3.8. Revolute clearance connection contact modes. [28]

Assume that the shell is attached to link a and the pin to link b, as shown in Figure 3.5, so that Equation 3.8 gives the displacement of the pin relative to the shell. Figure 3.9 shows side and end views of such a model in a perturbed state. The amount of clearance in a real joint is small, but has been exaggerated in the figure for illustration. The axial clearance is L_g at each end of the pin, and the radial clearance is r_g. The radius of the pin is r_p, and its length is 2L.

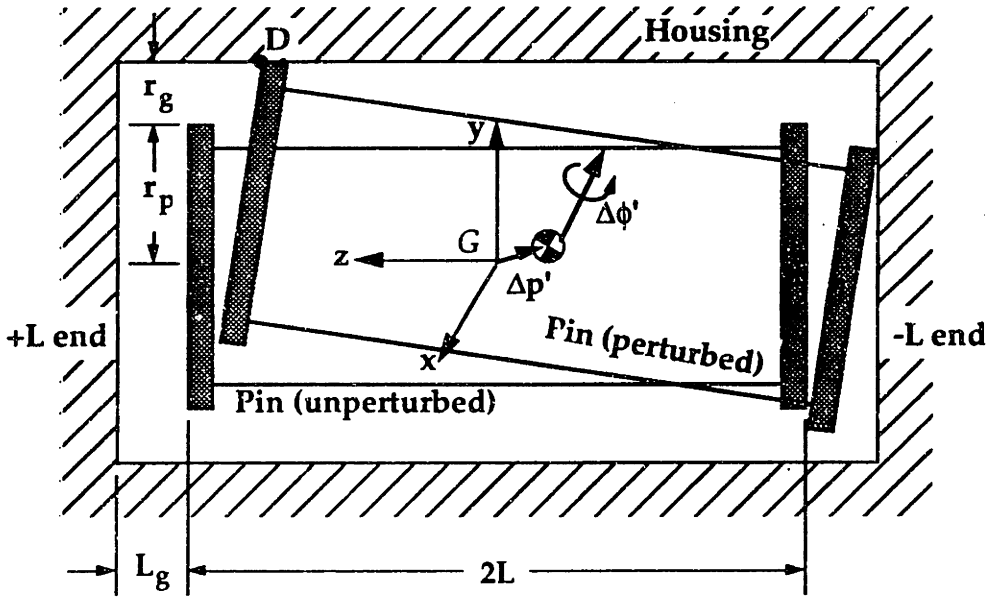

a. Side View

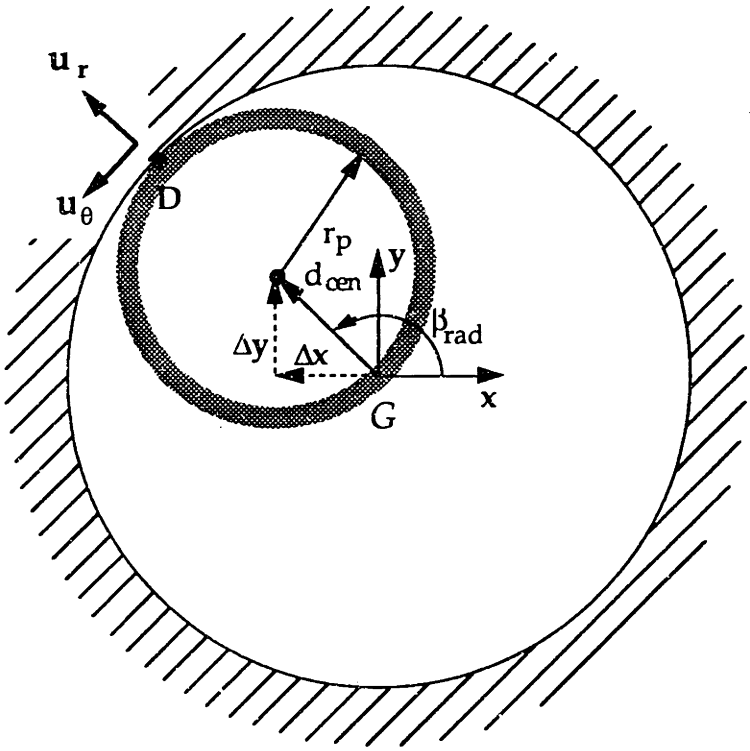

b. End View

Figure 3.9. Revolute clearance connection. [59]
a) Side view.
b) End view.

In the Hartenberg-Denavit method, the nominal motion of a revolute joint is always a rotation about the link's z axis, and therefore the length axes of the shell and pin are *nominally* aligned with the z axis of the shell's reference frame, N_a. Since the shell is part of a flexible link, the perturbation rotations of the shell, $\phi_{a,2}$ in Figure 3.7, result in the axis of the shell no longer lying along the z axis of the N_a frame. Therefore, define a local coordinate frame G attached to node (a,2), as shown in Figure 3.9. When $\phi_{a,2}$ is zero, i.e. the perturbation rotation of node (a,2) is zero, the axes of G align with the axes of N_a. By the definition of G, its z axis always lies along the centerline of the shell. When $\phi_{a,2}$ is non-zero, G rotates relative to N_a. The components of the perturbation rotation vector, $\phi_{a,2} = \{ \phi_{a,2,x} \ \phi_{a,2,y} \ \phi_{a,2,z} \}^T$, are small. Then a transformation matrix $\Phi_{a,2}$ may be defined:

$$\Phi_{a,2} = \begin{bmatrix} 1 & \phi_{a,2,z} & -\phi_{a,2,y} \\ -\phi_{a,2,z} & 1 & \phi_{a,2,x} \\ \phi_{a,2,y} & -\phi_{a,2,x} & 1 \end{bmatrix} \tag{3.24}$$

The matrix $\Phi_{a,2}$ is a small-rotation approximation to the exact rotational transformation matrix between the N_a and G reference frames. In the G frame, the perturbation vector of the pin with respect to the shell, Equation 3.8, becomes:

$$(\Delta \mathbf{p})_G = \Phi_{a,2} \, \Delta \mathbf{p} \tag{3.25}$$

Analogous definitions may be made for $(\Delta\phi)_G$, $(\Delta\dot{\mathbf{p}})_G$, etc. Since $\Phi_{a,2}$ is, approximately, a unitary rotation matrix, its inverse is $\Phi_{a,2}^T$. This inverse matrix would be used to transform vectors represented in the G frame into their components in the N_a frame, for example, $\Delta \mathbf{p} = \Phi_{a,2}^T \, (\Delta \mathbf{p})_G$.

In practice, comparison of simulations of the SCARA robot using ASSET, discussed at the end of this chapter, showed no substantive difference in predicted contact force magnitude whether $\Phi_{a,2}$ was used or not. This

suggests that the correction applied by $\Phi_{a,2}$ may be too small to matter, and some computation time can be saved by removing it. However, the derivation of contact forces in this section will retain $\Phi_{a,2}$ for completeness.

In the following discussion, the terms "axial" and "radial" will be used. "Axial" means the z axis direction of *G*, that is, along the length axis of the shell. "Radial" denotes directions in a plane parallel to the end caps of the shell, or the x-y axes of *G*, perpendicular to the axial direction.

Axial contact occurs when the impact ring touches an end plane of the shell because its axial motion exceeds L_g, as suggested at the right in Figure 3.9a. Radial contact occurs when the impact ring touches the cylindrical part of the shell because its radial motion exceeds r_g, as suggested at the left in Figure 3.9a.

The ends of the pin and shell are called "+L" and "-L," according to the sign of their z coordinate. The equations are presented here for the +L end, but can be used for the -L end simply by reversing the sign of L wherever L occurs.

E.1. Radial Contact

The maximum radial position of a point on the circumference of the +L end of the pin occurs at point D in Figure 3.9b. Point D lies on an extension of the radial vector that locates the center of the pin, at Δx, Δy in the Figure 3.9b. The displacements of the center of the +L end of the pin in response to $(\Delta \mathbf{p})_G$ and $(\Delta \phi)_G$ are:

$$\begin{aligned} \Delta x &= (\Delta \mathbf{p})_{G,x} + L\,(\Delta \phi)_{G,y} \\ \Delta y &= (\Delta \mathbf{p})_{G,y} - L\,(\Delta \phi)_{G,x} \end{aligned} \tag{3.26}$$

where a notation such as $(\Delta \mathbf{p})_{G,y}$ refers to the y component of the vector $(\Delta \mathbf{p})_G$. The test for radial contact is that the magnitude of the displacement, d_{cen}, exceeds r_g, where:

$$d_{cen} = \sqrt{\Delta x^2 + \Delta y^2} \tag{3.27}$$

The angle locating the point of contact in a radial plane is β_{rad}, shown in Figure 3.9b, and defined by:

$$\left.\begin{aligned} \sin(\beta_{rad}) &= \frac{\Delta y}{d_{cen}} \\ \cos(\beta_{rad}) &= \frac{\Delta x}{d_{cen}} \end{aligned}\right\} \text{ only if } d_{cen} \geq r_g \tag{3.28}$$

The axial location of this point is z_D:

$$z_D = L + (\Delta \mathbf{p})_{G,z} + r_p[(\Delta \phi)_{G,x} \sin(\beta_{rad}) - (\Delta \phi)_{G,y} \cos(\beta_{rad})] \tag{3.29}$$

and, therefore, the location vector of a point of radial contact is $(\mathbf{d}_{rad})_C$:

$$(\mathbf{d}_{rad})_G = [\Delta x + r_p \cos(\beta_{rad})]\,\mathbf{i} + [\Delta y + r_p \sin(\beta_{rad})]\,\mathbf{j} + z_D\,\mathbf{k} \tag{3.30}$$

where **i**, **j** and **k** are the unit vectors of the *G* reference frame. Radial and tangential unit vectors at the point of contact are $\mathbf{u}_r$ and $\mathbf{u}_\theta$, defined:

$$\begin{aligned} \mathbf{u}_r &= \cos(\beta_{rad})\,\mathbf{i} + \sin(\beta_{rad})\,\mathbf{j} \\ \mathbf{u}_\theta &= -\sin(\beta_{rad})\,\mathbf{i} + \cos(\beta_{rad})\,\mathbf{j} \end{aligned} \tag{3.31}$$

Equations 3.26 to 3.31 are valid at the -L end of the pin if the sign of L is reversed wherever L occurs. Simultaneous radial contact at both ends of the pin is possible.

If the contact condition, Equation 3.28, is met, the amount of interference between the pin and the cylindrical shell is s:

$$s = d_{cen} - r_g; \quad d_{cen} \geq r_g \tag{3.32}$$

The radial speed of the pin relative to the shell at the point of impact is:

$$\dot{s} = (\mathbf{v}_{cont})_G \cdot \mathbf{u}_r \tag{3.33}$$

where $(\mathbf{v}_{cont})_G = \Phi_{a,2}\,\mathbf{v}_{cont}$ and $\mathbf{v}_{cont}$ is defined in Equation 3.12. For a revolute joint, $\mathbf{V}_{nom}$ in Equation 3.12 is zero, $\boldsymbol{\Omega}_{nom}$ is the joint's nominal angular velocity, and $\mathbf{d}$ is $(\Phi_{a,2})^T(\mathbf{d}_{rad})_G$, using Equation 3.30.

Now the normal contact forces due to radial interference between the pin and shell may be calculated. The unit vector $\mathbf{u}_r$ defines a normal to the shell's cylindrical surface. Assuming linear stiffness and damping models:

$$(\mathbf{f}_{rad})_G = \begin{cases} 0; & (k*s + b*\dot{s}) < 0 \\ (k*s + b*\dot{s})\,\mathbf{u}_r\,; & (k*s + b*\dot{s}) \geq 0 \end{cases} \tag{3.34}$$

The condition $(k*s + b*\dot{s}) \geq 0$ prevents tensile contact force, as in Equation 3.16.

Friction forces are caused by sliding motions of the pin relative to the shell. At a point of radial contact, velocity components in the axial and tangential directions produce sliding motion. These components are:

$$(\mathbf{v}_{slid})_G = (\mathbf{v}_{cont})_G - \dot{s}\,\mathbf{u}_r \tag{3.35}$$

and they may be applied to a ramped Coulomb friction model similar to that suggested for the spherical clearance connection in Equations 3.21 and 3.22:

$$(\mathbf{f}_{slid})_G = \begin{cases} c\,\mu\,|\mathbf{f}_{rad}|\,\mathbf{u}_t; & |\mathbf{f}_{rad}| > 0 \\ 0; & |\mathbf{f}_{rad}| \leq 0 \end{cases} \tag{3.36}$$

where

$$c = \begin{cases} \dfrac{|\mathbf{v}_{slid}|}{v_{tol}}; & |\mathbf{v}_{slid}| \leq v_{tol} \\ 1; & |\mathbf{v}_{slid}| > v_{tol} \end{cases} \tag{3.37}$$

The contact forces cause a torque about the center of the shell,

$$(\Gamma_{rad})_G = (\mathbf{d}_{rad})_G \times [(\mathbf{f}_{rad})_G + (\mathbf{f}_{slid})_G] \tag{3.38}$$

where $(\mathbf{d}_{rad})_G$ comes from Equation 3.30. The generalized forces that result from contact, $[(\mathbf{f}_{rad})_G + (\mathbf{f}_{slid})_G]$ and $(\Gamma_{rad})_G$, may then be referenced to the N_a frame by multiplying by $\Phi_{a,2}^{-1}$: $\mathbf{f}_{rad} = \Phi_{a,2}^{-1}\,[(\mathbf{f}_{rad})_G + (\mathbf{f}_{slid})_G]$, etc. The generalized forces $\mathbf{f}_{rad}$, $\mathbf{f}_{slid}$ and Γ_{rad} are added to $\mathbf{f}_{e,a}$, then negated, transformed into the N_b frame by multiplying by $(\mathbf{T}_a^b)^{-1}$, and added to $\mathbf{f}_{e,b}$, as explained at the end of Section C.

Equations 3.26 to 3.38 implement a model for radial contact in a revolute clearance connection, with linear stiffness and damping for the normal components of contact force and Coulomb friction for the sliding components of contact force. The analysis must be repeated separately at the +L and -L ends of the pin to account for the possibility of contact at each end. Note that only Equations 3.26 and 3.27 are needed to check for the existence of contact; the remaining equations are used only if the contact condition $d_{cen} \geq r_g$ is met. If modeling of sliding friction is not required, then Equations 3.35 to 3.37 are not used and $(\mathbf{f}_{slid})_G$ in Equation 3.38 is zero. Other contact force models, including nonlinear ones, can be used by changing Equations 3.34, 3.36 and 3.37.

E.2. Axial Contact

The axial position of points on the circumference of the +L end of the pin is:

$$z_{ax} = L + (\Delta \mathbf{p})_{G,z} + r_p[(\Delta\phi)_{G,x} \sin(\gamma) - (\Delta\phi)_{G,y} \cos(\gamma)\,] \qquad (3.39)$$

where γ is a parameter that varies from 0 to 2π, and corresponds to the angular location of the point in the *G* reference frame's x-y plane. Axial contact occurs if there is a point on the circumference of the end of the pin

where z_{ax} is greater than $L+L_g$.[2] The extreme values of Equation 3.39 are the minimum and maximum axial positions of the end of the pin, and occur when γ meets the condition:

$$\tan(\gamma_{ax}) = -(\Delta\phi)_{G,x}/(\Delta\phi)_{G,y} \tag{3.40}$$

Equation 3.40 is satisfied by both:

$$\sin(\gamma_{ax}) = \frac{-(\Delta\phi)_{G,x}}{\sqrt{(\Delta\phi)^2_{G,x} + (\Delta\phi)^2_{G,y}}}, \quad \cos(\gamma_{ax}) = \frac{(\Delta\phi)_{G,y}}{\sqrt{(\Delta\phi)^2_{G,x} + (\Delta\phi)^2_{G,y}}} \tag{3.41}$$

and:

$$\sin(\gamma_{ax}) = \frac{(\Delta\phi)_{G,x}}{\sqrt{(\Delta\phi)^2_{G,x} + (\Delta\phi)^2_{G,y}}}, \quad \cos(\gamma_{ax}) = \frac{-(\Delta\phi)_{G,y}}{\sqrt{(\Delta\phi)^2_{G,x} + (\Delta\phi)^2_{G,y}}} \tag{3.42}$$

One of Equations 3.41 and 3.42 maximizes Equation 3.39, and the other minimizes it. To find the maximum axial displacement of the end of the pin, both Equations 3.41 and 3.42 must be substituted into 3.39 and the resulting two values of z_{ax} compared against the contact condition, $z_{ax} > L+L_g$. If contact is found, the location of the contact point from the origin of *G* is:

$$(d_{ax})_G = [\Delta x + r_p \cos(\gamma_{ax})]\,\mathbf{i} + [\Delta y + r_p \sin(\gamma_{ax})]\,\mathbf{j} + z_{ax}\,\mathbf{k} \tag{3.43}$$

where the values of $\cos(\gamma_{ax})$ and $\sin(\gamma_{ax})$ used in Equations 3.43 and 3.39 are taken from Equation 3.41 or 3.42, whichever one satisfies the contact condition.

Using procedures similar to those already explained for radial contact, the axial interference may be defined:

$$s = z_{ax} - L_g\,; \quad \text{only if } z_{ax} \geq L + L_g \tag{3.44}$$

---

[2]The contact condition at the -L end of the pin is z_{ax} *less than* $-L-L_g$, where z_{ax} is calculated from Equation 3.39 by substituting -L for L.

$$\dot{s} = (\mathbf{v}_{cont})_G \cdot \mathbf{k} \tag{3.45}$$

In Equation 3.45, $\mathbf{k}$ is the z-direction unit vector in the G frame. Then, the contact force normal to the end plane of the shell, with linear stiffness and damping, is $\mathbf{f}_{ax}$:

$$(\mathbf{f}_{ax})_G = \begin{cases} 0; & (k*s + b*\dot{s}) < 0 \\ (k*s + b*\dot{s})\,\mathbf{k}; & (k*s + b*\dot{s}) \geq 0 \end{cases} \tag{3.46}$$

Again the condition on $(k*s + b*\dot{s})$ ensures that the contact force is compressive.

Sliding occurs in the radial plane and the sliding velocity is:

$$(\mathbf{v}_{slid})_G = (\mathbf{v}_{cont})_G - [(\mathbf{v}_{cont})_G \cdot \mathbf{k}]\,\mathbf{k} \tag{3.47}$$

leading to a sliding force due to Coulomb friction in the radial plane:

$$(\mathbf{f}_{slid})_G = \begin{cases} c\,\mu\,|\mathbf{f}_{ax}|\dfrac{(\mathbf{v}_{slid})_G}{|\mathbf{v}_{slid}|}; & |\mathbf{f}_{ax}| > 0 \\ 0; & |\mathbf{f}_{ax}| \leq 0 \end{cases} \tag{3.48}$$

where

$$c = \begin{cases} \dfrac{|\mathbf{v}_{slid}|}{v_{tol}}; & |\mathbf{v}_{slid}| \leq v_{tol} \\ 1; & |\mathbf{v}_{slid}| > v_{tol} \end{cases} \tag{3.49}$$

The same notation, $(\mathbf{f}_{slid})_G$, has been used to indicate the force due to sliding friction in both Equation 3.36 and 3.48, because of their similar physical meaning. However, the normal force in Equation 3.36 is $\mathbf{f}_{rad}$, while the normal force in Equation 3.48 is $\mathbf{f}_{ax}$.

The normal and sliding axial contact forces produce a torque about the center of the shell:

$$(\Gamma_{ax})_G = (\mathbf{d}_{ax})_G \times [(\mathbf{f}_{ax})_G + (\mathbf{f}_{slid})_G] \tag{3.50}$$

As before, the resultant forces and torques are then transformed from the G frame into the N_a frame, added to $\mathbf{f}_{e,a}$, negated and transformed into the N_b frame, and added to $\mathbf{f}_{e,b}$.

Equations 3.39 to 3.50 implement a model for axial contact in a revolute joint, using linear stiffness and damping models for the normal components of contact force and Coulomb friction for the sliding component of contact force. Axial contact at both ends of the pin simultaneously is possible and must be checked for. The same equations apply if the sign of L is reversed wherever L occurs. The contact condition in Equation 3.44 becomes $z_{ax} \leq -L-L_g$ at the -L end of the pin.

Equations 3.24 to 3.50 comprise a model for revolute clearance connections.

F. Other Joint Models

A geometric model for prismatic clearance connections is shown in Figure 3.6. The prismatic clearance model consists of a sliding shell, of length l_s, and a guide rod of sides l_1, l_2.

This model may be analyzed using the same procedures that have been applied to the spherical and revolute clearance connection models. For prismatic joints, the nominal angular velocity, Ω_{nom} in Equation 3.12, is zero. The nominal linear velocity, $\mathbf{V}_{nom}$ in Equation 3.12, has magnitude equal to the relative sliding velocity between the shell and guide rod, and its direction is the **z** axis of the reference frame attached to the slider shell. As suggested by Figure 3.6, contact might occur between an inside corner of the shell and a corner of the guide rod, along an edge of the shell and a surface of the guide rod, along an edge of the shell and a corner of the guide rod, or between flat

surfaces of the shell and guide rod. In Chapter 5, a somewhat different contact model for a prismatic joint is presented in detail. That model is adapted to the instrumented sliding joint used for the experimental work in this thesis.

Clearance joint force models as described here are potentially valuable design tools, since they can provide detailed information about non-ideal system dynamic behavior due to clearance impacts. Force models for two specific joint geometries have been discussed in Sections D and E of this chapter, and a third may be found in Chapter 5. Clearance joint force models for many other types of joints can be constructed using the methods described in this chapter once a geometric model for the joint parts has been formulated. Geometric models for several joints have been presented in reference [112], for example. The joint displacements computed by Equations 3.8 and 3.9 are used with the joint's geometric model to detect whether and where internal contact occurs, and to calculate a displacement-dependent component of the contact force. Equations 3.10 to 3.12 are used to calculate velocity-dependent components of the contact force, including sliding friction. These contact forces and any resulting torques may be applied to the system's dynamic model by using the link external force vectors, as described at the end of Section C and the end of Section B.1.

In order to use Equations 3.8 to 3.12 to compute the relative motions of the parts of a joint, the small rotation assumption of Equation 3.9 must be valid, and the joint parts should be associated with interface nodes of two links connected by a force constraint, as described in Section B.

G. Example: A SCARA Manipulator

Figure 3.10 shows a SCARA manipulator with revolute clearance joints. Its dynamic behavior was simulated to demonstrate the ASSET spatial modeling software. Figures 3.10 and 3.12 to 3.15 and much of the material in this section have appeared in reference [59]. The manipulator has three links, two spatial revolute clearance joints, and one ideal prismatic joint. The Hartenberg-Denavit N_0, N_1 and N_2 reference frames are shown on Figure 3.10, and the 4x4 matrix parameters of the manipulator are given in Table 3.1.

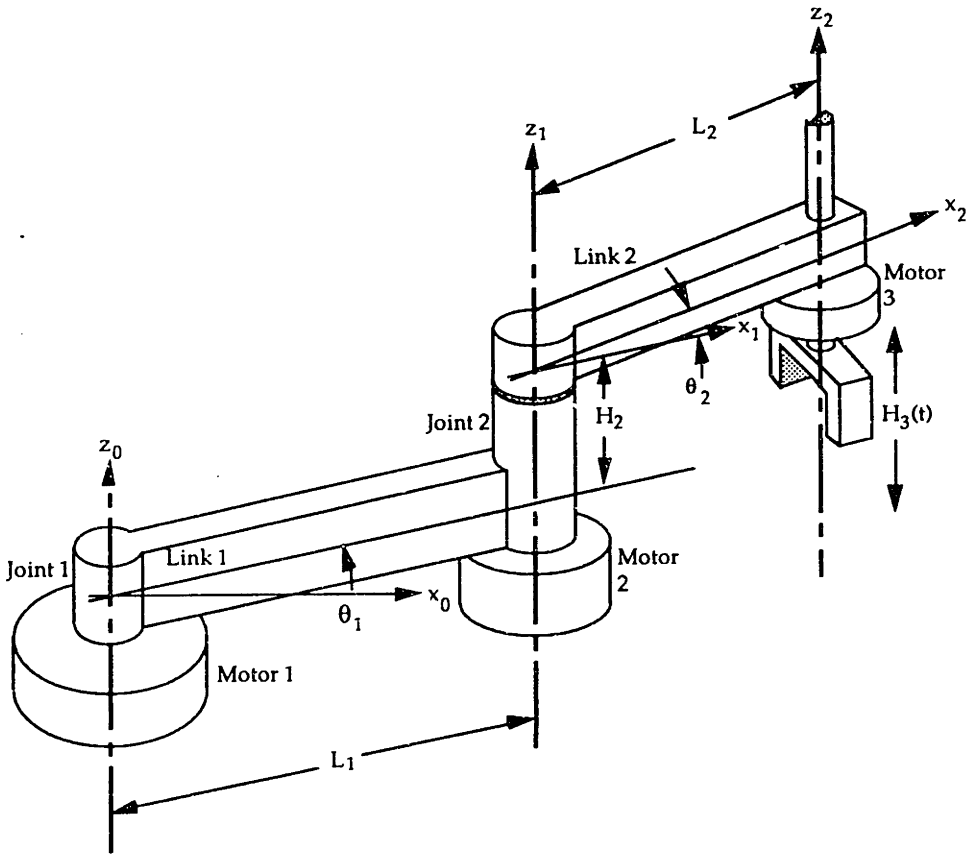

Figure 3.10. SCARA robotic manipulator, showing Hartenberg-Denavit reference frames. [59]

Table 3.1. SCARA Manipulator 4x4 matrix parameters.

Link	θ (radian)	L (meter)	α (radian)	H (meter)	Joint Type
1	$\theta_1(t)$	0.5	0	0	Revolute
2	$\theta_2(t)$	0.3	0	0.03	Revolute
3	0	0	0	$H_3(t)$	Prismatic

The mechanical properties of the manipulator's links are summarized in Table 3.2. The mass listed for each link includes the masses of attached motors and integral bearings, and, for link 3, the end effector and payload. Links 1 and 2 are modeled as flexible links, with distributed mass and flexibility. Link 3 and the end effector are modeled as a single rigid body. Motors are modeled as lumped masses and inertias at the interface node points.

Joints 1 and 2 are modeled by identical spatial revolute clearance connections with dimensions and clearances given in Table 3.3. The radial and axial contact stiffnesses of these joints are taken as 100. x 10^6 N/m. The linear damping coefficient associated with this stiffness is 363. N-s/m, based on 3.3 kg effective mass and an assumed second-order damping ratio of 1%. The sliding friction forces are neglected. The prismatic joint between links 2 and 3 is modeled as ideal, with no clearance or compliance.

Links 1 and 2 are modeled by finite element models, using 32 beam elements of approximately equal length for link 1, and 31 elements for link 2. Component mode synthesis is performed on both links with a cutoff frequency of 2000 Hz. After CMS, the link 1 model retains 3 modes with frequencies of 689, 742 and 1931 Hz. The link 2 model retains 2 modes, with frequencies of 825 and 1652 Hz.

Table 3.2. Manipulator Mechanical Properties.

Link	Length (meter)	Construction	Motor Mass (kg)	Motor Inertia ($kg\text{-}m^2$)	Link Mass (kg)
1	0.5	box section 0.03 m /side, of 0.002 m thick Al.	3.0	7.3×10^{-3}	3.3
2	0.3		1.2	5.3×10^{-4}	2.2
3	Rigid Body				0.9

Table 3.3. SRCC Dimensions.

L = 0.03 m	L_g = 50. x 10^{-6} m (0.002"), 0
r_p = 0.01 m	r_g = 50. x 10^{-6} m (0.002"), 0

A proportional plus derivative control system is designed with gains chosen by assuming that all the mechanical elements of the manipulator are completely rigid. The bandwidth and damping ratio change with different manipulator configurations, but are chosen to be 50 Hz and 0.707 for all joints in the configuration with both joint angles equal to zero. The control system gains are shown in Table 3.4.

Table 3.4. Control System Parameters.

Joint	Position Gain	Velocity Gain
1	$2105 \frac{\text{N-m}}{\text{radian}}$	$29.7 \frac{\text{N-m-sec}}{\text{radian}}$
2	$1320 \frac{\text{N-m}}{\text{radian}}$	$18.6 \frac{\text{N-m-sec}}{\text{radian}}$
3	$9000 \frac{\text{N}}{\text{m}}$	$127 \frac{\text{N-sec}}{\text{m}}$

G.1. Link Compatibility

Because of the presence of clearance joints, there are no constrained degrees of freedom on links 1 or 2. Therefore, the $\mathbf{B}_i$ matrices for these links, used in

Equation 3.4, are constant, and all of their terms are either one or zero. The **q** vector contains entries for every degree of freedom on both links. The assignment of global degrees of freedom to the link perturbation vectors is shown in Figure 3.11. Each link has twelve degrees of freedom associated with its two interface node points. As noted previously, link 1 has three modal degrees of freedom; therefore the $\mathbf{a}_1$ vector appears as **q**(1) to **q**(15). Link 2 has two modal degrees of freedom, so the $\mathbf{a}_2$ vector appears as **q**(16) to **q**(29). Link 3 is connected to link 2 by an ideal prismatic joint. Link 3 is modeled as a rigid body, and all of its degrees of freedom except its vertical translation are constrained. Therefore, link 3 has six displacement coordinates, but only one independent coordinate. Thus, there are thirty coordinates in the **q** vector.

The $\mathbf{B}_1$ matrix has dimensions [15x30], with zeros everywhere except for an identity matrix in the (1,1) to (15,15) elements. The $\mathbf{B}_2$ matrix is [14x30], with zeros everywhere except for an identity matrix in the (1,16) to (14,29) elements. The $\mathbf{B}_3$ matrix has dimensions [6x30], contains both constant and time varying terms that depend on $h_3(t)$, the nominal position of the center of gravity of link 3, and shares some columns with $\mathbf{B}_2$. The x,y,z translation and x,y,z rotation degrees of freedom at joint 3 on link 2 are **q**(22) to **q**(27). Non-zero elements of the $\mathbf{B}_3$ matrix are:

$$\begin{aligned} \mathbf{B}_3(1,22) &= 1. \quad & \mathbf{B}_3(1,26) &= -h3(t) \\ \mathbf{B}_3(2,23) &= 1. \quad & \mathbf{B}_3(2,27) &= h3(t) \\ \mathbf{B}_3(3,30) &= 1. \quad & \mathbf{B}_3(4,25) &= 1. \\ \mathbf{B}_3(5,26) &= 1. \quad & \mathbf{B}_3(6,27) &= 1 \end{aligned} \tag{3.57}$$

The implementation of ASSET allows for compressed storage of the **B** matrices, greatly reducing the number of zero elements that must be stored and optimizing matrix products that involve the **B** matrices. Due to this

compression, only fifteen elements of $\mathbf{B}_1$, 14 of $\mathbf{B}_2$, and twelve elements of $\mathbf{B}_3$, including some zero elements not shown in Equation 3.57, actually require storage.

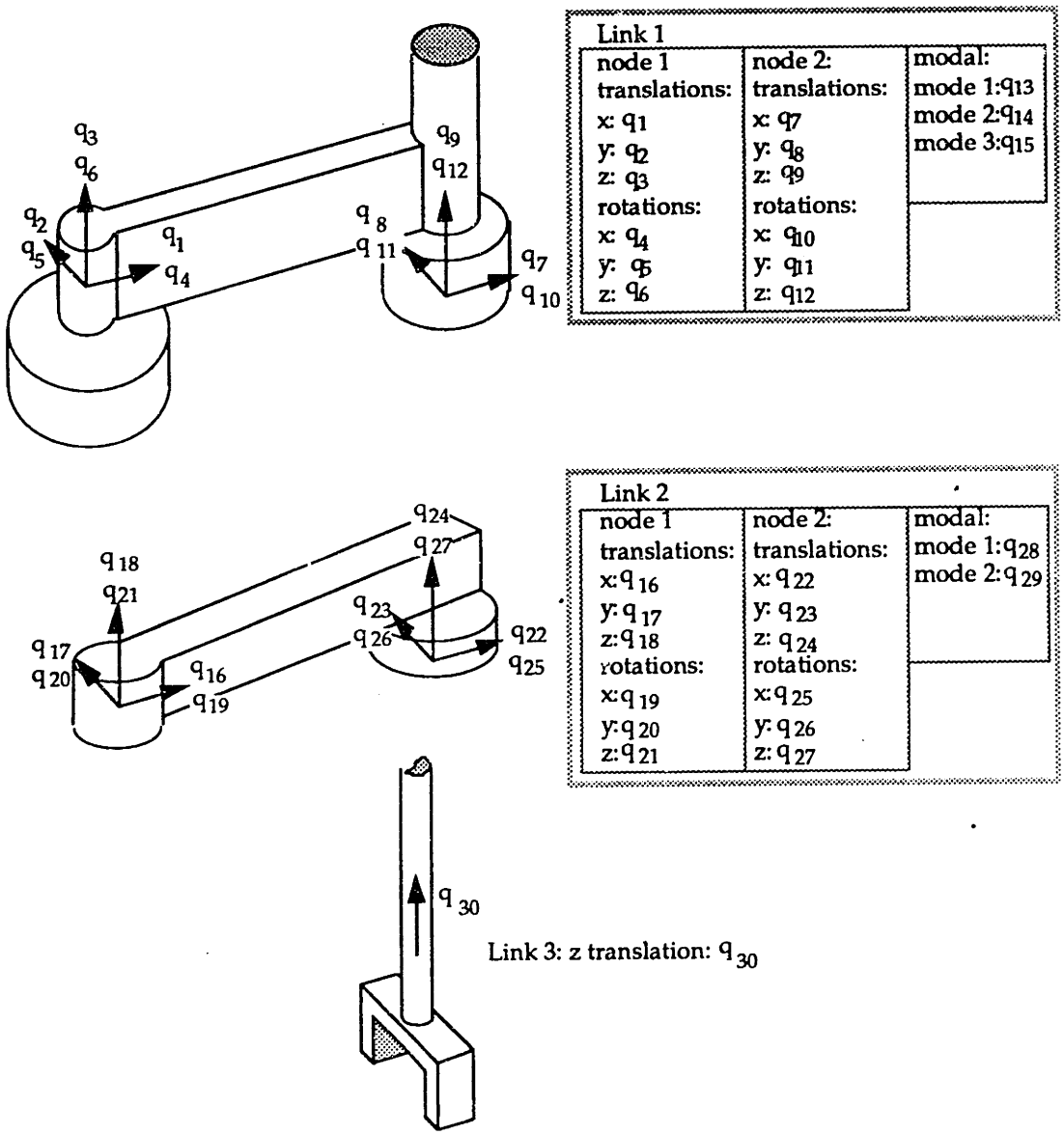

Figure 3.11. Global variables in the SCARA simulation.
Link 1: $q_1 \ldots q_{15}$
Link 2: $q_{16} \ldots q_{29}$
Link 3: q_{30}

The design goal set for the manipulator was to move a payload rapidly, placing it within 10 mm of a target position. The dynamic behavior of this manipulator was simulated with ASSET.

G.2. Results

Figure 3.12 shows the commanded path of the manipulator and its predicted response path with 50 μm (0.002 in) axial and radial SRCC clearance. The position errors in the predicted path are magnified ten times to make them visible on this figure. Because of the bending and twisting of the manipulator's links, and the spatial effects of the joint clearances and compliances, the dynamic motion of the end effector is a complex path in three-dimensional space. The nominal path for this case study includes motions of both revolute joints and the cylindrical joint. It is assumed that, just prior to the motion shown, the manipulator is at rest after reaching down to grasp a 0.4 kg payload, and that its bearing clearances are compressed. The manipulator is then commanded to move both revolute joints with constant acceleration for 0.15 seconds, next with constant velocity from 0.15 to 0.30 seconds, then with constant deceleration from 0.30 to 0.45 seconds, so that the joints are commanded to come to rest with a 45° displacement at the end of 0.45 seconds. The commanded joint angles are shown in Figure 3.13. The prismatic joint commanded motion has the same acceleration, constant velocity and deceleration pattern, but with a total displacement of 0.9 m. These rapid and large-scale motions and the clearance impacts they caused excite vibrations in the manipulator.

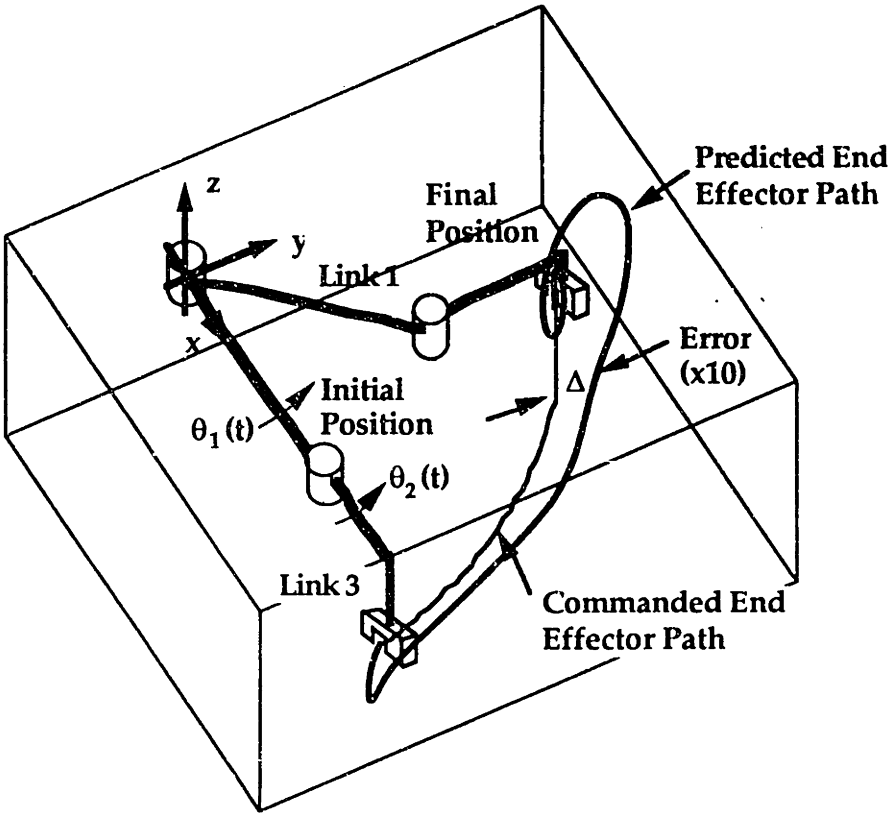

Figure 3.12. Commanded and predicted end effector paths. Errors magnified 10 times. [59]

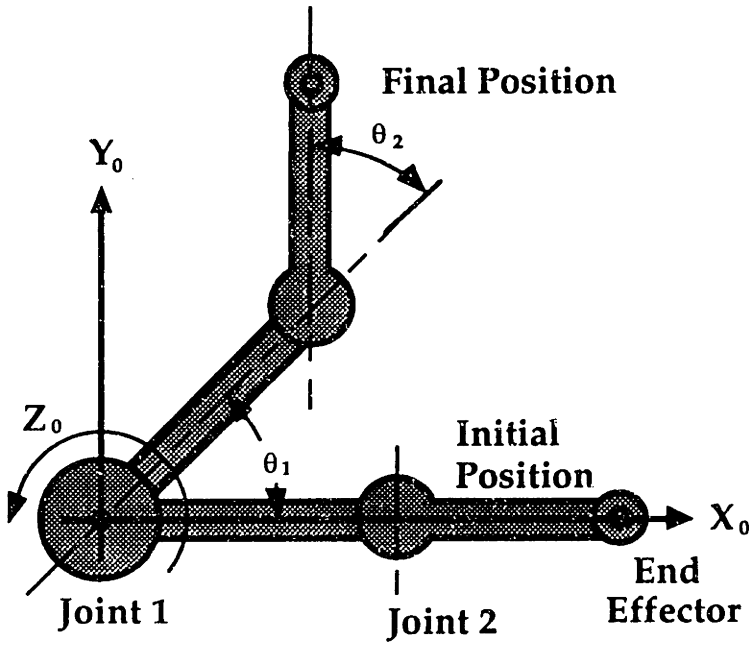

Figure 3.13. Top view of SCARA commanded joint angles. [59]

For many manipulator applications, such as precision assembly, it is important to have the end effector position error settle quickly within a small tolerance. Figure 3.14 shows the predicted end effector position error magnitudes for zero clearance and for 50 μm radial and axial clearance in the revolute joints. The plot starts at 450 msec, just as the commanded motion ceases. In both cases, the errors shown are caused by link mass and flexibility and control system dynamics, and could not have been modeled by a technique that ignored these effects. In the zero-clearance dynamic simulation, the manipulator requires about 150 msec after the end of the commanded motion to settle within a 10 mm error band, and the final error is approximately 7 mm. Modeling bearing clearances increases the predicted final tip error to more than 10 mm, and also increases the settling time. Ignoring the effects of clearance gives a prediction that the design would meet its specification if a settling time greater than 150 msec were allowed. However, including the effects of clearance in this model changes the result to a prediction that the manipulator would not meet its performance goal.

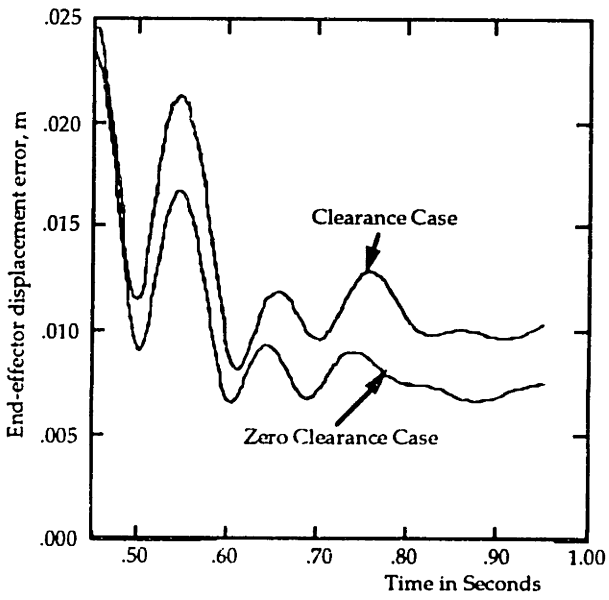

Figure 3.14. Predicted end effector error magnitude. [59]

Figure 3.15 shows the predicted internal bearing forces for the system, with and without joint clearances. Without clearance, the predicted peak internal bearing force is approximately 100 N, Figure 3.15a. The large difference in the predicted bearing force caused by a small clearance of 50 μm is shown in Figure 3.15b. The force prediction with clearance shows very large impact forces at the start of motion, caused as the manipulator moves from its rest position to begin lifting the payload. Significant impacts are predicted shortly after the command path switching points at 150, 300 and 450 msec. Figure 3.16 is the first one-tenth second of Figure 3.15b, plotted against an expanded time scale. The initial impact forces are predicted to be almost 450 N, or approximately 4.5 times larger than the highest force in the zero clearance case. The fact that the forces never drop to zero suggests that a corner of the impact ring remains lightly in contact with the wall of the housing, due to reaction forces from the actuators. These nearly impulsive forces can excite the links and other parts of the system, causing noise which may be unacceptable in a high performance product. Besides the performance degradation, these rapid and large forces may damage the bearings or other parts of the manipulator if they are not considered in its design. Later chapters of this thesis will show that, while the prediction of substantial force amplification due to impacts at clearance joints is readily believable, the values predicted by numerical simulation are not likely to be precisely accurate.

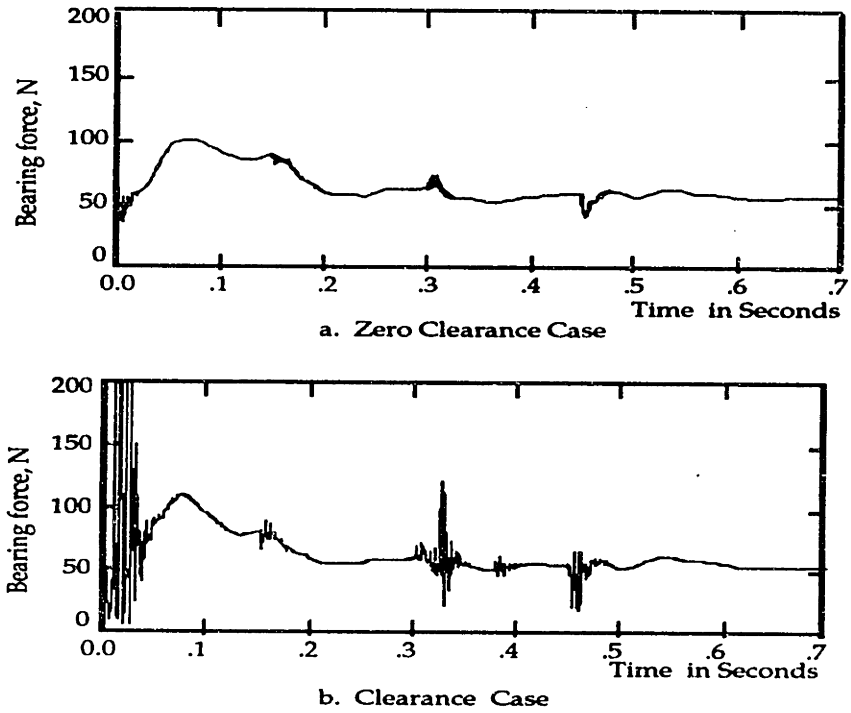

Figure 3.15. Predicted joint 1 contact force magnitudes. [59]
a) Zero bearing clearance.
b) 50 μm bearing clearance.

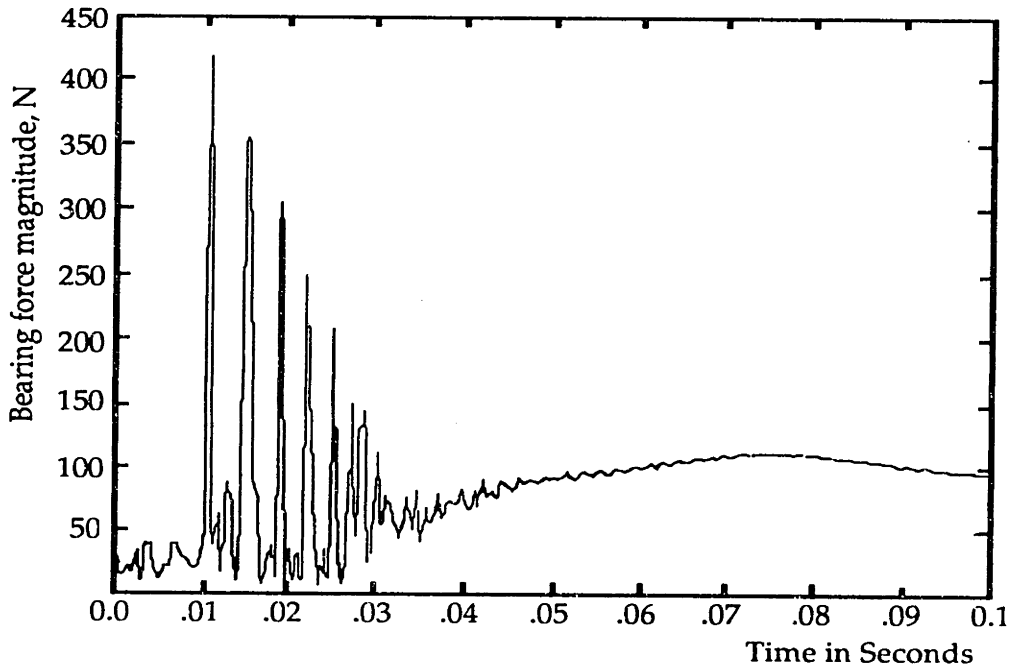

Figure 3.16. Predicted joint 1 contact force magnitude. 50 μm clearance. Expanded time scale. [59]

H. Summary

This chapter has presented a numerical modeling technique, implemented in the software system ASSET, that has been developed as a tool for the design of spatial machine systems with large scale kinematic motions, flexible links, clearance connections, and other effects such as control systems. A technique that modeled such systems with ideal joints was described. An extension to the technique that allows clearance connection force models was described. Then, detailed models for two types of clearance connections that are found in many machine systems, and a discussion on developing such models for other joint configurations, were given. Finally, an example of the method, using a design for a SCARA robotic manipulator, was given. For this machine system, the technique predicts large increases in internal contact forces and a significant deterioration in end point accuracy due to internal bearing clearances. Experiments reported in the next chapters of this thesis will evaluate the reliability of such numerical predictions.

Chapter 4. The Impact Beam System

A. System Description

In order to evaluate the validity of the computer-based modeling methods presented in Chapter 3, two experimental systems were devised and tested, and the experimental results compared with predictions from ASSET. The first of these systems is the impact beam system, the subject of this chapter. The second system is the spatial slider crank, discussed in Chapter 5.

Many of the results and figures in this chapter have appeared in reference [25].

The simple impact beam system (IBS), shown schematically in Figure 4.1, consists of a beam held at one end by a zero-clearance bearing. At the other end of the beam there is a one-dimensional adjustable clearance joint. The beam is excited by an external force, shown as F(t) in the figure, applied so that the end at the clearance connection will move back and forth in the clearance joint, generating impact forces. The assembly is mounted to a baseplate and may be enclosed within a cover. The IBS is an extension of the Impact Beam Model proposed in the past [30] for studying systems with clearances and link flexibility. Each of the elements of the IBS is designed to represent a feature typical of machine systems: the beam represents a flexible link; the clearance connection represents a bearing with internal clearance; the baseplate and cover represent the support structure and enclosures. The purpose of the IBS is to permit the study of clearance impacts without interactions among multiple nonlinearities. Its design excludes nonlinear nominal kinematic motions and multiple clearance connections. Despite the simplicity of the IBS, the results from its experimental and analytical models provide some

interesting insights into the behavior of machine systems with internal impacts.

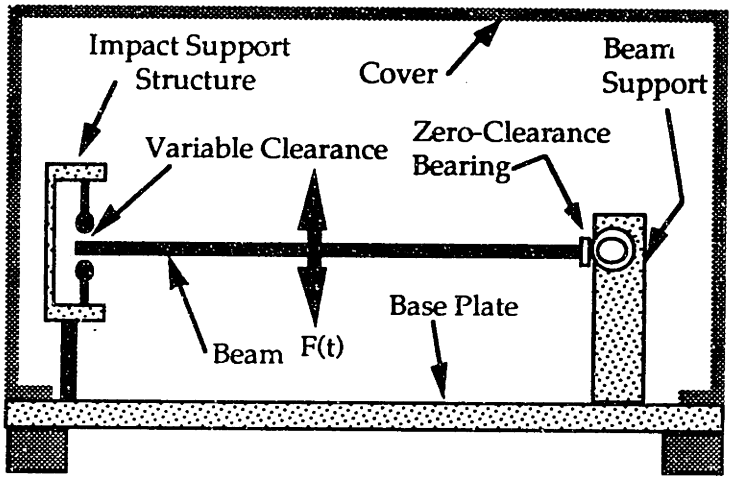

Figure 4.1. Schematic diagram of the impact beam system (IBS).

B. An Experimental Impact Beam System

An experimental version of the IBS, shown in Figure 4.2, was constructed. Charles Oppenheimer did much of the design and construction of the IBS. The experimental IBS uses either an aluminum or a steel beam. Two covers were fabricated for the IBS. Both are the same size. One is made of aluminum panels screwed to a steel frame, and the other is a one-piece fiberglass design. An electrodynamic shaker provides the force input to the IBS. The dimensions of these parts are listed in Table 4.1, referenced to the axes shown on Figure 4.2a.

Table 4.1. IBS Construction.

Element	x-dimension	y-dimension	z-dimension
Al. Beam	11" (28 cm)	0.75" (1.9 cm)	0.125" (0.318 cm)
Steel Beam	11" (28 cm)	0.75" (1.9 cm)	0.25" (0.635 cm)
Al. Baseplate	15.4" (39 cm)	12" (30.5 cm)	0.5" (1.27 cm)
Cover	15.8" (40.1 cm)	12.6" (32 cm)	10.2" (25.9 cm)
Steel Flexure Pivot	0.16" (0.4 cm)	0.75 (1.9 cm")	0.005" (0.0127 cm)

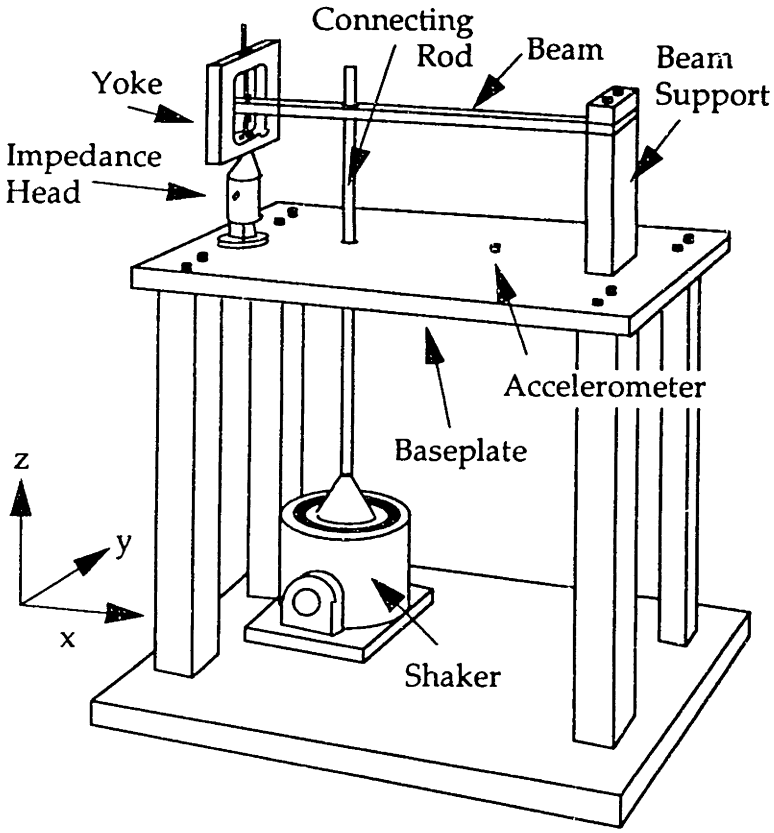

a) Schematic.

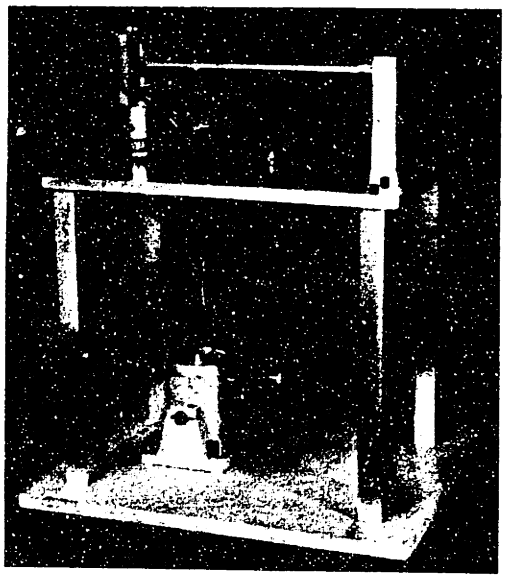

b) IBS experimental system.

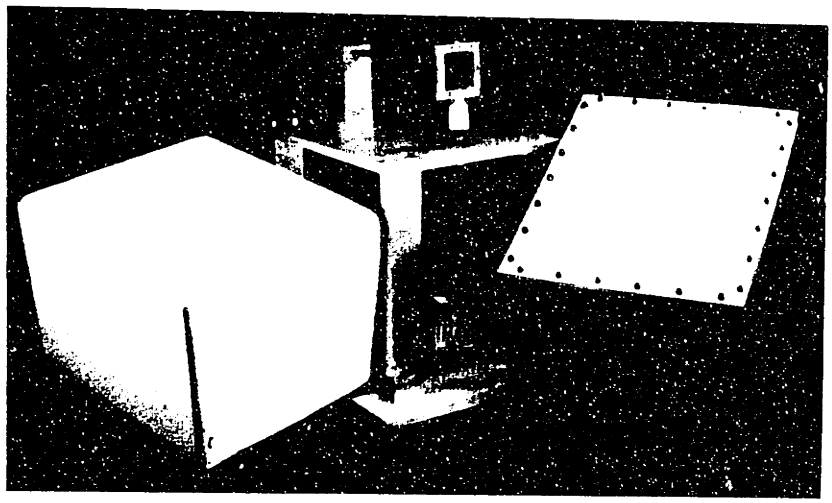

c) IBS with its fiberglass and metal covers.

Figure 4.2. An experimental model of the IBS.

The mounting methods of the steel and aluminum beams differ. The aluminum beam is simply cantilevered from the beam support post. Because the steel beam's much greater stiffness would require large shaker forces to deflect its free end if it were cantilevered, it is mounted to the beam support post using a flexure pivot. Either method provides a zero clearance beam support bearing.

A close-up of the IBS's impact yoke structure and instrumented clearance joint is shown in Figure 4.3. Clearances used in these studies ranged from 0 (no clearance) to ±0.020". This range is typical of the clearances found in many machine systems. Clearances are always listed as ±1/2 the total free motion of the end of the beam. The equipment can be adjusted so that the rest position of the beam is centered in the clearance gap.

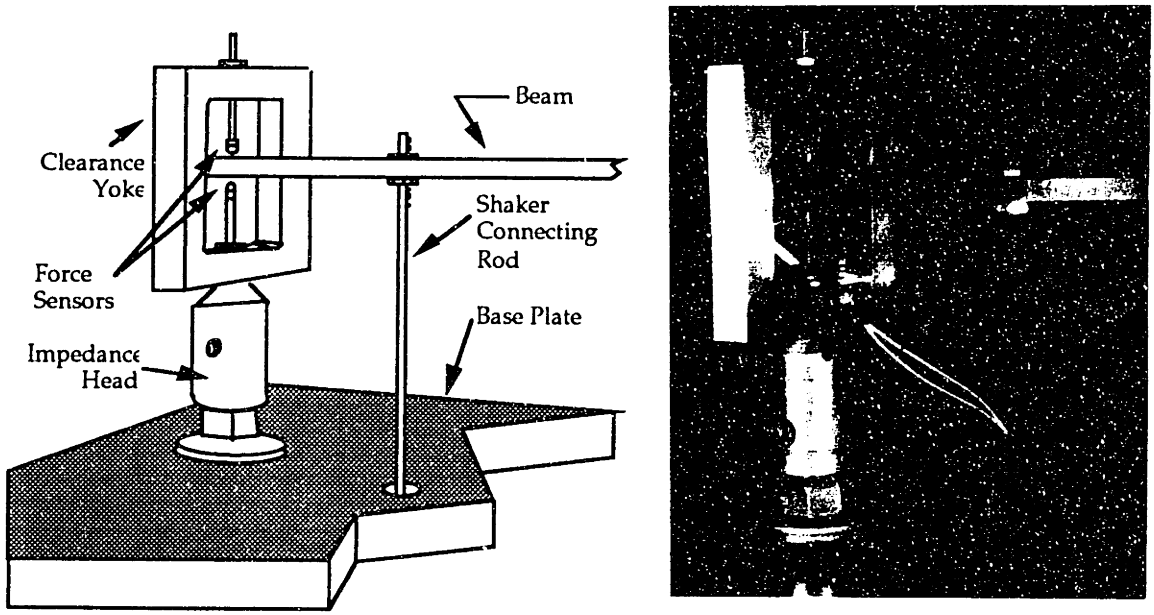

Figure 4.3. Adjustable clearance joint of the IBS.

The impedance head shown in Figure 4.3 provides an indirect measurement of the contact forces. This signal is accurate for low frequencies, but was found to be dominated by the dynamics of the yoke at frequencies above 400

Hz. Therefore, the piezoelectric contact force sensors shown in Figure 4.4 were developed to measure directly the impact forces at their tips, and were found to be accurate for frequencies up to at least 10,000 Hz. All impact force data presented here were collected using these force sensors, except Figure 4.9. Figure 4.4 shows an exploded schematic view and photographs of a contact sensor, consisting of a polarized piezoelectric ceramic element, a non-polarized ceramic insulator, brass contact washers, a steel or brass impact tip, a center screw and insulating teflon bushing, and a machined mounting stud. The force sensors were designed by Peng-Yun Gu and Uwe Müller.

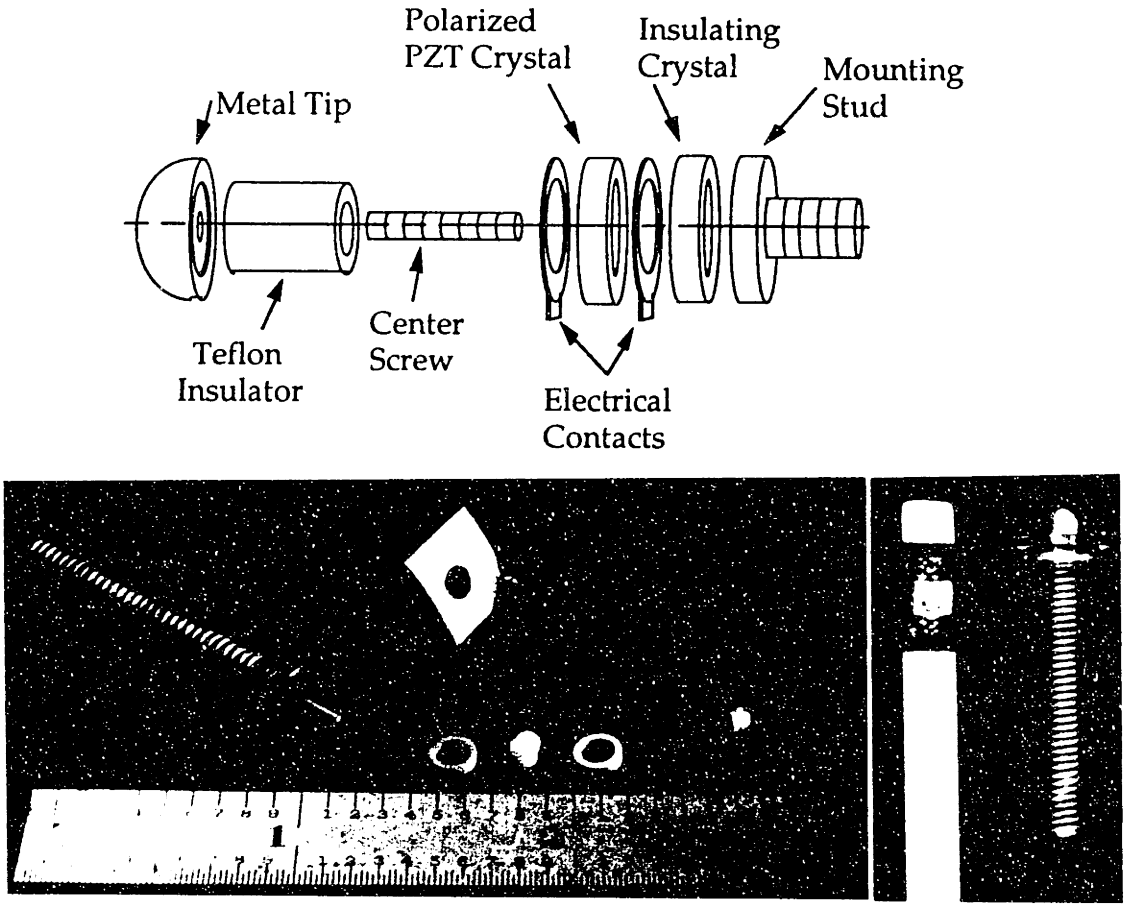

Figure 4.4. Contact sensor.

When a force is imposed on the metal tip, it is resisted by the piezoelectric element and the center screw. The change in loading of the piezoelectric

element causes a small deformation and a flow of charge, which is collected by the brass washers and converted to a measurement signal by an external charge amplifier. Therefore, the device produces a charge proportional to the imposed force as long as the deformations of the piezoelectric element and the center screw remain in the linear elastic range. Because of the small mass of the impact head, approximately 0.9 gm, and large stiffnesses of the mounting components, the contact sensor can measure high bandwidth forces, characteristic of metal-to-metal impacts. Because the accumulated charge bleeds off slowly, these sensors are not suitable for DC or extremely low frequency force measurements. However, with the charge amplifiers used, accurate response to 0.5 Hz or somewhat lower is possible.

The IBS's force sensors are individually calibrated. The procedure used is to connect a charge amplifier to the force sensor, then allow a mass of known weight to rest on the sensor until the charge amplifier's output voltage settles. The charge amplifier's gain, in volts/pico Coulomb, is known. By lifting the mass and observing the change in voltage, a calibration factor for the force sensor, in pico Coulomb/pound, can be established. The calibration factor used for each sensor is the average of 10 such trials. This method provides a low frequency calibration. However, tests of a typical force sensor showed essentially flat magnitude response and zero phase shift to slightly above 10 kHz. The same calibration procedure is used for the spatial slider crank system's force sensors, Chapter 5.

PCB Piezotronics accelerometers are mounted near the center of the baseplate and the top panel of the cover, and near one of the corners of the cover, to monitor the structural vibrations of the IBS. A Bruel and Kjaer 2702 power amplifier is used to drive the Ling 603 shaker. The power amplifier operates

in current controlled mode, minimizing the effect of the shaker's velocity-induced back EMF. The sine wave signal input to the shaker is provided by different sources, depending on the experimental requirements: both a General Radio 2215 digital FFT analyzer, also used to collect the data, and a Wavetek analog signal generator are used to provide signals with limited precision. When it is necessary to generate highly stable signals at closely spaced frequencies, an analog Spectral Dynamics signal generator is used, with a Hewlett-Packard period counter to monitor the waveform's stability and to measure its frequency precisely. Data collection for the IBS is done with a General Radio 2215 16 channel digital FFT analyzer. This analyzer samples data at a constant 65 kHz rate, and then uses software techniques to perform filtering for analysis of signals with frequency content up to 25 kHz. A Nicolet 3021 digital storage oscilloscope is also used. The IBS uses PCB 462A charge amplifiers to condition the signal from the piezoelectric contact sensors. A block diagram of the IBS instrumentation is shown in Figure 4.5.

Feeler gauges are used to adjust the clearance gap. Using this method, any desired clearance can be set with approximately ±0.001" accuracy and repeatability. Once the clearance is set, the DC component of the shaker's current can be varied to assure that the rest position of the beam is precisely centered between the contact sensors. Centering is done by supplying with shaker with a low frequency, very small amplitude sine wave superimposed on a DC current. The sine wave amplitude and the DC current are adjusted so that the beam's stroke causes it to barely touch either force sensor at the extremes of its stroke. The B&K 2702 power amplifier provides controls to facilitate these adjustments.

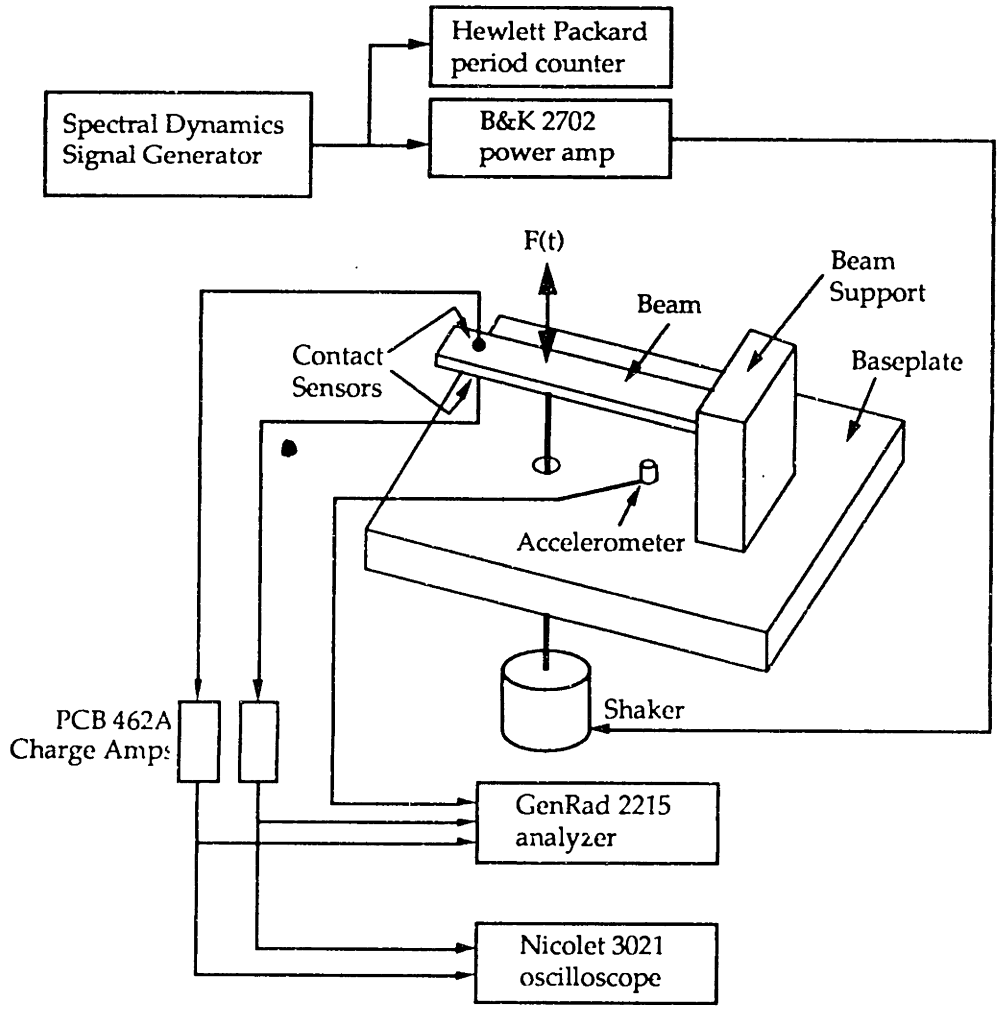

Figure 4.5. IBS instrumentation and signal flows.

C. Analytical Models of the Impact Beam System

Analytical models of varying complexity were constructed to represent the IBS in ASSET. The simplest is a rigid base model, in which the only dynamic elements are the beam, modeled using Finite Elements, and the electrodynamic shaker. The beam support post, and the yoke holding the force sensors, shown in Figure 4.2, are treated as rigid. The elements of this model are shown in Figure 4.6. The cantilevered mounting of the aluminum beam is modeled as a clamped boundary condition. The flexure pivot

mounting of the steel beam is modeled as infinitely stiff for motions in all directions except the bending and translation driven by the shaker. Further details of the dynamic model are given in Appendix F.

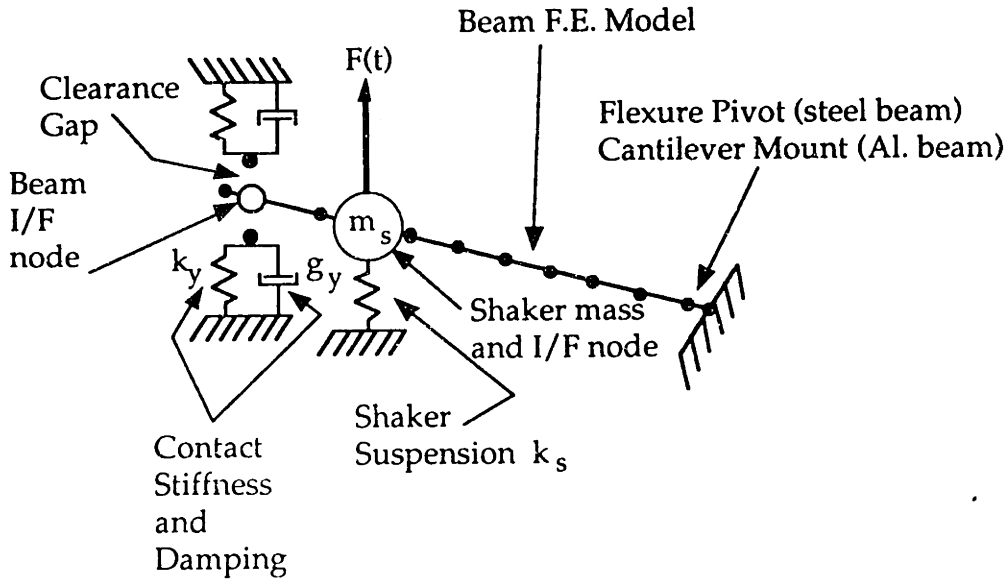

Figure 4.6. Rigid base dynamic model.

A more complete flexible base model was also implemented. It adds linear elastic FEM structural models for the impact yoke, connecting rod, beam support and base plate to the system. The base plate boundary conditions are taken as clamped at the four corners, and free elsewhere along the edges. The finite element mesh used for the flexible base model is shown in Figure 4.7. Finally, the IBS's cover may be modeled by adding a finite element representation of the cover to the flexible base model. In both the flexible base and flexible base with cover models, the only nonlinear element in the system model remains the clearance connection. All structural elements are assumed to be linear elastic, modeled using standard FE techniques.

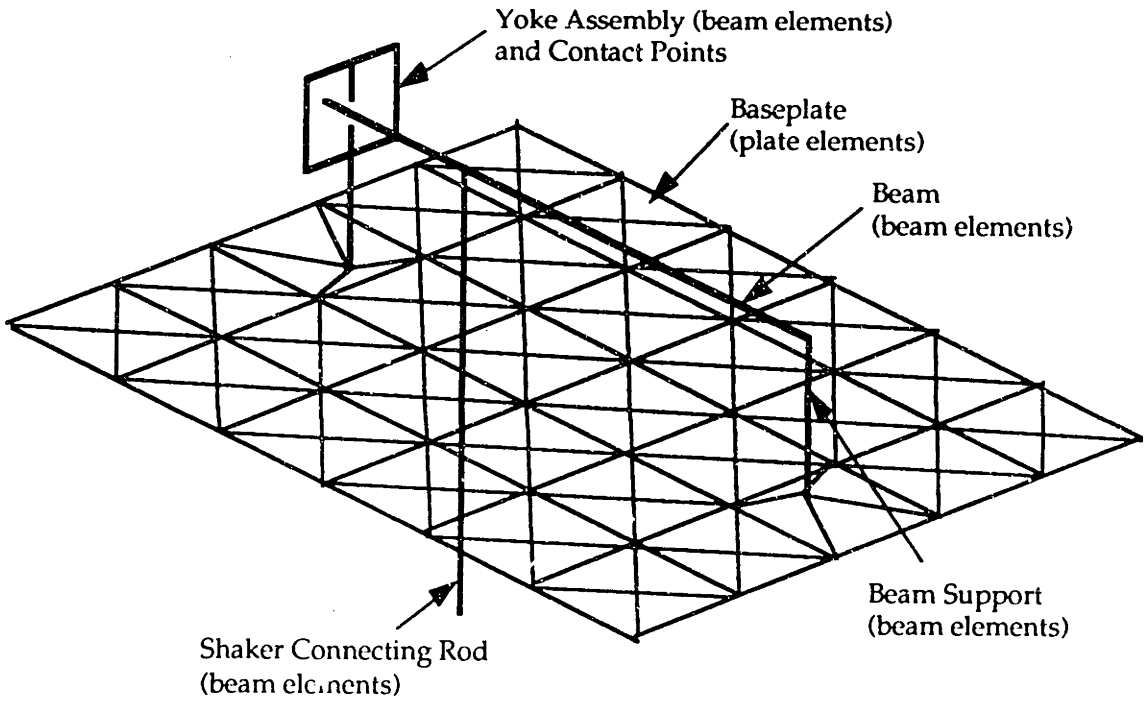

Figure 4.7. Flexible base FE model.

Contact forces are modeled by locating an FE node at the point on the beam that corresponds to the point of contact with the instrumented clearance bearing elements, i.e., the force sensors. As suggested by Figure 4.6, the contact force model is basically an impact pair [29]. This is a one-dimensional clearance connection force model, as discussed in Chapter 3. It has a zero force zone to model the clearance gap, and a contact region with compliance and damping for displacements exceeding the gap value. The stiffness coefficients are calculated using a linearized Hertzian contact analysis, and varied according to the beam construction, as listed in Table 4.2. The damping coefficient is based on an assumed linear damping ratio, an assumed portion of the beam mass as effective mass, and the calculated contact stiffness. Details are in Appendix F. The clearance gap is exaggerated for illustration in Figure 4.6. In the experimental IBS, the gap is adjustable but always a very small fraction of the beam's length.

Table 4.2. Contact Parameters in the IBS Analytical Models.

	Aluminum Beam	Steel Beam
Contact Stiffness	$5.5 \times 10^4 \frac{\text{lbf}}{\text{in}} \left(9.6 \times 10^6 \frac{\text{N}}{\text{m}}\right)$	$8.4 \times 10^4 \frac{\text{lbf}}{\text{in}} \left(1.5 \times 10^7 \frac{\text{N}}{\text{m}}\right)$
Contact Damping	$0.040 \frac{\text{lbf-s}}{\text{in}} \left(7.0 \frac{\text{N-s}}{\text{m}}\right)$	$0.11 \frac{\text{lbf-s}}{\text{in}} \left(19.6 \frac{\text{N-s}}{\text{m}}\right)$

For all the simulation results reported here, all initial conditions are set to zero. The computer used is a MicroVAX II, with the VMS operating system. The computer time required for a simulation ranges from 4 to 7 hours of CPU time per second of simulation. The IMSL subroutine DGEAR is used to perform numerical integration. This subroutine implements Gear's method, a variable-time-step predictor-corrector method. Simulations with a higher input frequency require more CPU time per second of simulation time, because there are more impacts per second. DGEAR's automatic time step adjustment causes the time step to become smaller during a simulated impact.

D. Impact Beam System Dynamic Response

The impact forces measured by the force sensors in the experimental IBS were compared with impact forces predicted by the analytical IBS models. For all results presented here, the driving force applied to the shaker, F(t) in Figure 4.6, was sinusoidal with ± 2 lbf amplitude.

D.1. Peak Impact Force Response Trends

Figure 4.8 shows calculated and experimentally measured bearing force histories for a half cycle of a 5 Hz shaker driving force. The steel beam was

used, with ±0.005" bearing clearance. The rigid base analytical model was used to generate Figure 4.8b and the other simulation results that will be presented, except where noted. These results show excellent agreement between the calculation and experiment, both qualitatively and quantitatively. The peak magnitude of the initial impact force as well as the overall shape of the curve, including resonant vibrations of the beam as it rests against the contact point, are well predicted by the simulation.

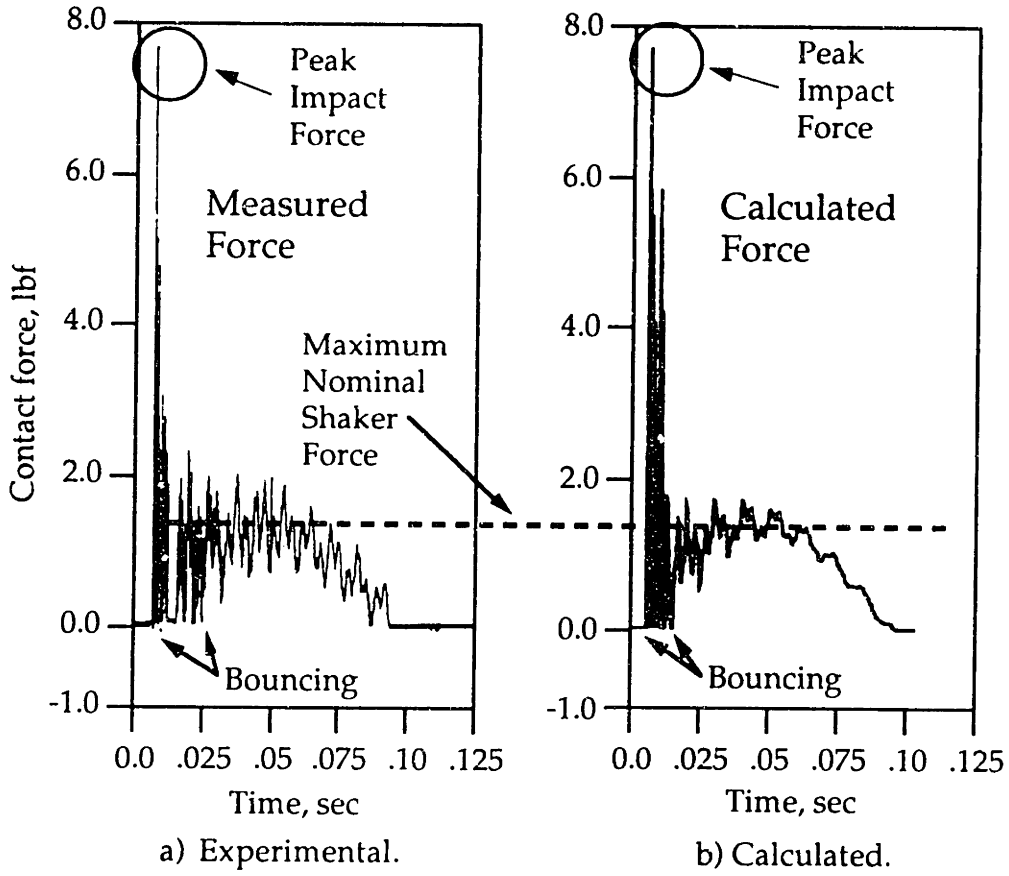

Figure 4.8. One half cycle of IBS contact force.

These figures show the form typical of impact events. There is an initial, large impact force. This initial force is followed by a period of bouncing in and out of contact, ending at about 0.020 seconds. For the remainder of the half cycle, the beam is steadily in contact with the bearing. The contact force

during this period shows a half cycle of the sinusoidal shaker driving force with superimposed decaying oscillations that are due to the beam's structural vibrations. At about 0.1 seconds, the beam loses contact, and a similar force profile occurs for the other bearing half after the beam crosses the clearance gap. Without impacts, the peak contact force, due to the 5 Hz shaker driving force alone, would be about 1.4 lbf. The impact force, however, is almost 8 lbf. The impact force is more than 5 times the nominal force. This amplification of nominal bearing forces due to impacts is well known and can have important degrading effects on system performance [29, 30, 36, 44, 59].

Figure 4.9 shows the force measured by the impedance head at the base of the yoke. Clearly, this measurement is inferior to that of the contact sensors shown in Figure 4.8. While the peak magnitude and underlying 5 Hz component of the force are accurately measured, the details of the contact force are lost in the relatively higher-frequency resonant response of the yoke structure. In addition, the large negative pulse immediately after the initial impact is obviously incorrect. If the negative pulse were an accurate indication of the contact force, it would indicate a tensile contact force, which is physically impossible. This negative pulse is due to ringing of the yoke and its support structure. Finite element analysis of the yoke and contact sensor adjusting screws shows a first resonant frequency around 400 Hz, far above the 5 Hz shaker driving frequency used in Figures 4.8 and 4.9. However, the high bandwidth of impact forces excites the yoke structure and baseplate, producing ringing.

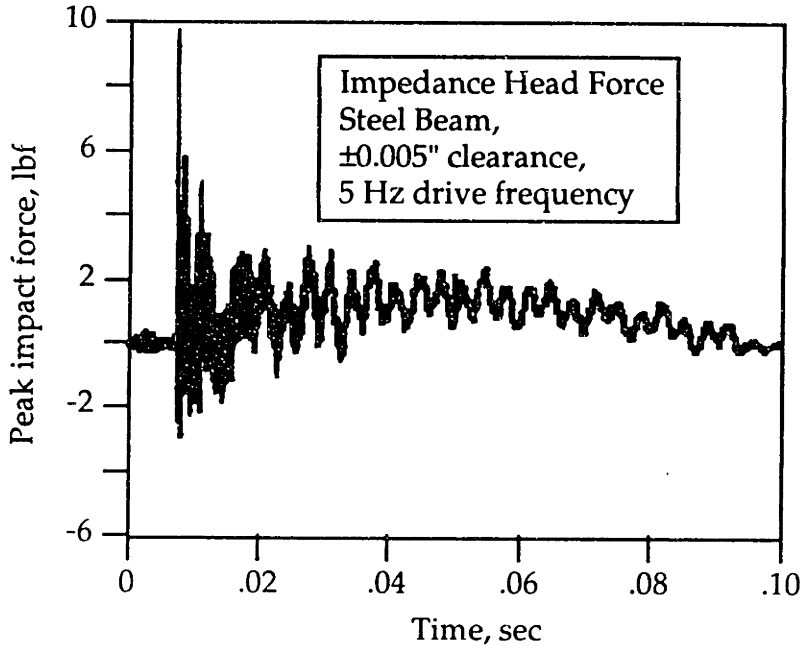

Figure 4.9. Impact force measured at impedance head.

Figure 4.10 shows a plot of peak impact forces for the steel beam IBS with a driving force frequency of 5 Hz, plotted as a function of clearance. The calculated peak forces are taken from output results like Figure 4.8b, after the simulation had gone through several cycles to allow startup transients to decay. The simulation predicts symmetrical impact forces in most cases, i.e., the force histories for the upper and lower force sensors are the same. The experimental peak forces are taken from results like Figure 4.8a. The experiment does not always give symmetrical force histories for the upper and lower impact sensors. To plot the results in Figure 4.10, force histories are taken from the upper and lower force sensors. The maximum force peak from each sensor is selected from these time histories, and then averaged to generate the experimental data points in the figure. The length of the time histories, and the trigger point and sampling rate of the acquisition system, are adjusted to assure that at least two or three peak forces are available for each sensor on every time history.

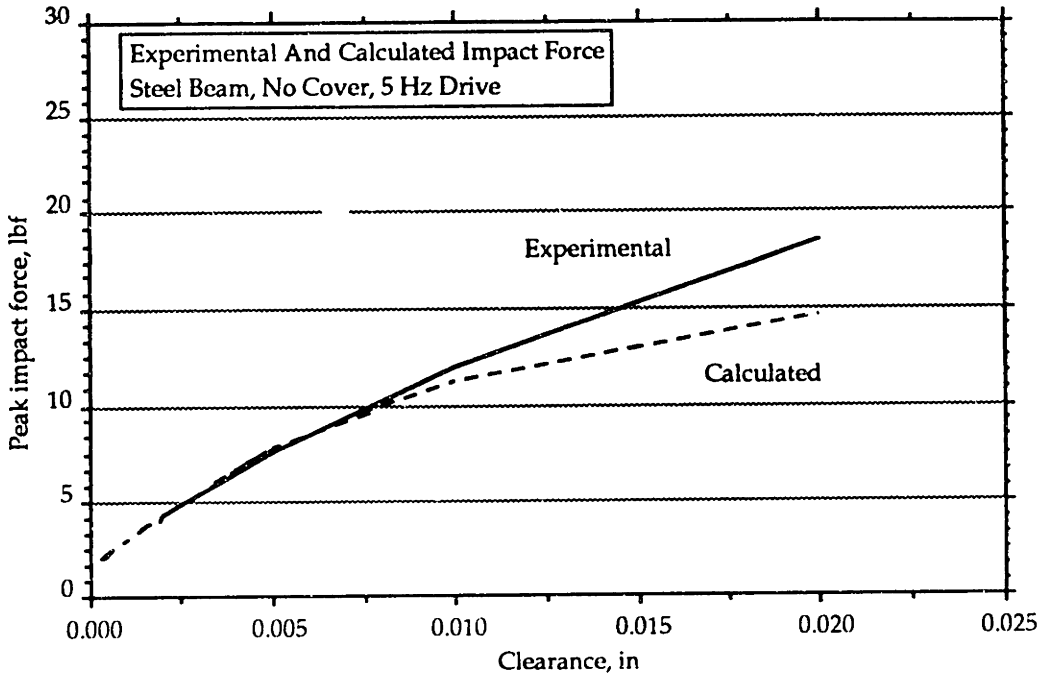

Figure 4.10. Steel beam impact force. Experimental and calculated trends as clearance is varied. 5 Hz drive frequency.

In Figure 4.10, the agreement between simulation and experiment appears better for smaller clearances. The trend of increasing peak impact force with increasing clearance is clearly predicted by the simulation and verified in the experiment. Note that at the largest clearance, ±0.020", the predicted impact force is about 15 lbf, over 10 times the maximum nominal force of 1.4 lbf. The measured impact force is even higher. Comparable results for the aluminum beam with 5 Hz drive frequency appear in Figure 4.11. Note that the vertical scales of Figures 4.10 and 4.11 are different. Impact forces at a given drive frequency and clearance setting are lower for the aluminum beam than for the steel beam, reflecting its lower mass, softer surface properties, and the additional stiffness of its cantilevered mount. This effect is both observed in the experiment and predicted by the simulation. For the aluminum beam driven at 5 Hz, the simulation consistently predicts larger impact forces than are measured in the experiment.

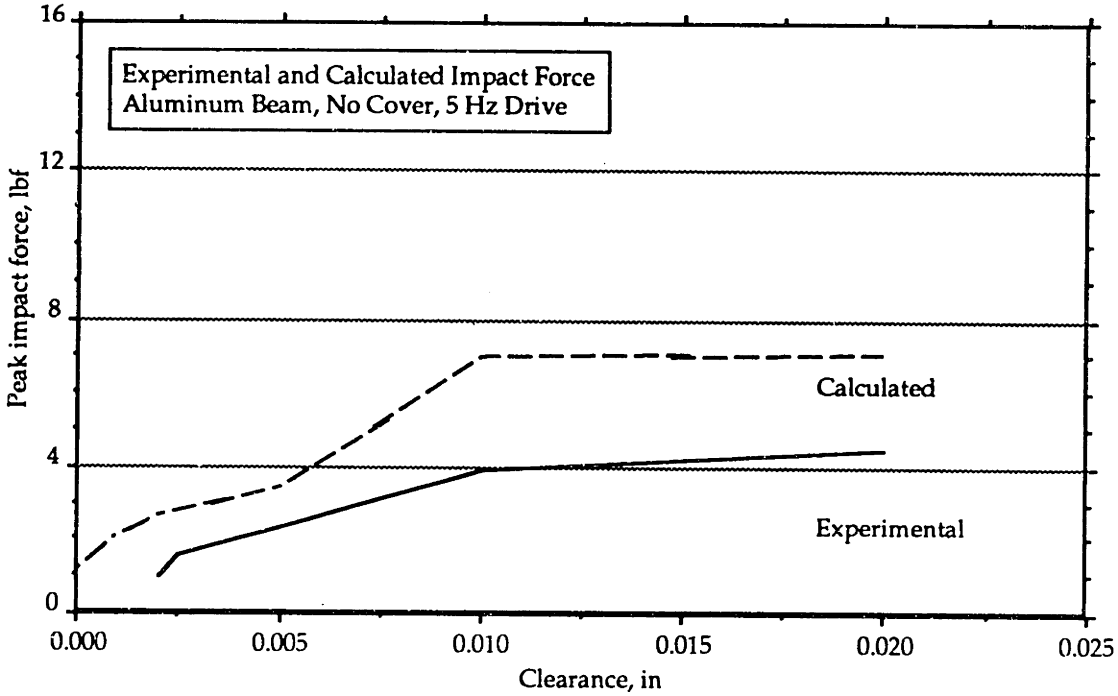

Figure 4.11. Aluminum beam impact force. Experimental and calculated trends as clearance is varied. 5 Hz drive frequency.

Figure 4.12 shows results for the steel beam driven at 20 Hz. Comparable results for the aluminum beam are shown in Figure 4.13. As for the data at 5 Hz, the simulation correctly predicts the trend in force as the clearance gap is varied. Compared with Figures 4.10 and 4.11, both the experimental and predicted forces in Figures 4.12 and 4.13 are larger, in response to the increased driving speed. At the largest clearance for the steel beam, the measured peak impact force is about 20 times the nominal, zero clearance force. As at 5 Hz, agreement between predicted and measured impact force is better for smaller clearances.

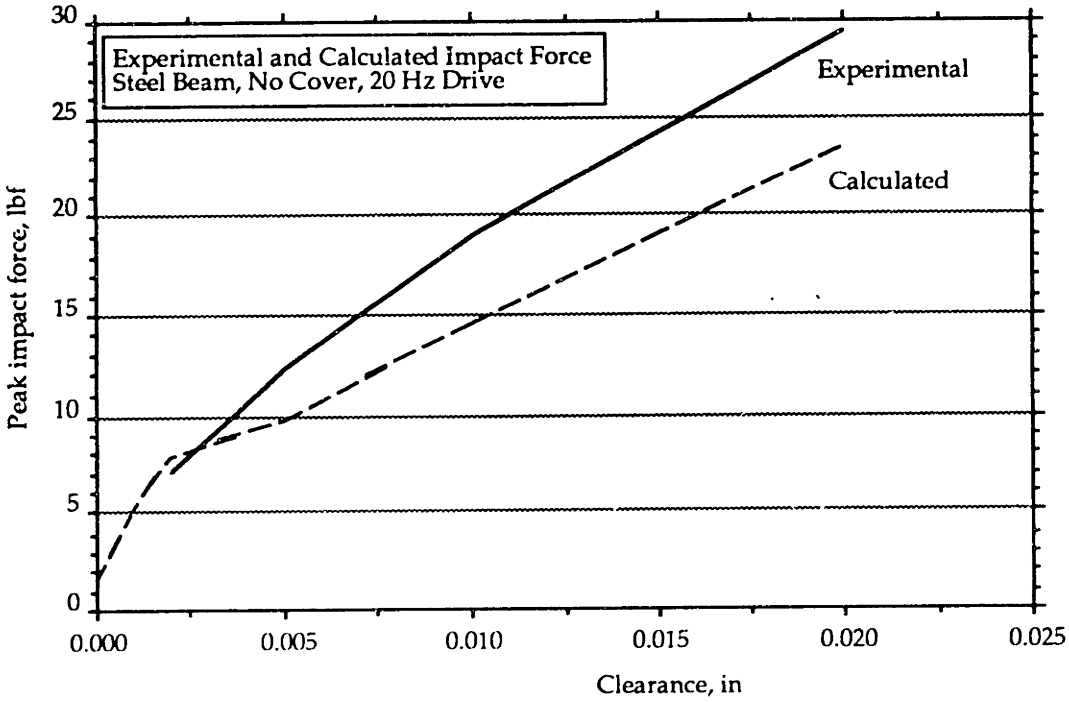

Figure 4.12. Steel beam impact force. Experimental and calculated trends as clearance is varied. 20 Hz drive frequency.

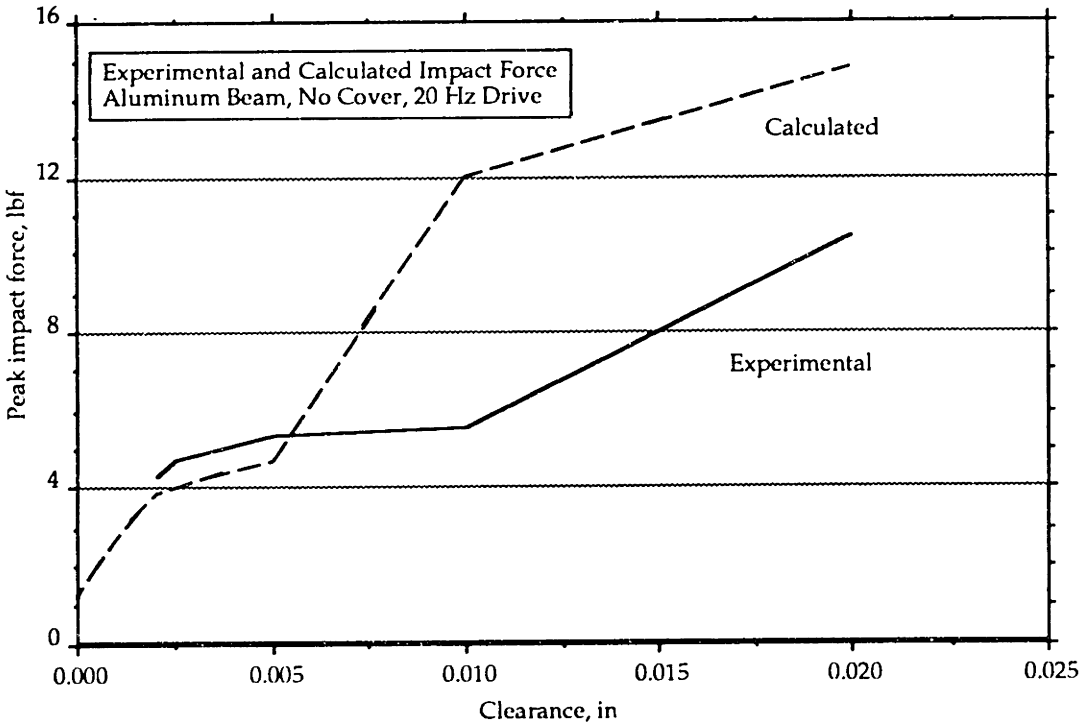

Figure 4.13. Aluminum beam impact force. Experimental and calculated trends as clearance is varied. 20 Hz drive frequency.

These results are typical of the situation at several values of clearance and drive frequency for both beams. The simulation predicts peak impact forces quite well for low frequency and/or small clearance. At high drive frequency and large gap clearance, the prediction, while still of the correct order of magnitude, does not agree nearly as well with experimental results.

D.2. Detailed Peak Impact Force Studies

The reluctance of the experiment to be modeled accurately at higher drive frequencies and clearances led to a series of experiments with the IBS, in which the clearance and beam construction were held constant, and the shaker drive frequency was varied by small, precisely controlled increments over a narrow frequency range. The shaker frequency was provided by a stable analog source, and its period was monitored with a digital period counter to maintain a stability of 2 parts in 10,000 or better during the time required for data collection.

Figure 4.14 shows the interesting results obtained using the steel beam with the clearance gap set to ±0.005", for drive frequencies bracketing 20 Hz. Data were collected in ensembles of 15 impact peaks at each frequency point and averaged for the upper and lower force sensors. In most cases, the two sensors showed very similar results and the averaging had little effect. The solid curve in the figure plots the means of these ensembles of experimentally measured impact peaks. The error bars show ±1 standard deviation for each ensemble of 15 points. The dashed curve shows the results of the rigid base simulation model. This figure shows how sensitive the impact forces can be to small changes in parameters. For a small change in shaker drive frequency, from 19.5 Hz to 21 Hz, the mean experimental impact

force changes from approximately 31 N (7 lbf) to 80 N (18 lbf), an increase of 150%. It should be noted that the lowest natural frequency of the steel beam, with free-free end conditions, is approximately 430 Hz, well above the approximately 20 Hz drive frequency used in this series of experiments. In many types of machine systems familiar to designers, structural excitation is supplied at the fundamental frequency and first few harmonics of the driving element. This is not the case in the IBS. As will be shown later, the forces generated by impacts contain broadband spectral energy far above the nominal frequency of the shaker.

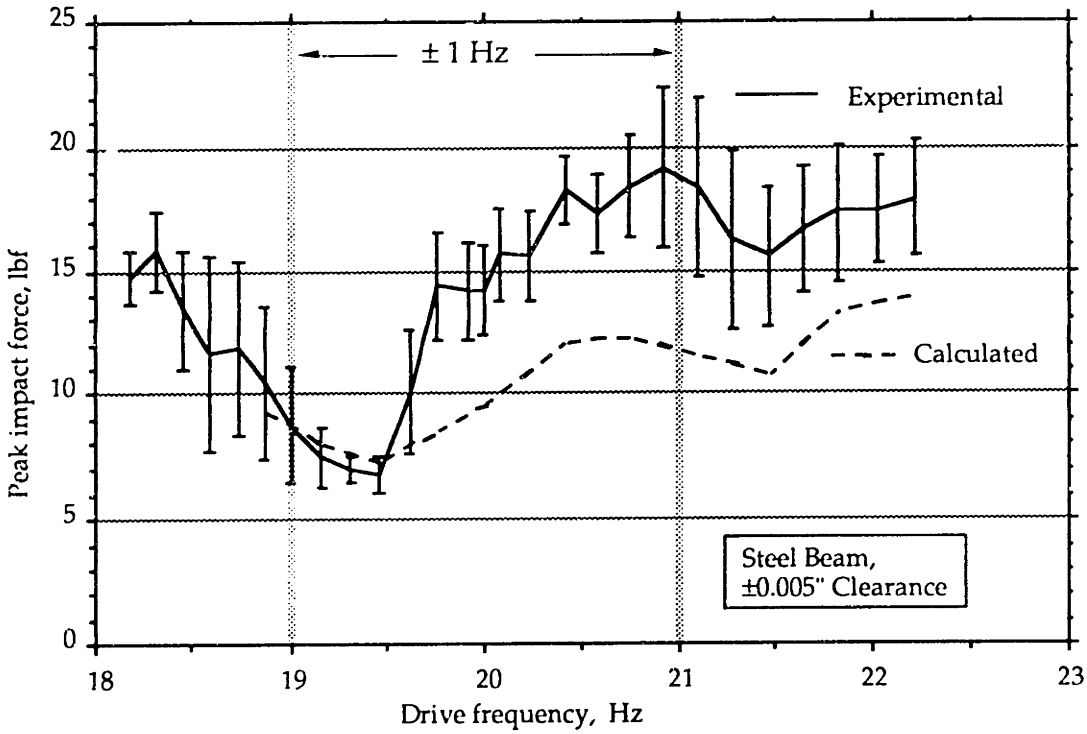

Figure 4.14. IBS sensitivity to input speed, bracketing 20 Hz.

The standard deviations of the experimental peak impact force ensembles, shown by the error bars, change as markedly as their means. The standard deviation at 19.5 Hz is about 10% of the mean; at 21 Hz, it is approximately 33% of the mean. Thus, not only are the average peak impacts at 21 Hz much

greater than those at 19.5 Hz, but also the impact forces are highly aperiodic from one machine cycle to the next. It should be emphasized that great care was taken in these experiments to assure that the operating parameters were held stable. The IBS is able to produce highly varying impact forces in response to highly stable inputs.

Figure 4.15 shows results of a similar set of experiments, again with the steel beam and gap clearance at ±0.005", but for drive frequencies around 5 Hz. As in Figure 4.14, the data were collected in ensembles of 15 impact peaks at each frequency. The curve shows the means of the ensembles and the error bars show ±1 standard deviation for each ensemble. At 4.85 Hz, the average peak impact is approximately 7.7 lbf; around 5.05 Hz, it is about 10.9 lbf. Thus, there is a variation in force of about 40% for a 0.2 Hz change in drive frequency. While less than the 150% force variation noted around 20 Hz, this is still a mark of the surprising sensitivity of the peak impact force to small changes in drive frequency. Note that this behavior is observed in the experiment, and is in no way a numerical artifact of the analytical model. Standard deviations of the impact force ensembles for drive frequencies around 5 Hz, Figure 4.15, are consistently much smaller than those around 20 Hz, Figure 4.14.

The conclusion that appears to emerge from these studies is that, while the impact beam system exhibits underlying trends similar to those seen in earlier studies [29, 30], namely that the impact forces increase as clearance and drive frequency are increased, it is clear that these trends are not smooth curves. The trends exhibit substantial and important local variability. In addition, there can be significant variation in impact peaks from one cycle to the next of the input force, even when care is taken to assure stable inputs.

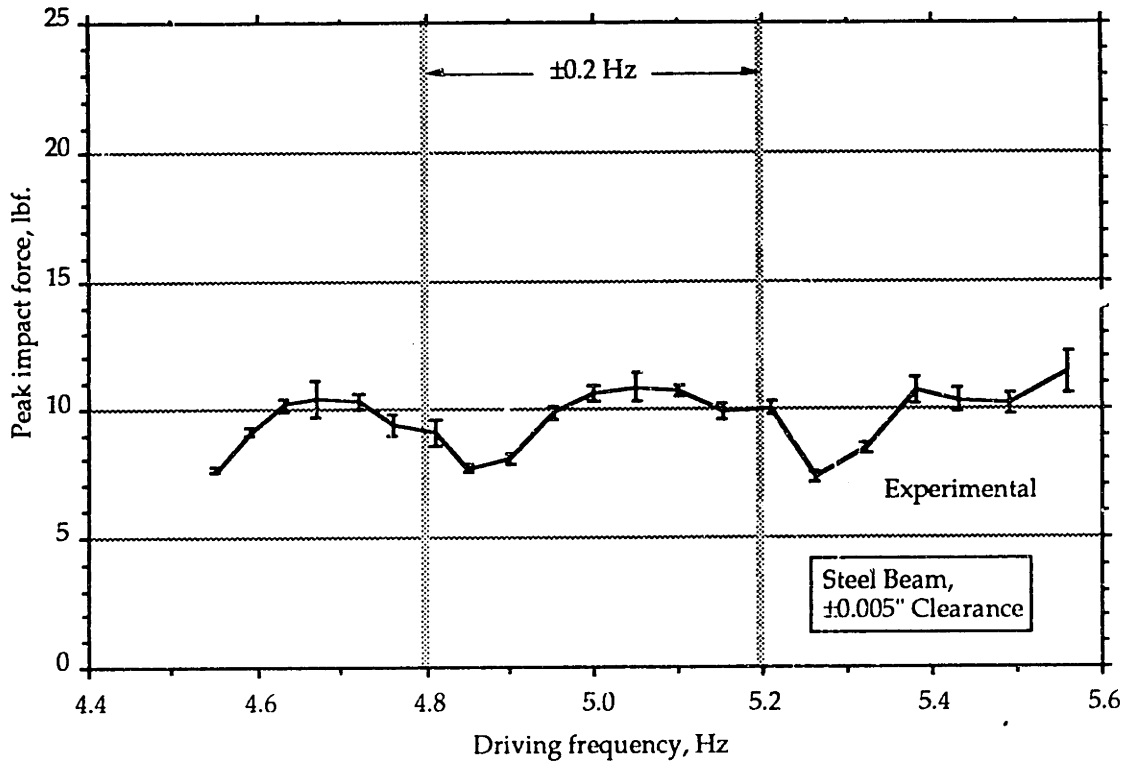

Figure 4.15. IBS Sensitivity to input speed, bracketing 5 Hz.

The extreme sensitivity of the average impact forces to operating conditions may be caused by the nonlinear dynamics introduced by the clearance. Linear systems always respond at the frequencies of their excitations. This is not true of nonlinear systems, especially when the nonlinearity is a clearance with impacts. Impact forces generated at a clearance connection have a nearly impulsive nature with a broadband, high frequency spectral characteristic. In the IBS, these impact forces act as excitation to what is essentially a linear elastic beam and supporting structure, exciting many high frequency modes of vibration in unpredictable ways. Figure 4.16 shows a frequency-averaged autospectrum of the force sensor output for a sequence of impacts with 20 Hz shaker drive frequency and ±0.005" clearance, using the steel beam. Data were collected using a digital FFT analyzer until the frequency-averaged autospectrum was stable. The highly nonlinear nature of the clearance

connection "smears" the pure-tone 20 Hz shaker force input very broadly in the frequency domain, so that there is significant excitation even at frequencies above 10 kHz, the 500th harmonic of the input frequency. Depending on the relationship between the frequencies of the peaks in the impact force spectrum and the frequencies of structural modes in the IBS, the structure may respond to the impact forces at very different amplitudes with very small changes in operating conditions, leading to large changes in the structural vibration levels for small changes in shaker drive frequencies. This effect, possibly in combination with the coupling effect between structural vibration and impact force proposed below, may be responsible for the high sensitivity of the mean impact force to drive frequency observed in Figures 4.14 and 4.15.

It is known that the modal response of structures in high frequency ranges is likely to be extremely sensitive to variations in the structure or assembly of the system [111]. Impact forces can provide broadband excitation to a structure, extending to frequencies many decades above the nominal operating speed of the machine. The difficulty of modeling the dynamics of even a single structural mode excited near resonance is well known, and impact force excitation is likely simultaneously to excite several modes on their resonances.

As discussed in Chapter 2, reference [111] describes a practical upper frequency limit to accurate structural modeling that arises when the natural vibration modes of a structure become so sensitive to strucural parameters that the modes are strongly affected by structural variations that cannot be known to the modeler. Such variations might be caused by, for example, manufacturing tolerances. This relationship between modeling accuracy and

uncertainty in structural parameters is fundamental and occurs at some modal order, or natural frequency, for any structure. Once the limit is reached, *realistic* numerical models for higher order structural modes cannot be constructed, because it is not possible to know the structure's parameters precisely enough. Note that the numerical model can be mathematically precise and computationally tractable, while not being "realistic."

The behavior is aggravated in the IBS by the nonlinear clearance connection. Plainly, the high frequency energy in a typical impact force spectrum, Figure 4.16, can excite high order structural modes. The interaction between the peaks in the frequency spectrum of the excitation and the peaks in the modal response of the structure means that one would not expect a second, nominally "identical" IBS to produce experimental results that would be identical or even closely resembling those presented here, and, by the same token, no numerical model would be expected to correspond to any particular physical realization of an IBS. Hence, it is not surprising that even a "very accurate" analytical model can not duplicate the behavior of an experimental system. Note that the modeling limit is due to the physics of the system – its extreme sensitivity to minute parameter variations – and does not arise because of finite computing power. The implication for the goal of highly accurate modeling of machine systems is clear: it may not be achievable, regardless of how much computer power is available.

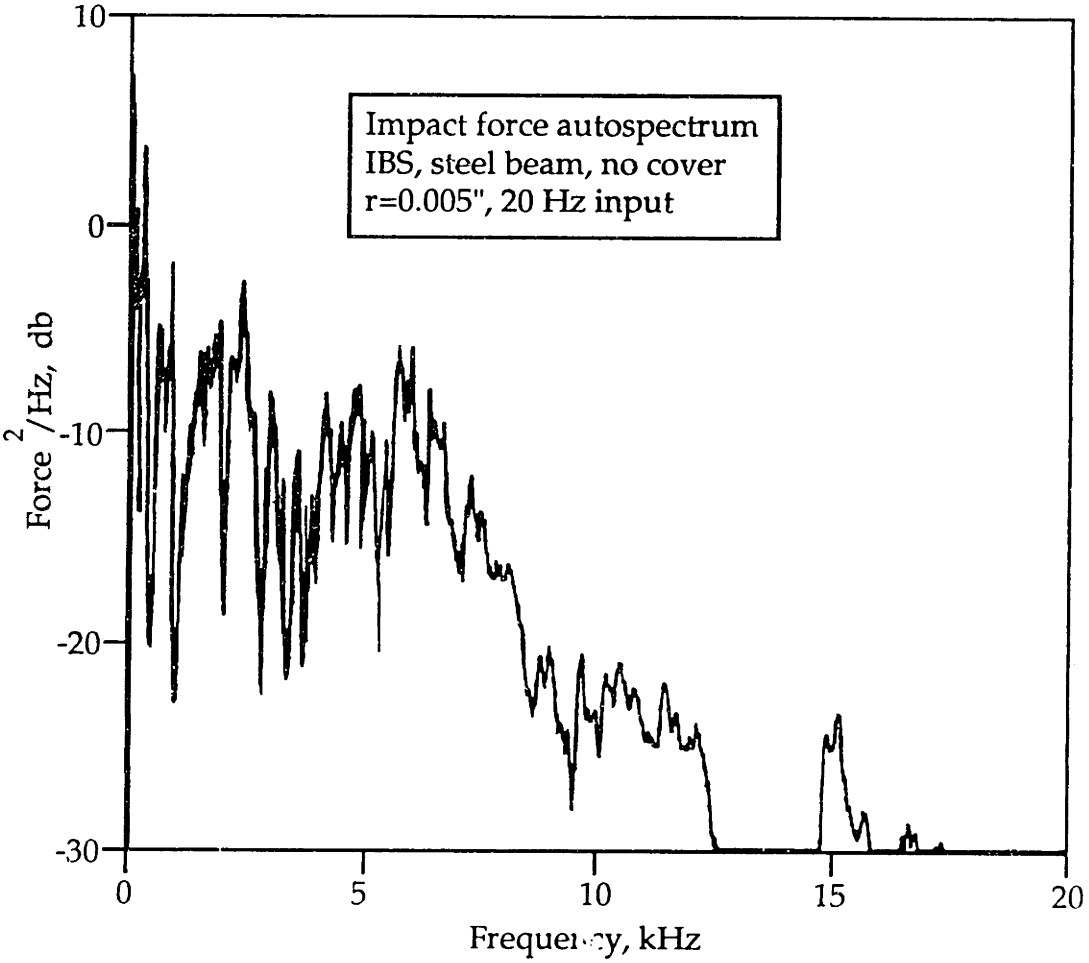

Figure 4.16. IBS impact force autospectrum.

The large observed cycle-to-cycle variation in impact forces, indicated by large standard deviations, might be explained by residual structural vibrations that do not decay between impacts. The magnitude of an impact force peak is strongly affected by the relative velocity of the impacting members just before contact. Thus, if the vibrations of the beam and the nominally stationary force sensors are large at the instant just before impact, the peak impact force may have a substantial component due to differences in velocity caused by vibration. Since these vibrations do not have a simple harmonic relationship with the basic driving frequency applied to the beam, the result would appear as a non-periodic variation in the impact forces, and the amount of the variation would be expected to correlate with the level of residual vibration

just prior to an impact event. The acceleration of the baseplate, measured by an accelerometer located near its center, as shown in Figure 4.2, is a sensitive indicator of system vibration. Figure 4.17a shows measurements of the baseplate acceleration for a 5 Hz shaker driving frequency, and Figure 4.17b for a 20 Hz driving frequency. Both Figure 4.17a and 4.17b are for the steel beam with ±0.005" clearance. Clearly, the system's vibrations decay almost entirely between impacts with 5 Hz drive frequency, and they do not decay between impacts at 20 Hz. This characteristic mechanism may account for the higher standard deviations observed in impact force peaks at the higher drive frequency. This non-periodic force variation may be mathematically chaotic [43, 99]. A full consideration of this question is beyond the scope of this thesis, but investigations into chaotic and other nonlinear behaviors caused by machine system clearances are currently underway in our laboratory [45]. In any event, as discussed above this behavior has some important implications for machine designers.

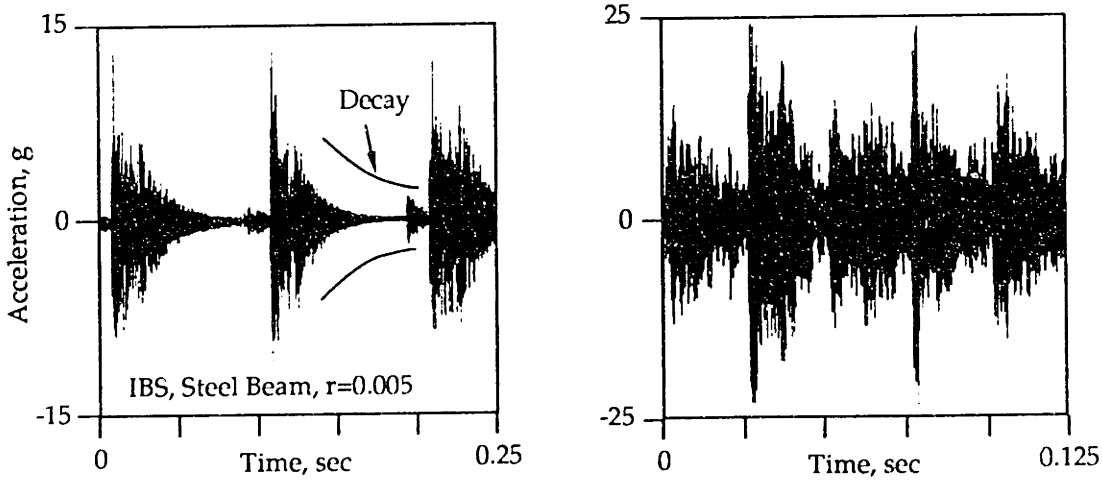

a) 5 Hz input. b) 20 Hz input.

Figure 4.17. Baseplate acceleration. (NOTE: Scales are different.)

D.3. Effect of Structural Variations on Peak Impact Force

The above results have been without a cover installed on the IBS. As described earlier, the IBS has two covers that can easily be changed or removed to provide a means of varying its structure. A comparison of experimentally measured peak impact forces using the steel beam with these covers is shown in Figure 4.18. The construction of the cover, whether of fiberglass or aluminum, does not have a strong affect on the impact forces. When operating the IBS with either cover is compared to operation with no cover, a small effect on impact forces seems to occur. The cover appears to reduce the impact forces slightly at a driving frequency of 5 Hz, and to increase them slightly when at 20 Hz. However, it should be noted that the observed changes in mean force apparently due to covers are small, the same or less than the standard deviations observed at these frequencies. In fact, these apparent differences may be due to experimental variations. In collecting these results, the clearance gap was readjusted between observations with and without the covers. The equipment available permitted the gap to be reset within a tolerance estimated at ±0.001". This is potentially a source of significant error, due to the sensitivity of the IBS to its operating parameters. Such variations in clearance could be responsible for the apparent differences in results with and without covers in Figure 4.18.

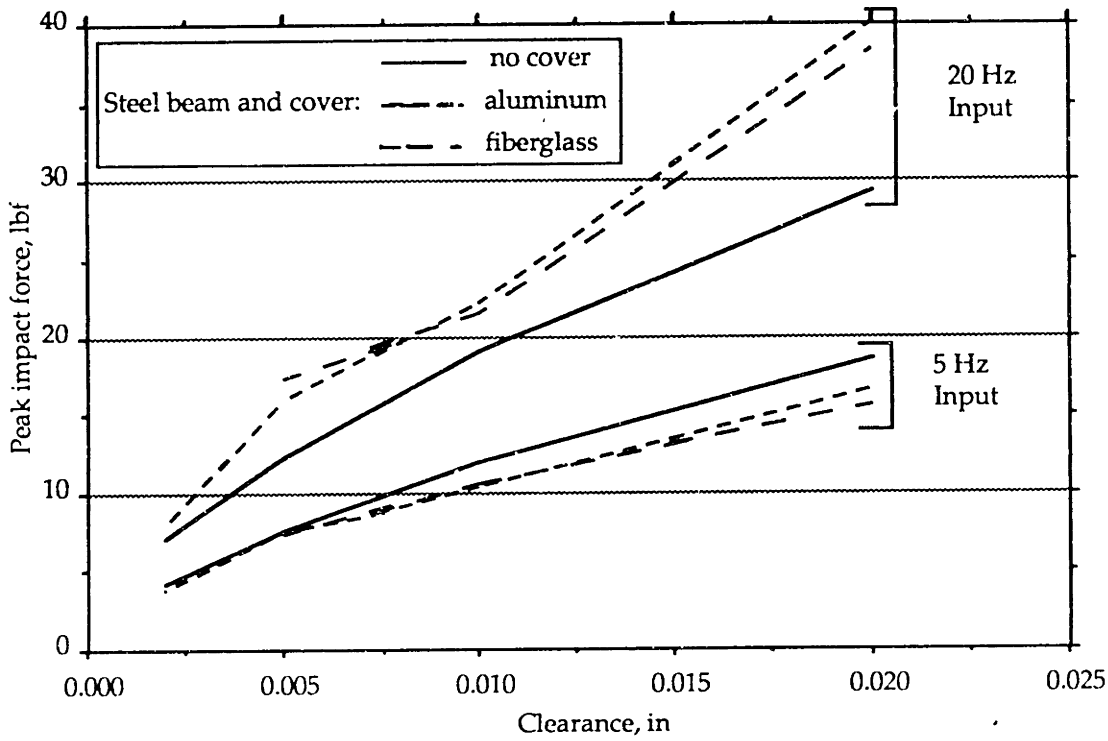

Figure 4.18. Experimental impact force vs. clearance. Different covers. 5 and 20 Hz drive frequency.

Figure 4.19 compares peak impact forces without a cover and with the metal cover for a number of closely spaced frequencies around 20 Hz, again using the steel beam, with ±0.005" gap clearance. The solid curve in this figure is reproduced from Figure 4.14, without a cover, and the dashed curve shows results with the metal cover mounted on the IBS. In collecting these data, measurements with and without the metal cover were made without readjusting the clearance gap; therefore no experimental error due to a slightly different gap setting was incurred. In these results, which provide a much more detailed view of the IBS's behavior than Figure 4.18, the cover has very little effect on the overall character and magnitude of the peak impact force curve. However, there are detail differences, possibly corresponding to changes in structural resonances introduced by the cover.

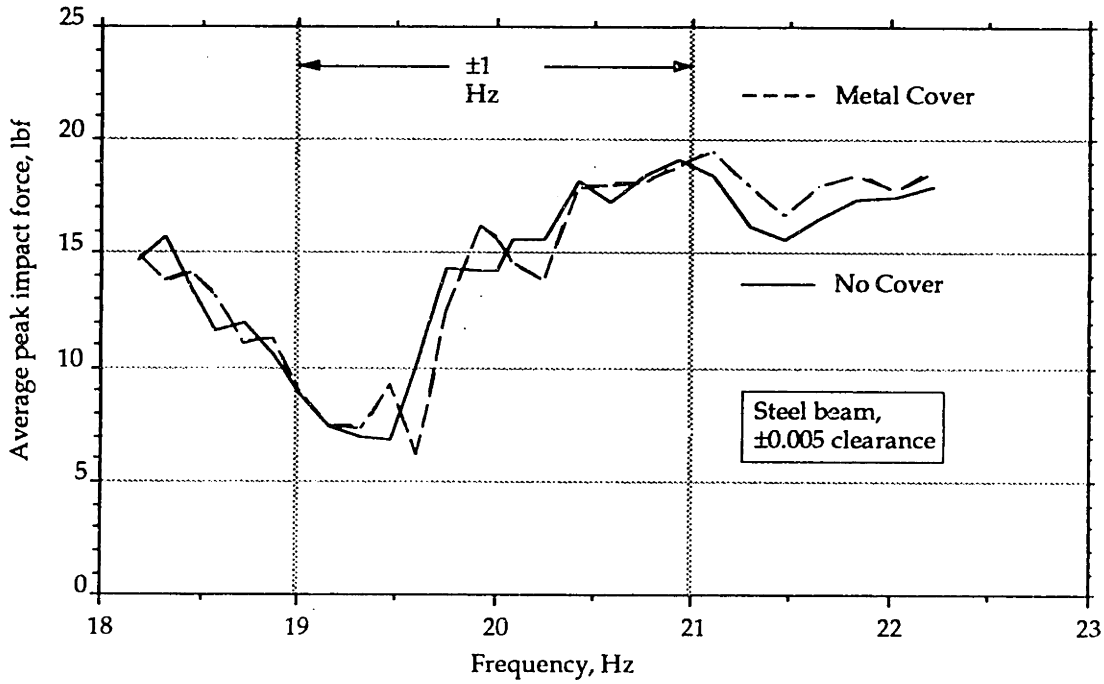

Figure 4.19. IBS sensitivity to input speed and cover. Bracketing 20 Hz.

The flexible base model developed in ASSET for these studies can model the effects of changing the base plate and cover parameters. A cover can be included in this model as a simple extension of the FE model of the baseplate. Typical results from the flexible base model without a cover are compared with rigid base model results, for the steel beam at 5 Hz driving speed and two clearance values, in Table 4.3.

Table 4.3. Peak Impact Forces.

Clearance	Rigid Base Model	Flexible Base Model
±0.010 in (±0.254 mm)	11.1 lbf (49.4 N)	8.5 lbf (37.8 N)
±0.020 in (±0.508 mm)	14.6 lbf (64.9 N)	12.1 lbf (53.8 N)

As expected from previous work, introducing additional compliance into the system model, in this case, that of the baseplate, reduces the predicted impact forces [30], and the basic trend of increasing impact force with increasing clearance is still seen with the more elaborate flexible base model. The

computational cost of the flexible base model was found to be about 10 times that of the rigid base model. In addition, because of computational constraints, a coarse finite element model had to be used for the flexible base. It is expected to be accurate only up to around 200 Hz, vs. about 5000 Hz for the finite element model of the beam in the rigid base model.

D.4. Structural Vibration Response

It can be shown experimentally that the covers affect the structural response of the IBS. Figure 4.20 shows the peak acceleration measured in the center of the baseplate for the aluminum beam IBS with 20 Hz drive frequency and varying clearances. The different curves show the peak baseplate acceleration when there is no cover attached and when the metal and fiberglass covers are attached. While there is little difference between the two covers, it is clear that adding a cover affects the baseplate acceleration. The cover wicks away energy from the baseplate, reducing its overall motion and therefore its acceleration.

As might be expected, a cover affects the power level of the sound radiated by the IBS as well. However, surprisingly, the IBS with metal cover is louder than the uncovered IBS, while the IBS with fiberglass cover is quieter. A discussion of sound radiation by the IBS is beyond the scope of this thesis, but may be found in reference [81].

Numerical simulations of the structural vibration, using the flexible base model and finite element models for the covers, did not agree well on a one-to-one basis with measurements taken from the accelerometers near the center of the baseplate, the center of the cover, and one of the corners of the

cover. No results of these simulations are shown here. Such accelerations are strongly affected by the high frequency components of the structural vibrations, which are poorly modeled in the numerical simulations. While it is clear from the experimental results that the support structures and covers affect the structural vibrations of the IBS, a comprehensive study of these effects is beyond the scope of this thesis. Work is underway to develop a more computationally practical method [81].

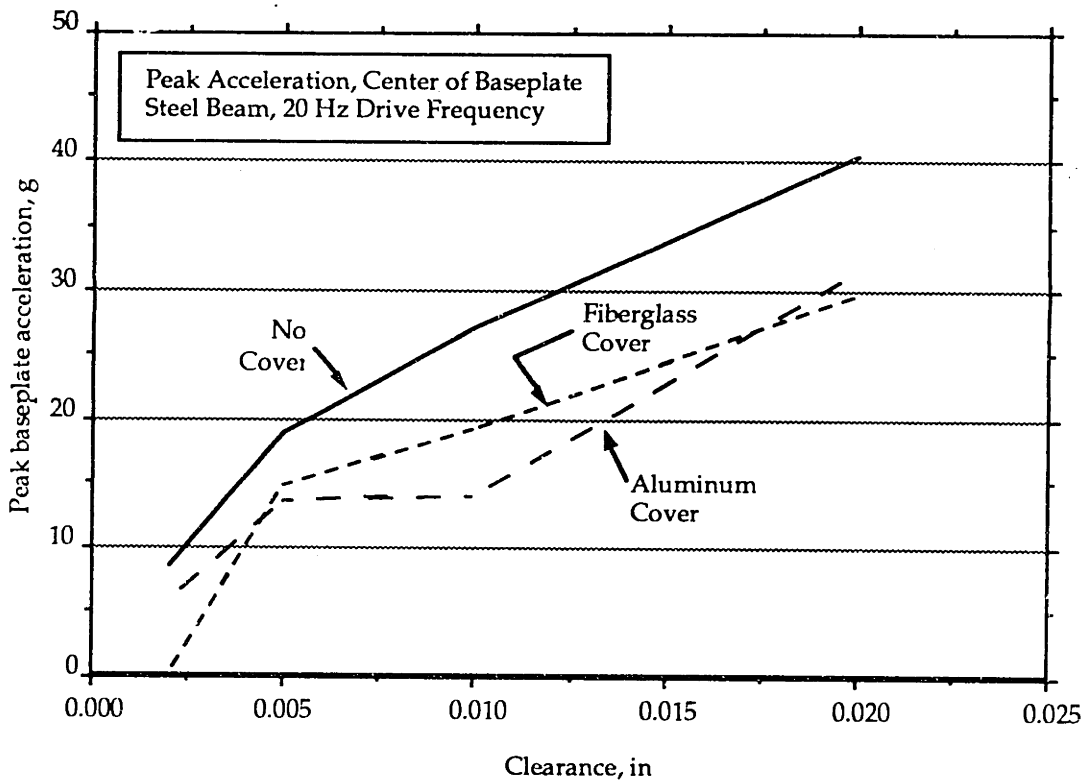

Figure 4.20. Trend of peak baseplate acceleration vs. clearance. Comparison of different covers.

E. Summary

Clearances between links affect the behavior of a machine system. In particular, impact forces generated in a clearance when the links hit each other can have important consequences for machine system behavior. Such clearances are inherently nonlinear. The IBS discussed here is designed so that the effects of such nonlinearities are particularly prominent, and it is equipped with instrumentation that permits observation of the clearance impact forces as well as some measures of structural vibration.

By observing data from an experimental IBS and predictions from a numerical IBS model, some insights about the behavior of machine systems with clearances may be had. These include the following:

- The impact forces generated at clearance connections tend broadly to increase as the machine system's driving speed and the amount of clearance are increased.
- These trends are subject to very substantial local variations and can be extremely sensitive to the driving speed of the machine. Well behaved linear systems do not exhibit such high sensitivities.
- A machine system's auxiliary structures, such as its mounting base and covers, may affect its structural dynamics. However, they do not appear to have a large effect on the magnitude of the clearance impact forces.
- Impact forces are nearly impulsive. Therefore, they have a broadband, high bandwidth energy spectrum, with the ability to excite many structural resonances in a machine system. Thus, to be accurate, machine system models for structural vibrations would have to include detailed models of the machine's support structures and enclosures. Such accurate, high frequency models may be unobtainable for practical systems with reasonable manufacturing tolerances.

- The magnitude of clearance impact forces can be many times the magnitude of the nominal forces that would exist without clearances. Amplifications of 20 times were observed for the IBS in these studies, and other researchers have reported similar and even higher amplifications.
- Machine systems with clearance impacts do not necessarily have a steady state operating mode. Steady inputs might not produce steady outputs. Such a phenomenon is impossible with linear systems.
- It is accepted that many nonlinear dynamic systems exhibit chaotic behavior, which can be characterized in part by lack of a steady state response and extreme sensitivity to initial conditions. The IBS displays some markers of chaotic behavior. However, an investigation of the nature of chaos in the IBS is beyond the scope of this thesis, and is a subject of some current work in our laboratory [45].
- Fundamental limits related to the sensitivity of structural response, our ability to manufacture, and the sensitivity of nonlinear clearance impacts to operating parameters, conspire to make highly accurate models for machine systems an extremely difficult problem. However, as shown in this chapter, designers can use numerical methods to obtain results that are usable, but must be applied with knowledge of their limitations.
- Designers of machine systems must be aware that high peak forces may occur where there are clearances and impacts, as in bearings. Detailed numerical models such as those discussed here may provide rough estimates of the forces that will be encountered. However, these estimates must be regarded with caution. Even in such a relatively simple system as the IBS, a factor of 2 difference between predicted and measured forces is easily possible.

Chapter 5. The Spatial Slider Crank System

A. System Description

The IBS, the subject of the last chapter, purposely excludes nonlinear kinematics and multiple links from its design. However, real machine systems often have multiple links, and the nonlinearities associated with large, spatial relative motions, including large rotations, in addition to clearance connections. To study the interactions between these common machine system characteristics and clearance connections, the spatial slider crank mechanism discussed in this chapter was developed.

A spatial slider crank (SSC), illustrated in Figure 5.1, is a mechanism with fully spatial, nonlinear kinematics. The moving parts are a crank, turned by a motor; a connecting rod that runs from the crank to a slider; and the slider itself, which runs along a stationary guide rod. A ball joint connects the crank and connecting rod, and a universal joint connects the connecting rod and the slider. An SSC may also be built with a ball joint instead of a universal joint between the connecting rod and the slider; however, the resulting mechanism would have an unconstrained kinematic degree of freedom because the connecting rod could rotate about its length axis. The joint between the slider and the guide rod is a prismatic sliding joint. This joint constrains the slider's motion to linear translation along the guide rod.

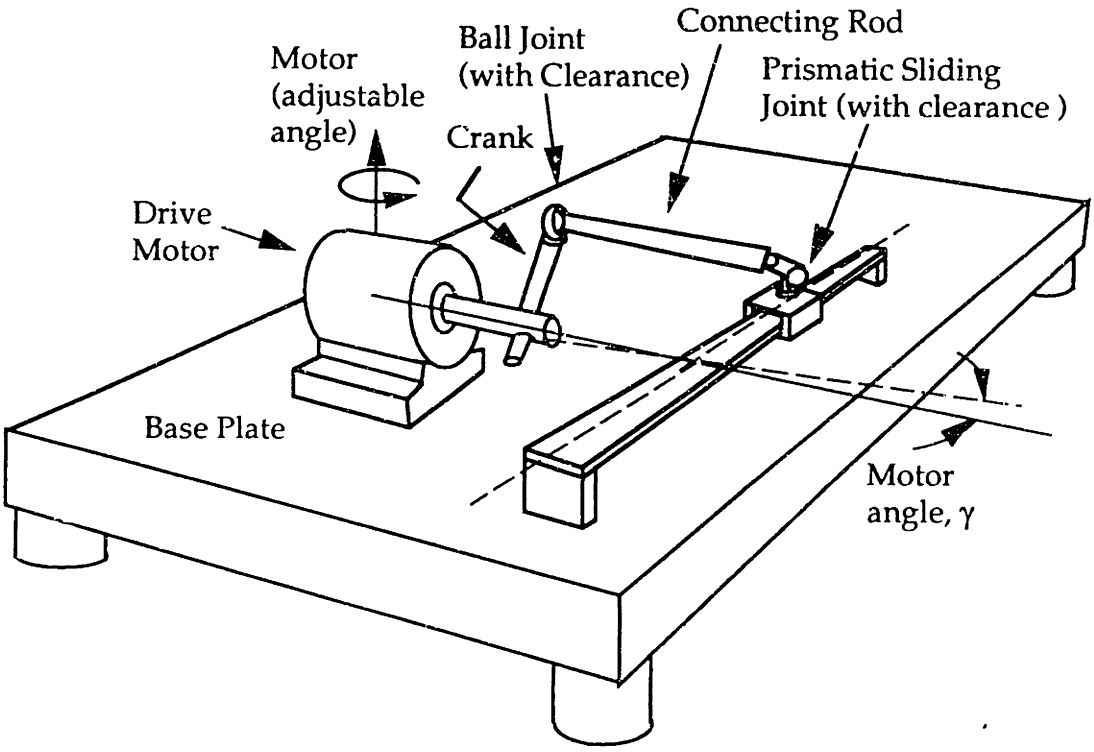

Figure 5.1. Schematic of a spatial slider crank.

A spatial slider crank is a spatial version of the well-known planar slider crank mechanism. The revolute joints of a planar slider crank are replaced in an SSC with a ball joint and a universal joint. These allow the angle between the axis of rotation of the crank and the axis of the slider to be adjusted. An SSC degenerates kinematically into a planar slider crank when the angle between the crank axis and the guide rod is 90 degrees and the guide rod and crank lie in the same plane. When the guide rod is offset from the plane of the crank, a co-planar slider crank is formed. When the angle between the crank's axis and the slider's axis is different from 90 degrees, the spatial slider crank has fully spatial kinematics. One application of the spatial slider crank mechanism is in variable stroke devices such as that pictured in Figure 5.2. Following reference [79], in this thesis the SSC's configuration is characterized

by the "motor angle," which is 90° minus the angle between the crank axis and the slider axis. Thus, the planar slider crank has a 0° "motor angle."

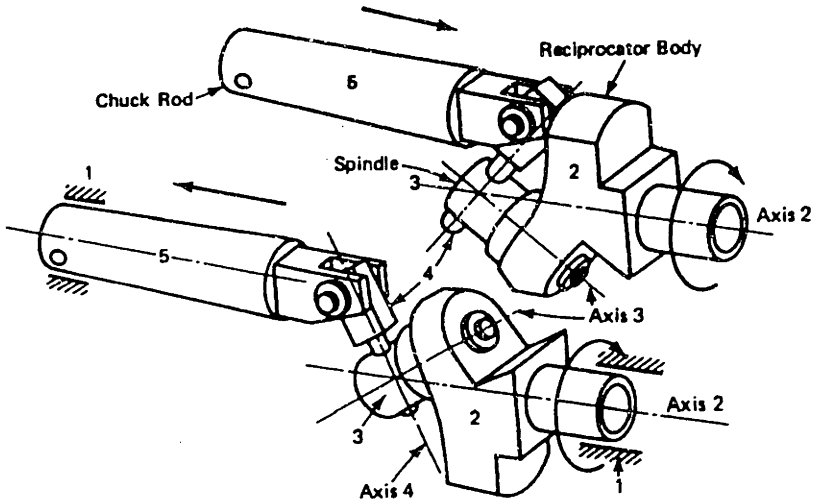

Figure 5.2. A variable stroke mechanism. (*Advanced Mechanism Design: Analysis and Synthesis, Vol. 2,* G. Sandor and A. Erdman, Prentice-Hall Inc, © 1984, page 549.)

B. An Experimental Spatial Slider Crank

Two views of the experimental spatial slider crank with two motor angles are shown in Figures 5.3a and 5.3b. Figure 5.3b, with 0° motor angle, mimics a planar slider crank. The "crank" is a flywheel, to help stabilize the machine's speed without complex motor controls. Figure 5.3c shows the ball joint, the connecting rod, and the yoke that holds the shell of the sliding joint. The ball joint and sliding prismatic joint are implemented in this mechanism as instrumented clearance joints with adjustable clearance; these joints are illustrated in Figures 5.4 and 5.5. The connecting rod is a 0.25" diameter by 7.5" long steel rod. An alternate, more flexible connecting rod, the same length but 0.125" in diameter, can also be installed. Mounting hardware causes the effective kinematic length of the connecting rod to be 9". Either

rod is attached at one end to the shell of the instrumented, adjustable clearance ball joint. This joint is mounted to the flywheel at a point 2" from its center of rotation. At its other end, the rod is attached through a ball bearing to a yoke, Figure 5.6, that allows the slider shell to pivot on a pair of ball bearings. Use of the yoke and pivot rather than a universal joint avoids applying a large torque to the slider shell. Such an applied torque can cause lockup of the mechanism due to friction in the sliding joint. The instrumented, adjustable clearance slider rides on a ground steel guide rod with a 0.5" square cross section. The angle between the motor and the slider axis can be varied between 90° and 65°, causing the slider stroke to vary between 4" and 3.6". This 25° range of motor axis adjustment is limited by the ball joint. The instrumented, adjustable clearance joints developed for this project use miniature versions of the force sensors used in the IBS's clearance joint. Their clearances are adjustable from near zero to 0.040" or greater. All components of the spatial slider crank are mounted on an aluminum baseplate 0.5" thick, 22" long and 18" wide. The instrumented joints are run lubricated with light machine oil. The spatial slider crank runs at speeds from 50 to 250 rpm.

The basic dimensions of this machine were developed in a Master's thesis, reference [79]. Most of the design and fabrication of the instrumented joints was done by Uwe Müller and Erin O'Connell. The contact force sensors are similar to those designed by Peng Yun Gu for the impact beam system. All of their contributions are gratefully acknowledged.

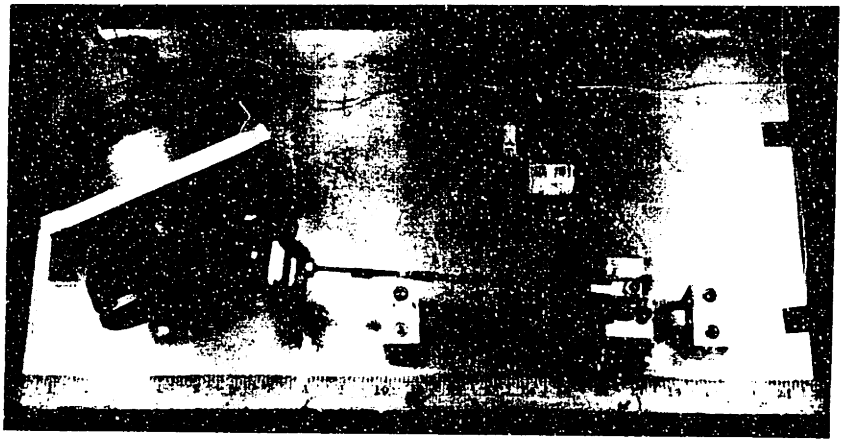

a.) Top view, 25° motor angle

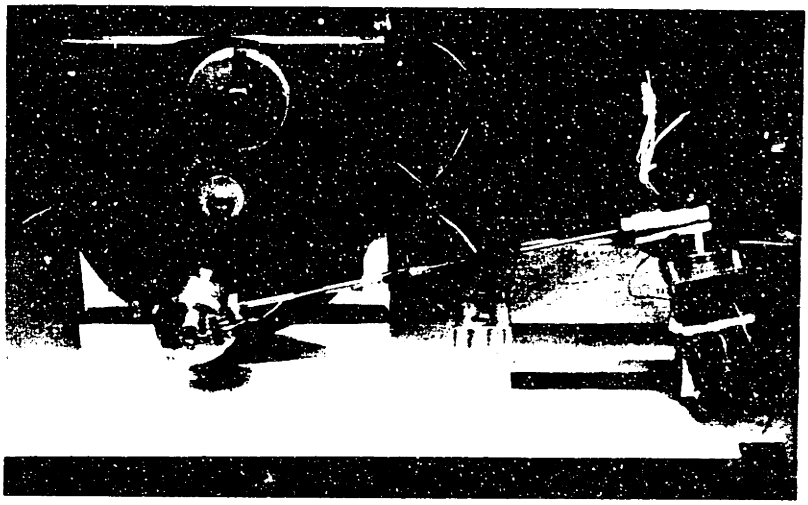

b.) Front view, 0° motor angle.

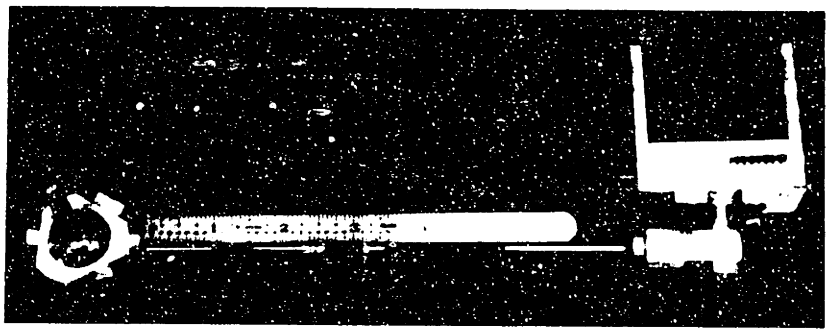

c.) Ball joint, connecting rod and slider yoke.

Figure 5.3. The experimental SSC.

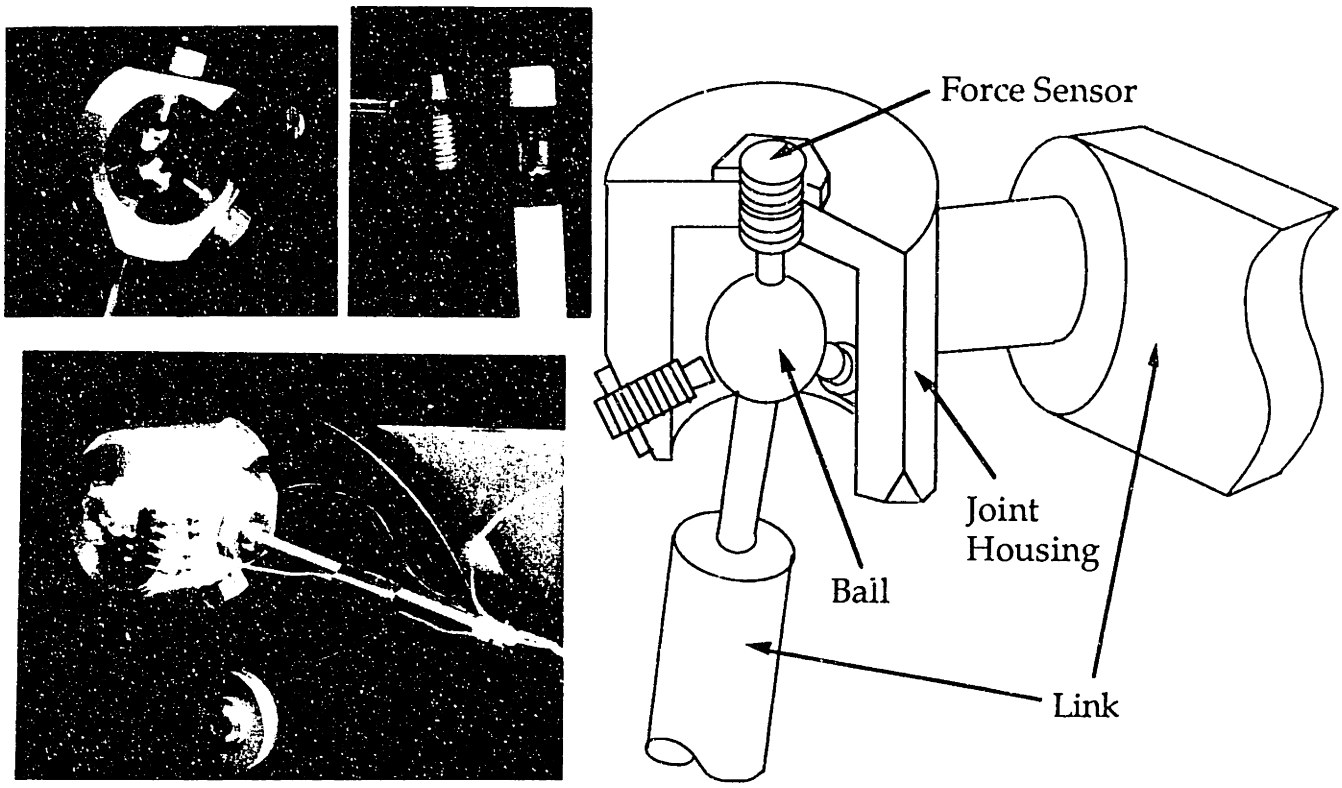

Figure 5.4. Instrumented, adjustable clearance ball joint.

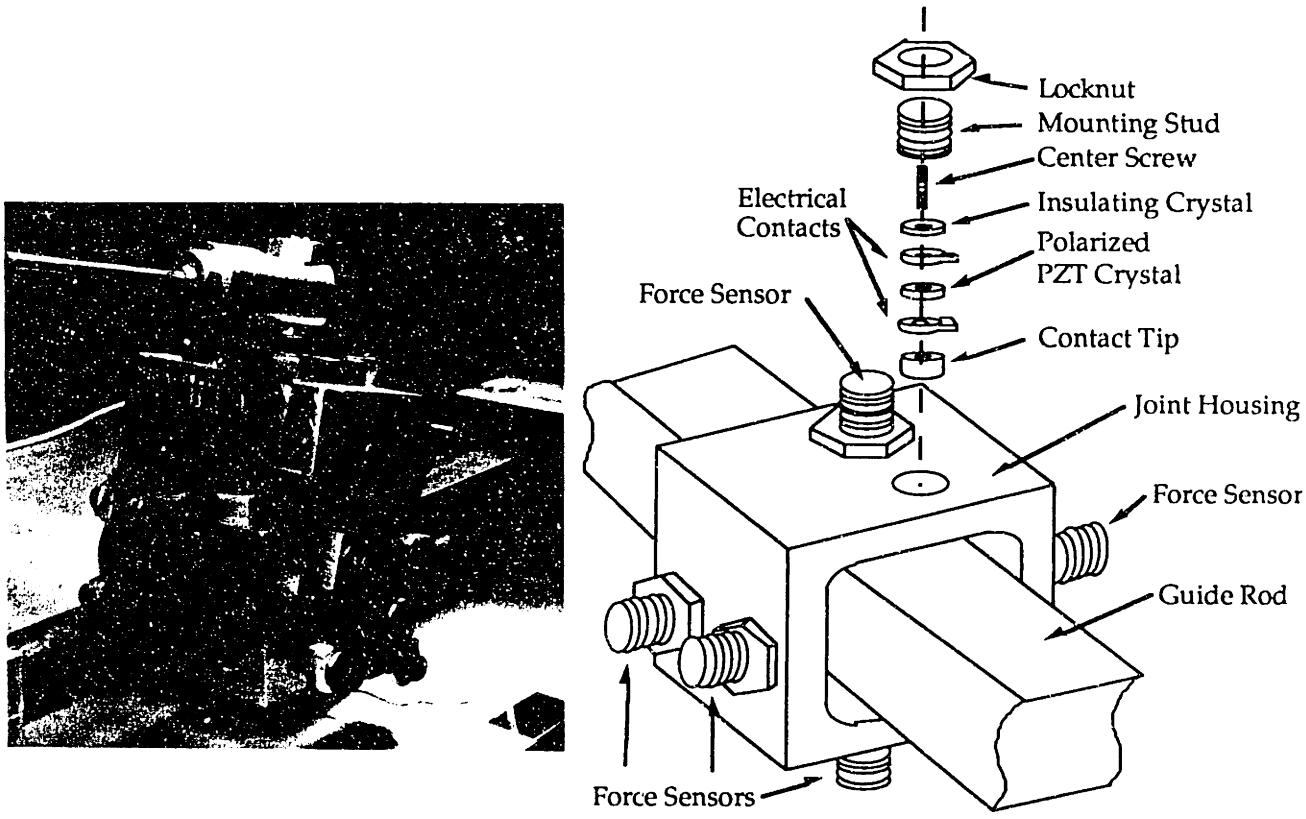

Figure 5.5. Instrumented, adjustable clearance prismatic joint.

The instrumented ball joint, shown in several views in Figure 5.4, has four force sensors placed symmetrically so that they retain a 5/8" diameter spherical ball, which is made of hardened steel. The force sensors used in the ball joint have steel tips, ground to a flat surface. One force sensor is also shown in Figure 5.4. The instrumented prismatic joint, shown in Figure 5.5, has eight sensors, set in an off-center symmetrical pattern that allows the slider to resist turning moments, and forces perpendicular to the guide rod. Its force sensors are like those of the instrumented ball joint, except that their tips are brass, turned to an approximately hemispherical shape of 0.188" diameter. There are four vertical and four horizontal force sensors. The sensors of both joints are mounted on standard 1/4–28 screw bodies. Clearance is adjusted by screwing the sensors in and out of their threaded mounting holes, and locking them with brass clamp nuts. The shell of the prismatic joint is supported in a yoke, Figure 5.6. The end of the connecting rod mounts to a bearing at the top of the yoke, and the slider shell is supported on ball bearings between the sides of the yoke.

The ball joint's force sensors are adjusted to a symmetrical zero clearance position during assembly of the joint. In this position, the ball is held in contact with all four sensors with zero clearance, and the centerlines of the sensors intersect at a point coincident with the center of the ball. The positions of the force sensors are marked at this point to give a symmetrical, zero clearance reference position. Then to set the joint's clearance to a given value, the sensors are backed out by equal increments until a feeler gauge can be inserted between one sensor and the ball, with the ball in contact with the other three sensors. The convention adopted here is that the ±value noted for clearance indicates the feeler gauge that could be inserted between one

sensor and the ball in this manner. Note that the locus of free motion of the ball in this joint is not spherical, because contact can occur between the ball and up to three sensors simultaneously.

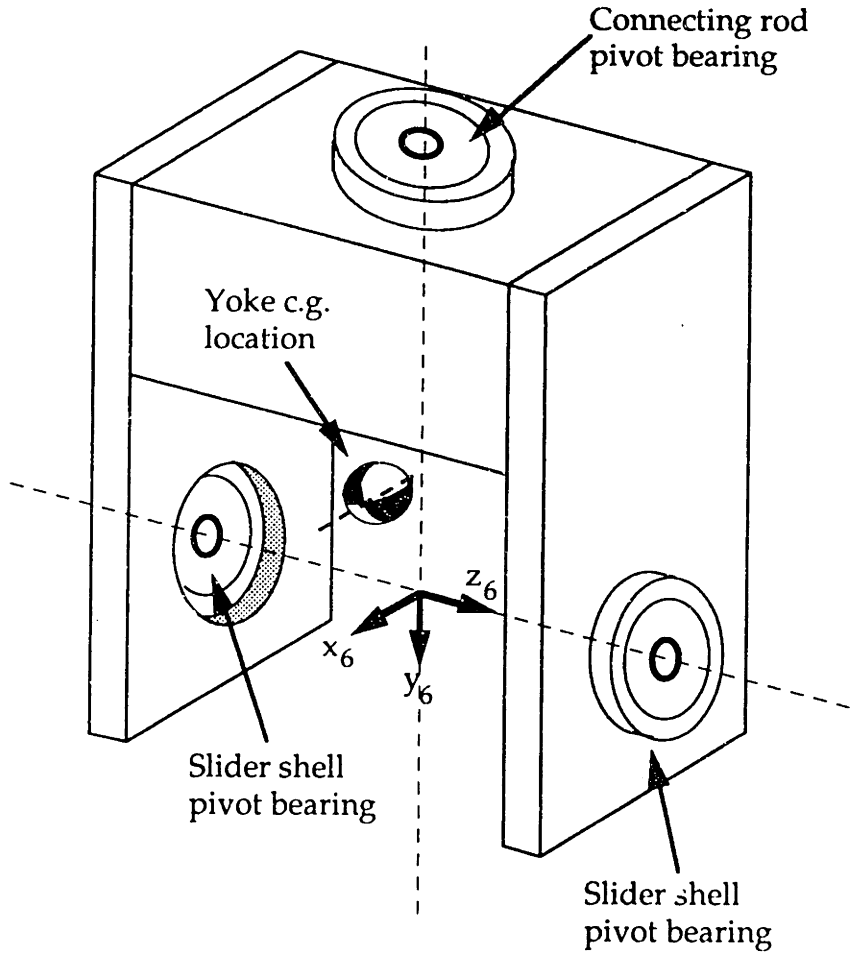

Figure 5.6. SSC slider yoke.

The sensors on the slider are also first set in a zero clearance symmetrical reference position, by adjusting them so that the slider guide rod is held in the center of the slider shell. Measurements of this center position are made using a depth gauge on a caliper micrometer. The positions of the force sensors are marked when the symmetrical zero reference position is found. To adjust clearance in the slider, shims of the indicated ±value are stacked on adjacent sides of the slider guide rod and the force sensors adjusted until they

are all equally backed out from their zero positions, and there is just enough clearance to remove the shim stacks from the slider guide rod with some friction.

For both joints, it is likely that fabrication tolerances and uncertainties in setting the initial zero clearance position result in actual devices with somewhat poorer precision than designed.

Figure 5.7 shows a signal flow diagram for the SSC's data acquisition setup. Force sensor data are collected from the spatial slider crank using a Concurrent 6000 computer with laboratory data acquisition hardware and software. This equipment can acquire several channels of data simultaneously; simultaneous multichannel data acquisition is important for the spatial slider crank because both of its joints may have multiple points in contact at any instant. Signal conditioning for the force sensors in the instrumented clearance joints is performed by 8 Endevco, B&K and PCB charge amplifiers. A Frequency Devices 9016 multichannel programmable analog filter provides anti-aliasing filtering. The availability of only 8 charge amplifiers means that contact force data cannot be acquired concurrently from the ball joint and the slider, and therefore a means is provided to switch the data acquisition equipment from one joint to the other. Other equipment includes a Hewlett-Packard variable regulated DC power supply for the spatial slider crank's motor, monitoring equipment for the motor's integral tachometer, and a photonic sensor that reads an optical mark on the flywheel to provide a once per revolution sync pulse. The 12 force sensors used in the instrumented ball and sliding joints were individually calibrated using the same procedure as for the IBS's force sensors. Since the force sensors are mounted to moving parts of the mechanism, it is necessary to connect them

to the stationary charge amplifiers. This connection is made with 40 gauge copper wires that exert minimal external forces on the instrumented joints as the SSC goes through its motion. Although the wires are unshielded for part of their run, electrical noise was not a problem.

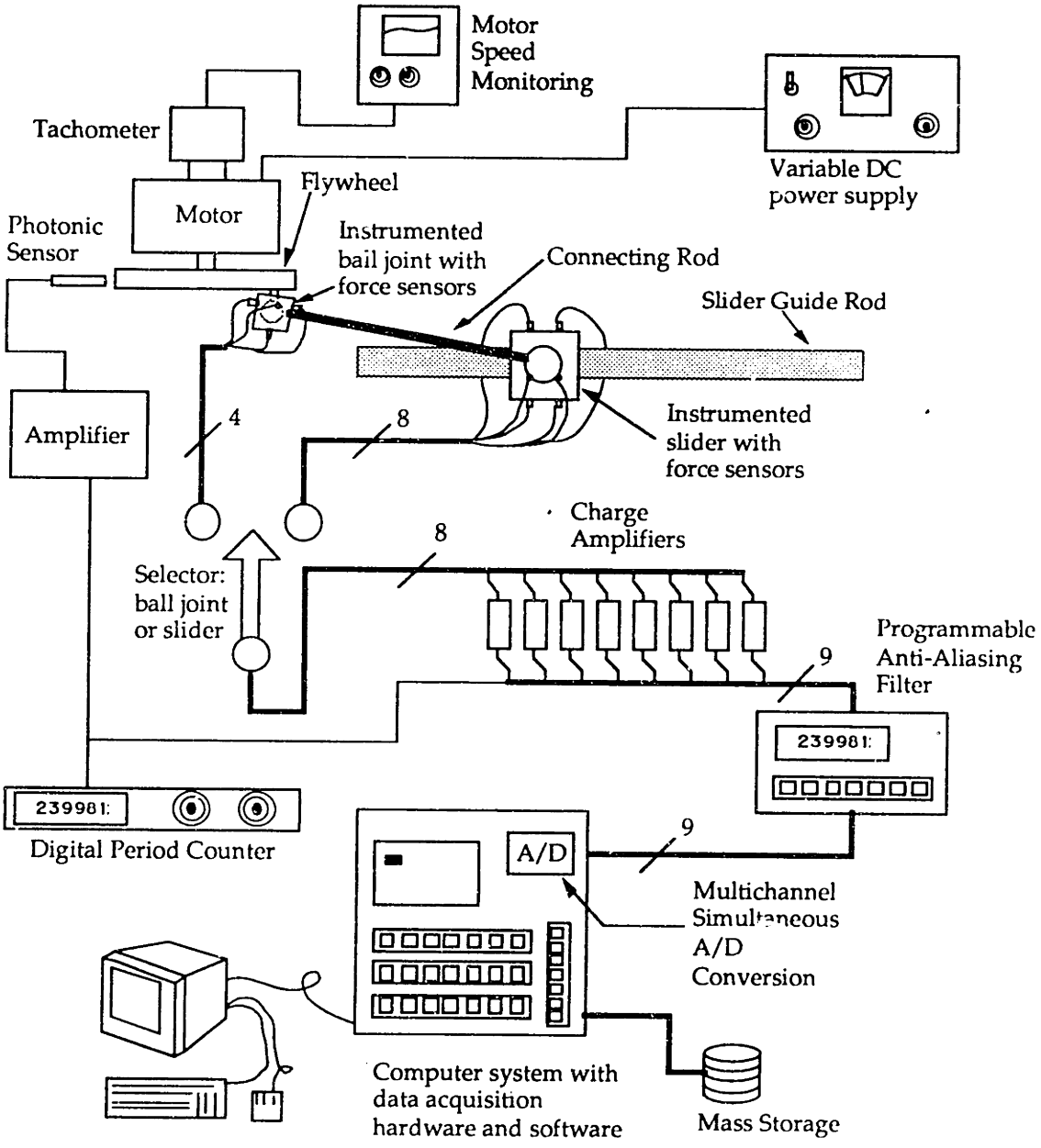

Figure 5.7. SSC Data acquisition signal flows.

C. Analytical Model of the Spatial Slider Crank

C.1. Clearance Joints

The analytical model of the spatial slider crank uses the spherical clearance connection force model discussed in Chapter 3, Section D, to represent the ball joint. The clearance connection force model used for the prismatic joint is described in detail in Section C.4, below. In both models, contact forces are modeled as having linear stiffness and damping components. The ball joint model neglects sliding friction. The prismatic joint model includes sliding friction, as discussed in Section C.4. The linear stiffness and damping contact force coefficients used in the models are listed in Table 5.1. The stiffness values listed in the table are based on a linearized Hertzian contact analysis. Further details may be found in Appendix F. The parameters in the second column of Table 5.1 are used with Equation 3.16 for the spherical clearance joint model. The parameters in the third column are used with Equation 5.5 for the prismatic clearance joint model.

Table 5.1. Contact Parameters in the Spatial Slider Crank Analytical Model.

	Ball Joint Model	Prismatic Joint Model
Contact Stiffness	$1.6 \times 10^5 \frac{\text{lbf}}{\text{in}} \left(2.8 \times 10^7 \frac{\text{N}}{\text{m}}\right)$	$8.2 \times 10^4 \frac{\text{lbf}}{\text{in}} \left(1.4 \times 10^7 \frac{\text{N}}{\text{m}}\right)$
Contact Damping	$0.25 \frac{\text{lbf-s}}{\text{in}} \left(44 \frac{\text{N-s}}{\text{m}}\right)$	$0.29 \frac{\text{lbf-s}}{\text{in}} \left(51 \frac{\text{N-s}}{\text{m}}\right)$

C.2. Kinematic Model

The Hartenberg-Denavit reference frames used in the numerical model are shown in Figure 5.8. The Hartenberg-Denavit model of the SSC's kinematics consists of seven links: link 0 is the inertial reference frame; link 1 is the base

and motor; link 2 is the crank/flywheel; links 3 and 4 are zero length kinematic links associated with the ball joint; link 5 is the connecting rod; link 6 is the slider yoke; link 7 is the slider. The sliding joint could be considered the eighth joint and the slider guide rod the eighth link. However, since the slider guide rod is attached to the baseplate, it can be modeled as part of link 1, thereby enforcing kinematic closure of the mechanism. The Hartenberg-Denavit parameters for the 7 links are listed in Table 5.2. The nominal motions, $\theta_3(t)$ to $\theta_7(t)$, and their derivatives, must be provided by a separate analysis of the kinematics. The numerical simulation as written assumes constant motor speed, $\theta_2(t) = \Omega t$.

Table 5.2. SSC Hartenberg-Denavit parameters.

Link	θ	L	α	H
1	0	0	0	0
2	Ωt	2"	0	0
3	$\theta_3(t)$	0	+90°	0
4	$\theta_4(t)$	0	-90°	0
5	$\theta_5(t)$	0	+90°	9"
6	$\theta_6(t)$	0	-90°	2.45"
7	$\theta_7(t)$	0	+90°	0

These Hartenberg-Denavit (H-D) parameters are associated with the following dimensions in the SSC: L_2 is the crank length; H_5 is the length of the connecting rod, and H_6 is the yoke height, measured from the end of the connecting rod to the pivot of the slider shell. Also, L_7 is the height of this pivot above the centerline of the slider, zero as fabricated. In H-D kinematic notation, a ball joint is expressed as three spatially coincident revolute joints. The joint angles corresponding to these revolutes are θ_3, θ_4 and θ_5. Angle θ_6 is associated with the revolute joint between the connecting rod and the yoke,

and θ_7 with that between the yoke and the slider. Although the SSC has only one kinematic degree of freedom, the equations that represent the nominal motion of its links are quite complex. They are given in Appendix E.

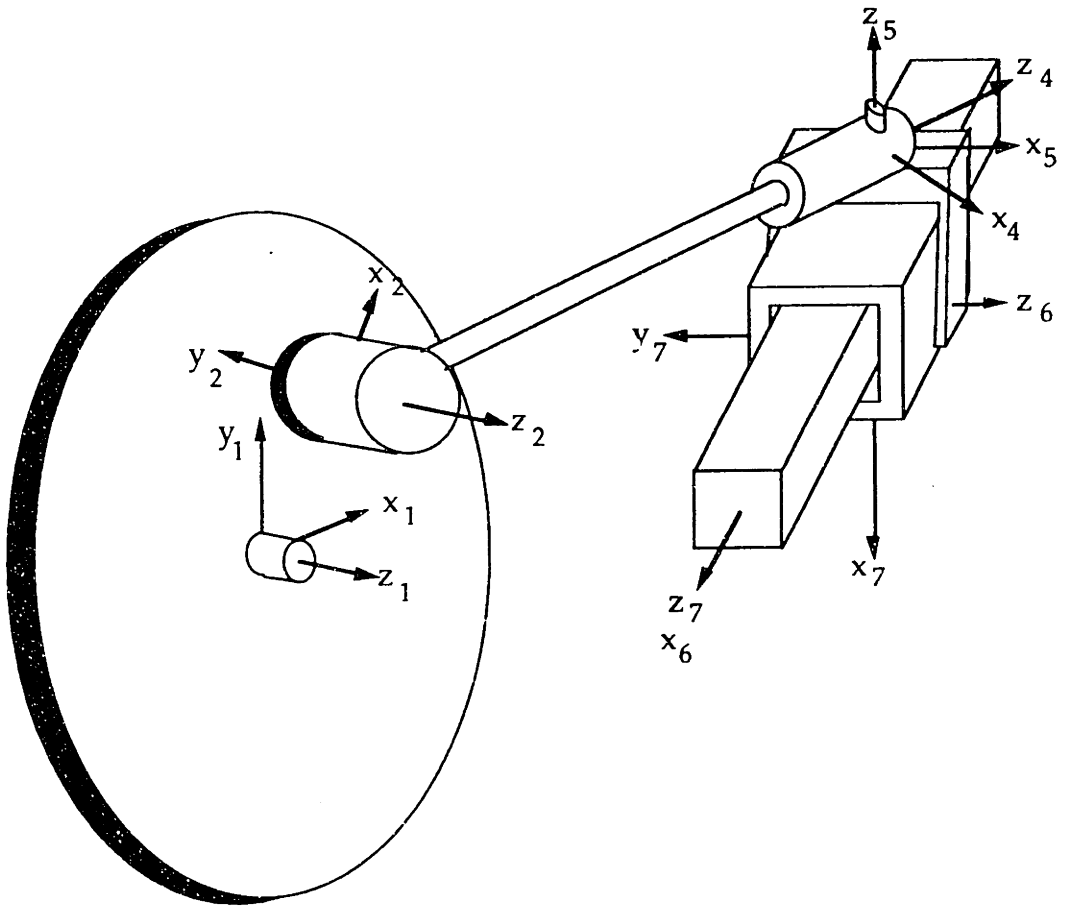

Figure 5.8. SSC numerical model. Hartenberg-Denavit coordinate frames.

C.3. Link Models and Global Compatibility

In the numerical simulation of the SSC, the connecting rod is modeled as a flexible link with 37 nodes and 36 beam elements, each element 0.25" long. The interface nodes are nodes 1 and 2; node 1 is at the ball joint and node 2 at the yoke. The other 35 finite element nodes are internal nodes. Extra lumped mass to account for the ball joint housing is added at node 1. Simulation of the SSC with 8 CMS modes retained, with a highest natural frequency of 4970

Hz, did not appear to predict significantly different impact force magnitudes from simulation with no retained modes, and does require more CPU time. Therefore for most of the SSC numerical simulations, the connecting rod is modeled using 12 interface perturbation coordinates, all of them dynamically independent degrees of freedom, and no CMS modes. The other elements of the numerical model with significant mass, the yoke and slider, are modeled as rigid bodies, joints 6 and 7 are modeled as ideal revolute joints. Therefore, each of links 6 and 7 has six perturbation coordinates but only one independent degree of freedom. The independent degrees of freedom correspond physically to the perturbation rotation of the yoke about the z_6 axis and perturbation rotation of the slider shell about the z_7 axis shown in Figure 5.8. The dynamic simulation with no retained CMS modes for the connecting rod therefore has 14 independent degrees of freedom. These are assigned as follows: q_1 through q_6 are the x,y,z perturbation translations and x,y,z perturbation rotations of node 1 of the connecting rod; q_7 through q_{12} are similarly defined for node 2 of the connecting rod. Degree of freedom q_{13} is assigned to the yoke's θ_6–direction perturbation rotation, and q_{14} to the slider shell's θ_7–direction perturbation rotation. The flywheel, yoke, slider guide rod and baseplate are assumed to be rigid, and the motor is assumed to rotate at constant speed. Therefore the position of the crank is a known function of time. No perturbations are associated with it and no dynamic degrees of freedom are assigned to it.

Degrees of freedom are associated with links 5, 6 and 7, and therefore compatibility matrices $\mathbf{B}_5$, $\mathbf{B}_6$ and $\mathbf{B}_7$ must be defined. Link 5 has a force constraint at the ball joint and a kinematic constraint at the yoke pivot. However, the independent degrees of freedom resulting from the prismatic

joint's force constraint are transformed through the slider and yoke pivot bearings to the yoke pivot end of link 5. Therefore the $\mathbf{B}_5$ matrix consists of a [12x14] matrix with an identity matrix in the (1,1) to (12,12) elements, and all zeros in columns 13 and 14. Because joints 6 and 7 are modeled as ideal joints, the corresponding **B** matrices have time varying terms. They are listed in Tables 5.3 and 5.4. Blank cells in the tables are zero. Note that several columns are all zero and have been compressed into one column in the listings. For brevity, a notation has been used in which C_6 represents $\cos(\theta_6)$, S_7 represents $\sin(\theta_7)$, etc. H_6 is the height of the yoke, listed in Table 5.2, and y_{cg} is the y-location of the center of mass of the yoke in the N_6 reference frame, calculated to be -0.856". These matrices appear in the definitions of the links' perturbations: $\mathbf{a}_6 = \mathbf{B}_6\mathbf{q}$ and $\mathbf{a}_7 = \mathbf{B}_7\mathbf{q}$, Equation 3.4. For reference, the elements of the system **q** vector and of the **a** vectors have been listed across the top and down the left sides of the matrices.

To construct the simulation, it is necessary to compute the first and second time derivatives of $\mathbf{B}_6$ and $\mathbf{B}_7$ as well. These matrices involve $\dot{\theta}_6$, $\dot{\theta}_7$, $\ddot{\theta}_6$, and $\ddot{\theta}_7$. These derivatives are found by differentiating the equations for θ_6 and θ_7 given in Appendix E.

The mass properties of the rigid body links, 6 and 7, are listed in Table 5.5. The mass added to node 1 of the connecting rod finite element model, to account for the mass of the ball joint housing, is also shown. For links 6 and 7, the moments of inertia are calculated at the center of gravity and referenced to the axes of N_6 for link 6 and N_7 for link 7. The slider shell is symmetric and its center of gravity is at its geometric center. The calculated center of gravity of the yoke is shown in Figure 5.6.

Table 5.3. B_6 Compatibility Matrix.

	q_1 to q_6	q_7	q_8	q_9	q_{10}	q_{11}	q_{12}	q_{13}	q_{14}
$p_{6,1,x}$		C_6	S_6		$-S_6(H_6-y_{cg})$	$C_6(H_6-y_{cg})$			
$p_{6,1,y}$				-1					
$p_{6,1,z}$		$-S_6$	C_6		$-C_6(H_6-y_{cg})$	$-S_6(H_6-y_{cg})$			
$\theta_{6,1,x}$					C_6	S_6			
$\theta_{6,1,y}$								1	
$\theta_{6,1,z}$					$-S_6$	C_6			

Table 5.4. B_7 Compatibility Matrix.

	q_1 to q_6	q_7	q_8	q_9	q_{10}	q_{11}	q_{12}	q_{13}	q_{14}
$p_{7,1,x}$		C_7C_6	C_7S_6	$-S_7$	$-C_7S_6H_6$	$C_7C_6H_6$			
$p_{7,1,y}$		$-S_6$	C_6		$-C_6H_6$	$-S_6H_6$			
$p_{7,1,z}$		S_7C_6	S_7S_6	C_7	$-S_7S_6H_6$	$S_7C_6H_6$			
$\theta_{7,1,x}$					C_7C_6	C_7S_6		S_7	
$\theta_{7,1,y}$									1
$\theta_{7,1,z}$					S_7C_6	S_7S_6		$-C_7$	

Table 5.5. SSC Model Lumped Mass Properties.

	ball joint housing	Link 6 (yoke)	Link 7 (slider shell)
mass $\left(\frac{lbm}{386}\right)$	4.0×10^{-4}	2.21×10^{-3}	6.38×10^{-4}
I_x $\left(\frac{lbm * in^4}{386}\right)$	n.a.	6.21×10^{-3}	2.77×10^{-4}
I_y $\left(\frac{lbm * in^4}{386}\right)$	n.a.	2.23×10^{-3}	2.77×10^{-4}
I_z $\left(\frac{lbm * in^4}{386}\right)$	n.a.	1.43×10^{-3}	3.45×10^{-4}

C.4. Prismatic Joint Clearance Force Model

In the experimental instrumented prismatic joint, shown in Figure 5.5, internal contact occurs between the guide rod and the force sensor tips. A clearance connection model designed to correspond to the physical joint as closely as possible was constructed, and the details of that model will be given now.

In the model, the only type of contact is point contact between the hemispherical tips of the force sensors and the flat sides of the guide rod. There are eight possible contact points, two on each of the four sides in the shell. The locations of the contact points in the model correspond to the locations of the force sensor tips in the physical joint. Contact may exist at up to four points simultaneously. Dimensional variables and the locations of the contact points are shown in Figures 5.9a, 5.9b and 5.9c. The contact points are set in a symmetric but lopsided pattern so that the shell can resist torques about the z axis. The reference numbers assigned to the contact points in Figures 5.9a and 5.9b will be used in the following discussion. A subscript "p" will be used in this section as an index for the contact point numbers shown in the figure.

The coordinates of the contact point locations, in the N_7 reference frame of the slider, are shown in Figure 5.9a and listed in Table 5.6. The two sections of the table are for "vertical" force sensors, which measure contact forces in the N_7 frame's x-direction, and "horizontal" force sensors, which measure contact forces in the N_7 frame's y-direction. Length "a" is the dimension of either side of the square guide rod. Lengths T_w and T_z are slider shell

parameters, shown in Figure 5.9. The table also lists the unit vector in the N_7 frame in the direction of compressive contact force for each contact point.

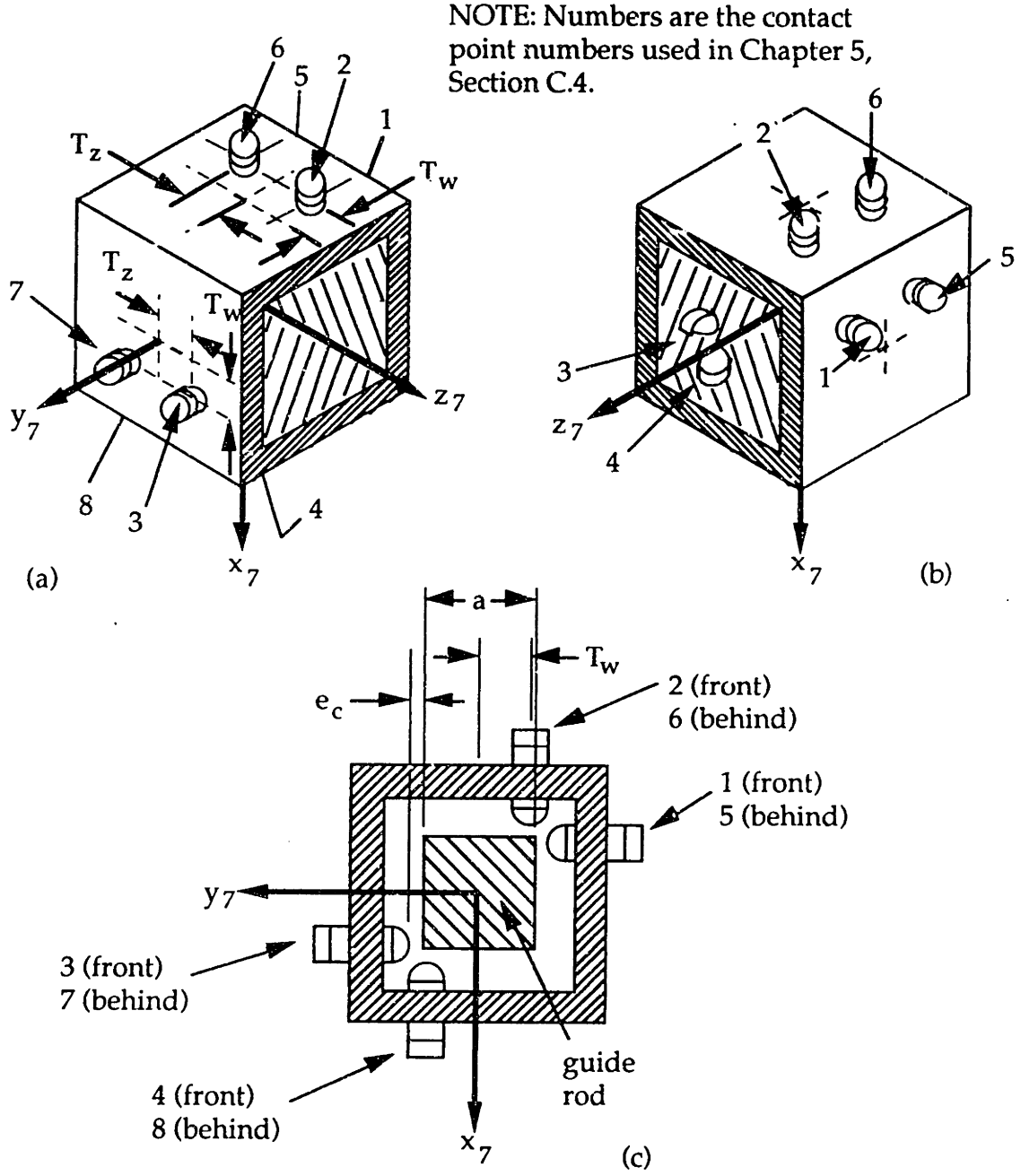

Figure 5.9. SSC prismatic joint clearance force model.

In the SSC's kinematic model, the slider shell is link 7 and the guide rod is part of link 1, as discussed in Section C.2. In order to express the motion of

the guide rod relative to the slider shell using Equations 3.8 to 3.12, define "link a" as the slider shell, link 7 in the Hartenberg-Denavit kinematic model, and "link b" as the guide rod, part of link 1 in the kinematic model. This choice of the slider shell as link a and the guide rod as link b, moving relative to link a, is not the intuitively obvious one. Since the guide rod is physically stationary, the natural choice would appear to be the rod as link a and the slider shell as link b, implying motion of the slider shell relative to the rod. However, choosing the slider shell as link a allows relative motions of the joint to be analyzed in the shell's N_7 reference frame, and the contact forces can then be applied directly to the $\mathbf{f}_{e,7}$ link interface force vector, Equations C.28 and 3.1. The "obvious" choice of the guide rod as link a would necessitate an additional transformation of the contact forces from the N_1 frame into the N_7 frame.

Table 5.6. Prismatic Joint Contact Point Locations.

horizontal sensors
y-direction force

sensor p	x	y	z	force dir.
1	$-T_w$	$\frac{a}{2} + e_c$	T_z	+j
3	T_w	$\frac{-a}{2} - e_c$	T_z	-j
5	$-T_w$	$\frac{a}{2} + e_c$	$-T_z$	+j
7	T_w	$\frac{-a}{2} - e_c$	$-T_z$	-j

vertical sensors
x-direction force

sensor p	x	y	z	force dir.
2	$\frac{-a}{2} - e_c$	T_w	T_z	-i
4	$\frac{a}{2} + e_c$	$-T_w$	T_z	+i
6	$\frac{-a}{2} - e_c$	T_w	$-T_z$	-i
8	$\frac{a}{2} + e_c$	$-T_w$	$-T_z$	+i

The nominal motion of the joint is relative translation of the guide rod relative to the slider, and it occurs along the z axis. The amount of clearance with the joint centered, shown in Figure 5.9c, is e_c on all four sides, assumed to be the same in both the x and y directions.

All eight potential contact points must be checked individually for contact. Equations 3.8 and 3.9 are used to form the joint perturbations $\Delta\mathbf{p}$ and $\Delta\phi$, using the $\mathbf{a}_7$ link perturbation vector to form the $\mathbf{p}_{a,2}$ and $\phi_{a,2}$ perturbation vectors. Since the guide rod, link b, has no perturbations, $\mathbf{p}_{b,1}$ and $\phi_{b,1}$ are zero. At each potential contact point, the amount of movement of the guide rod with respect to the slider shell in response to the perturbations $\Delta\mathbf{p}$ and $\Delta\phi$ is δ_p:

$$\delta_p = \Delta\mathbf{p} + \Delta\phi \times \mathbf{d}_p \tag{5.1}$$

where $\mathbf{d}_p$ is a vector that locates the potential contact point with respect to the center of the slider shell. The elements of $\mathbf{d}_p$ for the eight contact points, p = 1...8, are given in Table 5.6. Expanding δ_p in terms of the components of the $\Delta\mathbf{p}$, $\Delta\phi$ and $\mathbf{d}_p$ vectors gives:

$$\begin{aligned}\delta_p = &[(\Delta\mathbf{p})_x + (\Delta\phi)_y\, \mathbf{d}_{p,z} - (\Delta\phi)_z\, \mathbf{d}_{p,y}]\,\mathbf{i} + \\ &[(\Delta\mathbf{p})_y + (\Delta\phi)_z\, \mathbf{d}_{p,x} - (\Delta\phi)_x\, \mathbf{d}_{p,z}]\,\mathbf{j} + \\ &[(\Delta\mathbf{p})_z + (\Delta\phi)_x\, \mathbf{d}_{p,y} - (\Delta\phi)_y\, \mathbf{d}_{p,x}]\,\mathbf{k}\end{aligned} \tag{5.2}$$

where **i**, **j** and **k** are the N_7 frame unit vectors and $\mathbf{d}_{p,x}$, $\mathbf{d}_{p,y}$, and $\mathbf{d}_{p,z}$, indicate the x, y and z elements of the $\mathbf{d}_p$ vector. For x-direction contact points, listed in Table 5.6, contact occurs if the **i** component of δ_p indicates that the guide rod moves e_c or more in the x direction toward the contact point; for y-direction contact points, contact occurs if the **j** component of δ_p indicates motion of e_c or more toward the contact point.

The amount of interference between the guide rod and slider is $|s_p|$, where s_p is calculated according to Table 5.7. Table 5.7 also lists the condition on s_p that determines whether contact exists at each point.

If contact occurs, the rate of change of the amount of interference is found from:

$$\dot{s}_p = \begin{cases} \mathbf{v}_{cont} \cdot \mathbf{i} & \text{for i-direction contact} \\ \mathbf{v}_{cont} \cdot \mathbf{j} & \text{for j-direction contact} \end{cases} \tag{5.3}$$

where $\mathbf{v}_{cont}$ is from Equation 3.12. Ω_{nom} in Equation 3.12 is zero. $\mathbf{V}_{nom}$ is purely in the **k** direction and is found from a kinematic analysis of the mechanism to be $\frac{\dot{x}_6}{\cos(\gamma)}$, where $\dot{x}_6$ is found by differentiating x_6, Appendix E, and γ is the motor angle, see Figure 5.1. Expanding Equation 5.3 and simplifying gives:

$$\dot{s} = \begin{cases} (\Delta\dot{\mathbf{p}})_x + (\Delta\dot{\phi})_y\, \mathbf{d}_{p,z} - (\Delta\dot{\phi})_z\, \mathbf{d}_{p,y} & \text{for i-direction contact} \\ (\Delta\dot{\mathbf{p}})_y + (\Delta\dot{\phi})_z\, \mathbf{d}_{p,x} - (\Delta\dot{\phi})_x\, \mathbf{d}_{p,z} & \text{for j-direction contact} \end{cases} \tag{5.4}$$

Therefore the following table of contact conditions may be constructed:

Table 5.7. Contact Conditions, Prismatic Joint.

contact point p	s_p	contact if...	$\dot{s}_p$
1	$(\Delta\mathbf{p})_y - (\Delta\phi)_z T_w - (\Delta\phi)_x T_z - e_c$	$s_1 > 0$	$(\Delta\dot{\mathbf{p}})_y - (\Delta\dot{\phi})_z T_w - (\Delta\dot{\phi})_x T_z$
2	$(\Delta\mathbf{p})_x + (\Delta\phi)_y T_z - (\Delta\phi)_z T_w + e_c$	$s_2 < 0$	$(\Delta\dot{\mathbf{p}})_x + (\Delta\dot{\phi})_y T_z - (\Delta\dot{\phi})_z T_w$
3	$(\Delta\mathbf{p})_y + (\Delta\phi)_z T_w - (\Delta\phi)_x T_z + e_c$	$s_3 < 0$	$(\Delta\dot{\mathbf{p}})_y + (\Delta\dot{\phi})_z T_w - (\Delta\dot{\phi})_x T_z$
4	$(\Delta\mathbf{p})_x + (\Delta\phi)_y T_z + (\Delta\phi)_z T_w - e_c$	$s_4 > 0$	$(\Delta\dot{\mathbf{p}})_x + (\Delta\dot{\phi})_y T_z + (\Delta\dot{\phi})_z T_w$
5	$(\Delta\mathbf{p})_y - (\Delta\phi)_z T_w + (\Delta\phi)_x T_z - e_c$	$s_5 > 0$	$(\Delta\dot{\mathbf{p}})_y - (\Delta\dot{\phi})_z T_w + (\Delta\dot{\phi})_x T_z$
6	$(\Delta\mathbf{p})_x - (\Delta\phi)_y T_z - (\Delta\phi)_z T_w + e_c$	$s_6 < 0$	$(\Delta\dot{\mathbf{p}})_x - (\Delta\dot{\phi})_y T_z - (\Delta\dot{\phi})_z T_w$
7	$(\Delta\mathbf{p})_y + (\Delta\phi)_z T_w + (\Delta\phi)_x T_z + e_c$	$s_7 < 0$	$(\Delta\dot{\mathbf{p}})_y + (\Delta\dot{\phi})_z T_w + (\Delta\dot{\phi})_x T_z$
8	$(\Delta\mathbf{p})_x - (\Delta\phi)_y T_z + (\Delta\phi)_z T_w - e_c$	$s_8 > 0$	$(\Delta\dot{\mathbf{p}})_x - (\Delta\dot{\phi})_y T_z + (\Delta\dot{\phi})_z T_w$

The SSC simulation uses a contact model with linear stiffness and damping. Therefore, the normal contact force at each contact point is:

$$f_{nor,p} = \begin{cases} (k*s_p + b*\dot{s}_p); & (k*s_p + b*\dot{s}_p)*s_p > 0 \\ 0; & (k*s_p + b*\dot{s}_p)*s_p < 0 \end{cases} \tag{5.5}$$

Equation 5.5 is applied separately for each contact point, but only when s_p meets the condition given in Table 5.7. The additional condition $(k*s_p + b*\dot{s}_p)*s_p > 0$ in Equation 5.5 guarantees compressive contact force by forcing $f_{nor,p}$ and s_p to have the same sign if $f_{nor,p}$ is non-zero. Note that, since Table 5.7 and Equation 5.5 give both a magnitude and sign to the scalar $f_{nor,p}$, only the unit direction vector – not its sign – is taken from Table 5.6. Using contact point 2 as an example, find from Table 5.6 that point 2 is an x-direction contact point, and its compressive contact forces are in the -**i** direction. Therefore, its contact force vector is $\mathbf{f}_{nor,2} = f_{nor,2}\,\mathbf{i}$, where $f_{nor,2}$ is non-zero only if both $s_2 < 0$, Table 5.7, and $(k*s_2 + b*\dot{s}_2)*s_2 > 0$, Equation 5.5, are true. These conditions result in the scalar $f_{nor,2}$ being non-positive, so that the vector $\mathbf{f}_{nor,2}$ is either 0 or in the -**i** direction.

Each contact normal force also produces a torque, $\Gamma_p = \mathbf{d}_p \times \mathbf{f}_{nor,p}$. Procedures for adding resultant torques to the joint interface forces have been discussed in Chapter 3.

Finally, as with the other joint models, a sliding friction force component may also be computed at the contact points. A simplified model might neglect the perturbation velocity components and compute only the friction force due to the nominal velocity. In this case, the friction force at each contact point is

$$\mathbf{f}_{fric,p} = c * \mu * |f_{nor,p}| * \text{sign}(\mathbf{V}_{nom}) * \mathbf{k} \qquad (5.6)$$

where c represents a ramping function to assure that the force is continuous when the velocity passes through zero, similar to Equation 3.37. The force produces a torque; finally, the forces and torques resulting from normal and sliding contact are summed to find the resultants, the components of which are added to the $f_{c,7}$ vector.

For the studies reported here, v_{tol} in the friction force ramping function was 0.1 in/sec, which is 1% of the peak slider speed at a motor speed of 50 rpm. The contact stiffness and damping coefficients used, k and b in Equation 5.5, are listed in the third column of Table 5.1. They are based on a linearized Hertzian contact analysis, and on estimates of the effective mass and damping ratio associated with contact. See Appendix F for details.

D. Results of Experimental Contact Force Measurements

D.1. Introduction

The SSC experimental system was operated at several speed and clearance settings, and contact forces in the instrumented ball joint and instrumented sliding joint were measured. Figure 5.10 shows the contact force measured at one of the upper vertical force sensors on the slider, during a 10 second period, while the spatial slider crank was being operated at 230 rpm with ±0.0025" clearance in both the sliding and ball joints. About 38 cycles appear on the figure, and there is a distinctive once per cycle force peak caused by impacts.

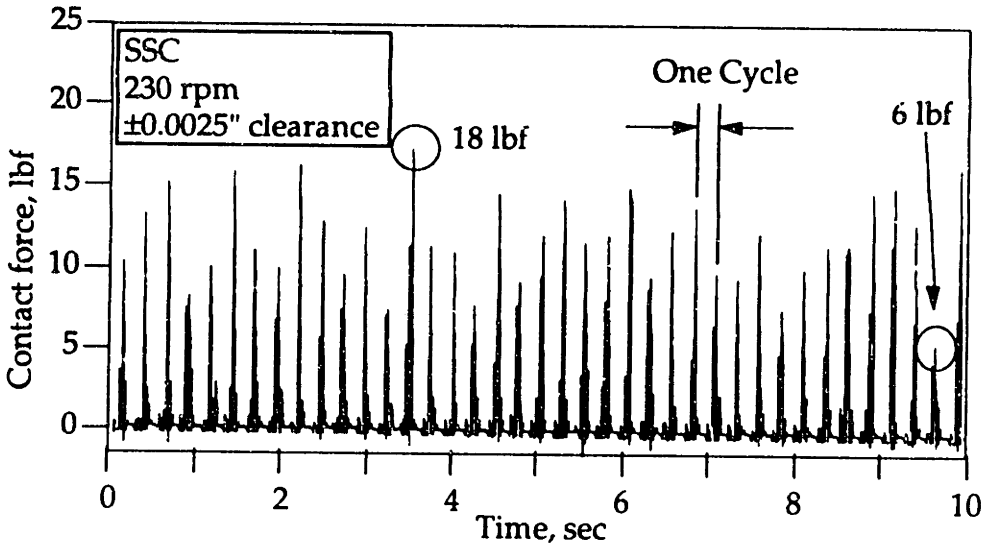

Figure 5.10. Slider vertical contact force, experimental. One sensor.

As with the IBS, there is a great deal of non-periodic variability in impact forces as the spatial slider crank goes through cycles of motion at constant speed. This is consistent with suspected chaotic behavior in systems with impacts [45]. The contact force shown in Figure 5.10 is clearly not consistent from cycle to cycle. The cyclic peaks vary from approximately 6 to 18 lbf. Examination of traces similar to Figure 5.10 on an expanded time scale shows that impacts in the spatial slider crank follow a pattern similar to those seen with the IBS in Figure 4.8: an initial, large and very short peak, a short period of bouncing, and then a period in contact. Figure 5.11 shows this phenomenon.

D.2. 0° Motor Angle

Initially, the SSC was operated with the motor angle set to zero and zero horizontal offset between the guide rod axis and the center of the ball joint. Figure 5.11 shows a slider vertical contact force history taken from operation of the SSC at 200 rpm with ±0.005" clearance in both the ball and sliding

joints. In this figure, the outputs of all four vertical force sensors on the slider have been summed after digitization to create the trace shown. A time of zero seconds corresponds to a 0° crank angle.

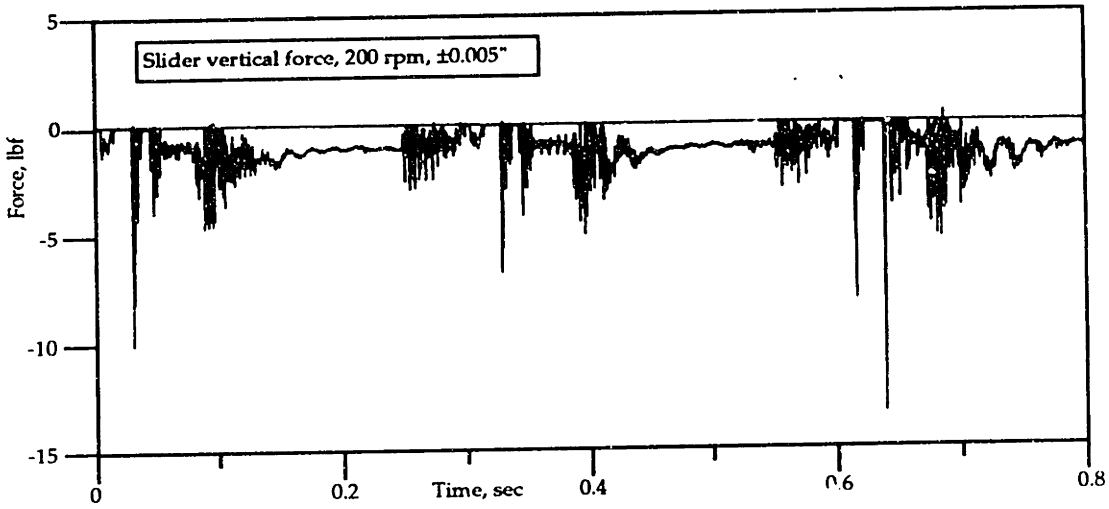

Figure 5.11. Slider vertical contact force, experimental. Sum of all vertical sensors.

The outputs of the two upper force sensors, numbers 2 and 6 in Figure 5.9, are multiplied by -1 before summing so that the weight of the slider appears in Figure 5.11 as a negative force. The fact that there are only a few data points with positive force shows that contact with the lower force sensors is extremely rare.

At 200 rpm, each cycle requires 0.3 seconds. Therefore, the plot shows 2 2/3 cycles of motion. The extremes of the slider's travel occur at 0° and 180° crank angle, or 0 and 0.15 seconds, 0.3 and 0.45 seconds, etc. The plot clearly shows moments of free flight with zero force, impact forces and periods of bouncing, and periods of constant contact. The trace shows some periodic behavior, especially in the second half of each cycle, where the contact force is nearly constant and is highly repeatable in each cycle. The events from 0.25 to 0.3, and 0.55 to 0.6 seconds are probably due to structural vibration caused by

impacts elsewhere in the system; note that there is no distinct free flight zone during these periods and that the force levels are quite similar for the two events recorded. The large impacts, which occur at about .03, .303 and .603 seconds after free flight periods, exhibit a great deal of variation in peak impact forces. The peak force varies from about 6.8 to about 13.3 lbf. As in the IBS, bearing contact forces in the SSC's slider consist of highly repeatable nominal forces and superimposed, highly variable peak impact forces.

Figure 5.12 shows ball joint contact force data for the same conditions as Figure 5.11. This figure shows the magnitude of the contact force after vectorially adding the outputs of the ball joint's four sensors. The raw data showed that at least one force sensor was in contact with the ball at all times. Therefore, there is no real free-flight period on this force history. Even though contact is never lost completely, large impact forces can be generated, because the ball can impact against a force sensor while it is still in contact with one or two others. This behavior results in a contact force magnitude that contains peaks due to impacts, but is never zero. However, a true ball joint, consisting of just a ball and socket, might show different behavior.

There are also large and regular force variations, for example between 0.1 and 0.2 seconds, and again between 0.4 and 0.5 seconds, on this figure. The relatively slow rise time and regular appearance of these forces suggests that they are not impacts. These forces are probably due to play in the pivot bearing on top of the slider yoke, possibly interacting with friction in the slider. Both clearance joints were run lubricated with light machine oil, but it is impossible to eliminate all friction. These effects are discussed in some detail in Section D.5, "Experimental Considerations," later in this chapter.

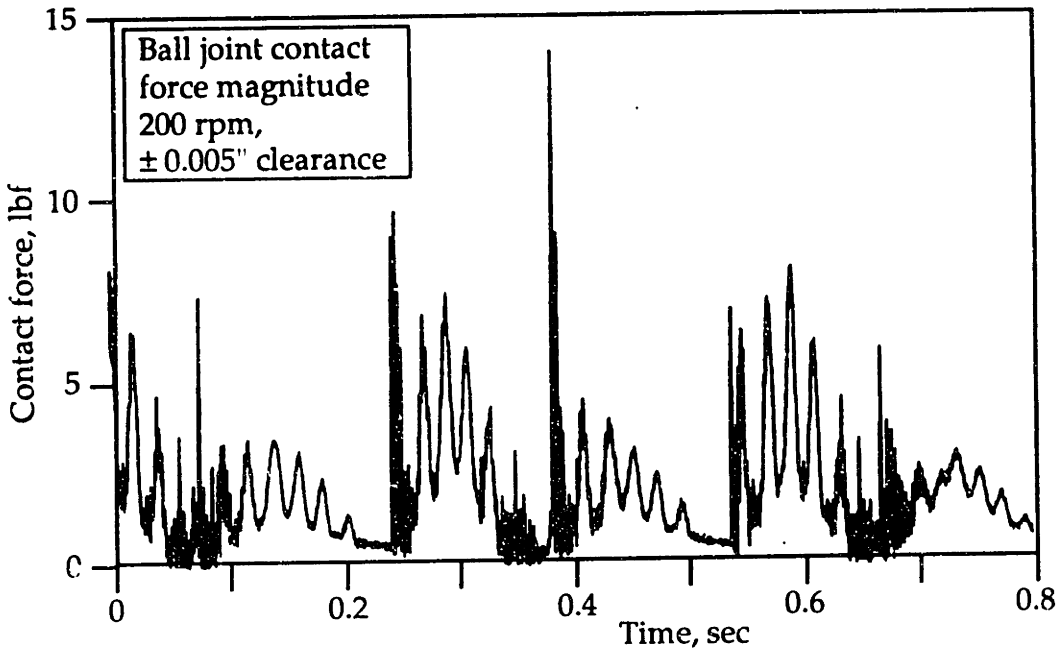

Figure 5.12. Ball joint contact force magnitude, experimental.

Figure 5.12 shows that the SSC exhibits the pattern seen in the IBS and in Figure 5.11 of large and varying impact forces superimposed on regular and cyclic nominal contact forces. Note that the largest impact, which is at 0.39 seconds, appears to be a cyclic impact occurring about 0.09 seconds into each cycle. It varies in magnitude from 14.1 to 5.9 lbf. There is also a second, apparently cyclic impact, at 0.25 and 0.55 seconds. Its magnitude is comparable to two of the samples of the first cyclic impact but considerably lower than the 14.1 lbf peak. The very fast rise time of these forces, and the bouncing behavior just after the initial peak, are indications that the events discussed are impacts. As explained in Section D.5, since there was no free flight zone for the ball joint in this experiment, the absolute magnitude of the contact force could not be directly determined from the force sensor data.

Figure 5.13, and the figures similar to it, 5.14, 5.16 and 5.17, show both peak contact forces and the degree of variability of contact forces observed during

operation of the SSC under different conditions. The upper curves in these plots are the maximum impact/contact forces observed from the time histories. The lower curves show the smallest observed peak force value occurring at the same phase angle as the maximum peak force. The separation between curves indicates the degree of cyclic variability in the machine's contact forces. Periodic behavior produces curves with little separation, while highly separated curves indicate highly aperiodic behavior.

Some explanation regarding the construction of these figures may be helpful before discussing their content. The SSC was operated at several speed / clearance settings. For each combination of speed and clearance, experimental data similar to Figures 5.11 and 5.12, showing several cycles of machine operation and a number of contact force peaks, were collected from the slider and ball joint force sensors. Every such time history contributes two points, one to each of the upper and lower curves, to the plots of Figure 5.13, 5.14, 5.16 or 5.17. The procedure used is best explained by an example. Figure 5.11 is for 200 rpm, ±0.005" clearance, and thus contributed the two points at 200 rpm in Figure 5.13c. The peak force observed in Figure 5.11 is 13.3 pounds, at 0.64 seconds. This point is plotted on Figure 5.13c at 200 rpm, 13.3 pounds. The time of the peak in Figure 5.11, 0.64 seconds, is about 0.04 seconds after the start of a machine cycle. Of all force peaks occurring about 0.04 seconds after the start of a machine cycle recorded on Figure 5.11, the one at approximately 0.33 seconds, 6.8 pounds, is the smallest. Therefore, it was plotted on the lower curve of Figure 5.13, at 200 rpm, 6.8 pounds. Figures 5.13, 5.14, 5.16 and 5.17 were generated in this manner from slider and ball joint contact force time histories.

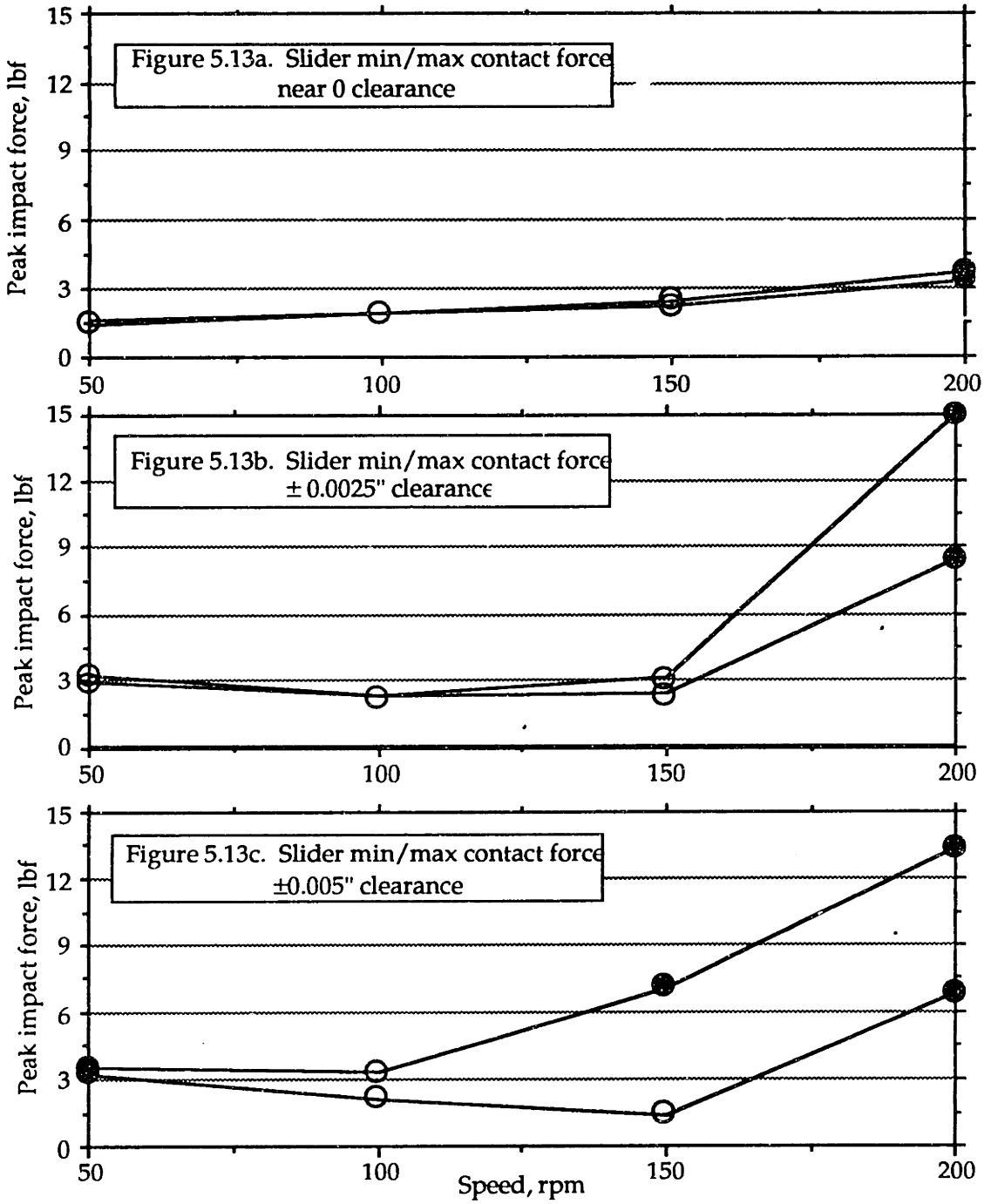

Figure 5.13. Slider peak vertical contact force vs. speed, 0 motor angle, experimental.
a) Near zero clearance.
b) ±0.0025" clearance.
c) ±0.005" clearance.

NOTE: ● indicates peak force caused by impact;
○ indicates peak force *not* caused by impact.

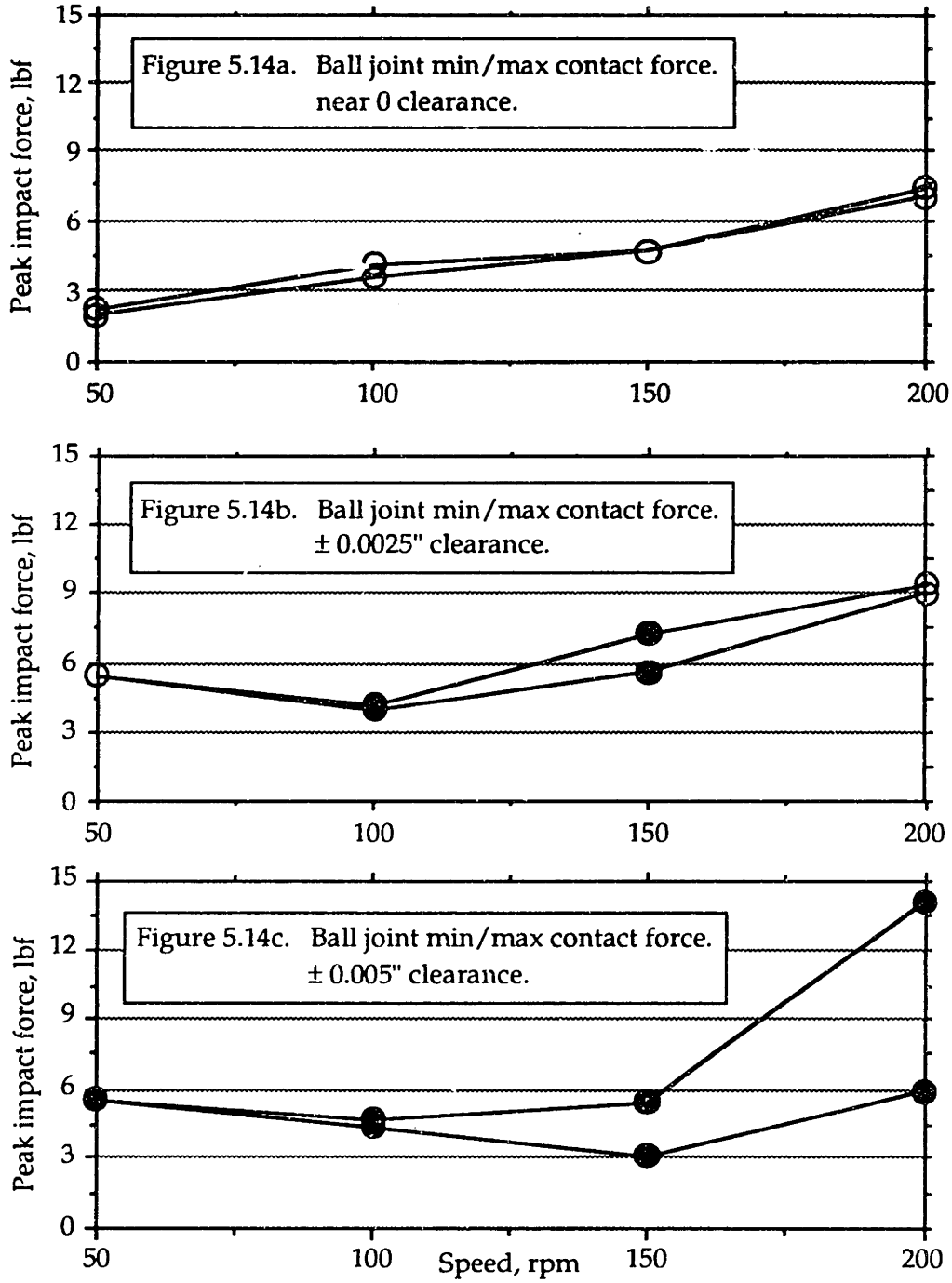

Figure 5.14. Ball joint peak contact force magnitude vs. speed, 0 motor angle, experimental.
a) Near zero clearance.
b) ±0.0025" clearance.
c) ±0.005" clearance.

NOTE: ● indicates peak force caused by impact;
○ indicates peak force *not* caused by impact.

Points plotted with a black dot indicate that the force peak was due to impact; an open circle indicates a force peak *not* caused by impact.

The SSC cannot run with truly zero clearance in the ball joint and sliding joint. For Figures 5.13a, 5.14a, 5.16a and 5.17a, "near zero" clearance was obtained by adjusting the slider and ball joint clearances to the smallest value that would permit the mechanism to run freely. The small remaining clearance could not be measured accurately with the tools available. However, it is less than ±0.001".

Figure 5.13 reveals that the expected trend of increasing contact force peaks as speed increases is not always present in the SSC's slider. The peak contact force is nearly constant for speeds from 50 to 150 rpm, rising strongly only above 150 rpm. The static weight of the yoke and slider, about 1.1 lbf, is the minimum level of the measured peak contact force. In cases where there was no slider impact, shown with open circles, the plotted peak forces are due to forces transmitted through the SSC mechanism, for instance from impacts at the ball joint, or from the yoke's top pivot bearing. It is surprising that, in Figures 5.13b and 5.13c, the minimum peak force falls slightly as the speed increases to 150 rpm. A possible explanation is that the speed of the slider may affect friction forces between the slider and its guide rod. Since the slider friction force vector is oriented horizontally along the axis of the slider guide rod, it does not directly affect the vertical contact forces shown here. However, it can affect the vertical force through indirect coupling. All the forces required to move the slider are transmitted by the connecting rod. Since the connecting rod is not horizontal for most of the cycle, the force it transmits has a vertical component that increases when the horizontal component necessary to overcome friction increases. This vertical

component then affects the vertical contact force measured by the slider's force sensors. High speeds might contribute to hydrodynamic lubrication in the slider force sensor tips[1], which, through this indirect force coupling mechanism, may account for the reduction in force as the machine speeds up.

As shown by the open and filled circles on the plots, slider impacts begin between 150 and 200 rpm for all the clearances tested. It is well known that, in many mechanisms, gravity can preload the clearance joints and prevent impacts until the machine's speed is high enough that the dynamic forces exceed the gravity forces.

Figure 5.14 shows contact data for the ball joint, using the same rules to generate the plots as Figure 5.13. As in Figure 5.13, the black dots indicate force peaks due to impacts, and open circles mark peaks apparently not due to impacts. Because the ball joint never experiences true free flight for any of the tested conditions, the determination of whether impact occurred is less reliable than for the slider. The static load at the ball joint could not be measured directly but was estimated to be 0.2 lbf, based on the measured masses of the components and the weight distribution expected from their layout. This static load varies slightly with the crank angle. As in the slider data, these data for the ball joint contact force reveal a trend that is nearly flat from 50 to 150 rpm, and rises steeply with the onset of consistent slider impacts between 150 and 200 rpm.

---

[1]Although the slider's force sensor tips were designed to be hemispherical, in operation they quickly developed small flat spots from sliding along the guide rod and from impacts.

The nominal force required to move the slider back and forth is due to its acceleration, proportional to the square of the motor speed, and its peak value at 200 rpm is calculated to be 3 lbf. The calculation of nominal forces is discussed in Section E of this chapter. Slider friction dominates the ball joint force, and it causes a halting, jerky motion of the slider that can be observed even at high operating speeds, and is very strongly noticeable at low speeds. This phenomenon is thought to be the cause of oscillations in force like those seen in several parts of Figure 5.12, for example from 0.4 to 0.5 seconds. The slider velocity is zero at 0° and 180° crank angle, and the data acquisition is triggered so that t equals 0 at 0° crank angle. Thus, the major oscillations in ball joint contact force coincide with the ends of its stroke, where the slider velocity is low and static friction is most important. At lower motor speeds, when there are no impacts, the magnitude of these oscillations stays about the same and dominates the ball joint force, which is the reason that the peak force changes relatively little from 50 to 150 rpm.

The minimum ball joint force shows the same surprising dip at 150 rpm, 0.005" clearance that was seen in Figure 5.13. The data collected to create Figures 5.13 and 5.14 came from different experimental runs since the hardware did not allow concurrent acquisition of data from the ball joint and the slider. Thus, these data suggest that, as the SSC's speed increases up to 150 rpm, the force transmitted in the connecting rod really is reduced, and the dip noted in Figure 5.13 is not an anomaly from that set of experiments.

Note that the peak forces for cycles in which impacts occurred rise strongly with speed. Therefore the data show that, in some cycles where there is no impact, the peak bearing force is relatively low; in others, where impacts occur, the peak force is much higher. Such behavior observed in successive

cycles of nominally constant operation is another indication of the variability that clearances can introduce in machine system operation.

The two points at 200 rpm in Figure 5.14b, at 9 to 9.3 lbf, are somewhat unusual since in this particular condition, the peak forces measured were not due to impacts. Vibrations, similar to those seen around 0, 0.3 and 0.6 second in Figure 5.12 for 0.005" clearance, were large enough that they were larger than the impact forces. Clear impacts did occur on the time history, similar to those in Figure 5.12, but their force magnitudes were lower than the non-impact peaks.

These data show that the experimental SSC is capable of highly variable, complex behavior. Recreating this behavior with some fidelity is a requirement for useful software-based design tools. The SSC simulation results will be discussed in Sections E and F, after some more experimental results have been presented.

D.3. 25° Motor Angle

The SSC was constructed so that the motor angle could be varied to give it fully spatial kinematics. To explore the effects of this change, the motor angle was set to 25°. The position of the motor was set so that the connecting rod swung equally to either side of the slider guide rod as shown in Figure 5.15.

Figures 5.16 and 5.17 are plots of data similar to Figures 5.13 and 5.14, except with 25° motor angle. Comparison of Figure 5.13 with 5.16, and Figure 5.14 with 5.17, shows that changing the motor angle to 25° has very little effect on the ball joint and slider impact forces. The same trends are apparent and the magnitudes of the curves agree closely. In cases where there are no impacts,

the forces agree extremely well. In cases where impacts occur, the agreement is less good, but this could be due to the highly variable nature of impact forces and the relatively small sample of cyclic impacts observed.

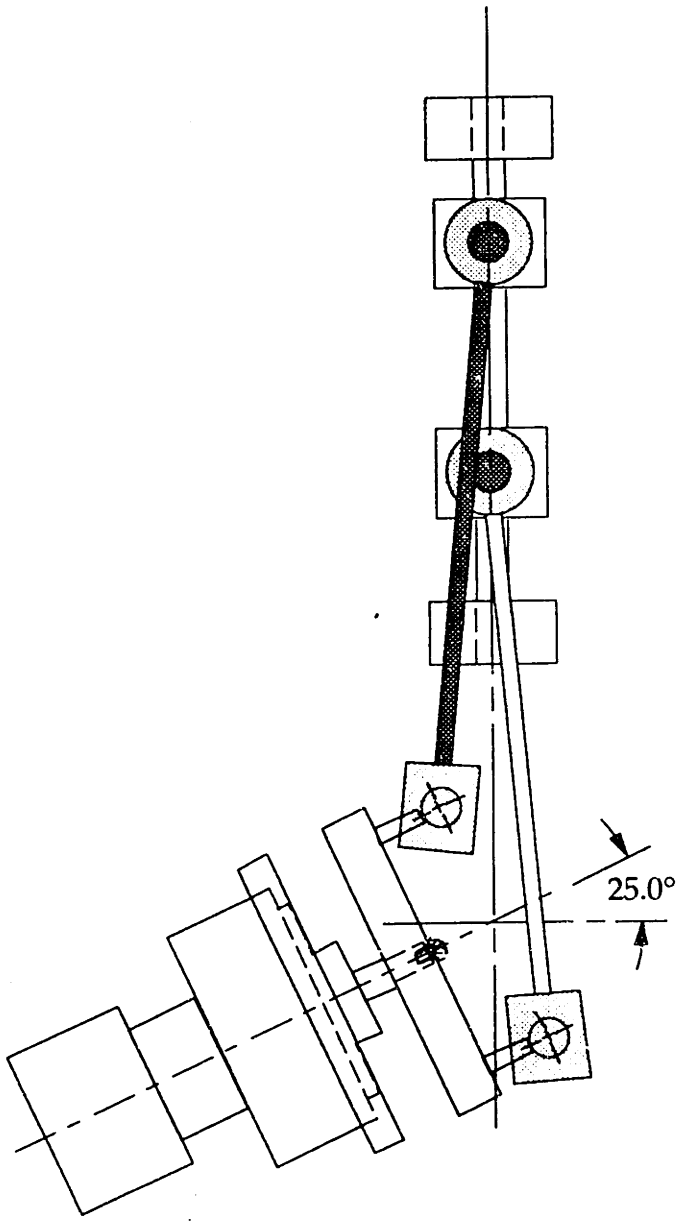

Figure 5.15. Plan view of the SSC, 25° motor axis angle.

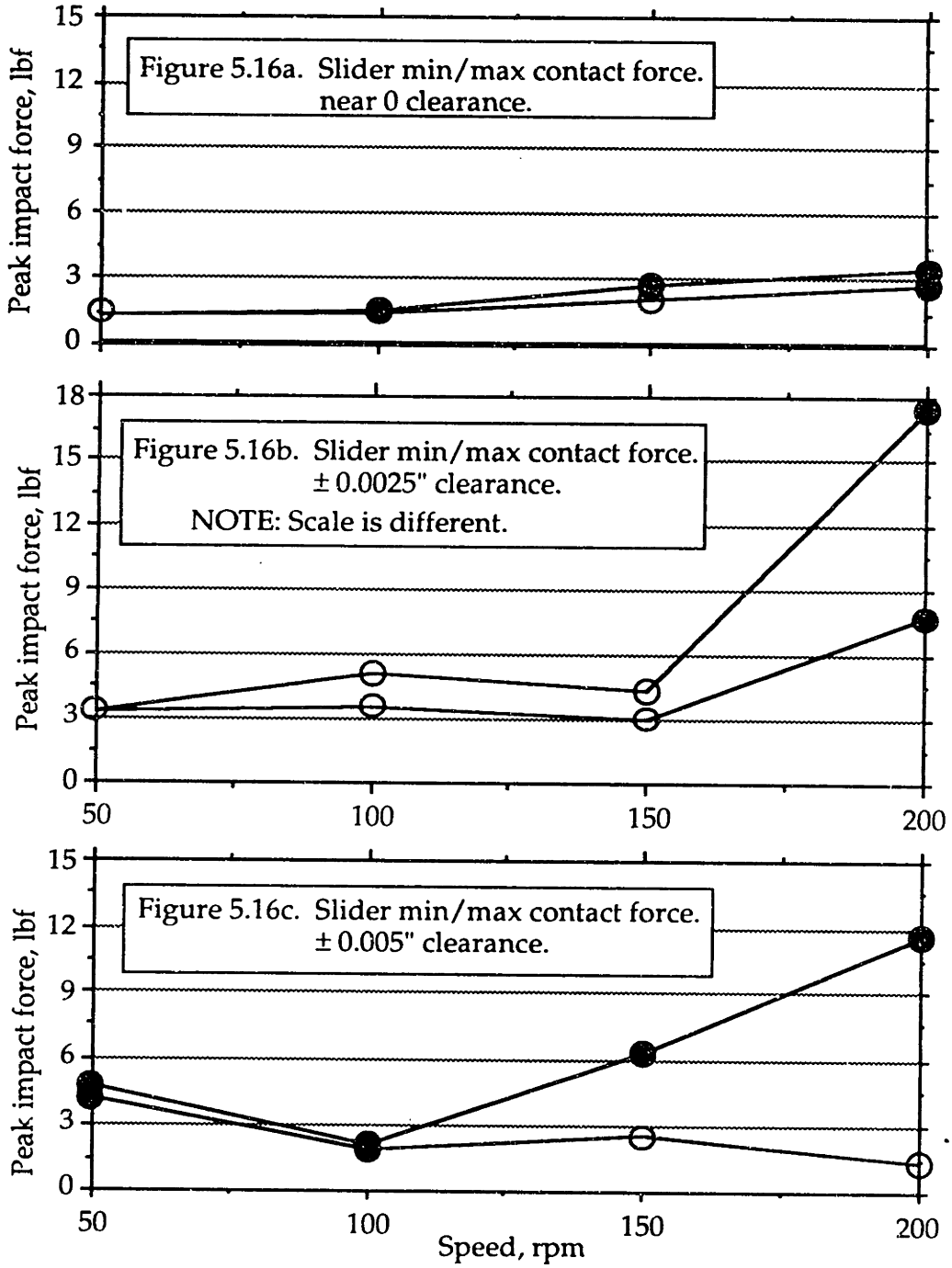

Figure 5.16. Slider peak vertical contact force vs. speed, 25° motor angle, experimental.
a) Near zero clearance.
b) ±0.0025" clearance.
c) ±0.005" clearance.

NOTE: ● indicates peak force caused by impact;
○ indicates peak force *not* caused by impact.

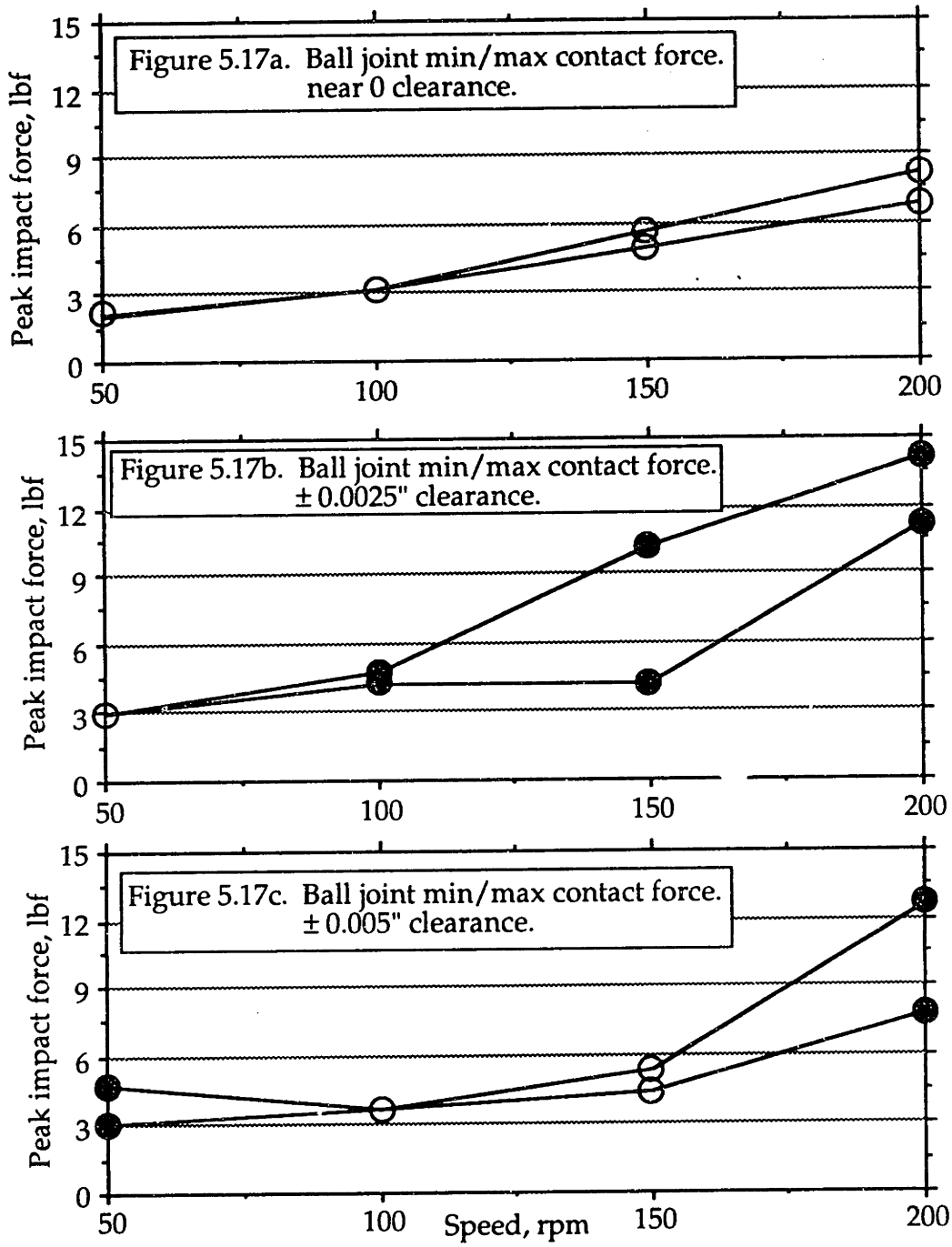

Figure 5.17. Ball joint peak contact force magnitude vs. speed, 25° motor angle, experimental.
a) Near zero clearance.
b) ±0.0025" clearance.
c) ±0.005" clearance.

NOTE: ● indicates peak force caused by impact;
○ indicates peak force *not* caused by impact.

D.4. Slider Horizontal Contact Forces

Nominally, at 0 motor axis angle, the horizontal forces are zero because the system is planar. At 25° motor angle, the simulation predicts very small horizontal slider forces. Experimentally, the slider rotates about the axis of the upper yoke pivot bearing to the limits allowed by the clearance, continually banging back and forth against the guide rod at its front and rear corners. The forces caused by varying the motor angle are so small compared with these impacts that they cannot be distinguished in the data. Figure 5.18 shows this. Figure 5.18a plots the positive and negative components of the slider horizontal contact force for 200 rpm operation with 0.005" clearance and 25° motor angle. The positive and negative peaks are caused by impacts. Summing these components and plotting the resultant force produces Figure 5.18b, showing that the positive and negative impacts are almost perfectly coincident in time and almost exactly the same in magnitude. The remaining noise level is of the same order as the sideways force due to nominal motion that the simulation predicts. Similar results were seen at all other speeds and clearances.

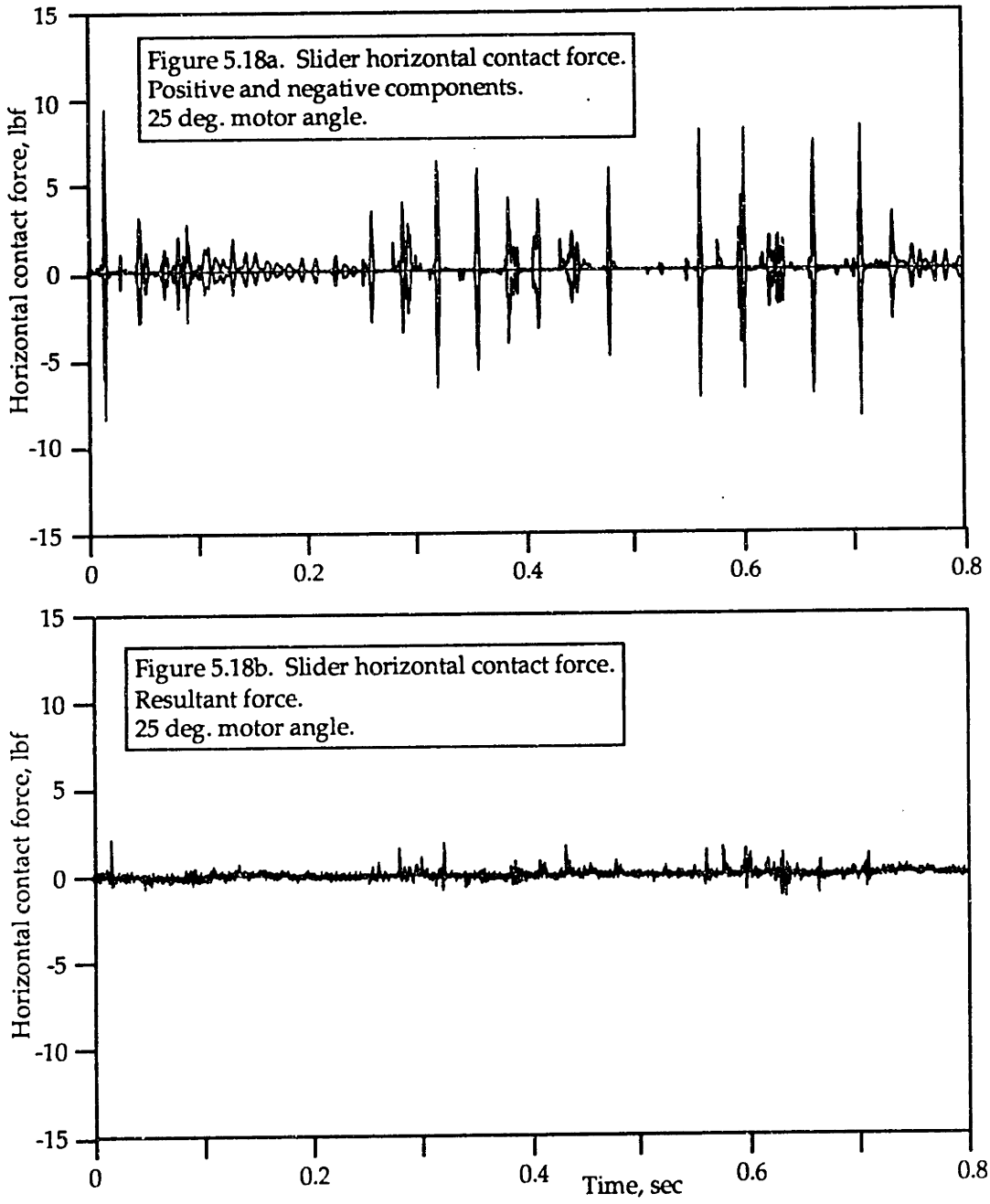

Figure 5.18. Slider horizontal contact force, 25° motor angle, experimental.
a) Positive and negative components.
b) Resultant.

D.5. Experimental Considerations

Several characteristics of the experimental SSC make it more difficult than the IBS to control precisely.

The operating speed of the SSC has two aspects: its "nominal speed," given by the period required for one revolution of the flywheel, and its "instantaneous speed," the angular velocity of the motor / flywheel at any instant in time. Nominal speed is calculated from the time elapsed between sync pulses generated by a photonic sensor once per revolution of the flywheel. Instantaneous speed is monitored using an oscilloscope to observe the output of a tachometer attached to the motor. Due to the substantial mass of the system's reciprocating elements, the yoke and slider, it is not possible to maintain constant instantaneous speed as the SSC operates. The flywheel was designed to relieve this problem by greatly increasing the rotary inertia of the system, but it cannot entirely eliminate the effect. At 200 rpm nominal speed, instantaneous speed variations are around 5% of the nominal speed, and they increase at lower speeds. To improve this situation would require either an even larger flywheel or implementing a feedback loop to control the motor speed.

At higher experimental speeds, 100 rpm and above, the nominal speed of the SSC drifts no more than a few percent over relatively long times, of the order of several minutes. This is because the instantaneous speed variations are largely caused by the repeatable reciprocating motions of the yoke and slider, so the variations of instantaneous speed are highly periodic and do not affect the overall nominal speed. However, at 50 rpm, other factors have a large effect, and apparently random instantaneous variations of 50% of the nominal speed and even more are not uncommon. These large, non-repeatable variations in the instantaneous speed result in large variations in the nominal speed. In general it was not possible to maintain a constant 50 rpm nominal speed for periods longer than a few seconds. In typical

operation, with the input voltage to the motor at about 1.7 V and controlled to ±0.005 V, the period of the flywheel might vary from 1.4 sec (43 rpm) to .9 sec (67 rpm) in 30 seconds or less. The degree of such behavior is itself highly variable. The cause of these variations is uncertain but suspected to be related to minor variations in contact friction as the slider moves on the guide rod. Reducing the clearance improves the problem, possibly by causing the slider to follow more nearly the same path on every cycle of motion. It may be noted that such behavior is yet another manifestation of nonlinearity in the SSC, although this nonlinearity appears to be related to friction rather than to clearance impacts. This problem would be difficult to solve by a reasonable increase in the size of the flywheel, but probably could be improved by feedback control of the motor speed.

Another problem concerns play in the pivot bearing atop the yoke. This is a plain ball bearing that is required to sustain angular loading, not a recommended loading condition for such bearings. Over the course of experiments it developed some angular play, which, like any other clearance, led to high impact forces at points of motion reversal in the cycle. These forces, possibly interacting with friction in the slider and ball joints, are felt to be the main reason for the large contact force variations, not associated with impact in the instrumented joints, that were measured in several experiments. Redesigning the connecting rod – to – yoke pivot would be desirable.

Friction in the ball joint and slider joint was noted to be a problem when the SSC was operated without lubrication, causing jerky motion and chattering in both the slider and the ball joint. For all results reported here, these joints were run lubricated with light machine oil, which greatly reduced the

problems. However, friction effects, possibly interacting with the pivot bearing clearance, still caused visible jerkiness in the slider's motion, especially at low speeds.

The piezoelectric force sensors and the instrumentation charge amplifiers do not respond at zero frequency. If the average value of the force applied to a sensor is not zero, the amplifier's output drifts slowly toward an equilibrium where zero volts corresponds to the average value of the force. The time constant associated with this drift depends on the specific force sensor and charge amplifier combination; for the 12 sensors on the SSC and the 8 amplifiers used with them, time constants were of the order of 3 to 30 seconds. Since the contact forces measured by the sensors in the slider and ball joint are always compressive, the average force applied to a sensor is certain to be non-zero, and the output voltage is certain to have a DC offset such that zero volts does not imply zero contact force. This and other factors, such as low sensor resistance due to contamination, and sensor temperature changes, combine to make the amount of the DC offset unpredictable. Therefore, while *changes* in contact force can be detected by observing the output voltage of the charge amplifier, the *absolute* magnitude of contact force cannot be known without some external calibration. When impacts occur at a sensor, that calibration is available by looking for the characteristic short flat trace that occurs just before an impact. Since the sensor is out of contact in this period, its contact force must be zero, and the DC offset can be established and subtracted from the data. The zero levels in Figure 5.11, for instance, were established in this manner. When there is no loss of contact, this method is not available. Such situations occur, for instance, at low speeds in the slider, or at any speed for some of the sensors in the ball joint.

In these cases, an absolute level was established for the data presented here by estimating force levels based on the weight of the mechanism and its nominal motion, and then adjusting the DC offset of the experimental traces to match the estimated force level. Thus, while the reported changes and variability in contact forces are felt to be reliable, the reported absolute magnitudes are estimates except in cases where the force sensors lost contact and a zero level could be established. The force sensors in the IBS, see Chapter 4, are subject to the same effects. However, the operation of that machine guarantees a relatively long zero force period for each sensor in every cycle, and the zero level is easy to determine.

E. Numerical Simulations of Contact Force

In Section C, details of the procedure used to construct the SSC model in ASSET were given. Now some results of the ASSET model and some insights gained from exercising it are presented. For most of the results presented here, a Microvax II running VMS was used.

E.1. Zero Clearance Performance

The basic ability of the simulation to predict dynamic forces in the mechanism is shown in Figure 5.19. The "rigid body" curve is the predicted value of the axial component of the connecting rod force as the SSC operates at 200 rpm, with zero motor angle. This curve was generated by a simplified rigid body analysis of the SSC's motion, treating the slider yoke and slider shell as a single rigid body and neglecting the mass of the connecting rod itself. The "ASSET" curve was generated using ASSET's spatial flexible body nonlinear mechanism analysis capability, with the joint clearance set to zero

for both the slider and the ball joint, and slider friction included in the model. Finally, the "experimental" curve is from an experimental measurement in which the joint clearances were set as close to zero as possible while still permitting free motion of the mechanism.

The rigid body simulation and the ASSET simulation, Figures 5.19a and 5.19b, agree quite closely. The ASSET simulation shows superimposed vibrations due to the flexible links in the system. Agreement with the experimental results, Figure 5.19c, is good although not exact. There is some uncertainty regarding the true value of the coefficient of friction between the slider and the guide rod, and it should be noted that it is impossible to completely eliminate clearances in the experimental mechanism. Experience gained from the IBS, Chapter 4, suggests that exact agreement between simulation and experiment is unlikely when clearances are present.

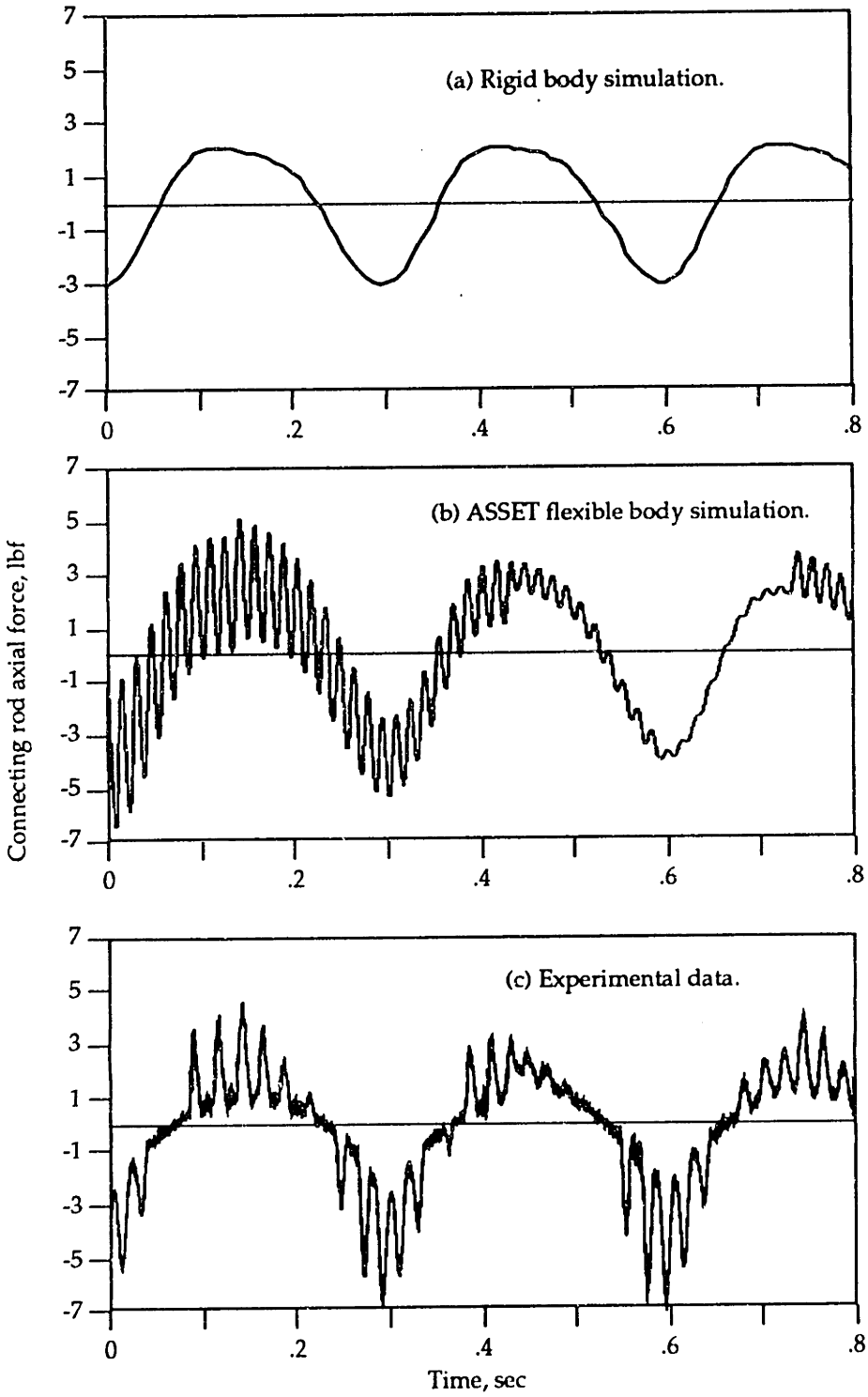

Figure 5.19. Axial component of connecting rod force, 200 rpm, zero clearance.
a) Rigid body simulation.
b) ASSET Flexible body simulation.
c) Experimental data.

E.2. Sensitivity to Parameter Variations

The SSC numerical simulation demonstrates great sensitivity to parameters. The plots in Figure 5.20 demonstrate this characteristic. Figure 5.20a and Figure 5.20b are slider vertical contact force time histories. The motor speed was 500 rpm, with ±0.0025" clearance in both clearance joint models. These plots were produced from ASSET runs with identical initial conditions and, with two exceptions, identical parameters. The exceptions are the distances T_w and T_z between the slider force sensors and the center of the slider, see Figure 5.9. Nominally, T_w = 0.15" and T_z = 0.325". Those values, to the limit of double precision arithmetic on the computer,[1] were used to generate Figure 5.20a. The nominal values were changed by approximately 1.5×10^{-8} inch for T_z, and 7.5×10^{-9} inch for T_w, to produce Figure 5.20b. The change in T_z is about 3.8×10^{-10} meter or 0.00038 μmeter. Thus, the change in parameters between Figures 5.20a and 5.20b is many orders of magnitude smaller than the machining tolerance of even the highest precision work. Note also that dimensions of the order of 10^{-10} meter are smaller than the grain structure of materials such as aluminum and steel. Experience and logic suggest that such minute variations should have no measurable effect on the machine's performance.

Figures 5.20a and 5.20b show a qualitative similarity, evident to the eye, in the number, magnitude and timing of the impact peaks within each cycle. They

---

[1]Neither 0.325 nor 0.15 can be represented exactly as a binary fraction. In a finite length binary number, the maximum truncation error, or epsilon, is 1/2 the least significant bit. The floating point double precision format on this computer has 56 bits of precision. For 0.325, the most significant bit is 2^{-2}, so the least significant bit is 2^{-57} and the machine epsilon is 3.5×10^{-18}. Similarly, for 0.15 the machine epsilon is 1.7×10^{-18}.

are quite different in detail, as seen in Figure 5.20c, in which 5.20a and 5.20b are compared. The plots are nearly the same for the first 0.05 second. After that, despite their qualitative similarity, the plots become increasingly different as impacts occur at different times and with different magnitudes. The nonlinearity of the clearance connection amplifies the tiny difference in parameters between the two simulations so that it causes a significant difference in results.

This behavior of the simulation reinforces some of the conclusions of the studies of the IBS system, namely, that simulations of machine systems with clearances can not, in general, produce results that are accurate to arbitrary levels of detail; that it is not possible to manufacture machines that are "identical;" and that the same machine cannot be run twice in exactly the same manner. The magnitude of real world variations in parameters and initial conditions greatly exceeds that used to generate the differences in these plots.

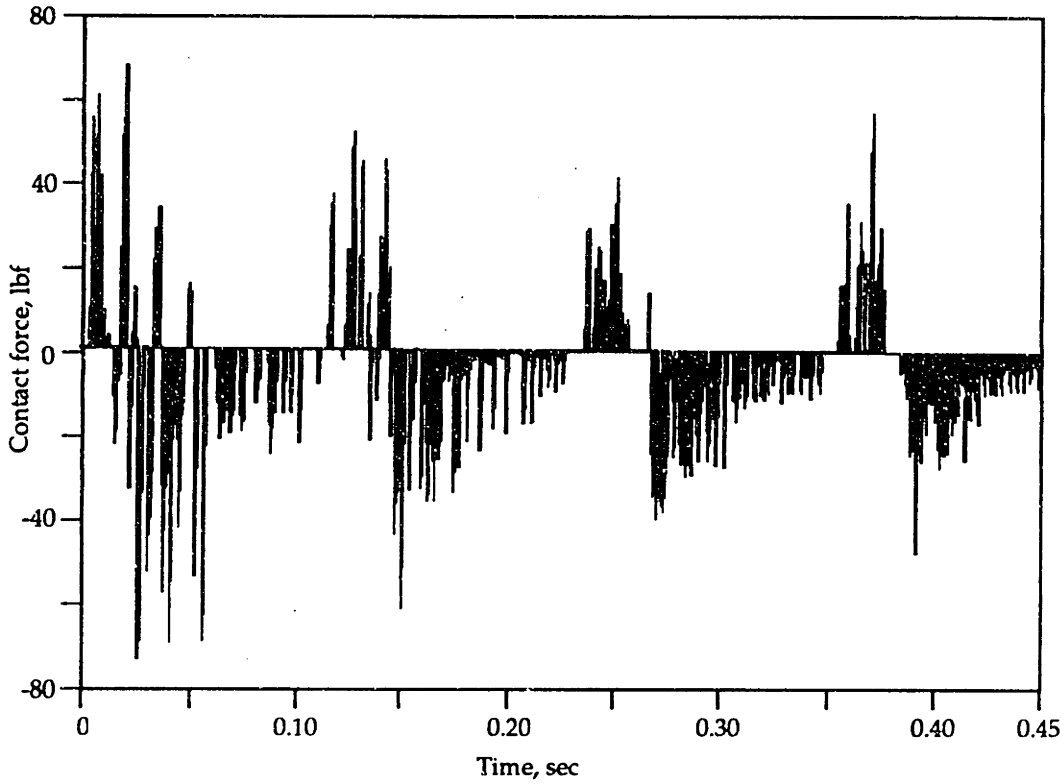

a) Original values of T_w and T_z parameters.

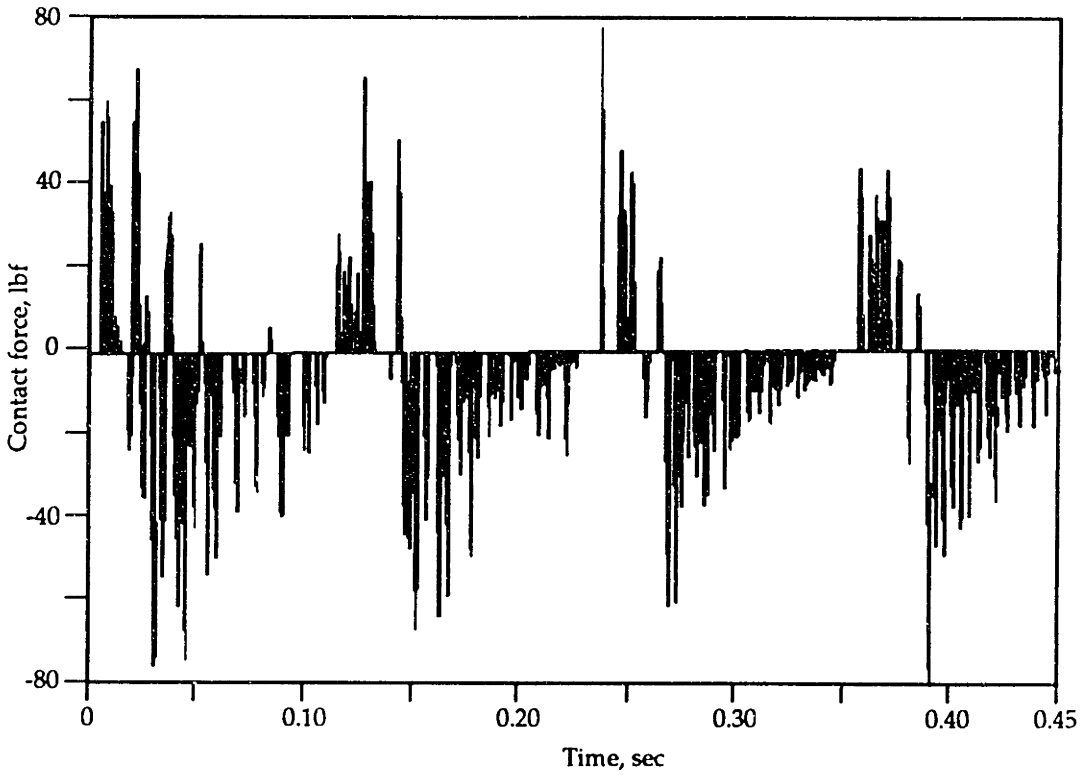

b) T_w and T_z varied (see text).

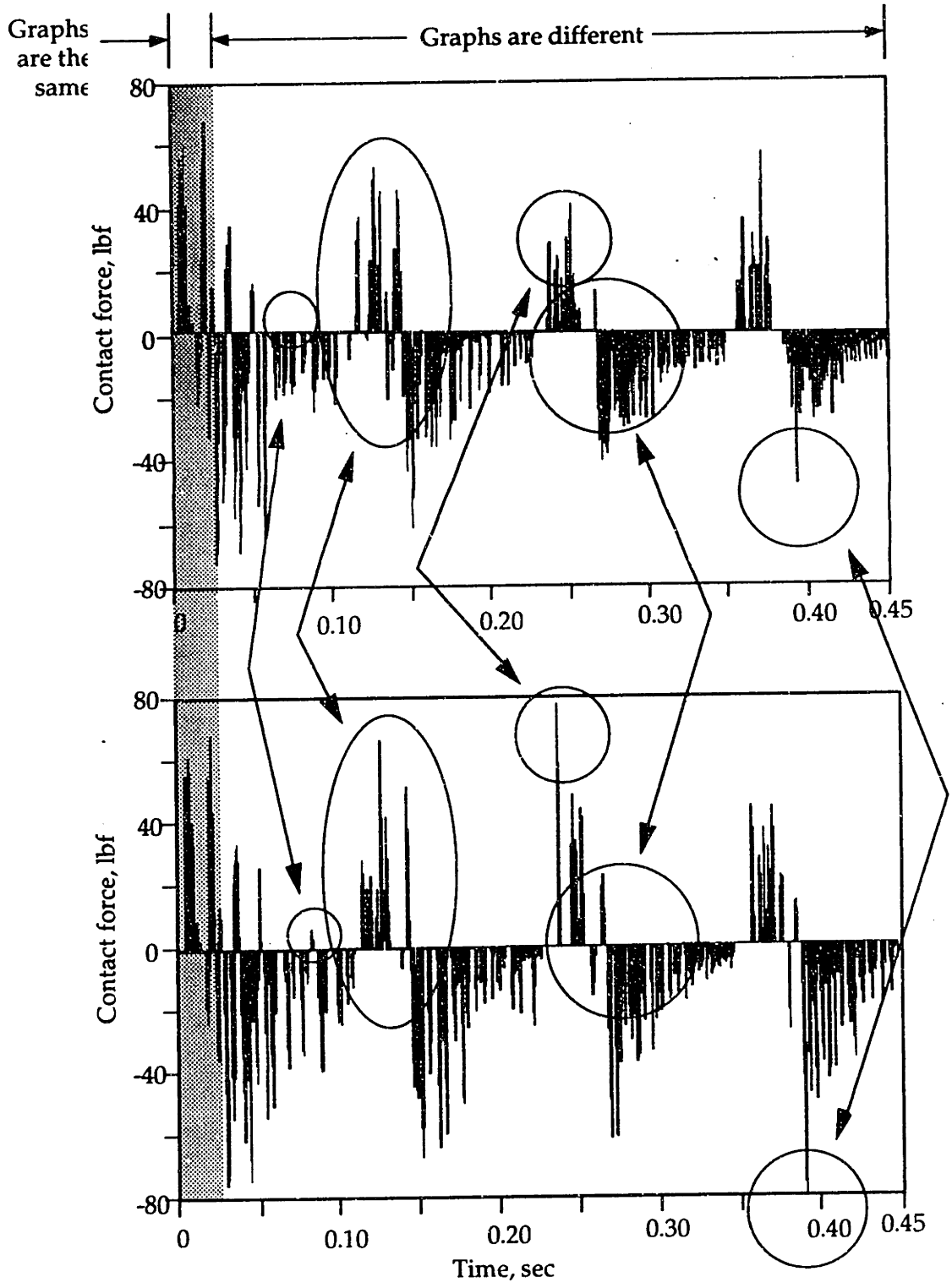

c) Differences between 5.20a and 5.20b.

Figure 5.20. Sensitivity of the SSC simulation to small parameter variations.

This sensitivity need not prevent such simulations from providing useful design information. For many practical purposes, such as designing bearings, a detailed time history of contact force is not required. What might be more useful is a prediction of the magnitude of peak force and the frequency with which a given force level occurs, i.e., a histogram, plotting contact force levels vs. the fraction of time in a cycle that a given force level is met or exceeded. In this sense, Figures 5.20a and 5.20b appear to predict similar performance of the SSC. As noted above, they have a qualitative similarity in terms of the magnitude and number of force peaks, the histogram information that would be most useful to a designer. This interpretation supports the physical intuition that such small changes in parameters should result in negligible changes in behavior for most physical systems, and suggests that a statistically-based method may be a more appropriate way to understand this class of systems. The theory and implementation of such a method are beyond the scope of this thesis, but are treated in another thesis in our lab, reference [81].

E.3. Prolonged Initial Transients

As just discussed, a more meaningful definition of "accuracy" in the context of numerical simulations of machine systems might be related to statistical measures of performance, such as a force histogram, instead of detailed measures, such as the time histories presented above [81]. To be reliable, such statistical performance measures must be based on observations of many cycles of machine operation. Nonlinear dynamic simulations with many degrees of freedom are computationally intensive. Thus, there is a practical conflict between the need to minimize the number of cycles computed, in

order to keep the computational demand to a reasonable level, and the need to have many cycles for statistical reliability. This issue aggravated by the difficulty of determining whether apparent variability in a simulation is due to initial conditions that will die away, and which should be disregarded, or to a real prediction of variability, which must not be disregarded. The plots in Figure 5.21 illustrate these points.

Figure 5.21a is a simulated history of the contact force magnitude at the ball joint for conditions of 0.0025" clearance, 150 rpm motor speed, 0° motor angle, and the coefficient of friction, μ in Equation 5.6, set to zero. It shows a transient period due to initial conditions that ends after 0.1 second, after which the force settles into a highly repeatable cyclic pattern with no impacts. The simulation has been continued for 1.5 seconds, or 3.75 cycles of SSC motion. Figure 5.21b is a simulation identical to 5.21a, except that here μ has been set to 0.1. This change causes a greatly different prediction of the contact force. Again there is a period of initial conditions. Examination of the curve from 0.7 to 0.8 and 1.1 to 1.2 seconds, where similar contact force behavior is predicted in two successive cycles, suggests that the initial transients have died away for simulation times greater than approximately 0.7 seconds. Thus, in these last two cycles of Figure 5.21b, the simulation appears to predict large and varying impact forces. The peak force in the simulation, after the initial condition period, is 16.5 lbf at about 0.08 seconds into the fourth cycle; the minimum peak at this time in the third cycle is 6.8 lbf. Referring to Figure 5.14b, the experimental maximum and minimum peak forces were 7.3 and 5.6 lbf at this combination of speed and clearance. The prediction errs conservatively. The differences between Figures 5.21a and 5.21b suggest that adding Coulomb friction to the simulation model has a very strong effect on

the model's predictions. This might well be a reasonable prediction of the behavior of the real system, suggesting that a designer could be seriously misled by a numerical simulation of the machine's performance that ignored the effects of slider friction.

The parameters and initial conditions used to generate Figure 5.21c are identical to those of Figure 5.21b. In this figure, the simulation has been carried to 7.125 cycles, and plainly its prediction is somewhat different from Figure 5.21b. After 1.7 seconds, about 4 cycles, the predicted force settles into an almost periodic form with small impacts, and peak cyclic forces of about 4 lbf, not due to impacts. It appears that adding sliding friction to the model can extend the time over which initial transients are felt. Comparing only the last two cycles in Figures 5.21a and 5.21c, the model with friction, Figure 5.21c, predicts light impact forces and slight variability from cycle to cycle, compared with no impacts and almost perfect cyclic repeatability without friction, in Figure 5.21a. The peak force predicted, 4 lbf, is now considerably less than the peak measured force of 7.3 lbf. More fundamental than the error in magnitude is the fact that the simulation predicts a peak force not caused by impacts, and predicts only very light impacts, while the experiment showed strong impacts. Interestingly, although the contact forces predicted in the last cycles of Figure 5.21c are qualitatively different from those in Figure 5.21b, the addition of Coulomb friction to the model still causes it to predict light impacts, different from the prediction of no impacts after the initial transients without friction in Figure 5.21a. The point, though, is that the apparently reasonable prediction of Figure 5.21b turned out to be due to initial transients.

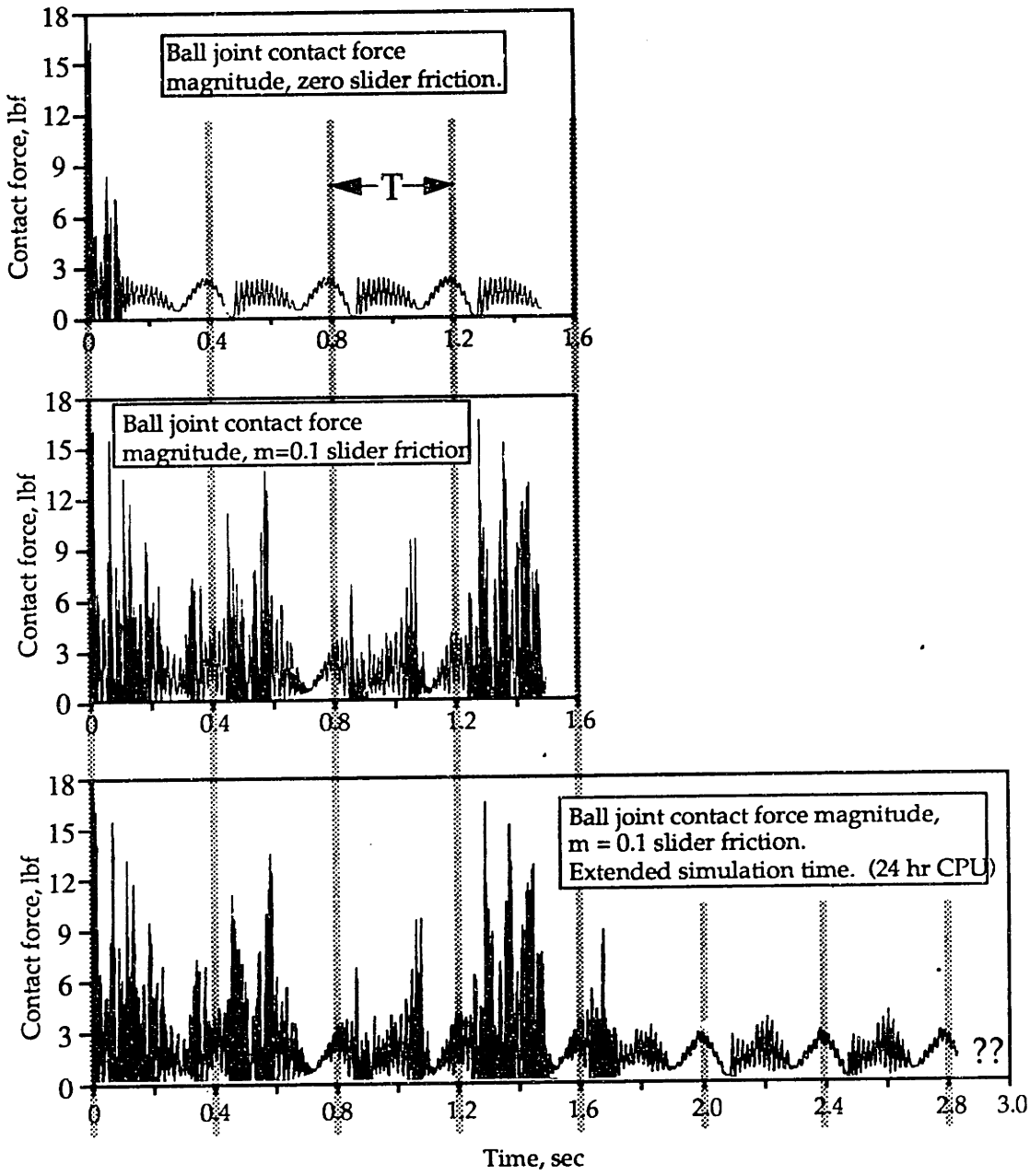

Figure 5.21. Duration of initial transients in the SSC simulation.
a) $\mu = 0$, 3.75 cycles of motion.
b) $\mu = 0.1$, 3.75 cycles of motion.
c) $\mu = 0.1$, 7.125 cycles of motion.

In the preceding discussion it was suggested that the last two cycles of Figure 5.21b appeared to represent the "settled" state of the simulation, a conclusion plainly contradicted by Figure 5.21c. The conclusion was based on examination of the portions of the curve in Figure 5.21b where impacts do not occur, at the beginning of each cycle, around t equal to 0, t equal to 0.2, t equal to 0.8 and t equal to 1.2. There is a progression from behavior dominated by the initial conditions around t equal to 0 to behavior that appears repeatable around t equal to 0.8 and t equal to 1.2. In addition, in Figure 5.21a, a system that is identical except for the amount of sliding friction, all traces of initial conditions disappear shortly after t equal to 0.1. Finally, while the peak forces in Figure 5.21b are very high in the initial moments, they are lower in the third cycle, and rise again in the fourth, suggesting variability resulting from the machine's operation rather than from initial transients. Thus, looking only at Figures 5.21a and 5.21b, it is reasonable to conclude that the initial conditions have substantially died away in the last two cycles of 5.21b. That they have not, as shown in 5.21c, is surprising and disturbing, and suggests the difficulty of determining when non-periodic variability in predicted results is due to initial conditions and when it is a true prediction of the simulation. In linear systems, initial conditions die away smoothly and the system approaches its final behavior "monotonically." That may not be the case when a system has clearance impacts.

E.4. High CPU Time Requirements

As noted, these simulations can require large amounts of computer time. On a Microvax II, the simulation that generated Figure 5.21a required 10 hours, 38

minutes of CPU time, that of 5.21b, 15 hours, 25 minutes, and that of 5.21c, 24 hours, 38 minutes. The motor speed has little direct effect on the amount of computer time required per second of simulation time for the SSC model. However, the computer time does go up as the number of impacts increases. The CPU time required suggests that dynamic simulations of systems such as the SSC may be more practical when run on computers at least comparable to the fastest workstations that are currently available, of the order of 10 to 50 times faster than a Microvax II. It should be noted that Figure 5.21c does not really provide enough data after the initial conditions have disappeared; it would be desirable to have 3 or 4 more cycles of SSC motion predicted in order to collect statistics on the contact force. Based on the time required for Figure 5.21c, the CPU time required on a Microvax II to simulate 4.5 seconds of motion, or 11.25 cycles instead of 7.125 cycles, is estimated to be 38 hours.

F. Comparison of Experimental and Numerical Results

In order to assess the ability of the SSC simulation to predict contact forces, simulations were run with parameters chosen to model some of the experimental cases whose results were summarized in Figures 5.13 and 5.14. Where experimental and simulated time histories of contact forces are compared, the time axes of the data have been adjusted so that zero time corresponds to the same crank angle for both the experiment and simulation. Thus it is possible to compare not only peak forces, but the timing of those forces within a motion cycle. However, the lessons of the IBS system, Chapter 4, suggest that close agreement between predicted and measured impacts will be the exception rather than the rule.

Figure 5.22 shows experimentally measured vertical contact forces at the slider, collected for nominal conditions of 150 rpm motor speed, 0° motor angle, and ±0.0025" clearance in both the slider and ball joint. These conditions correspond to the simulations of Figure 5.21. Each cycle requires 0.4 seconds at this motor speed. Comparing Figure 5.22 with the final cycles of Figure 5.21c shows that the simulation correctly predicts light impacts just past 0.1 second into each cycle, at 2.1 and 2.5 seconds in Figure 5.21c and 0.1, 0.5 and 0.9 second in Figure 5.22. However, the magnitude of these impacts, ranging from 5.6 to 7.3 lbf in the experimental data, is only 2.5 to 2.6 lbf. in the simulation. The simulation predicts a higher peak force, probably not caused by impacts since there is no free flight zone and the force rise time is relatively long, from 0.2 to 0.25 second into the cycle. This peak does not appear in the experimental data. Finally, a local force maximum appears at the beginning of each cycle in both the simulated and experimental data, 2.0, 2.4 and 2.8 seconds in Figure 5.21c, 0.4 and 0.8 second in Figure 5.22, although the predicted magnitude is again lower. As discussed in Section D, the peak forces at the beginning of each cycle in the experimental curve may be due to factors not included in the simulation model, in particular excess play in the pivot joint at the top of the yoke. If these peaks are ignored and the "baseline" level of the force curve in this area is used, then the peak force measured at the beginning of each cycle is 1.3 lbf., about half the value predicted in the simulation.

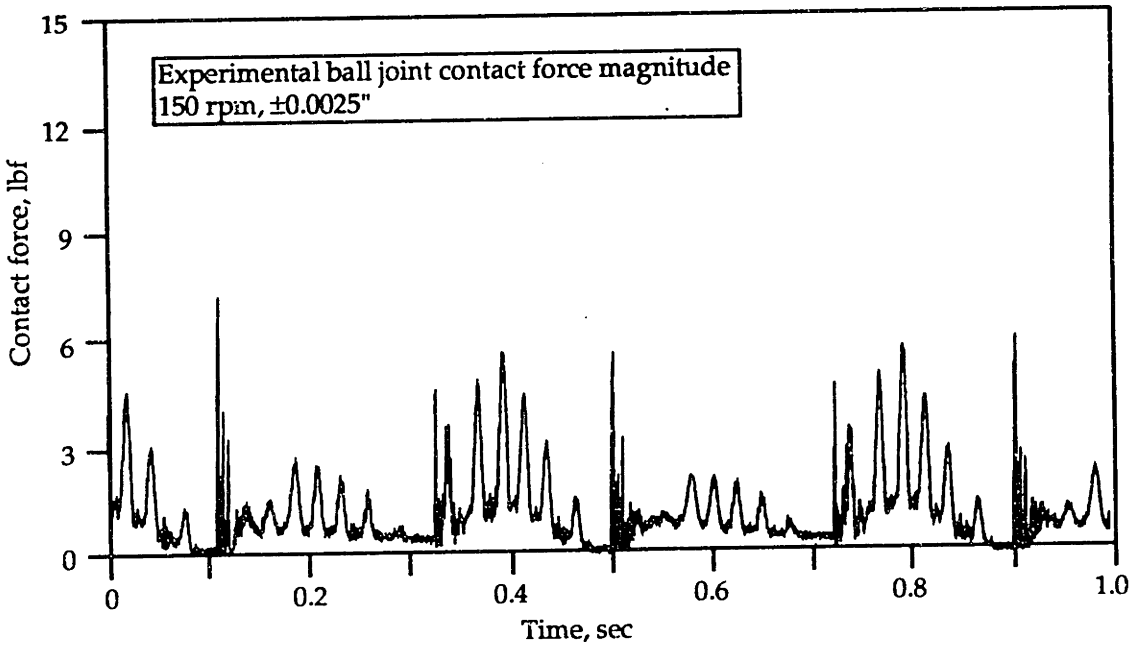

Figure 5.22. Ball joint contact force magnitude, 150 rpm, 0.0025" clearance, experimental.

Figures 5.23 and 5.24 are the predicted and measured vertical contact forces at the slider for the same conditions of 150 rpm, 0° motor angle and ±0.0025" clearance as the ball joint forces in Figures 5.21 and 5.22. Figure 5.23 is from the same simulation that generated Figure 5.21. After decay of the initial transients, ending around 1.8 seconds, the simulation predicts no loss of contact and no impacts. The experimental data, Figure 5.24, show brief loss of contact and light impact forces of 2.4 to 3.1 lbf. in each cycle. Thus, in Figure 5.23, the simulation errs qualitatively in that it does not predict impacts, while impacts are present in the experimental data. The simulation does predict impacts for times previous to 1.8 seconds, which is qualitatively correct although the predicted impacts are generally of greater magnitude than the measurements. However, this is the region where the simulation result is thought to be affected by initial transients.

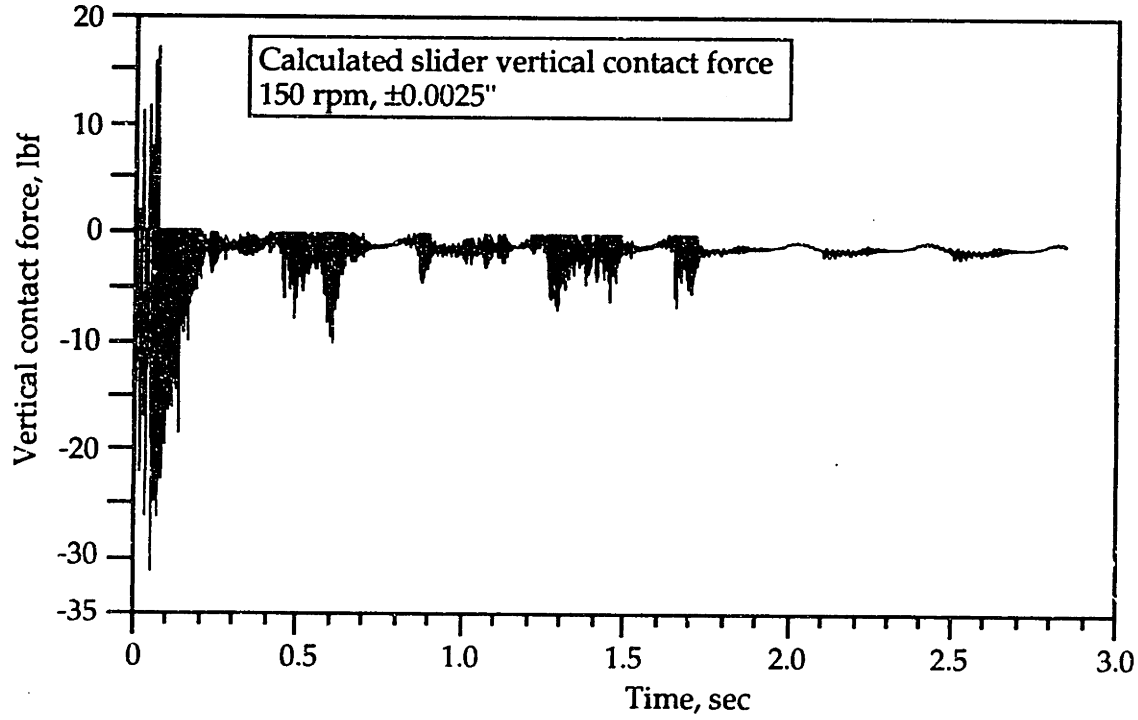

Figure 5.23. Slider vertical contact force, 150 rpm, ±0.0025" clearance, calculated.

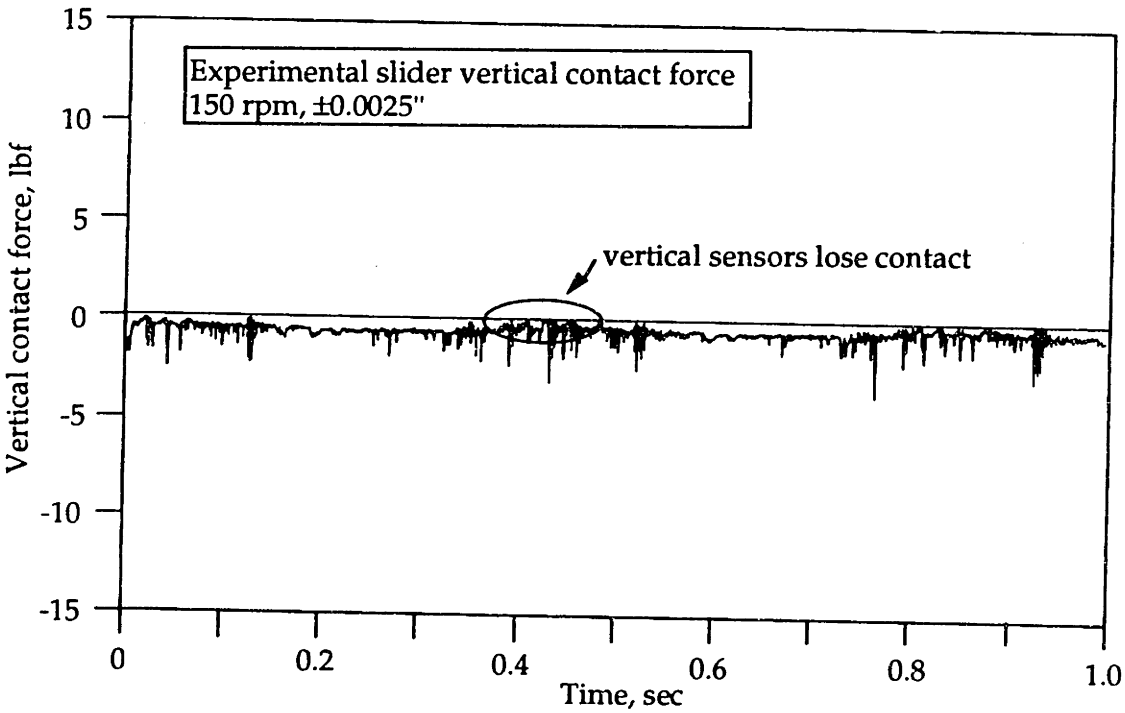

Figure 5.24. Slider vertical contact force, 150 rpm, ±0.0025" clearance, experimental.

Simulations were run for several combinations of motor speed and clearance, and the predicted peak forces are shown in Figure 5.25, for the slider vertical contact force, and Figure 5.26, for the ball joint contact force magnitude. These figures can be compared with Figures 5.13 and 5.14, the experimental data. The four points marked with asterisks on Figures 5.25 and 5.26 represent peak forces that were caused by impacts. However, the potential problem of persistent initial transients, discussed in the preceding section, was not recognized before many of the simulation runs were completed, and may have affected the data that generated these points. The open circles mark a peak contact force not caused by impact; these points are felt not to be subject to the persistent initial transient problem.

For both joints, the simulation predicts little change in peak forces between 0 clearance and ±0.0025" clearance. Also, the simulation never predicts impacts at these clearances, for any speed. This prediction is qualitatively incorrect for some cases at 150 and 200 rpm motor speed, where impacts were observed in the experimental system; cf. Figures 5.13 and 5.14. In the absence of impacts, the contact forces are dominated by the nominal motion and the friction model in the slider. For ±0.005" clearance, the simulation again predicts no impacts and virtually identical forces dominated by nominal motion and friction at 50 and 100 rpm, but it predicts the onset of impacts at 150 rpm, with a consequent large increase in peak force.

Examination of Figures 5.13a and 5.13b, and 5.14a and 5.14b, shows that the experimental data confirm that there is relatively little change in contact forces in both joints as the speed changes from 50 to 100 rpm at both 0 and 0.0025" clearance, with either no impacts or, only at ±0.0025" clearance and 100 rpm, very light, repeatable impacts.

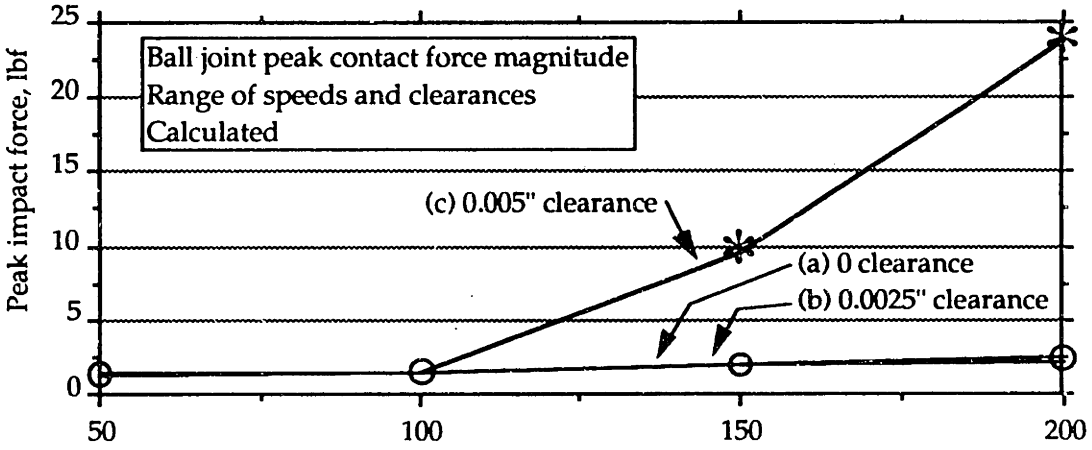

Figure 5.25. Slider peak vertical contact force vs. speed, calculated.
a) 0 clearance.
b) ±0.0025" clearance.
c) ±0.005" clearance.

NOTE: O indicates peak force not caused by impact,
* indicates possible numerical problems (see text).

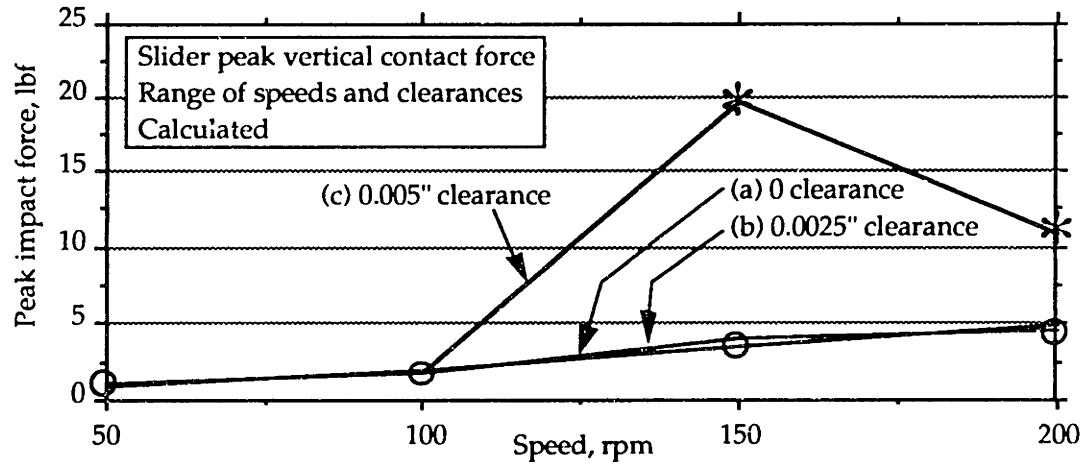

Figure 5.26. Ball joint peak contact force magnitude vs. speed, calculated.
a) 0 clearance.
b) ±0.0025" clearance.
c) ±0.005" clearance.

NOTE: O indicates peak force not caused by impact,
* indicates possible numerical problems (see text).

For slider, Figures 5.13a and 5.13b, measured contact forces at these speeds and clearances are 1.4 to 1.9 lbf at near zero clearance, and 2.3 to 3.3 lbf at ±0.0025" clearance. The simulation predicts contact forces of 1.3 to 1.6 lbf for both

clearances. The prediction is qualitatively correct except at ±0.0025" clearance at 100 rpm, where no impacts are predicted but the experiment shows light impacts. The simulation predicts the correct magnitude of forces at zero clearance, and somewhat underpredicts the forces at ±0.0025" clearance.

For the ball joint, Figures 5.14a and 5.14, the experimental forces vary a little more, from 1.9 to 5.4 lbf., and the simulation predicts values around from 0.8 to 1.9 lbf. In the experimental data at these speeds, the ball joint contact force is dominated by vibrations thought to arise from play in the top pivot bearing of the yoke, an effect that is not included in the simulation.

The simulation's prediction is very different at 200 rpm for ±0.0025" clearance in both joints. The prediction is that there will be no impacts, with peak contact forces of 2.4 lbf in the slider, 4.4 lbf in the ball joint. The experimental data show strong impact forces in the slider, Figure 5.13b at 200 rpm, with magnitudes of 8.5 and 15 lbf observed. As discussed in Section D above, the experimental data also show impacts in the ball joint at this speed, although non-impact forces were greater and generated the points in Figure 5.14b at 9.0 and 9.4 lbf. At 150 rpm and ±0.0025" clearance, the experimental data shows impacts in the ball joint and the beginning of impacts in the slider, where some cycles have impact, and some do not. The simulation again predicts no impacts in either joint.

For ±0.005" clearance, the simulation predicts well the onset of impacts at around 150 rpm in both joints, seen in the measured data in Figures 5.13c and 5.14c, and the simulation also predicts impacts at 200 rpm. However, it is possible that these predictions are influenced by initial transients, similar to Figure 5.21b. If the simulations were extended, the prediction of impacts might disappear, as in Figure 5.21c.

G. Summary

The spatial slider crank system includes large rotation kinematic nonlinearities and adjustable clearance connections. It has been designed to complement the impact beam system discussed in Chapter 4, by providing an environment for investigating the effects of clearance connections that is more complex and more representative of many machine systems. As with the IBS, an analytical model and an experimental version of the system were constructed.

- Instrumented clearance joints were constructed for the ball joint and the sliding joint of the SSC.
- A nonlinear simulation, including the SSC's kinematics, joint clearance models, flexibility in the connecting rod, and Coulomb friction in the prismatic joint, was constructed.
- The greater complexity of the SSC, compared with the IBS, makes it more difficult to control the experiment precisely. One unanticipated effect, play in the slider yoke's top pivot bearing, may have affected the experimental data at certain points.
- Varying the SSC's motor axis angle from 0 to 25°, the limit of the experimental equipment, causes little observable difference in the impact forces.
- When no impacts or only very light impacts occur, the SSC's contact forces are highly repeatable from cycle to cycle. This result is seen in both the experimental and calculated data.

- When large impacts occur, the SSC's contact forces vary from cycle to cycle. This result is seen in the experimental data.
- The data acquisition method used does not provide long-term time histories that would be required to generate reliable statistical measurements. Nonetheless, the data show regimes of SSC operation where much or little cyclic variability in force is seen, and indicate the magnitude of contact forces.
- The details of the simulation show great sensitivity to variations in parameters.
- The simulation predicts nominal motion forces fairly accurately and provides a good prediction of the observed contact forces when the experimental system does not have impacts.
- The addition of sliding friction to the slider model causes a substantial qualitative change in the simulation's behavior.
- The highly varying nature of impact forces seen in the experimental data, and the highly sensitive predictions of the simulation, both suggest that statistical means of characterizing the contact forces may be more appropriate for some design purposes than the time histories shown here [81].
- Transients due to initial conditions may persist for an unexpectedly long time in the simulation; running the simulation longer is a way to detect this problem. However, it has serious consequences for the amount of computational power required to achieve reasonable turnaround times for iterative design.

- The simulation often fails to predict that impacts will occur when they are seen in the experimental data. Due to the unexpected persistence of initial transients, the simulation results may be unreliable in the cases where it does appear to predict impacts. In two cases where the problem of persistent transients was addressed, predictions of impacts by the simulation disappeared, in qualitative disagreement with the experimental data.
- Experimentally, the SSC and IBS show broad similarity in certain respects. When impacts occur, they tend to be highly varying from cycle to cycle and to be much larger than the nominal motion forces. Increasing speed and clearance generally increase the impact forces in cases where impacts occur. This supports an important insight into machine system behavior gained from the IBS and is consistent with suspected chaotic behavior [45].
- The SSC also shows certain fundamental differences from the IBS. There are operating speeds for which impacts do not occur. Under certain conditions, the nominal motion forces appear to decrease with speed over a limited range. These differences probably result from effects that are less important for the behavior of the IBS, particularly gravity and friction.
- The use of computer-based simulations in the design of complex machine systems with clearances must be approached with caution. Such simulations can provide valuable insights into the behavior of the machine system, for example, nominal dynamic forces. However, since the behavior of physical systems is itself highly complex and variable, software simulations are unlikely to be able to provide accurate, detailed information about phenomena such as peak bearing impact forces.

Chapter 6. Conclusion

A. Summary of the Thesis

Each of Chapters 3, 4 and 5 concludes with a section summarizing the results of that chapter. The reader is referred to these chapter summaries for conclusions regarding the experimental and analytical work done, and insights into the behavior of the machine systems treated. This chapter attempts to assess the contributions of this thesis toward the goal of improved design techniques for machine systems.

This thesis is an analytical and experimental study of clearance joints in machine systems. It introduces a new modeling method, intended to be useful in designing spatial machine systems with clearance connections. This new method achieves a higher level of detail in machine system dynamic models by adding a description of the internal behavior of clearance joints to an existing dynamic modeling method. The resulting models can consider many non-ideal effects found in real machines, such as nonlinear spatial motion, distributed structural mass and flexibility effects, control systems and actuators, and clearance connection contact/impact forces. After discussing the new method, the thesis reports experimental work done to validate the method's predictions in two machines that contain clearance joints. Instrumented clearance joints, new experimental tools, were developed to support these experiments. The experimental results have revealed some machine system behaviors that have not been widely understood, principally the reluctance of these systems to respond steadily and repeatably even when driven with steady inputs, and their sensitivity to small variations in operating conditions. These behaviors may have important consequences

that designers of high performance machine systems with clearance connections should consider. The presence of such unpredictability and high sensitivity in *physcial* systems leads to difficult *modeling* challenges.

The new clearance connection force model is a nonlinear one that predicts impact and contact forces generated between the parts of a clearance connection while the machine is in operation. The forces generated by internal impact/contact are then applied to a nonlinear dynamic model of the machine system [100]. The clearance connection model includes a free flight zone when the internal parts are out of contact, and linear or nonlinear surface compliance and damping models when the internal parts touch. The connection's internal sliding friction may be included. The method requires a detailed description of the internal geometry and surface properties of the connection. An integrated machine system numerical simulation computer package was written that includes the new clearance modeling method and also supplies a library of clearance force models for a few common connection types. The package interfaces with standard finite element modeling techniques and is intended to be useful in the design of complex machine systems, by predicting contact/impact forces in internal joints, and the effects of those forces on the motions and vibrations of the other elements of a machine system.

Two experimental systems with adjustable clearance joints were constructed to evaluate the performance of the modeling technique. The first is the impact beam system (IBS). Its nominal motion is limited to planar, linear elastic deflections of a single cantilevered beam, excited by an electrodynamic shaker. The only significant nonlinearity in the IBS is an adjustable clearance gap at the "free" end of the cantilevered beam. The clearance gap is set by

brass-tipped force sensors; when the beam moves up and down, its "free" end hits these sensing elements and the impact force can be recorded. The spectral energy content of impact forces is shown to be extremely broadband. Thus, it is capable of exciting many structural resonances. Even when the beam is driven by a sinusoidal force at a tightly controlled, steady frequency, the impact forces measured at the clearance gap may be highly aperiodic. In addition, the average value of impact forces can change markedly in response to small changes in operating frequency. These experiments provide empirical evidence that designers of mechanisms where clearance impacts are important must be prepared for high degrees of variability, sensitivity and unpredictability in impact forces.

The second experimental system is a spatial slider crank (SSC). This system includes spatial, large rotation nonlinear kinematics and two instrumented clearance joints with adjustable clearance, a ball joint and a prismatic joint. The intent of this system is to investigate interactions between clearance nonlinearities and other nonlinearities frequently found in complex machine systems. Like the IBS, the SSC produces significantly aperiodic impact forces while operating under nominally steady conditions. In addition, its response is influenced by factors not directly related to impacts. While a complete investigation is beyond the scope of this thesis, sliding friction in the joints appears to be one important factor. The experiments with the SSC validated the lessons of the IBS, that systems with impacts are capable of unpredictable and sensitive behavior. If designers rely on a simplified understanding of such machine systems, they may be misled.

The sensitive and highly varying response of the IBS and SSC *physical* systems suggests that accurate *numerical modeling* of these systems may be

difficult. An accurate numerical model would display the same sensitivity to parameters seen in the physical system. Thus, since there is always uncertainty regarding the exact values of physical parameters, an "accurate" numerical model may correctly predict the behavior of a machine system – but the physical system the designer has in mind is likely to be different in significant ways. In addition, the same sensitivity to parameters means that two "identically manufactured" machines may have different performance. This expectation is met in the numerical simulations of the IBS and SSC. Some of the same variability in response and sensitivity to parameters seen in the experimental systems is also seen in the simulations. Therefore, as expected, the predictions of the simulations agree broadly with experimental observations, but not in detail. In addition, the simulations suggest the possibility of chaotic behavior in these systems. Treatment of this topic is beyond the scope of this thesis, but is a topic of research in our lab [45].

Thus, this thesis suggests that designers may find numerical models of machine systems with clearances to be helpful design tools in some situations. The models may be capable of predicting some general aspects of machine behavior and performance, for example, the onset of impacts in bearings or orders of magnitude of impact forces. Such simulations should be used for design only with an awareness of their limitations and a cautious attitude toward their specific predictions. For example, the models are unlikely to predict accurately the full details of a time history of impact forces.

B. Suggestions for Future Work

Several areas for future research are suggested by the results in this thesis.

From a design viewpoint, it would be useful to have a better method to characterize impact forces at a clearance connection and their effect on machine system vibration. One possibility, a statistical description oriented toward noise radiation, is treated in part by a thesis from our laboratory, being completed concurrently with this one [81].

More investigations into the nature of impacts and interactions between impacts and the structural and kinematic characteristics of machine systems can only yield deeper insights into the behavior of these systems. In particular, the effect of changing the structural parameters of the SSC, such as with a less-stiff connecting rod, might be a place to begin. Another thesis from our laboratory, expected to be completed in 1993, will address issues of chaotic behavior in the IBS [45].

Investigating the effect of structural vibration on impact variability might result in useful design information on how to minimize both the magnitude and variability of impact forces. A preliminary experiment might test the hypothesis suggested in Chapter 4 by attempting to apply structural damping to the IBS.

As discussed in Chapter 5, it is likely that some of the experimental data from the SSC were adversely affected by excess play in one of its bearings. A redesign of this part of the apparatus may be desirable before it is used for more experimental work.

Some other research has suggested that very significant reductions in peak impact forces may be had with thin compliant layers applied to one of the contacting surfaces [3]. It would be relatively easy to modify the joints of the IBS and the SSC in this way, to further evaluate this behavior and also to

investigate its effects on other aspects of performance. For example, such a layer might increase friction in the SSC's sliding joint; such friction is thought to have a significant effect on the SSC's behavior.

C. Acknowledgements

Several people have contributed significantly to this research. They have been acknowledged at appropriate points in the body of the thesis, but I want to repeat their names here. Thanks to: (Dr.) Peng-Yun Gu; Uwe M. Müller; Erin M. O'Connell; Dr. Charles H. Oppenheimer.

Many thanks also, especially to my thesis supervisor, Professor Steven Dubowsky, and to the other members of my thesis committee, Professors Klaus-Jürgen Bathe and Warren P. Seering, for their excellent ideas and constant support.

The experimental work was done in the Acoustics, Vibrations and Machine Dynamics Lab at MIT.

This research was supported in part by grants from the National Science Foundation and NASA. Their generous support is gratefully acknowledged.

Bibliography

1. Ackermann, J., and Müller, P.C., "Dynamical Behavior of Nonlinear Multibody Systems due to Coulomb Friction and Backlash," *Proc. IFAC/IFIP/IMACS International Symposium on the Theory of Robots*, Vienna, Austria, Dec. 3-5, 1986, pp. 289-294.
2. Agrawal, O.P., and Shabana, A.A., "Dynamic Analysis of Multibody Systems using Component Modes," *J. of Computers and Structures*, v. 21, 1985, pp. 1303-1312.
3. Akay, A., "On the Reduction of Noise Emission from High Speed Mechanical Systems," *Proceedings of the 7th World Congress on the Theory of Machines and Mechanisms*, Seville, Spain, Sep. 17-22, 1987, pp. 833-836.
4. Alizade, R.I., et al., "Mathematical Models for the Analysis and Synthesis of Spatial Mechanisms, Part I: Four Link Spatial Mechanisms; Part II: Five Link Spatial Mechanisms; Part III: Six Link Spatial Mechanisms; Part IV: Seven Link Spatial Mechanisms," *Mechanism and Machine Theory*, v. 18, n. 5, 1983, pp. 301-307, 309-315, 317-322, 323-328.
5. Ansari, K.A., and Khan, N.U., "Nonlinear Vibrations of a Slider Crank Mechanism," *Applied Mathematical Modeling*, v. 10, n. 2, Apr.l 1986, pp. 114-118.
6. Asano, N., "A Dynamic Substructuring Method for Elastoimpact Stress Analysis using the Finite Element Method," *Bulletin of the JSME*, v. 26, n. 218, Aug. 1983, pp. 1308-1314.
7. Bagci, C., "Dynamic Motion Analysis of Plane Mechanisms with Coulomb and Viscous Damping via the Joint Force Analysis," *J. of Engineering for Industry*, May 1975, pp. 551-560.
8. Bagci, C., and Khosravi, F., "Dynamics of Spatial Mechanisms with Coulomb and Viscous Friction Forces in Bearings with Surface Contacts," *Proc. ASME Design Engineering Tech. Conf.*, Oct. 5-8, 1986, paper no. 86-DET-192.
9. Bahgat, B.H., and Willmert, K.D., "Finite Element Vibrational Analysis of a Planar Mechanism," *Mechanism and Machine Theory*, v. 11, 1976, pp. 47-71.
10. Bakr, E.M., and Shabana, A.A., "Geometrically Nonlinear Analysis of Multibody Systems," *J. of Computers and Structures*, v. 23, 1986, pp. 739-751.
11. Bakr, E.M., and Shabana, A.A., "Effect of Geometric Elastic Non Linearities on the Impact Response of Flexible Multi-Body Systems," *J. of Sound and Vibration*, v. 112, n. 3, 1987, pp. 415-432.
12. Bathe, K.J., Lee N.S., and Bucalem, M.L., "On the Use of Hierarchical Models in Engineering Analysis," *Computer Methods in Applied Mechanics and Engineering*, v. 82, n. 1, Sep. 1990, pp. 5-26.

13. Balasubramonian, A., and Raghavacharyulu, E., "Vibrating Response of an Elastic Coupler of a 4-Bar Linkage," *Mechanism and Machine Theory*, v. 22, n. 2, 1987.
14. Besseling, J.F., Jonker, J.B., and Schwab, A.L., "Kinematics and Dynamics of Mechanisms," *Delft Progress Report*, v. 10, n. 2, Mar. 1985, pp. 160-172.
15. Bricout, J.N., Debus, J.C., and Micheau, P., "A Finite Element Model for the Dynamics of Flexible Manipulators," *Mechanism and Machine Theory*, v. 25, n. 1, 1990, pp. 119-128.
16. Celigueta, J.T., and de Jalon, J., "Analysis of Mechanisms with Flexible Links using Component Mode Synthesis," *Proc., 7th World Congress on the Theory of Machines and Mechanisms*, Sep. 17-22, 1987, Seville, Spain.
17. Cetinkunt, S., and Book, W.J., "Symbolic Modeling and Dynamic Simulation of Robotic Manipulators with Compliant Links and Joints," *Robotics and Computer-Integrated Manufacturing*, v. 5, n. 4, 1989, pp. 301-310.
18. Chace, M.A., and Smith, D.A., "DRAM - Digital Computer Program for the Dynamic Analysis of Generalized Mechanical Systems," *Transactions of the SAE*, v. 80, 1971, pp. 969-983.
19. Chapnik, B.V., Heppler, G.R., and Aplevich, J.D., "Modeling Impact on a One-Link Flexible Robotic Arm," *IEEE Trans. on Robotics and Automation*, v. 7, n. 4, Aug. 1991, pp. 479-488.
20. Chaudhary, A.B., and Bathe, K.J., "Solution Method for Static and Dynamic Analysis of Three-Dimensional Contact Problems with Friction," *Computers and Structures*, v. 24, n. 6, 1986, pp. 855-873.
21. Christensen, E.R., and Lee, S.W., "Nonlinear Finite Element Modeling of the Dynamics of Unrestrained Flexible Structures," *Computers and Structures*, v. 23, n. 6, 1986, pp. 819-829.
22. Cummings, G.A., and Means, K.H, "Experimental Measurement of Bearing Loads in a High-Speed Slider Crank Mechanism," *Proc. 1986 ASME Design Engineering Technical Conference*, Oct. 5-8, 1986, paper no. ET-153.
23. Davidson, I., and Dick, M.D., "The Dynamics of a Spatial Slider Crank Mechanism Mounted on a Flexible Cantilever," *Proc. 7th World Congress on the Theory of Machines and Mechanisms*, Seville, Spain, Sep. 17-22, 1987, pp. 515-518.
24. Davitashvili, N.S., and Sharashenidze, G.S., "Dynamic Study of a Spherical Four-Bar Crank and Rocker Link Mechanism with Clearances," *Proc. 7th World Congress on the Theory of Machines and Mechanisms*, Seville, Spain, Sep. 17-22, 1987, v. 1, pp. 545-548.
25. Deck, J.F., and Dubowsky, S., "On the Limitations of Predictions of the Dynamic Response of Machines with Clearance Connections," *Proc. 1992 ASME Mechanisms Conference*, to appear.

26. Denavit, J., Hartenberg, R.S., "A Kinematic Notation for Lower-Pair Mechanisms Based on Matrices," *J. of Applied Mechanics*, Jun. 1955, pp. 215-221.

27. Dubowsky, S., "On Predicting the Dynamic Effects of Clearances in Planar Mechanisms,", *J. of Engineering for Industry*, v. 93, ser. B, n. 1, 1974, pp. 317-323.

28. Dubowsky, S., Deck, J.F.,and Costello, H.M., "The Dynamic Modeling of Flexible Spatial Machine Systems with Clearance Connections," *ASME J. of Mechanisms, Transmissions and Automation in Design*, v. 109, n. 1, 1987, pp. 87-94.

29. Dubowsky, S., and Freudenstein, F., "Dynamic Analysis of Mechanical Systems with Clearances, Part I: Formation of Dynamic Model," and "Part II: Dynamic Response," *ASME J. of Engineering for Industry*, v. 93, ser. B, n. 1, 1971, pp. 305-316.

30. Dubowsky, S., and Gardner, T.N., "Dynamic Interactions of Link Elasticity and Clearance Connections in Planar Mechanical Systems," *ASME J. of Engineering for Industry*, v. 97, n. 2, May 1975, pp. 652-661.

31. Dubowsky, S., and Gardner, T.N., "Design and Analysis of Mulitlink Flexible Mechanisms with Multiple Clearance Connections," *ASME J. of Engineering for Industry*, v. 99, ser. B, n. 1, Feb. 1977, pp. 88-96.

32. Dubowsky, S., Gu, P.-Y., and Deck, J.F., "The Dynamic Analysis of Flexibility in Mobile Robotic Manipulator Systems," *Proc. of the 8th World Congress on the Theory of Machines and Mechanisms*, Prague, Czechoslovakia, 1991.

33. Dubowsky, S., and Maatuk J., "The Dynamic Analysis of Elastic Spatial Mechanisms," *Proceedings of the 4th World Congress on Machines and Mechanisms*, Newcastle-Upon-Tyne, England, IME, London, England, 1975.

34. Dubowsky, S., and Moening, M.F., "An Experimental and Analytical Study of Impact Forces in Elastic Mechanical Systems with Clearances," *Mechanism and Machine Theory*, v. 13, 1978, pp. 451-465.

35. Dubowsky, S., and Morris, T., "An Analytical and Experimental Study of the Acoustical Noise Produced by Machine Links," *ASME J. of Mechanical Design*, v. 105, n. 3, July 1983, pp. 393-401.

36. Dubowsky, S., Norris, M., Aloni, E., and Tamir, A., "An Analytical and Experimental Study of the Prediction of Impacts in Planar Mechanical Systems with Clearances," *ASME J. of Mechanisms, Transmissions and Automation in Design*, v. 106, n. 4, 1984, pp. 444-451.

37. Dubowsky, S., Prentis, J.M., and Valero, R.A., "On the Development of the Criteria for the Prediction of Impact in the Design of High Speed Systems with Clearances," *Proc. of the 5th World Congress on the Theory of Machines and Mechanisms*, ASME, 1979.

38. Dubowsky, S., and Young, S.C., "An Experimental and Analytical Study of Connection Forces in High Speed Mechanisms," *J. of Engineering for Industry*, v. 97, ser. B, n. 4, 1975, pp. 1166-1174.

39. Earles, S.W.E., and Seneviratne, L.D., "Some Kinematic Effects of Clearances in Revolute Joints of Linkage Mechanisms," *Proc. of the 7th World Congress on the Theory of Machines and Mechanisms*, Seville, Spain, Sep. 17-22, 1987.

40. Giovagnoni, M., and Rossi, A., "Transient Analysis of a Flexible Crank," *Mechanism ana Machine Theory*, v. 24, n. 4, 1989, pp. 231-243.

41. Gilmore, B.J., and Cipra, R.J., "The Automatic Determination of Constraint Changes in Dynamic Multibody Systems," *Proc. of the 1986 ASME Design Engineering Technical Conference*, Oct. 5-8, 1986, paper no. 86-DET-158.

42. Gilmore, B.J., and Cipra, R.J., "Simulation of Planar Dynamic Mechanical Systems with Changing Topologies: Part I: Characterization and Prediction of the Kinematic Constraint Changes; Part II: Implementation Strategy and Simulation Results for Example Dynamic Systems," *Proc. of the 1987 ASME Design Engineering Technical Conference, Volume II: Robotics, Mechanisms and Machine Systems*, Sep. 27-30, 1987.

43. Gleick, J., *Chaos: Making a New Science*, Penguin Books, New York, NY, 1987.

44. Goodman, T.P., "Dynamic Effects of Backlash," *Machine Design*, v. 35, 1963, pp. 150-157.

45. Gu, P.-Y., *Chaotic Behavior of Machine Systems: Analysis and Implications for Design*, PhD Thesis, MIT Department of Mechanical Engineering, Cambridge, MA, anticipated Aug., 1993.

46. Haines, R.S., "A Theory of Contact Loss at Revolute Joints with Clearance," *J. of Mechanical Engineering Science*, v. 22, No. 3, 1980, pp. 129-136.

47. Haines, R.S., "Survey: Two-Dimensional Motion and Impact at Revolute Joints," *Mechanism and Machine Theory*, v. 15, n. 5, 1980, pp. 361-370.

48. Haines, R.S., "An Experimental Investigation into the Dynamic Behavior of Revolute Joints with Varying Degrees of Clearance," *Mechanism and Machine Theory*, v. 20, n. 3, 1985, pp. 221-231.

49. Hartman, J.B., "Anticipating Dynamic Behavior," *Machine Design*, v. 26, 1954, pp. 118-124.

50. Haug, E.J., Wu, S.C., and Yang, S.M., "Dynamics of Mechanical Systems with Coulomb Friction, Stiction, Impact and Constraint Addition - Deletion - Pt. I: Theory," *Mechanism and Machine Theory*, v. 21, n. 5, 1986, pp. 401-406.

51. Wu, S.C., Yang, S.M., and Haug, E.J., "Dynamics of Mechanical Systems with Coulomb Friction, Stiction, Impact and Constraint Addition - Deletion - Pt. II: Planar Systems," and "Pt. III: Spatial Systems," *Mechanism and Machine Theory*, v. 21, n. 5, 1986, pp. 407-425.
52. Heiman, M.S., Sherman, P.J., and Bajaj, A., "On the Dynamics and Stability of an Inclined Impact Pair," *J. Sound and Vibration*, v. 114, n. 3, 1987, pp. 533-547.
53. Hunt, K.H., and Crossley, F.R., "Coefficient of Restitution Integrated as Damping in Vibroimpacts," *J. of Applied Mechanics*, v. 97, 1975, pp. 440-445.
54. Hurty, W.C., "Dynamic Analysis of Structural Systems Using Component Modes," *AIAA J.*, v. 3, n. 4, 1965, pp. 678-685.
55. Imam, I., and Sandor, G.N., "High Speed Mechanism Design: A General Approach," *J. of Engineering for Industry*, v. 97, n. 2, May 1975, pp. 609-628.
56. Imam, I., Skreiner, M., and Sadler, J.P., "A New Solution to Coulomb Friction in Mechanism Bearings: Theory and Application," *J. of Mechanical Design*, v. 103, Oct. 1981, pp. 764-775.
57. Johnson, R.C., "Impact Forces in Mechanisms," *Machine Design*, v. 35, 1963, pp. 150-157.
58. Jonker, J.B., "Dynamics of Spatial Mechanisms with Flexible Links," *Technische Hogeshule Delft Report No. 171*, 1984.
59. Kakizaki, T., Deck, J.F., and Dubowsky, S., "Modeling the Spatial Dynamics of Robotic Manipulators with Flexible Links and Joint Clearances," *Proc. 1990 ASME Mechanisms Conf.*, Sep. 16-19, 1990, pp. 343-350.
60. Kane, T.R., Ryan, R.R., and Banerjee, A.K., "Dynamics of a Cantilever Beam Attached to a Moving Base," *AIAA J. of Guidance*, Mar.-Apr. 1987, pp. 139-151.
61. Khulief, Y.A., *Dynamic Analysis of Flexible Multi-Body Systems with Intermittent Motion*, PhD Thesis, U. of Illinois at Chicago, 1985.
62. Khulief, Y.A., "Restitution and Friction in Impact Analysis of Multibody Systems Executing Plane Motion," *Proc. 1986 ASME Design Engineering Technical Conference*, Oct. 5-18, 1986, paper no. 86-DET-50.
63. Khulief, Y.A., and Shabana, A.A., "Impact Responses of Multi-Body Systems with Consistent and Lumped Masses," *J. of Sound and Vibration*, v. 104, n. 2, 1986, pp. 187-207.
64. Khulief, Y.A., and Shabana, A.A., "Dynamics of Multibody Systems with Variable Kinematic Structure," *J. of Mechanisms, Transmissions and Automation in Design*, v. 108, n. 2, Jun. 1986, pp. 167-175.

65. Khulief, Y.A., and Shabana, A.A., "Dynamic Analysis of Constrained Systems of Rigid and Flexible Bodies with Intermittent Motion," *J. of Mechanisms, Transmissions and Automation in Design*, v. 108, n. 1, 1986, pp. 38-45.

66. Kim, S.S., and Haug, E.J., "Selection of Deformation Modes for Flexible Multibody Dynamics," *Proc. of the 1987 ASME Design Technical Conference, Vol. II, Robotics, Mechanisms and Machine Systems*, Sep. 27-30, 1987, pp. 401-410.

67. Kobrinskii, A.Y., and Babitsky, V.I., "Periodic Movements of a Two Mass Vibration System in a Cavity," *Trub. Mash. Meth*, v. 103, 1964, pp. 56-70., (in Russian).

68. Kohler, S., and Weber, C., *Etude des chocs dans les systemes multicorps*, Ecole Nationale Supérieure d'Arts et Métiers, ENSAM STR-1, 1989-1990, (in French).

69. Koppens, W.P., Sauren, A.A.H.J., Velpaus, F.E., and van Campen, D.H., "The Dynamics of a Deformable Body Experiencing Large Displacements," *Proc., ASME 1988 Winter Annual Meeting, Applied Mechanics Div.*, Nov. 28 - Dec. 2, 1988, paper no. 88-WA/APM-44.

70. Koppens, W.P., *The Dynamics of Systems of Deformable Bodies*, PhD Thesis, Technische Universiteit Eindhoven, Jan. 31, 1989.

71. Liao, D.X., Sung, C.K., Thompson, B.S., and Soong, K., "A Note on the Quasi-Static Responses, Dynamic Responses and the Super-Harmonic Resonances of Flexible Linkages: Some Experimental Results," *Proc. 1986 ASME Design Engineering Technical Conf.*, Oct. 5-8, 1986, paper no. 86-DET-146.

72. Liou, F.W., and Erdman, A.G., "Experimental Motion Analysis of Flexible Mechanism and Drive System using High Speed Camera and Digital Imaging Techniques," *Mechanism and Machine Theory*, v. 24, n. 4, 1989, pp. 257-266.

73. Lowen, G.G., and Chassapis, C., "The Elastic Behavior of Linkages: An Update," *Mechanism and Machine Theory*, v. 21, n. 1, 1986, pp. 33-42.

74. Masurekar, V., and Gupta, K.N., "Theoretical and Experimental Kineto-Elastodynamic Analysis of High-Speed Linkage," *Mechanism and Machine Theory*, v. 24, n. 5, 1989, pp. 352-334.

75. Moorhead, A.D., *The Development of a Model of Clearances in a Spatial Revolute Joint*, MS Thesis, UCLA Dept. of Mechanical Engineering, Los Angeles, CA, May 1982.

76. Mo'tofi, A., and Dadbin, A., "Impact Type Loading Mechanisms," *Proc. 1986 ASME Design Technical Conf.*, Oct. 5-8, 1986, paper no. 86-DET-170.

77. NASA Goddard Space Flight Center, "DISCOS - A Digital Computer Program for the Dynamic Simulation of Controls and Structure," Aug. 30, 1979, GSC-12422.

78. Nguyen D.T., Noah, S.T., Kettleborough, C.F., "Impact Behavior of an Oscillator with Limiting Stops. Part I: Parametric Study. Part II: Dimensionless Design Parameters," *J. of Sound and Vibration*, v. 109, n. 2, Sep. 1986, pp. 293-307.

79. O'Connell, E., *Dynamic Response of a Spatial Slider Crank Mechanism with Clearances and Link Elasticity*, MS Thesis, MIT Department of Mechanical Engineering, Cambridge, MA, Aug. 1990.

80. Oppenheimer, C.H., *Predicting the Acoustics of an Experimental Machine Enclosure with Finite Element and Boundary Element Techniques*, MS Thesis, MIT Dept. of Mechanical Engineering, Cambridge, MA, Jan. 1988.

81. Oppenheimer, C.H., *Impact-Induced Noise and Vibration in Machine Systems for Design*, PhD Thesis, MIT Department of Mechanical Engineering, Cambridge, MA, Sep. 1992.

82. Orlando, N., and Berenyi, T., "Dynamic Continuous Path Synthesis of Industrial Robots using the ADAMS Computer Program," *J. of Mechanical Design*, v. 103, n. 3, Jul. 1981, pp. 602-607.

83. Palej, R., "On a Direct Method of Analyzing Impacting Mechanical Systems," *J. of Sound and Vibration*, v. 108, n. 2, Jul. 1986, pp. 191-198.

84. Perera, O., and Seering, W.P., "Prevention of Impact in Bearings of Four-Bar Linkages," *J. of Mechanisms, Transmissions and Automation in Design*, v. 105, n. 3, 1983, pp. 592-598.

85. Peurach, J., and Tongue, B.H., "Chaotic Response of a Slider Crank Mechanism," *J. of Vibration and Acoustics*, v. 113, Jan. 1991, pp. 69-73.

86. Rubin, S., "Improved Component Mode Respresentation for Structural Dynamic Analysis," *AIAA Journal*, v. 13, n. 8, 1975, pp. 995-1006.

87. Sadler, J.P., "Dynamic Analysis of Mechanisms Including Coulomb Friction via Equilibrium Equations," *Proc., 3rd OSU Applied Mechanisms Conference*, 1973, pp. 13.1-13.11.

88. Schielen, W., "Non-Linear Phenomena in Multibody System Dynamics," *Delft Progress Report*, v. 10, n. 2, 1985, pp. 105-120.

89. Shabana, A.A., "Automated Analysis of Constrained Systems of Rigid and Flexible Bodies," *J. of Vibration, Acoustics, Stress and Reliability in Design*, v. 107, Oct. 1985, pp. 431-439.

90. Shabana, A.A., "Dynamics of Inertia Variant Flexible Systems using Experimentally Identified Parameters," *J. of Mechanisms, Transmissions and Automation in Design*, v. 108, n. 3, Sep. 1986, pp. 358-366.

91. Shabana, A.A., and Wehage, R.A., "A Coordinate Reduction Technique for Dynamic Analysis of Spatial Substructures with Large Angular Rotation," *J. of Structural Mechanics*, v. 11, n. 3, 1983, pp. 401-431.

92. Shabana, A.A., and Wehage, R.A., "Variable Degree of Freedom Component Mode Analysis of Inertia Variant Flexible Mechanical Systems," *J. of Mechanisms, Transmissions and Automation in Design*, v. 105, n. 3, Sep. 1983, pp. 370-378.

93. Shabana, A.A., and Wehage, R.A., "Spatial Transient Analysis of Inertia Variant Flexible Mechanical Systems," *J. of Mechanisms, Transmissions and Automation in Design*, v. 106, n. 2, Jun. 1984, pp. 172-178.

94. Sheth, P.N., and Uicker, J.J., "IMP (Integrated Mechanism Program), a Computer-Aided Design Analysis System for Mechanisms and Linkages," *J. of Engineering for Industry*, v. 94, ser. B, 1972, pp. 454-464.

95. Shih, L., and Frank, A.A., "Dynamic Modeling and Analysis of General Linked Mechanisms with Compliance," *Proc. of the 1987 ASME Design Technical Conference, Vol. II, Robotics, Mechanisms and Machine Systems*, Sep. 27-30, 1987.

96. Smirnov, Y.P., "Equations of Impact of Systems with Friction," *Mechanics of Solids*, v. 20, n. 3, 1985, pp. 35-43.

97. Soong, K., and Thompson, B.S., "An Experimental Investigation of the Dynamic Response of a Mechanical System with Bearing Clearance," *Proc. 1987 ASME Design Technical Conference, Vol. II, Robotics, Mechanisms and Machine Systems*, Sep. 27-30, 1987, pp. 411-419.

98. Stammers, C.W., and Ghazavi, M., "Theoretical and Experimental Study of the Dynamics of a Four-Bar Chain with Bearing Clearance, Pin Motion, Contact Loss and Impact," *J. of Sound and Vibration*, v. 150, n. 2, Oct. 1991, pp. 301-315.

99. Stewart, I., *Does God Play Dice? The Mathematics of Chaos*, Basil Backwell Inc., Oxford, England, 1989.

100. Sunada, W.H., *Analysis of Flexible Spatial Mechanisms and Robotic Manipulators*, PhD Thesis, Department of Mechanical Engineering, University of California at Los Angeles, 1981.

101. Sunada, W., and Dubowsky, S., "The Application of Finite Element Methods to the Dynamic Analysis of Flexible Spatial and Co-Planar Linkage Systems," *ASME J. of Mechanical Design*, v. 103, n. 3, Jul. 1981, pp. 643-651.

102. Sunada, W., and Dubowsky, S., "On the Dynamic Analysis and Behavior of Industrial Robotic Manipulators with Elastic Members," *J. of Mechanisms, Transmissions and Automation in Design*, v. 105, n. 1, Mar. 1983, pp. 42-51.

103. Tanuwidjaja, B., *Simulation of the Dynamic Behavior of a Mechnism with Revolute Connections and Clearances Using the Finite Element Method*, Delft University of Technology, Delft, The Netherlands, Report WTHD 173, 1985, (in German).

104. Thompson, B.S., and Sung, C.K., "Analytical and Experimental Investigation of High-Speed Mechanisms Fabricated with Composite Laminates," *J. of Sound and Vibration*, v. 111, n. 3, Dec. 1986, pp. 399-428.

105. Thompson, B.S., and Sung, C.K., "Survey of Finite Element Techniques for Mechanism Design," *Mechanism and Machine Theory*, v. 21, n. 4, 1986, pp. 351-359.

106. Thompson B.S., Zuccaro, D., Gamache, D., and Gandhi, M.V., "An Experimental and Analytical Study of the Dynamic Response of a Linkage Fabricated from a Unidirectional Fiber-Reinforced Composite Laminate," *J. of Mechanisms, Transmissions and Automation in Design*, v. 105, n. 3, 1983, pp. 526-533.

107. Timoshenko, S.P., and Goodier, J.N., *Theory of Elasticity*, Third Edition, ©1970 McGraw-Hill, Inc.

108. Townsend, M.A., and Mansour, W.M., "A Pendulating Model for Mechanisms with Clearances in the Revolutes," *J. of Engineering for Industry*, v. 97, ser. B, 1975, pp. 354-358.

109. Uicker, J. J., 1969, "Dynamic Behavior of Spatial Linkages. Part 1: Exact Equations of Motion," *J. of Engineering for Industry*, v. 91, Feb. 1969, pp. 251-258.

110. Vjaters, I.I., and Earles, S.W.E., "On Evaluating Impact Interactions at Clearance Bearings in a Four-Bar Mechanism," *Proc. 1986 ASME Design Engineering Technical Conf.*, Oct. 5-8, 1986, paper no. 86-DET-173.

111. von Flotow, A.H., "The Acoustic Limit of Control of Structural Dynamics," *Large Scale Space Structures: Dynamics and Control, Springer Series in Computational Mechanics, Springer-Verlag 1988, pp.* 213-237.

112. Wang, H.H.S., *Design Methods for Minimization of Position Errors in Linkages*, PhD Thesis, Stanford University Dept. of Mechanical Engineering, 1987.

113. Wang, H.H.S., and Roth, B., "Position Errors Due to Clearances in Journal Bearings," *J. of Mechanisms, Transmissions and Automation in Design*, Vol. 111, Sep. 1989, pp. 315-320.

114. Wolz, U., and Wittenberg, J., "MESA VERDE: A Program for the Symbolic Generation of Equations for Multi-Body Systems," *Zeitschrift für Angewandte Mathematik und Mechanik*, v. 66, n. 5, 1986, pp. 399-400, (in German).

115. Wu, S.C., and Haug, E.J., "A Substructure Technique for Dynamics of Flexible Mechanical Systems with Contact-Impact," *Proc. 1987 ASME Design Engineering Technical Conf., Vol. II: Robotics, Mechanisms and Machine Systems*, Sep. 27-30, 1987.

116. Xu, W., "Dynamic Analysis of Spatial RCCC Linkage with Clearance," Proc., *The Fifth IFToMM International Symposium on Linkages and Computer Design Methods - Section II: Theory and Practice of Mechanisms*, Romania, Jul. 6-11, 1989, paper no. II-31.

117. Xu, W., and Zhang, Q., "Optimal Accuracy Synthesis of Industrial Robot - Allocation of Tolerances in Linkage Parameter and Joint Variable," *Robot, A Journal of the Chinese Society of Automation*, v. 2, n. 1, 1988.

118. Xu, W., and Zhang, Q., "Probabalistic Analysis and Monte Carlo Simulation of the Kinematic Error in a Spatial Linkage," *Mechanism and Machine Theory*, v. 24, n. 1, 1989, pp. 19-27.

119. Yoo, W.S., and Haug, E.J., "Dynamics of Articulated Structures. Part I: Theory. Part II: Computer Implementation and Applications," J. *Structural Mechanics*, v. 14, n. 2, 1986, pp. 105-126, 177-189.

120. Zhe, L., Li, L., and Shixian, B., "A New Method of Predicting the Occurrence of Contact Loss between Pairing Elements in Planar Linkages with Clearances," *Mechanism and Machine Theory*, v. 27, n. 3, 1992, pp. 295-301.

Appendix A. Perturbation Coordinates

The use of perturbation coordinates in dynamic mechanism analysis is well established [31, 100]. This appendix will provide a brief explanation of the concept, and a definition of the nomenclature as used in this thesis. Figure A.1 shows the terms used. The notation is taken from reference [100].

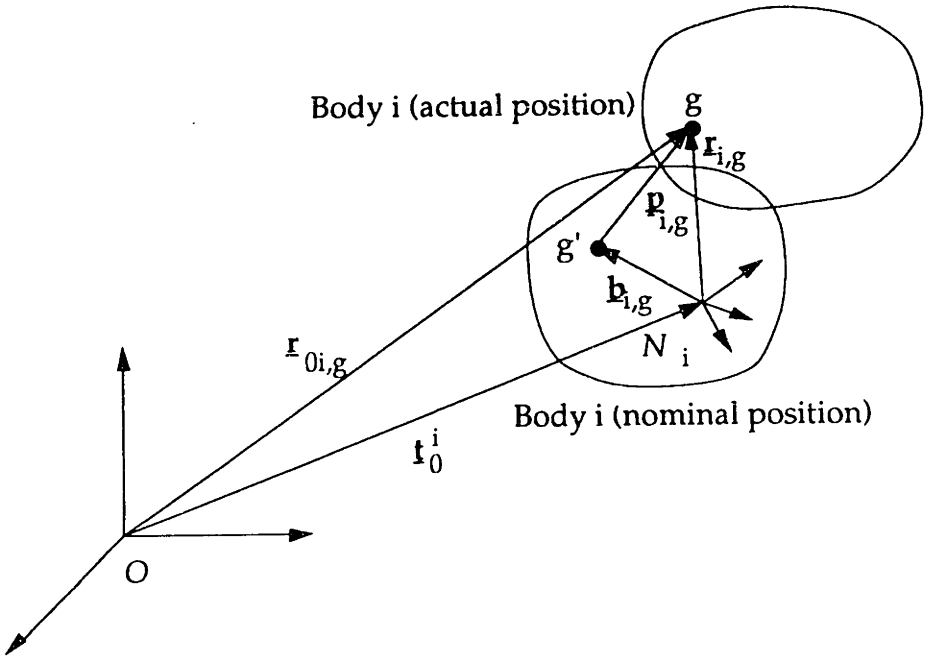

Figure A.1. Perturbation Coordinates.

Perturbation coordinates are the components of vectors, $\underline{p}_{i,g}$, that locate points, g, on a body, i, with respect to the nominal positions of those points, g'.

Frame N_i, fixed to the undeformed body at a convenient point, identifies the body's nominal location and orientation. The nominal motions of a body can be any defined sequence of positions and orientations. The convention chosen for this thesis is defined later in this appendix. When body i is in its nominal position, the position of N_i in the inertial frame is $\underline{t}^i_0$, and points g' on body i are located with respect to N_i by vectors such as $\underline{b}_{i,g}$. The $\underline{b}_{i,g}$ vectors

are constants that depend on the undeformed shape of the body. It follows that all points g' can be located with respect to the inertial frame *O* at all times as $\underline{t}_0^i + \underline{b}_{i,g}$.

The real position of body i differs from its nominal position because of rigid body translation and rotation, and, if i is a flexible body, deformations. Points such as g', identified when the body is in its nominal position, move to points such as g when the body assumes its real position. Point g is located with respect to g' by the perturbation vector, $\underline{p}_{i,g}$, and with respect to N_i by $\underline{r}_{i,g}$. From the sketch, it follows that $\underline{r}_{0i,g}$, the inertial position vector of point g, is:

$$\underline{r}_{0i,g} = \underline{t}_0^i + \underline{b}_{i,g} + \underline{p}_{i,g} \tag{A.1}$$

Since $\underline{t}_0^i$ gives the nominal position of N_i, by definition it is known at all times. Thus $\underline{r}_{0i,g}$ is known in terms of the known time function $\underline{t}_0^i$, the constant vector $\underline{b}_{i,g}$, and the perturbation vector $\underline{p}_{i,g}$. The use of perturbation coordinates in dynamic analysis means that, rather than using the components of $\underline{r}_{0i,g}$ as generalized coordinates, the components of the link perturbation vector, $\underline{p}_{i,g}$, are the generalized coordinates. Equation A.1 defines the transformation between the two sets of coordinates.

Perturbation coordinates are used to help avoid numerical difficulties when using a digital computer to perform numerical integration of the equations of motion.

For flexible bodies modeled by a finite element method, a convenient choice for the nominal coordinate frames is usually the finite element reference frames; then, the $\underline{b}_{i,g}$ vectors are just the coordinates of the finite element node points. For a rigid body, the nominal frame can be located at the center

of mass and a single $\underline{b}$ vector of zero length defined. The nominal positions of all bodies in a system are defined as their positions under the following conditions:

- no flexible deformations of any component in the system;
- all joints behave as ideal; i.e., zero clearance and compliance;
- non-ideal control system and actuator effects, such as lead, lag, resonance, noise, error and saturation, are ignored. Thus, the bodies are at their commanded positions at all times;
- the linear and angular displacements and velocities of the commanded positions are continuous functions of time.

Then, nonzero values of the perturbation coordinates are due to elastic deformation, control system and actuator dynamics, joint clearance effects, and the perturbations of preceding bodies in the kinematic chain. For typical machine systems, the magnitudes of these perturbations will be very small compared with the dimensions of the bodies. This fact justifies the assumption of small deformations, necessary when the perturbation coordinates are equated to finite element displacement coordinates.

Appendix B. 4x4 Matrix Notation; Hartenberg - Denavit Notation

A. 4x4 Matrices

In Appendix A, the use of perturbation coordinates was discussed, and the notions of nominal motion and nominal position were used. In this appendix, a systematic technique for defining and expressing the nominal motion is outlined. This technique provides a way to describe the orientations of the nominal frames, N_i, and their inertial position vectors, $\underline{t}_0^i$, as functions of time.

Figure B.1 show a 3x3 rotational transformation matrix, $\underline{T}_j^i$, and a 3x1 translation vector, $\underline{t}_j^i$, that together describe the position and orientation of the N_i reference frame with respect to the N_j frame. In general, 4x4 matrix methods combine such rotational and translational transformations to produce a matrix that can express the position vector of a point in space with respect to a new set of coordinate axes [26].

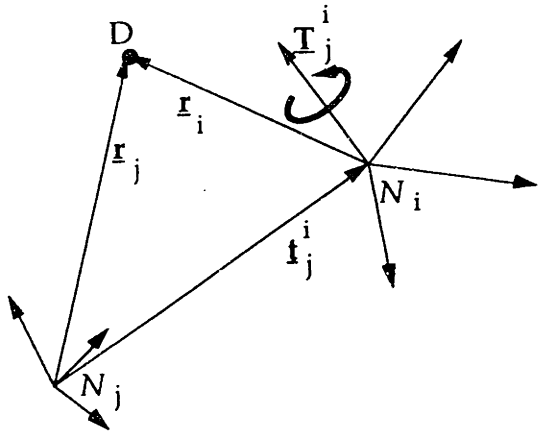

Figure B.1. 4x4 Matrix Definitions.

The 4x4 matrix representing the transformation between frames N_i and N_j is defined as follows:

$$\mathbf{T}_j^i = \begin{bmatrix} 1 & \underline{0}^T \\ \underline{t}_j^i & \underline{\mathbf{T}}_j^i \end{bmatrix} \tag{B.1}$$

in which $\underline{\mathbf{T}}_j^i$ is a 3x3 rotation matrix that expresses the orientation of frame N_i with respect to frame N_j; $\underline{t}_j^i$ is a 3x1 vector, defined in the N_j frame, that expresses the location of the origin of frame N_i; 1 is the scalar 1, and $\underline{0}^T$ is a 1x3 vector of zeros. The superscript T indicates the transpose of a column vector or a matrix, and the underscore indicates a 3x1 vector or 3x3 matrix.

A.1. Direction Vectors; Location Vectors

Suppose that the point D is located in the N_i reference frame by the vector $\underline{r}_i$, whose components are referenced to the N_i coordinate axes, as shown in Figure B.1. If the orientation of $\underline{r}_i$ in the N_j reference frame is desired, it can be found by multiplying $\underline{r}_i$ by the rotational transformation matrix $\underline{\mathbf{T}}_j^i$. This multiplication can be performed using the full 4x4 matrix by forming a 4x1 vector, whose first element is 0, from $\underline{r}_i$:

$$\{0\ (\underline{r}_i)_j\}^T = \mathbf{T}_j^i\ \{0\ \underline{r}_i\}^T \tag{B.2}$$

Note that $(\underline{r}_i)_j$ and $\underline{r}_i$ are the same vector in space; only the reference frame to which the vector's components are referenced has changed. To locate point D in the N_j frame, the distance from the N_j origin to the N_i origin, $\underline{t}_j^i$ in Figure B.1, which is the lower-left 3x1 vector of $\mathbf{T}_j^i$, must be added to $\underline{r}_i$. This can be done by forming another 4x1 vector from $\underline{r}_i$, but now with 1 as its first element:

$$\{1\ \underline{r}_j\}^T = \mathbf{T}_j^i\ \{1\ \underline{r}_i\}^T \tag{B.3}$$

This resultant is an entirely new vector, $\underline{r}_j$ in Figure B.1, that expresses the location of P relative to the N_j origin, with components referenced to the N_j frame. In general, 4x1 vectors whose first element is zero are used to express

directions or lines of action, and those whose first element is 1 are used to express *locations* in space.

B. Hartenberg – Denavit Notation

Equations B.2 and B.3 show by example how 4x4 transformation matrices can be used either to perform a rotational transformation that expresses the components of a vector in a different reference frame, or to locate a point in space with respect to a different reference frame. Hartenberg - Denavit notation is a systematic method for obtaining these 4x4 matrices [26]. Figure B.2 shows the coordinate frames for three links of a mechanism, and the Hartenberg - Denavit variables for the i^{th} frame. The heavy black curves indicate physical links, and the cylindrical shapes indicate joints. The joints in the figure could be either revolute or prismatic joints.

All joints can be described kinematically as compounds of revolute and prismatic joints. The joint axes are indicated in Figure B.2 by the long-short-short dashed lines. In Hartenberg-Denavit notation, reference frames are associated with each link, and the z-axis of each such reference frame lies along the axis of the joint that connects to the next link in the system's kinematic chain. It is also necessary to identify the distance lines - the mutual perpendiculars - between each pair of joint axes. These perpendiculars are indicated in the figure by the short dashed lines. The x-axis of each link coordinate frame lies along one of these lines.

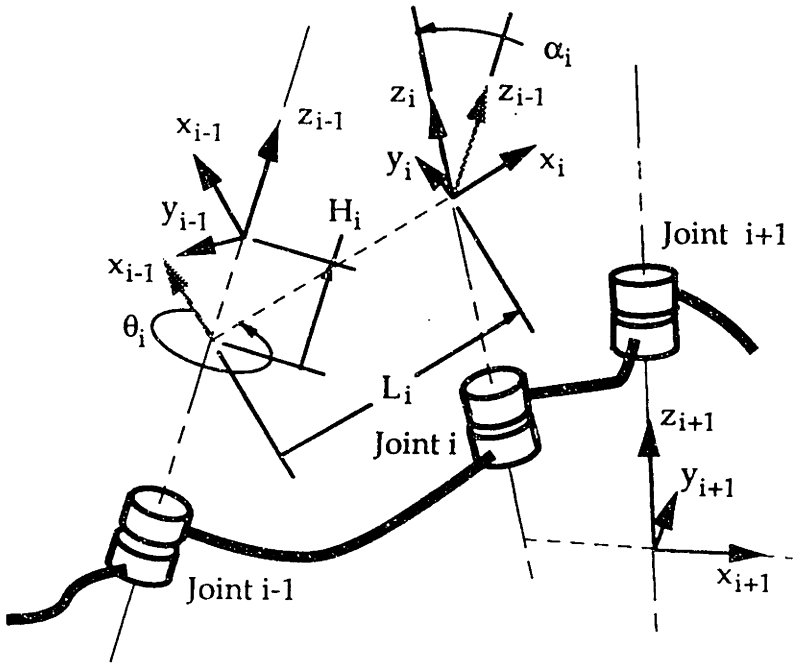

Figure B.2. Hartenberg - Denavit Notation.

To establish the position of the i^{th} reference frame, imagine a duplicate set of axes that initially is coincident with the axes of the i-1^{st} reference frame. These duplicate axes will be translated and rotated in four steps to become the i^{th} reference frame axes. As the first step, translate the duplicate axes along the z_{i-1} axis to the intersection of the perpendicular to the i^{th} joint axis. The distance moved is H_i; in Figure B.2, H_i is negative. In the second step, rotate the duplicate axes around the z_{i-1} axis until the x-axis of the duplicate set lies along the previously identified perpendicular distance line. This axis is now oriented in the x_i direction. The angle rotated is θ_i; in Figure B.2, θ_i is greater than 180°. As the third step, translate the axes along the perpendicular until the intersection with the i^{th} joint axis. The distance is L_i. The fourth and final step is to rotate the axes about the x_i axis until the z axis lies along the i^{th} joint axis; the angle rotated is α_i, shown in the Figure as an acute angle. (At the beginning of the fourth step, the z_i axis was still pointing in the z_{i-1}

direction.) The axes are now positioned and oriented as the i^{th} link Hartenberg - Denavit reference frame.

L_i and α_i are always constants that depend on the link geometry. For prismatic joints, H_i is the joint variable and θ_i is a constant that depends on the link's geometry. For revolute joints, θ_i is the joint variable, and H_i is a geometric constant.

A 4x4 transformation matrix can be constructed using the Hartenberg - Denavit distances and angles as follows:

$$T^i_{i-1} = \begin{bmatrix} 1 & \underline{0}^T \\ \underline{t}^i_{i-1} & \underline{\underline{T}}^i_{i-1} \end{bmatrix} \tag{B.4}$$

where,

$$\underline{t}^i_{i-1} = \{L_i\cos(\theta_i) \;\; L_i\sin(\theta_i) \;\; H_i\}^T \tag{B.5}$$

and

$$\underline{\underline{T}}^i_{i-1} = \begin{bmatrix} \cos(\theta_i) & -\sin(\theta_i)\cos(\alpha_i) & \sin(\theta_i)\sin(\alpha_i) \\ \sin(\theta_i) & \cos(\theta_i)\cos(\alpha_i) & -\cos(\theta_i)\sin(\alpha_i) \\ 0 & \sin(\alpha_i) & \cos(\alpha_i) \end{bmatrix} \tag{B.6}$$

In its fully expanded form, the matrix is:

$$T^i_{i-1} = \begin{bmatrix} 1 & 0 & 0 & 0 \\ L_i\cos(\theta_i) & \cos(\theta_i) & -\sin(\theta_i)\cos(\alpha_i) & \sin(\theta_i)\sin(\alpha_i) \\ L_i\sin(\theta_i) & \sin(\theta_i) & \cos(\theta_i)\cos(\alpha_i) & -\cos(\theta_i)\sin(\alpha_i) \\ H_i & 0 & \sin(\alpha_i) & \cos(\alpha_i) \end{bmatrix} \tag{B.7}$$

C. T-Matrix Properties

The following properties of 4x4 matrices that are formed according to the above procedure are stated without proof.

Multiplication: Transformations along the kinematic chain correspond to matrix products. For example, if $\mathbf{r}_i$ identifies a point D in space by its components in the i^{th} reference frame, and if $j \le i$, then:

$$\mathbf{r}_j = \mathbf{T}_j^{j+1}\,\mathbf{T}_{j+1}^{j+2} \cdots \mathbf{T}_{i-2}^{i-1}\,\mathbf{T}_{i-1}^{i}\,\mathbf{r}_i \tag{B.8}$$

where $\mathbf{r}_j$ is the position vector of D relative to the j^{th} reference frame. Both $\mathbf{r}_i$ and $\mathbf{r}_j$ are 4x1 vectors with 1 as the first element, following the example in Equation B.3. When j is the inertial frame, the result is the inertial position of D:

$$\mathbf{r}_0 = \mathbf{T}_0^1\,\mathbf{T}_1^2 \cdots \mathbf{T}_{i-1}^{i}\,\mathbf{r}_i \tag{B.9}$$

A corollary is that a transformation matrix between coordinate frames separated by several joints is a product of the individual transformation matrices:

$$\mathbf{T}_j^i = \mathbf{T}_j^{j+1}\,\mathbf{T}_{j+1}^{j+2} \cdots \mathbf{T}_{i-2}^{i-1}\,\mathbf{T}_{i-1}^{i};\ j < i \tag{B.10}$$

Transpose: Since the lower-right 3x3 submatrix of a T matrix is a rotation matrix, its transpose is its inverse. The following property can be demonstrated:

$$\mathbf{T}_{i-1}^{i\,T}\,\mathbf{T}_{i-1}^{i} = \begin{bmatrix} 1+\underline{t}_{i-1}^{i\,T}\underline{t}_{i-1}^{i} & \underline{t}_{i-1}^{i\,T}\underline{T}_{i-1}^{i} \\ \underline{T}_{i-1}^{i\,T}\underline{t}_{i-1}^{i} & \underline{I} \end{bmatrix} \tag{B.11}$$

where $\underline{I}$ is the 3x3 identity matrix.

Transpose of product: A standard matrix identity is:

$$\mathbf{T}_{j-1}^{i\,T} = (\mathbf{T}_j^{j+1}\,\mathbf{T}_{j+1}^{j+2} \cdots \mathbf{T}_{i-2}^{i-1}\,\mathbf{T}_{i-1}^{i})^T = \mathbf{T}_{i-1}^{i\,T}\,\mathbf{T}_{i-2}^{i-1\,T} \cdots \mathbf{T}_{j+1}^{j+2\,T}\,\mathbf{T}_j^{j+1\,T} \tag{B.12}$$

i.e., that the transpose of a matrix product is the reverse-order product of transposes.

Differentiation: Differentiation of a T matrix with respect to its joint variable, θ for a revolute joint and H for a prismatic joint, can be represented as a multiplication:

$$\frac{\partial \mathbf{T}_{i-1}^{i}}{\partial \theta_i} = \mathbf{Q}^{\theta}\mathbf{T}_{i-1}^{i} \; ; \qquad \frac{\partial \mathbf{T}_{i-1}^{i}}{\partial H_i} = \mathbf{Q}^{H}\mathbf{T}_{i-1}^{i} \tag{B.13}$$

Both joint differentiation matrices can be written:

$$\mathbf{Q}^{X} = \begin{bmatrix} 0 & \underline{0}^{T} \\ \underline{q}^{X} & \underline{\underline{Q}}^{X} \end{bmatrix} \tag{B.14}$$

where X stands for θ or H, as appropriate. The submatrices for each joint type are:

$$\underline{q}^{\theta} = \underline{0}; \quad \underline{\underline{Q}}^{\theta} = \begin{bmatrix} 0 & -1 & 0 \\ 1 & 0 & 0 \\ 0 & 0 & 0 \end{bmatrix}; \quad \underline{q}^{H} = \{0 \;\; 0 \;\; 1\}^{T}; \quad \underline{\underline{Q}}^{H} = [\underline{\underline{0}}] \tag{B.15}$$

Differentiation of product: The kinematic equations to be presented in Appendix C require differentiation with respect to time of products of T-matrices. The derivative of the T matrix between link i and the inertial frame, $\mathbf{T}_0^i$, with respect to a single joint variable is:

$$\frac{\partial \mathbf{T}_0^i}{\partial X_j} = \mathbf{T}_0^1 \mathbf{T}_1^2 \cdots \mathbf{T}_{j-2}^{j-1} \frac{\partial \mathbf{T}_{j-1}^{j}}{\partial X_j} \mathbf{T}_j^{j+1} \cdots \mathbf{T}_{i-1}^{i} = \mathbf{T}_0^{j-1} \frac{\partial \mathbf{T}_{j-1}^{j}}{\partial X_j} \mathbf{T}_j^i \tag{B.16}$$

because only the $\mathbf{T}_{j-1}^{j}$ matrix depends on the X_j joint variable. Using the Q matrices introduced in Equation B.13 the notation $\mathbf{U}_{i,j}$ is defined:

$$\mathbf{U}_{i,j} \equiv \mathbf{T}_0^{j-1} \mathbf{Q}_j \mathbf{T}_{j-1}^{i} \tag{B.17}$$

where $\mathbf{Q}_j$ is either $\mathbf{Q}^\theta$ or $\mathbf{Q}^H$ from Equation B.15, corresponding to a revolute or a prismatic joint j. The time derivative of $\mathbf{T}_0^i$ can be computed by applying the chain rule, so that the total derivative becomes a sum of products:

$$\frac{d\mathbf{T}_0^i}{dt} = \sum_{j=1}^{i} \mathbf{U}_{i,j}\, \dot{X}_j \tag{B.18}$$

where $\dot{X}_j$ is the time derivative of the joint variable of the j^{th} link. The second derivative of the $\mathbf{T}_0^i$ matrix is:

$$\frac{d^2\mathbf{T}_0^i}{dt^2} = \sum_{j=1}^{i} \mathbf{U}_{i,j}\, \ddot{X}_j + \sum_{k=1}^{i} \sum_{j=1}^{i} \mathbf{U}_{i,j,k}\, \dot{X}_j \dot{X}_k \tag{B.19}$$

where $\mathbf{U}_{i,j,k}$ is the derivative of $\mathbf{U}_{i,j}$ with respect to the k^{th} link variable:

$$\mathbf{U}_{i,j,k} \equiv \frac{\partial \mathbf{U}_{i,j}}{\partial X_k} = \frac{\partial^2 \mathbf{T}_0^i}{\partial X_j \partial X_k} \tag{B.20}$$

Depending on the values of j and k, $\mathbf{U}_{i,j,k}$ is expanded as one of the following:

$$\mathbf{U}_{i,j,k} = \begin{cases} \mathbf{T}_0^{k-1}\, \mathbf{Q}_k\, \mathbf{T}_{k-1}^{j-1}\, \mathbf{Q}_j\, \mathbf{T}_{j-1}^{i} & (k<j) \\ \mathbf{T}_0^{j-1}\, \mathbf{Q}_j\, \mathbf{Q}_j\, \mathbf{T}_{j-1}^{i} & (k=j) \\ \mathbf{T}_0^{j-1}\, \mathbf{Q}_j\, \mathbf{T}_{j-1}^{k-1}\, \mathbf{Q}_k\, \mathbf{T}_{k-1}^{i} & (k<j) \end{cases} \tag{B.21}$$

Note, however, that since the T-matrices are continuous functions of the joint variables, it is guaranteed that $\mathbf{U}_{i,j,k} = \mathbf{U}_{i,k,j}$, i.e. that the order of differentiation does not matter. That this is true is obvious from inspection of B.21.

Optimized Multiplication: for full matrices, the product of two n x n matrices requires n^3 operations, or 64 for 4x4 matrices. (One operation is a floating point multiplication and a floating point addition.) Because of the sparse nature of T–matrices, an optimized multiplication algorithm that uses only 37 operations, rather than 64, is possible.

Since any T–matrix has the form given in Equation B.1, a product of T–matrices has the form:

$$\begin{aligned} \mathbf{T}^{i}_{i-1}\,\mathbf{T}^{j}_{j-1} &= \begin{bmatrix} 1 & \underline{0}^{T} \\ \underline{t}^{i}_{i-1} & \underline{\mathbf{T}}^{i}_{i-1} \end{bmatrix} \begin{bmatrix} 1 & \underline{0}^{T} \\ \underline{t}^{j}_{j-1} & \underline{\mathbf{T}}^{j}_{j-1} \end{bmatrix} \\ &= \begin{bmatrix} 1 & \underline{0}^{T} \\ \underline{t}^{i}_{i-1} + \underline{\mathbf{T}}^{i}_{i-1}\,\underline{t}^{j}_{j-1} & \underline{\mathbf{T}}^{i}_{i-1}\,\underline{\mathbf{T}}^{j}_{j-1} \end{bmatrix} \end{aligned} \tag{B.22}$$

Thus, a T–matrix product can be implemented as a product of 2 3x3 matrices, a 3x3 times 3x1 matrix product, and a sum of two 3x1 vectors, requiring 27 + 9 operations and 3 extra floating point additions. Since addition is faster than multiplication on most computers, this is essentially 36 or 37 operations. A full 4x4 matrix multiplication requires 64 operations. Therefore, the optimized algorithm operates in slightly more than 1/2 the time of the general algorithm.

Equations B.1 to B.22 will be referenced in Appendix C.

Appendix C. Dynamic Equations

A. Perturbation Coordinates and Selector Vector Notation

Hartenberg - Denavit 4x4 matrix notation is widely known and used, and is reviewed in Appendix B as it applies to this thesis. This notation can describe a mechanism of arbitrary complexity whose links follow arbitrary paths through space. This appendix reviews the development of the equations of motion for a single link of the machine system. The presentation here is based on reference [100], but has been streamlined and simplified in several areas. Also, the notation of [100] has been changed slightly to conform to the conventions of this thesis.

A machine system is described by links, numbered 1 ... NL. Figure C.1 shows the finite element mesh for a typical link i, both in its nominal position and in its real position after deformations and rigid body motions have been applied. The black dots are the FE node points. A square matrix $\mathbf{K}_i$, and a diagonal matrix $\mathbf{M}_i$, exist and define the stiffness and mass characteristics of link i. The finite element formulation also implies that a vector of deformations from the reference position, $\mathbf{p}_i$, exists. There are NG_i finite element node points on link i, and each has six degrees of freedom, so that $\mathbf{M}_i$ and $\mathbf{K}_i$ have dimension $6*NG_i \times 6*NG_i$, and $\mathbf{p}_i$ has length $6*NG_i$. This number, $6*NG_i$, is $NDOF_i$, the number of degrees of freedom on the i^{th} link.

Figure C.1 shows the nominal location vector, $\underline{b}_{ig}$, the perturbation translation and rotation vectors, $\underline{p}_{ig}$ and $\underline{\phi}_{ig}$, the inertial location vector, $\underline{r}_{0,ig}$, and the velocity vector $\underline{v}_{ig}$ for a single node point, g, on link i. The figure also shows the nominal frame location vector, $\underline{t}_0^i$ for reference frame, N_i, and

the nominal rotation matrix, $\underline{T}_0^i$, which describes the orientation of N_i, with respect to the inertial reference frame, O. The concepts of perturbation coordinates and nominal motion are reviewed in Appendix A.

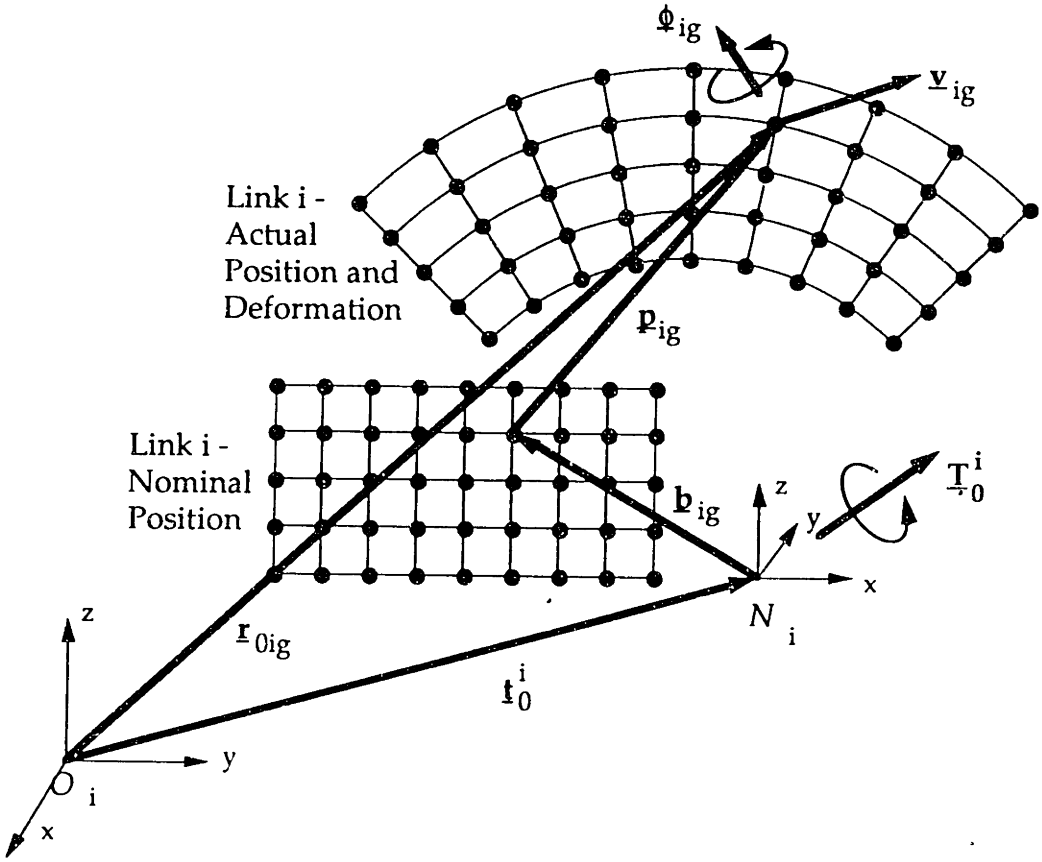

Figure C.1. Nominal and Perturbation Positions.

The generalized coordinates that describe the dynamics of each link are contained in the system's global coordinate vector, $\mathbf{q}$. The link perturbation vectors, $\mathbf{p}_i$, which describe the motions of all the FE node points, are derived from $\mathbf{q}$ using the compatibility and CMS relations, Equation 3.4, and 3.2. To express the perturbation vectors at each node point, reference [100] introduces selection vectors $\phi_{g,\beta}$. Selection vectors are also used in this thesis, but they are denoted $\sigma_{g,\beta}$, to avoid duplicated nomenclature. The selection vector $\sigma_{g,\beta}$ is defined as a function of the degree of freedom number, β, and the node

point number, g. β can assume values from 1 to $6*NG_i$, corresponding to each degree of freedom defined for link i, and g can have values from 1 to NG_i. The vector $\sigma_{g,\beta}$ is defined as follows:

$$\sigma_{g,\beta} = \begin{cases} \{0\,1\,0\,0\}^T \equiv \sigma_x \text{ if } \beta \text{ selects the x-DOF at grid point g.} \\ \{0\,0\,1\,0\}^T \equiv \sigma_y \text{ if } \beta \text{ selects the y-DOF at grid point g.} \\ \{0\,0\,0\,1\}^T \equiv \sigma_z \text{ if } \beta \text{ selects the z-DOF at grid point g.} \\ \{0\,0\,0\,0\}^T \text{ for all other values of } \beta. \end{cases} \tag{C.1}$$

This notation makes it possible to define a 4x1 perturbation direction vector at a node point as:

$$\mathbf{p}_{i,g} = \sum_{\beta=1}^{NDOF_i} \sigma_{g,\beta}\, p_{i,\beta} \tag{C.2}$$

where $p_{i,\beta}$ is the β^{th} element in the link i perturbation coordinate vector, $\mathbf{p}_i$. The definition of $\sigma_{g,\beta}$ causes $\mathbf{p}_{i,g}$ to be a 4x1 vector whose first element is zero. Using Equations A.1 and B.3, and noting that the components of the $\underline{\mathbf{b}}_{i,g}$ and $\underline{\mathbf{p}}_{i,g}$ vectors are defined in the N_i reference frame, then the inertial location of a node point is:

$$\begin{aligned} \mathbf{r}_{0,ig} &= \mathbf{T}_0^i\{\mathbf{b}_{i,g} + \mathbf{p}_{i,g}\} \\ &= \mathbf{T}_0^i\left\{\mathbf{b}_{i,g} + \sum_{\beta=1}^{NDOF_i} \sigma_{g,\beta}\, p_{i,\beta}\right\} \end{aligned} \tag{C.3}$$

Since $\mathbf{p}_{i,g}$ is a 4x1 vector beginning with zero, i.e. a *direction* vector, and $\mathbf{b}_{i,g}$ is a 4x1 vector that begins with one, a *location* vector, the result, $\mathbf{r}_{0,ig}$ is a 4x1 *location* vector.

B. Dynamic Formulation

Following the derivation in reference [100], the equations of motion for link i will be derived using Lagrange's equation, which is:

$$\frac{d}{dt}\left(\frac{\partial KE_i}{\partial \dot{p}_{i,\alpha}}\right) - \frac{\partial KE_i}{\partial p_{i,\alpha}} + \frac{\partial PE_i}{\partial p_{i,\alpha}} = f_{e,i,\alpha} \tag{C.4}$$

The link index i ranges from 1 to NL, the number of links in the machine system. The degree of freedom index, α, ranges from 1 to $NDOF_i$, which is the number of degrees of freedom associated with the finite element nodes of link i, and also the length of the link perturbation vector, $\mathbf{p}_i$. The right hand side, $f_{e,i,\alpha}$, is the external force applied to each degree of freedom. As α ranges from 1 to $NDOF_i$, the elements $f_{e,i,\alpha}$ define a vector $\mathbf{f}_{e,i}$, which is the vector of forces applied to the link. KE_i and FE_i are the kinetic and potential energy of link i in terms of the generalized coordinates $p_{i,\alpha}$ and generalized velocities $\dot{p}_{i,\alpha}$.

The potential energy stored in the link due to gravity can be written:

$$PE_{i,grav} = -\sum_{g=1}^{NG_i} M_{i,g}\, \mathbf{r}_{0,ig}{}^T\, \mathbf{g} \tag{C.5}$$

where $\mathbf{r}_{0,ig}$ is the position in the inertial reference frame of the g^{th} node point on the i^{th} link, $\mathbf{g}$ is the gravity direction vector, and $M_{i,g}$ is the element of the link's diagonal mass matrix, $\mathbf{M}_i$, that corresponds to node point g. The gravity vector $\mathbf{g}$ is a 4x1 direction vector with 0 as its first element. The summation is over all FE node points on link i. Substitute for $\mathbf{r}_{0,ig}$ from Equation C.3 to write:

$$PE_{i,grav} = -\sum_{g=1}^{NG_i} M_{i,g} \left[\mathbf{T}_0^i \left(\mathbf{b}_{i,g} + \sum_{\beta=1}^{NDOF_i} \sigma_{g,\beta}\, p_{i,\beta} \right) \right] \tag{C.6}$$

as the gravitational potential energy for link i.

For a finite element representation of an elastic body, the potential energy stored due to elastic deformations is:

$$PE_{i,elastic} = \frac{1}{2} \mathbf{p}_i^T \mathbf{K}_i \mathbf{p}_i \tag{C.7}$$

where $\mathbf{p}_i$ is the link's FE perturbation vector and $\mathbf{K}_i$ is the stiffness matrix. When this matrix product is expanded in terms of the components of the perturbation vector and stiffness matrix, it appears as:

$$PE_{i,elastic} = \frac{1}{2} \sum_{\gamma=1}^{NDOF_i} \sum_{\beta=1}^{NDOF_i} p_{i\gamma} K_{i\gamma\beta} p_{i\beta} \tag{C.8}$$

Finally, define the kinetic energy of the link. If $\mathbf{r}_{0,ig}$ is the position of the g^{th} node point in an inertial frame of reference, then its inertial velocity is $\dot{\mathbf{r}}_{0,ig}$. Note that, while $\mathbf{r}_{0,ig}$ is a 4x1 location vector, $\dot{\mathbf{r}}_{0,ig}$ is a 4x1 direction vector. The kinetic energy associated with node point g on link i is:

$$KE_{i,g} = \frac{1}{2} M_{ig} \dot{\mathbf{r}}_{0,ig}^T \dot{\mathbf{r}}_{0,ig} \tag{C.9}$$

M_{ig} is the translational mass located at the g^{th} node point, as in Equation C.5. This formulation neglects the kinetic energy due to rotary inertia of the node points, as is commonly assumed [100]. Equation C.9 is mathematically equal to, but computationally simpler than the formulation used in reference [100]. When Equation C.9 is summed for all node points on a link, the result is the kinetic energy for the entire link:

$$KE_i = \frac{1}{2} \sum_{g=1}^{NG_i} M_{i,g} \dot{\mathbf{r}}_{0,ig}^T \dot{\mathbf{r}}_{0,ig} \tag{C.10}$$

When Equation C.3 is differentiated to find the inertial velocity, $\dot{\mathbf{r}}_{0,ig}$, the result is:

$$\dot{\mathbf{r}}_{0,ig} = \dot{\mathbf{T}}_0^i \left(\mathbf{b}_{i,g} + \sum_{\beta=1}^{NDOF_i} \sigma_{g,\beta} p_{i,\beta} \right) + \mathbf{T}_0^i \left(\sum_{\beta=1}^{NDOF_i} \sigma_{g,\beta} \dot{p}_{i,\beta} \right) \tag{C.11}$$

The derivative of the transformation matrix product, $\dot{\mathbf{T}}$, can be calculated according to Equation (B.18).

Equations C.6, C.8, C.10 and C.11 can be used with Lagrange's Equation to derive the equations of motion for link i. By applying the formulation repeatedly as i varies from 1 to NL, the equations of motion for each link of the system can be derived in terms of the components of the mass and stiffness matrices, the components of the perturbation vector, and the Hartenberg - Denavit link variables that describe the nominal motion of the machine.

The total potential energy associated with link i is the sum of Equations C.6 and C.8, or:

$$PE_i = -\sum_{g=1}^{NG_i} M_{i,g}\left[\left(\mathbf{b}_{i,g}^T + \sum_{\beta=1}^{NDOF_i} \sigma_{g,\beta}^T p_{i,\beta}\right)\mathbf{T}_0^{iT}\right]\mathbf{g} + \frac{1}{2}\sum_{\gamma=1}^{NDOF_i}\sum_{\beta=1}^{NDOF_i} p_{i\gamma} K_{i\gamma\beta} p_{i\beta} \quad (C.12)$$

where the matrix transpose has been taken inside the brackets in Equation C.6.

The third term of Equation C.4 requires the partial derivative of Equation C.12 with respect to perturbation vector component $p_{i,\alpha}$. This is:

$$\frac{\partial PE_i}{\partial p_{i,\alpha}} = -M_{i,g}\,\sigma_{g,\alpha}^T\,\mathbf{T}_0^{iT}\,\mathbf{g} + \sum_{\beta=1}^{NDOF_i}\left(K_{i,\alpha\beta}\,p_{i,\beta}\right) \quad (C.13)$$

The symmetry of the FE stiffness matrix has been used to eliminate the factor of 1/2 from the second term of Equation C.13.

To form the second term of Equation C.4, a partial derivative of Equation C.10 is required:

$$\frac{\partial KE_i}{\partial p_{i,\alpha}} = \frac{1}{2}\sum_{g=1}^{NG_i} M_{i,g}\left(\frac{\partial}{\partial p_{i,\alpha}}\dot{\mathbf{r}}_{0,ig}^{\,T}\,\dot{\mathbf{r}}_{0,ig} + \dot{\mathbf{r}}_{0,ig}^{\,T}\frac{\partial}{\partial p_{i,\alpha}}\dot{\mathbf{r}}_{0,ig}\right) \quad (C.14)$$

Because the two terms inside the parentheses are identical scalars, Equation C.14 can be written:

$$\frac{\partial KE_i}{\partial p_{i,\alpha}} = \sum_{g=1}^{NG_i} M_{i,g}\left(\frac{\partial \dot{o}}{\partial p_{i,\alpha}} \dot{r}_{0,ig}{}^T \dot{r}_{0,ig}\right) \tag{C.15}$$

Now, substitute the transpose of Equation C.11 for $\dot{r}_{0,ig}{}^T$ to evaluate the partial derivative inside the parentheses. The result is:

$$\begin{aligned}\frac{\partial KE_i}{\partial p_{i,\alpha}} &= \sum_{g=1}^{NG_i} \left\{ M_{i,g}\left[\sigma_{g,\alpha}^T \dot{T}_0^{i\,T}\right]\left[\dot{r}_{0,ig}\right]\right\} \\ &= M_{i,g}\left[\sigma_{g,\alpha}^T \dot{T}_0^{i\,T}\right]\left[\dot{r}_{0,ig}\right]\end{aligned} \tag{C.16}$$

The summation over g can be eliminated, because the selection vector $\sigma_{g,\alpha}$ is nonzero only for values of g that refer to the node point at which degree of freedom α is defined. Therefore, all the terms containing $\sigma_{g,\alpha}$ are zero, except for the single term in which g is the index of the FE node point at which degree of freedom α occurs. This value of g is g = (α–1)\6 + 1, where "\" indicates integer division. The constant "6" in this expression is the result of using a spatial finite element formulation, which associates 6 degrees of freedom with each node point.

A similar sequence of operations for the partial derivative of Equation C.10 with respect to $\dot{p}_{i,\alpha}$ produces:

$$\frac{\partial KE_i}{\partial \dot{p}_{i,\alpha}} = M_{i,g}\left[\sigma_{g,\alpha}^T T_0^{i\,T}\right]\left[\dot{r}_{0,ig}\right] \tag{C.17}$$

Lagrange's equation requires the time derivative of Equation (C.17):

$$\frac{d}{dt}\left(\frac{\partial KE_i}{\partial \dot{p}_{i,\alpha}}\right) = M_{i,g}\left[\sigma_{g,\alpha}^T\right]\left[\dot{T}_0^{i\,T} \dot{r}_{0,ig} + T_0^{i\,T} \ddot{r}_{0,ig}\right] \tag{C.18}$$

State Lagrange's Equation as the sum of Equations C.18, the opposite of C.16, and C.13:

$$
\begin{aligned}
& M_{i,g}\left[\sigma_{g,\alpha}^{T}\right]\left[\dot{T}_0^{i^T}\,\dot{r}_{0,ig} + T_0^{i^T}\,\ddot{r}_{0,ig}\right] \\
& - M_{i,g}\left[\sigma_{g,\alpha}^{T}\,\dot{T}_0^{i^T}\right]\left[\dot{r}_{0,ig}\right] \\
& - M_{i,g}\,\sigma_{g,\alpha}^{T}\,T_0^{i^T}\,g + \sum_{\beta=1}^{NDOF_i}\left(K_{i,\alpha,\beta}\,p_{i,\beta}\right) = f_{e,i,\alpha}
\end{aligned}
\qquad \text{(C.19)}
$$

The first term on the first line cancels with the second line, leaving:

$$
M_{i,g}\left[\sigma_{g,\alpha}^{T}\right]\left[T_0^{i^T}\,\ddot{r}_{0,ig} - T_0^{i^T}\,g\right] + \sum_{\beta=1}^{NDOF_i}\left(K_{i,\alpha\beta}\,p_{i,\beta}\right) = f_{e,i,\alpha} \qquad \text{(C.20)}
$$

as the equation of motion excited by generalized force $f_{e,i,\alpha}$ on link i.

Next, expand the inertial acceleration, $\ddot{r}_{0,ig}$, in terms of the Hartenberg - Denavit nominal motion variables and their derivatives, and the perturbation coordinates and their derivatives.

Differentiating Equation C.11 with respect to time produces:

$$
\begin{aligned}
\ddot{r}_{0,ig} = {} & \ddot{T}_0^{i}\left(b_{i,g} + \sum_{\beta=1}^{NDOF_i}\sigma_{g,\beta}\,p_{i,\beta}\right) + 2\,\dot{T}_0^{i}\left(\sum_{\beta=1}^{NDOF_i}\sigma_{g,\beta}\,\dot{p}_{i,\beta}\right) \\
& + T_0^{i}\sum_{\beta=1}^{NDOF_i}\sigma_{g,\beta}\,\ddot{p}_{i,\beta}
\end{aligned}
\qquad \text{(C.21)}
$$

Substituting Equation C.21 into C.20 and grouping terms according to the order of the derivative of the perturbation coordinates results in:

$$
\begin{aligned}
& \left[M_{i,g}\,\sigma_{g,\alpha}^{T}\,T_0^{i^T}\right]\left[T_0^{i}\sum_{\beta=1}^{NDOF_i}\sigma_{g,\beta}\,\ddot{p}_{i,\beta} + 2\,\dot{T}_0^{i}\left(\sum_{\beta=1}^{NDOF_i}\sigma_{g,\beta}\,\dot{p}_{i,\beta}\right)\right] \\
& + \sum_{\beta=1}^{NDOF_i}\left[\left(M_{i,g}\,\sigma_{g,\alpha}^{T}\,T_0^{i^T}\,\ddot{T}_0^{i}\,\sigma_{g,\beta} + K_{i,\alpha\beta}\right)\,p_{i,\beta}\right] = \left[M_{i,g}\,\sigma_{g,\alpha}^{T}\,T_0^{i^T}\right]\left[g - \ddot{T}_0^{i}\,b_{i,g}\right] + f_{e,i,\alpha}
\end{aligned}
\qquad \text{(C.22)}
$$

It will be shown that the terms accompanying the second derivatives of $p_{i,\beta}$ form the finite element mass matrix, the terms accompanying the first derivatives form a "gyroscopic" damping matrix, and those accompanying the perturbation coordinates form the sum of a "gyroscopic" stiffness matrix and the finite element stiffness matrix. The terms on the right hand side of C.22 result from the applied forces, the mass of the machine in a gravity field, and D'Alembert forces due to the nominal rotations and accelerations of the machine system's links.

Substituting Equations B.18 and B.19 for $\dot{T}_0^i$ and $\ddot{T}_0^i$ in Equation C.22 results in:

$$\left[M_{i,g}\,\sigma_{g,\alpha}^T\,T_0^{iT}\right]\left[T_0^i\sum_{\beta=1}^{NDOF_i}\left(\sigma_{g,\beta}\,\ddot{p}_{i,\beta}\right)+\sum_{\beta=1}^{NDOF_i}\sum_{j=1}^{i}\left(2\,U_{i,j}\,\sigma_{g,\beta}\,\dot{p}_{i,\beta}\,\dot{X}_j\right)\right]$$
$$+\sum_{\beta=1}^{NDOF_i}\left[\left(M_{i,g}\,\sigma_{g,\alpha}^T\,T_0^{iT}\left[\sum_{j=1}^{i}\left(U_{i,j}\,\ddot{X}_j\right)+\sum_{k=1}^{i}\sum_{j=1}^{i}\left(U_{i,j,k}\,\dot{X}_j\,\dot{X}_k\right)\right]\sigma_{g,\beta}+K_{i,\alpha\beta}\right)p_{i,\beta}\right] \qquad \text{(C.23)}$$
$$=\left[M_{i,g}\,\sigma_{g,\alpha}^T\,T_0^{iT}\right]\left[g-\left[\sum_{j=1}^{i}\left(U_{i,j}\,\ddot{X}_j\right)+\sum_{k=1}^{i}\sum_{j=1}^{i}\left(U_{i,j,k}\,\dot{X}_j\,\dot{X}_k\right)\right]b_{i,g}\right]+f_{e,i,\alpha}$$

In Equation C.23, X_i and X_j represent the Hartenberg - Denavit kinematic variables for the i^{th} and j^{th} links. See Appendix B for more details.

At this point, the problem of formulating the equations of motion is formally complete. Equation C.23 is Equation C.4, stated in terms of the independent coordinates, their derivatives, and other expressions that are known functions of time and the physical properties of the system.

C. Symbolic Computation of Coefficients

To calculate the coefficients in Equation C.23 directly as they appear would be very wasteful. For instance, the calculation of each $U_{i,j,k}$ according to its

definition, Equation B.21, requires four 4x4 matrix multiplications, assuming that the work of computing all of the $\mathbf{T}_j^i$ has already been done. Since Equation C.23 requires j and k to vary from 1 to i, there are i^2 evaluations of $U_{i,j,k}$ for each value of i, and therefore $(2*NL^3 + 3*NL^2 + NL)/6$ evaluations of $U_{i,j,k}$ as i varies from 1 to NL. Even if the optimized 4x4 matrix multiplication algorithm presented in Appendix B is used, the effort to evaluate Equation C.23 by direct means grows rapidly as the number of links increases.

This direct implementation is more work than necessary. By taking advantage of the T-matrix properties reviewed in Appendix B, it is possible to evaluate every term in Equation C.23 as a sum of products that is at most a few terms in length, once the $\mathbf{T}_j^i$ matrices are known for i = 1 ... NL, j = 1 ... i. The savings is realized by doing some symbolic combinations of the terms in Equation C.23.

As α varies from 1 to $NDOF_i$, Equation C.23 is formulated $NDOF_i$ times for link i. This procedure is repeated for each link by letting i vary from 1 to NL, producing a set of "link equations of motion" for the machine system under analysis. Because each term of C.23 contains a summation over β, the equations for each link can be expressed in a matrix form. Define "dynamic" coefficient matrices $\mathbf{M}_i^{dyn}$, $\mathbf{G}_i^{dyn}$, and $\mathbf{K}_i^{dyn}$, multiplying the perturbation acceleration, velocity and displacement vectors, $\ddot{\mathbf{p}}_i$, $\dot{\mathbf{p}}_i$ and $\mathbf{p}_i$, respectively, and "dynamic" force vector $\mathbf{f}_i^{dyn}$. Then, Equation C.23 can be written compactly as:

$$\mathbf{M}_i^{dyn}\,\ddot{\mathbf{p}}_i + \mathbf{G}_i^{dyn}\,\dot{\mathbf{p}}_i + \mathbf{K}_i^{dyn}\,\mathbf{p}_i = \mathbf{f}_i^{dyn} \qquad (C.24)$$

where the elements of the matrices are:

$$M_{i,\alpha\beta}^{dyn} = M_{i,g}\sigma_{g,\alpha}^{T}\,\mathbf{T}_0^{iT}\,\mathbf{T}_0^{i}\,\sigma_{g,\beta} \qquad (C.25)$$

$$G^{dyn}_{i,\alpha\beta} = 2\, M_{i,g} \sum_{j=1}^{i} \left(\sigma^{T}_{g,\alpha}\, T_0^{iT} U_{i,j}\, \sigma_{g,\beta}\right)\dot{X}_j \tag{C.26}$$

$$K^{dyn}_{i,\alpha\beta} = M_{i,g}\left[\sum_{j=1}^{i}\left(\sigma^{T}_{g,\alpha}\, T_0^{iT} U_{i,j}\, \sigma_{g,\beta}\right)\ddot{X}_j + \sum_{k=1}^{i}\sum_{j=1}^{i}\left(\sigma^{T}_{g,\alpha}\, T_0^{iT} U_{i,j,k}\, \sigma_{g,\beta}\right)\dot{X}_j\,\dot{X}_k\right] + K_{i,\alpha\beta} \tag{C.27}$$

and elements of the dynamic force vector are:

$$f^{dyn}_{i,\alpha} = M_{i,g}\,\sigma^{T}_{g,\alpha}\, T_0^{iT}\, g - \left[M_{i,g}\right]\left[\sum_{j=1}^{i}\left(\sigma^{T}_{g,\alpha}\, T_0^{iT}\, U_{i,j}\, b_{i,g}\right)\ddot{X}_j + \sum_{k=1}^{i}\sum_{j=1}^{i}\left(\sigma^{T}_{g,\alpha}\, T_0^{iT}\, U_{i,j,k}\, b_{i,g}\right)\dot{X}_j\,\dot{X}_k\right] + f_{e,i,\alpha} \tag{C.28}$$

Recall that $f_{e,i,\alpha}$ are the elements of the externally applied force vector $f_{e,i}$, Equation C.4. All of the terms in Equations C.25 to C.28, except $f_{e,i,\alpha}$, can be classified as one of four basic forms, according to the manner in which T–matrix products and derivatives occur. The forms are:

$$\text{Form 1:}\quad \sigma^{T}_{g,\alpha}\, T_0^{iT}\, T_0^{i}\, \sigma_{g,\beta} \tag{C.29}$$

$$\text{Form 2:}\quad \sum_{j=1}^{i} \sigma^{T}_{g,\alpha}\, T_0^{iT}\, U_{i,j}\, \sigma_{g,\beta} \quad \text{-or-} \quad \sum_{j=1}^{i} \sigma^{T}_{g,\alpha}\, T_0^{iT}\, U_{i,j}\, b_{i,g} \tag{C.30}$$

$$\text{Form 3:}\quad \sum_{k=1}^{i}\sum_{j=1}^{i} \sigma^{T}_{g,\alpha}\, T_0^{iT}\, U_{i,j,k}\, \sigma_{g,\beta} \quad \text{-or-} \quad \sum_{k=1}^{i}\sum_{j=1}^{i} \sigma^{T}_{g,\alpha}\, T_0^{iT}\, U_{i,j,k}\, b_{i,g} \tag{C.31}$$

$$\text{Form 4:} \quad \sigma_{g,\alpha}^{T} \, T_0^{i\,T} \, g \tag{C.32}$$

Forms 2 and 3 occur in two variants, where the final factor is a 4x1 vector beginning with zero, $\sigma_{g,\beta}$, or a 4x1 vector beginning with one, $b_{i,g}$. Notice that each of Forms 1 to 4 is a scalar, not a vector or a matrix. In Equations C.24 to C.28, forms 1 to 4 are multiplied by additional scalars to produce the elements of the dynamic matrices.

Recall from Equation C.1 that $\sigma_{g,\alpha}$ and $\sigma_{g,\beta}$ are 4x1 vectors whose first element is always zero. Their last 3 elements form a 3x1 subvector, denoted $\underline{\sigma}_{g,\alpha}$, $\underline{\sigma}_{g,\beta}$. In addition, from Appendix B, all T matrices have the form:

$$T_j^i = \begin{bmatrix} 1 & \underline{0}^T \\ \underline{t}_j^i & \underline{T}_j^i \end{bmatrix} \tag{B.1}$$

Therefore, the vector $\sigma_{g,\alpha}^{T} \, T_0^{i\,T}$, which occurs in every one of Equations C.29 to C.32, can be expanded and partially evaluated as a 4x1 vector whose first element is zero:

$$\sigma_{g,\alpha}^{T} \, T_0^{i\,T} = \begin{Bmatrix} 0 & \underline{\sigma}_{g,\alpha}^{T} \, \underline{T}_0^{i\,T} \end{Bmatrix} \tag{C.33}$$

To evaluate Form 1, substitute Equations B.1 and C.33 into C.29 and expand:

$$\text{Form 1} = \begin{Bmatrix} 0 & \underline{\sigma}_{g,\alpha}^{T} \underline{T}_0^{i\,T} \end{Bmatrix} \begin{bmatrix} 1 & \underline{0}^T \\ \underline{t}_j^i & \underline{T}_j^i \end{bmatrix} \begin{Bmatrix} 0 & \underline{\sigma}_{g,\beta} \end{Bmatrix} \tag{C.34}$$

Evaluate Equation C.34:

$$\text{Form 1} = (0 + \underline{\sigma}_{g,\alpha}^{T} \underline{T}_0^{i\,T} \underline{T}_0^i \underline{\sigma}_{g,\beta}) \tag{C.35}$$

After substituting Equation B.12 and then, repeatedly, Equation B.11, Equation C.35 becomes:

$$\text{Form 1} = \left(\underline{\sigma}_{g,\alpha}^{T} \, \underline{I} \, \underline{\sigma}_{g,\beta} \right) = \left(\underline{\sigma}_{g,\alpha}^{T} \, \underline{\sigma}_{g,\beta} \right) \tag{C.36}$$

The vector product $\mathfrak{G}^{T}_{g,\alpha}\,\mathfrak{G}_{g,\beta}$, whose factors are defined by Equation C.1, is a scalar whose value is zero unless two conditions are simultaneously met: $\alpha = \beta$; and α,β refer to a translational degree of freedom located at node point g. In this case, its value is 1. Form 1 can be interpreted as a function of g, α and β with the following behavior:

$$\text{Form 1 (function } (g,\alpha,\beta)) : \begin{cases} 1 \text{ for } \alpha = \beta \text{ and } (g-1)*6 + 1 \le \alpha \le (g-1)*6 + 3 \\ 0 \text{ for all other } \alpha,\beta \end{cases} \tag{C.37}$$

Form 1 appears only in Equation C.25, where it is multiplied by the scalar coefficient $M_{i,g}$, the element of the finite element mass matrix that corresponds to the mass of the g^{th} node point on the i^{th} link. Therefore, the $\mathbf{M}_i^{dyn}$ matrix is a diagonal matrix, because Form 1 is zero for α not equal to β. Its elements are the same as the translational elements of the finite element mass matrix, because Equation C.37 is 1 when α equals β and they both select the g^{th} node point. Because kinetic energy due to the rotation of the finite elements was not included in Equation C.9, the elements of $\mathbf{M}_i^{dyn}$ that correspond to rotational degrees of freedom are zero. However, such a formulation results in a singular mass matrix for the link equations of motion, Equation C.24. To prevent this, formulate $\mathbf{M}_i^{dyn}$ as equal to the finite element mass matrix, $\mathbf{M}_i$, including finite element inertias for the rotational degrees of freedom. (The meaning of a singular mass matrix is that the object could have zero kinetic energy with non-zero velocity at one or more node points. This is impossible for any physical object.)

When Equation C.33 is applied to Form 2, and Equation B.17 is substituted for $\mathbf{U}_{i,j}$, the result is:

$$\text{Form 2:}\quad \begin{aligned} &\sum_{j=1}^{i} \left\{ \left\langle 0 \quad \underline{\sigma}_{g,\alpha}^{T} \underline{T}_0^{iT} \right\rangle \left[T_0^1 T_1^2 \cdots T_{j-2}^{j-1} Q_j T_{j-1}^{j} \cdots T_{i-1}^{i} \right] \right\} \{v\} \\ &= \sum_{j=1}^{i} \left\{ \left\langle 0 \quad \underline{\sigma}_{g,\alpha}^{T} \underline{T}_0^{iT} \right\rangle \left[T_0^{j-1} Q_j T_{j-1}^{i} \right] \right\} \{v\} \end{aligned} \tag{C.38}$$

In Equation C.38 and the following, the notation v is used to indicate the final vector $\mathbf{b}_{i,g}$ or $\sigma_{i,g}$ of a Form 2 expression. The vector v is defined $v \equiv \{n \quad \underline{v}\}$, in which n is one, if v represents $\mathbf{b}_{i,g}$, or zero, if v represents $\sigma_{i,g}$, and $\underline{v}$ is either $\underline{\mathbf{b}}_{i,g}$ or $\underline{\sigma}_{i,g}$.

Further expanding Equation C.38, the result is:

$$\text{Form 2:}\quad \sum_{j=1}^{i} \left\{ \left(\left\langle \underline{\sigma}_{g,\alpha}^{T} \underline{T}_0^{iT} \underline{T}_0^{j-1} \right\rangle \left\{ \underline{q}_j + \underline{Q}_j \underline{t}_{j-1}^{i} \right\rangle \right) \quad \left\langle \underline{\sigma}_{g,\alpha}^{T} \underline{T}_0^{iT} \underline{T}_0^{j-1} \underline{Q}_j \underline{T}_{j-1}^{i} \right\rangle \right\} \{v\} \tag{C.39}$$

where, as in Appendix B, $\underline{q}_j$ and $\underline{Q}_j$ select the revolute or prismatic forms of the differentiation matrix depending on the joint type selected by j. Applying the T–matrix transpose property to the product $\underline{T}_0^{iT} \underline{T}_0^{j-1}$ yields:

$$\text{Form 2:}\quad \sum_{j=1}^{i} \left\{ \left(\left\langle \underline{\sigma}_{g,\alpha}^{T} \underline{T}_{j-1}^{iT} \right\rangle \left\{ \underline{q}_j + \underline{Q}_j \underline{t}_{j-1}^{i} \right\rangle \right) \quad \left\langle \underline{\sigma}_{g,\alpha}^{T} \underline{T}_{j-1}^{iT} \underline{Q}_j \underline{T}_{j-1}^{i} \right\rangle \right\} \{v\} \tag{C.40}$$

Exploit the sparse nature of the Q^{θ} and Q^{H} differentiation matrices. Referring to Equation B.14, substituting the appropriate 3x1 vectors and 3x3 matrices for $\underline{q}_j$ and $\underline{Q}_j$, produces:

$$\text{Form 2:}\quad \begin{cases} \displaystyle\sum_{j=1}^{i} \left\{ \left(\left\langle \underline{\sigma}_{g,a}^{T} \underline{T}_{j-1}^{iT} \right\rangle \left\{ \underline{q}^{H} \right\rangle \right) \quad [\underline{0}] \right\} v \quad [\text{joint j is prismatic}] \\ \displaystyle\sum_{j=1}^{i} \left\{ \left(\left\langle \underline{\sigma}_{g,\alpha}^{T} \underline{T}_{j-1}^{iT} \right\rangle \left\{ \underline{Q}_j^{\theta} \underline{t}_{j-1}^{i} \right\rangle \right) \quad \left\langle \underline{\sigma}_{g,\alpha}^{T} \underline{T}_{j-1}^{iT} \underline{Q}_j^{\theta} \underline{T}_{j-1}^{i} \right\rangle \right\} v \quad \left[\begin{matrix} \text{joint j is} \\ \text{revolute} \end{matrix} \right] \end{cases} \tag{C.41}$$

Define the T–matrix product T_{j-1}^{i} as:

$$\mathbf{T}^{i}_{j-1} \equiv \begin{bmatrix} 1 & 0 & 0 & 0 \\ m_{21} & m_{22} & m_{23} & m_{24} \\ m_{31} & m_{32} & m_{33} & m_{34} \\ m_{41} & m_{42} & m_{43} & m_{44} \end{bmatrix} \equiv \begin{bmatrix} 1 & \underline{0}^{T} \\ \underline{t}^{i}_{j-1} & \underline{\mathbf{T}}^{i}_{j-1} \end{bmatrix} \tag{C.42}$$

Evaluate Equation C.41 by substituting the definitions of $\mathbf{T}^{i}_{j-1}$, $\underline{\mathbf{q}}^{H}$, $\underline{\mathbf{q}}^{\theta}$, $\underline{\mathbf{Q}}^{H}$ and $\underline{\mathbf{Q}}^{\theta}$ from Equations C.42 and B.15, and expand v :

Form 2:

$$\begin{cases} \sum_{j=1}^{i} \left(\underline{\sigma}^{T}_{g,\alpha} \begin{Bmatrix} m_{42} \\ m_{43} \\ m_{44} \end{Bmatrix} \right) n & \cdots \text{ if joint j is prismatic} \\ \sum_{j=1}^{i} \left(\left(\underline{\sigma}^{T}_{g,\alpha} \begin{Bmatrix} m_{32}m_{21} - m_{22}m_{31} \\ m_{33}m_{21} - m_{23}m_{31} \\ m_{34}m_{21} - m_{24}m_{31} \end{Bmatrix} \right) n + \left(\underline{\sigma}^{T}_{g,\alpha} \begin{bmatrix} 0 & -(m_{33}m_{22} - m_{23}m_{32}) & -(m_{34}m_{22} - m_{24}m_{32}) \\ m_{33}m_{22} - m_{23}m_{32} & 0 & -(m_{34}m_{23} - m_{24}m_{33}) \\ m_{34}m_{22} - m_{24}m_{32} & m_{34}m_{23} - m_{24}m_{33} & 0 \end{bmatrix} \right) \underline{v} \right) & \cdots \text{ if joint j is revolute} \end{cases} \tag{C.43}$$

Note that the vector $\underline{\sigma}^{T}_{g,\alpha}$ acts to select the first, second or third row of the matrix or vector that follows it, according to whether α selects an x, y or z-direction degree of freedom.

A similar, though more lengthy, process can be applied to Form 3. The steps will not be shown here. Form 3 requires additional T-matrix notations, because of the addition of a summation over k. They are:

$$\mathbf{T}^{i}_{k-1} \equiv \begin{bmatrix} 1 & 0 & 0 & 0 \\ l_{21} & l_{22} & l_{23} & l_{24} \\ l_{31} & l_{32} & l_{33} & l_{34} \\ l_{41} & l_{42} & l_{43} & l_{44} \end{bmatrix} \tag{C.44}$$

$$\mathbf{T}^{j-1}_{k-1} \equiv \begin{bmatrix} 1 & 0 & 0 & 0 \\ P_{21} & P_{22} & P_{23} & P_{24} \\ P_{31} & P_{32} & P_{33} & P_{34} \\ P_{41} & P_{42} & P_{43} & P_{44} \end{bmatrix} \tag{C.45}$$

Since $\mathbf{U}_{i,j,k} = \mathbf{U}_{i,k,j}$, the double summation in Form 3 can be evaluated as follows:

$$\text{Form 3:} \quad \sum_{k=1}^{i} \sum_{j=1}^{i} \sigma_{g,\alpha}^{T} \, \mathbf{T}_0^{i\,T} \, \mathbf{U}_{i,j,k} \, \mathbf{w} = \sum_{j=1}^{i} \sum_{k=1}^{j} f_{jk} \, \sigma_{g,\alpha}^{T} \, \mathbf{T}_0^{i\,T} \, \mathbf{U}_{i,j,k} \, \mathbf{w} \tag{C.46}$$

where $f_{jk} = \begin{cases} 2 \text{ if } j \neq k \\ 1 \text{ if } j = k \end{cases}$. Note also that a T-matrix with identical arguments, e.g. $\mathbf{T}_j^j$, is a 4x4 identity matrix.

D. Results

The objective of all these manipulations was to represent the coefficients in Equations C.26, C.27 and C.28 directly in terms of element of the T-matrices. These elements are defined for convenience in Equations C.42, C.44 and C.45. The results follow. In Equations C.47 to C.52, the subscrips γ and δ indicate the row and column of a matrix, or the row of a vector. Both γ and δ are functions with value ranging from 1 to 3, depending on α and β. The function to determine γ from α is $\gamma = \text{mod}((\alpha\text{-}1),6) + 1$, where mod() indicates the modulo, or remainder, function. Values of γ equal to 0, 4 or 5 have no meaning and are disregarded. The column selector, δ, is determined from the same formula: $\delta = \text{mod}((\beta\text{-}1),6) + 1$.

$$G_{i,\alpha\beta}^{dyn} = 2 \, M_{i,g} \sum_{j=1}^{i} \begin{pmatrix} 0 & \cdots \text{ if joint j is prismatic} \\ \dot{\theta}_j \left[\mathbf{T}_{j-1}^{i\,T} \, \underline{\mathbf{Q}}^{\theta} \, \mathbf{T}_{j-1}^{i} \right]_{\gamma,\delta} & \cdots \text{ if joint j is revolute} \end{pmatrix} \tag{C.47}$$

$K_{i,\alpha\beta}^{dyn} = K_{i,\alpha\beta} + K_{2,i,\alpha\beta} + K_{3,i,\alpha\beta}$, where $K_{i,\alpha\beta}$ is an element of the FE stiffness matrix, and:

$$K_{2,i,\alpha\beta} = M_{i,g} \sum_{j=1}^{i} \begin{pmatrix} 0 & \text{. . . if joint j is prismatic} \\ \ddot{\theta}_j \left[\underline{T}_{j-1}^{i\,T} \underline{Q}^{\theta} \underline{T}_{j-1}^{i} \right]_{\gamma,\delta} & \text{. . . if joint j is revolute} \end{pmatrix} \quad \text{(C.48)}$$

$$K_{3,i,\alpha\beta} = M_{i,g} \sum_{j=1}^{i} \sum_{k=1}^{j} \begin{pmatrix} 0 & \text{. . . if joint j or k is prismatic} \\ f_{jk} \dot{\theta}_j \dot{\theta}_k \left[\underline{T}_{k-1}^{i\,T} \underline{Q}^{\theta} \underline{T}_{k-1}^{j-1} \underline{Q}^{\theta} \underline{T}_{j-1}^{i} \right]_{\gamma,\delta} & \text{. . . if both joint j and joint k are revolute} \end{pmatrix} \quad \text{(C.49)}$$

$f_{i,\alpha} = f_{e,i,\alpha} + f_{g,i,\alpha} + f_{2,i,\alpha} + f_{3,i,\alpha}$, where $f_{e,i,\alpha}$ is an externally applied force, and:

$$f_{g,i,\alpha} = M_{i,g} \left\{ \underline{T}_0^{i\,T} \right\}_{\gamma} \mathbf{g} \quad \text{(C.50)}$$

$$f_{2,i,\alpha} = M_{i,g} \sum_{j=1}^{i} \begin{pmatrix} \ddot{\theta}_j \left\{ \underline{T}_{j-1}^{i\,T} \underline{q}^{H} \right\}_{\gamma} & \text{. . . if joint j is prismatic} \\ \ddot{\theta}_j \left(\left\{ \underline{T}_{j-1}^{i\,T} \underline{Q}^{\theta} \underline{t}_{j-1}^{i} \right\}_{\gamma} + \left[\underline{T}_{j-1}^{i\,T} \underline{Q}^{\theta} \underline{T}_{j-1}^{i} \right]_{\gamma} \underline{b}_{i,g} \right) & \text{. . . if joint j is revolute} \end{pmatrix} \quad \text{(C.51)}$$

$$f_{3,i,\alpha} = M_{i,g} \sum_{j=1}^{i} \sum_{k=1}^{j} \begin{pmatrix} 0 & \text{. . . if joint k is prismatic} \\ f_{jk} \dot{\theta}_j \dot{\theta}_k \left\{ \underline{T}_{k-1}^{i\,T} \underline{Q}^{\theta} \underline{T}_{k-1}^{j-1} \underline{q}^{H} \right\}_{\gamma} & \text{. . . if joint k is revolute and joint j is prismatic} \\ f_{jk} \dot{\theta}_j \dot{\theta}_k \left(\left\{ \underline{T}_{k-1}^{i\,T} \underline{Q}^{\theta} \underline{T}_{k-1}^{j-1} \underline{Q}^{\theta} \underline{t}_{j-1}^{i} \right\}_{\gamma} + \left[\underline{T}_{k-1}^{i\,T} \underline{Q}^{\theta} \underline{T}_{k-1}^{j-1} \underline{Q}^{\theta} \underline{T}_{j-1}^{i} \right]_{\gamma} \underline{b}_{i,g} \right) & \text{. . . if joint j and k are revolute} \end{pmatrix} \quad \text{(C.52)}$$

The $\mathbf{T}^T$ - $\mathbf{Q}$ - $\mathbf{T}$ products in Equations C.47 to C.52 are then expanded in terms of the pre-computed $\mathbf{T}$ matrices, using the definitions of Equations C.42, C.44 and C.45.

$$\underline{T}^{i\,T}_{j-1}\,\underline{Q}^{\theta}\,\underline{T}^{i}_{j-1} = \begin{bmatrix} 0 & -(m_{33}m_{22} - m_{23}m_{32}) & -(m_{34}m_{22} - m_{24}m_{32}) \\ m_{33}m_{22} - m_{23}m_{32} & 0 & -(m_{34}m_{23} - m_{24}m_{33}) \\ m_{34}m_{22} - m_{24}m_{32} & m_{34}m_{23} - m_{24}m_{33} & 0 \end{bmatrix} \quad \text{(C.53)}$$

$$\underline{T}^{i\,T}_{k-1}\,\underline{Q}^{\theta}\,\underline{T}^{j-1}_{k-1}\,\underline{Q}^{\theta}\,\underline{T}^{i}_{j-1} = \begin{bmatrix} \begin{Bmatrix} (l_{22}p_{32} - l_{32}p_{22})\,m_{32} + (l_{32}p_{23} - l_{22}p_{33})\,m_{22} \\ (l_{23}p_{32} - l_{33}p_{22})\,m_{32} + (l_{33}p_{23} - l_{23}p_{33})\,m_{22} \\ (l_{24}p_{32} - l_{34}p_{22})\,m_{32} + (l_{34}p_{23} - l_{24}p_{33})\,m_{22} \end{Bmatrix} \\ \begin{Bmatrix} (l_{22}p_{32} - l_{32}p_{22})\,m_{33} + (l_{32}p_{23} - l_{22}p_{33})\,m_{23} \\ (l_{23}p_{32} - l_{33}p_{22})\,m_{33} + (l_{33}p_{23} - l_{23}p_{33})\,m_{23} \\ (l_{24}p_{32} - l_{34}p_{22})\,m_{33} + (l_{34}p_{23} - l_{24}p_{33})\,m_{23} \end{Bmatrix} \\ \begin{Bmatrix} (l_{22}p_{32} - l_{32}p_{22})\,m_{34} + (l_{32}p_{23} - l_{22}p_{33})\,m_{24} \\ (l_{23}p_{32} - l_{33}p_{22})\,m_{34} + (l_{33}p_{23} - l_{23}p_{33})\,m_{24} \\ (l_{24}p_{32} - l_{34}p_{22})\,m_{34} + (l_{34}p_{23} - l_{24}p_{33})\,m_{24} \end{Bmatrix} \end{bmatrix} \quad \text{(C.54)}$$

$$\underline{T}^{i\,T}_{j-1}\,\underline{q}^{H} = \begin{Bmatrix} m_{42} \\ m_{43} \\ m_{44} \end{Bmatrix} \quad \text{(C.55)}$$

$$\underline{T}^{i\,T}_{j-1}\,\underline{Q}^{\theta}\,\underline{t}^{i}_{j-1} = \begin{Bmatrix} m_{32}m_{21} - m_{22}m_{31} \\ m_{33}m_{21} - m_{23}m_{31} \\ m_{34}m_{21} - m_{24}m_{31} \end{Bmatrix} \quad \text{(C.56)}$$

$$\underline{T}^{i\,T}_{k-1}\,\underline{Q}^{\theta}\,\underline{T}^{j-1}_{k-1}\,\underline{q}^{H} = \begin{Bmatrix} l_{32}p_{24} - l_{22}p_{34} \\ l_{33}p_{24} - l_{23}p_{34} \\ l_{34}p_{24} - l_{24}p_{34} \end{Bmatrix} \quad \text{(C.57)}$$

$$\underline{T}^{i\,T}_{k-1}\,\underline{Q}^{\theta}\,\underline{T}^{j-1}_{k-1}\,\underline{Q}^{\theta}\,\underline{t}^{i}_{j-1} = \begin{Bmatrix} (l_{22}p_{32} - l_{32}p_{22})\,m_{31} + (l_{32}p_{23} - l_{22}p_{33})\,m_{21} \\ (l_{23}p_{32} - l_{33}p_{22})\,m_{31} + (l_{33}p_{23} - l_{23}p_{33})\,m_{21} \\ (l_{24}p_{32} - l_{34}p_{22})\,m_{31} + (l_{34}p_{23} - l_{24}p_{33})\,m_{21} \end{Bmatrix} \quad \text{(C.58)}$$

E. Summary

Using Equations C.47 to C.58, all elements of the coefficient matrices in the link equations of motion, Equation C.24, can be determined from the time-varying nominal path data and the time-invariant link FE data. Equations C.53 to C.58 represent matrix products and T-matrix derivatives, symbolically

expanded in terms of the elements of the T-matrices T^i_j, j = 0 ... i. The symbolic expansion means that the work of calculating the T-matrix derivatives explicitly, according to Equations B.18 and B.19, does not need to be done.

Appendix D – Component Mode Synthesis, Ideal Joint Compatibility, and Global System Equations

A. Component Mode Synthesis

Component Mode Synthesis (CMS) is a technique that can reduce the size of a set of dynamic equations without serious loss of accuracy, when the input forces to the dynamic system have limited frequency bandwidth, by changing to a more efficient description of the motions of the system using a new set of generalized coordinates [54]. Since the new generalized coordinates usually describe a deformation of the structure rather than linear or angular motions at discrete node points, they are called "distributed coordinates." These distributed coordinates are a mapping of the displacement coordinates of the original equation of motion from a Cartesian coordinate space into a new coordinate space. The basis set of the new coordinate space is the eigenvectors of the link's finite element mass and stiffness matrices, as shown below.

Typically, a machine system link can be treated as a massy, elastic structure without damping, described after finite element meshing by a set of coupled equations of the form:

$$\mathbf{M}_i \ddot{\mathbf{p}}_i + \mathbf{K}_i \mathbf{p}_i = \mathbf{f}_i \tag{D.1}$$

In Equation D.1, $\mathbf{M}_i$ and $\mathbf{K}_i$ are square matrices of dimension $NDOF_i$. $NDOF_i$ is the number of generalized coordinates required to write the equations of motion. For a spatial analysis, $NDOF_i$ is 6 times the number of finite element nodes, excluding nodes that are fixed by the boundary conditions. Thus, the degree of the equations of motion can be extremely large if a dense finite element mesh is required for modeling accuracy.

The node points can be classified as "interface" and "internal" nodes, leading to a partitioned of Equation D.1 into "interface" and "free" sets. Interface nodes are defined as those nodes at which external forces may be applied; internal nodes are all the other nodes of the finite element model. The partitioned equations appear as follows:

$$\begin{bmatrix} \mathbf{M}_i^{II} & \mathbf{0} \\ \mathbf{0} & \mathbf{M}_i^{FF} \end{bmatrix} \begin{bmatrix} \ddot{\mathbf{p}}_i^{I} \\ \ddot{\mathbf{p}}_i^{F} \end{bmatrix} + \begin{bmatrix} \mathbf{K}_i^{II} & \mathbf{K}_i^{IF} \\ \mathbf{K}_i^{FI} & \mathbf{K}_i^{FF} \end{bmatrix} \begin{bmatrix} \mathbf{p}_i^{I} \\ \mathbf{p}_i^{F} \end{bmatrix} = \begin{bmatrix} \mathbf{f}_i^{I} \\ \mathbf{0} \end{bmatrix} \tag{D.2}$$

In Equation D.2, the superscript I refers to the interface partition of the link equations of motion, and the superscript F refers to the internal partition. Note that a **0** vector appears where $\mathbf{f}_i^F$ would be expected in Equation D.2. This emphasizes that the forces applied to the internal partition are, by definition, zero. External forces may be applied to the link only at the interface node points.

CMS can be applied to a finite element structural dynamic equation such as Equation D.2 by defining a CMS transformation matrix for each link, $\mathbf{A}_i$:

$$\mathbf{A}_i = \begin{bmatrix} 1 & 0 \\ -\mathbf{K}_i^{FF-1}\mathbf{K}_i^{FI} & \Phi_i \end{bmatrix} \tag{D.3}$$

In Equation D.3, the matrix Φ_i is the set of eigenvectors that solve the eigenvector problem that will be set up in Equation D.10. The link perturbation vector, $\mathbf{p}_i$, is defined in terms of mixed interface and distributed coordinates in vector $\mathbf{a}_i$:

$$\mathbf{p}_i = \mathbf{A}_i \mathbf{a}_i \tag{D.4}$$

$$\mathbf{a}_i = \begin{Bmatrix} \mathbf{p}_i^{I} \\ \eta_i \end{Bmatrix} \tag{D.5}$$

In Equation D.5, the subvector $\mathbf{p}_i^I$ is the interface portion of the $\mathbf{p}_i$ vector in Equation D.1, and the η_i subvector is the amplitudes of the mode shapes,

given by Φ_i. Substituting Equation D.4 into Equation D.1 and multiplying the result by $\mathbf{A}_i^T$ gives:

$$\overline{\mathbf{M}}_i \ddot{\mathbf{a}}_i + \overline{\mathbf{K}}_i \mathbf{a}_i = \overline{\mathbf{f}}_i \tag{D.6}$$

where

$$\overline{\mathbf{M}}_i = \mathbf{A}_i^T \mathbf{M}_i \mathbf{A}_i \tag{D.7}$$

$$\overline{\mathbf{K}}_i = \mathbf{A}_i^T \mathbf{K}_i \mathbf{A}_i \tag{D.8}$$

$$\overline{\mathbf{f}}_i = \mathbf{A}_i^T \mathbf{f}_i \tag{D.9}$$

The matrices $\overline{\mathbf{M}}_i$ and $\overline{\mathbf{K}}_i$ and the vector $\overline{\mathbf{f}}_i$ in these equations are the CMS-transformed mass and stiffness matrices and force vector. Since $\mathbf{A}_i$ contains only constants, its time derivatives are zero.

The basis set for the distributed coordinates is taken to be the eigenvectors of the FF submatrices of Equation D.2, i.e. Φ_i in Equation D.3 is defined as the solution of

$$\Phi_i^T \mathbf{M}_i^{FF} \Phi_i = \Omega_i^2 \Phi_i^T \mathbf{K}_i^{FF} \Phi_i \tag{D.10}$$

where Ω_i^2 is the diagonal matrix of the squares of the eigenvalues. Note that the internal matrices $\mathbf{M}_i^{FF}$ and $\mathbf{K}_i^{FF}$ are submatrices of the complete mass and stiffness matrices. They may be derived from the complete matrices by setting the interface degrees of freedom, $\mathbf{p}_i^I$, to zero. Thus the mode shapes defined by D.10 have zero motions at the interface node points.

So far, Equation D.6 is of the same order as the original equations of motion, Equation D.1, and is in fact dynamically identical. Modal truncation to reduce the order of the system is performed by using a truncated eigenvector matrix Φ' in Equation D.3 instead of the full set of eigenvectors. The decision as to which eigenvectors to retain in Φ' and which to eliminate is made on the basis of the natural frequencies corresponding to each eigenvector.

Eigenvectors whose natural frequencies are well above the expected bandwidth of the exciting forces are not kept. This procedure allows a reduction in the order of the dynamic equations after modal truncation, Equation D.6, while maintaining reasonable accuracy.

B. Ideal Joint Compatibility

Joint compatibility is the information that allows individual link dynamic equations to be coupled to form an equation of motion for an entire machine system. The compatibility conditions are enforced by the $\mathbf{B}_i$ matrices. By definition in this thesis, the term "ideal joint" means a joint modeled without compliance or clearance, and the term "clearance joint" means a joint model that can have both internal clearance and compliance. An ideal joint always adds at least one kinematic constraint to a system. The construction of **B** matrices for ideal joints will now be explained by example.

The compatibility matrix $\mathbf{B}_i$ for each link is defined such that the relationship:

$$\mathbf{a}_i = \mathbf{B}_i \mathbf{q} \tag{D.11}$$

holds between the reduced coordinates of each link, the $\mathbf{a}_i$ vector, and the vector of the system's generalized independent coordinates, $\mathbf{q}$.

Assume that two links, link i and link i+1, as shown in Figure D.1a, are to be joined by an ideal connection. Link i has perturbation coordinates $p_{i,x}$, $p_{i,y}$, and $p_{i,\theta}$ associated with an interface node point. Recall from Equation D.5 that the interface perturbation coordinates remain in the $\mathbf{a}_i$ coordinate vector after CMS; interface coordinates are not replaced with distributed coordinates. Link i+1 has

$p_{i+1,x}$, $p_{i+1,y}$, and $p_{i+1,\theta}$ associated with an interface node point. When these two interface node points are joined together by an ideal non clearance joint, some of the six perturbation coordinates $p_{i,x}$, $p_{i,y}$, $p_{i,\theta}$, $p_{i+1,x}$, $p_{i+1,y}$, and $p_{i+1,\theta}$ will no longer be independent. Which coordinates are constrained depends on the type of the joint. If the joint is, say, an ideal revolute joint, as shown in Figure D.1b, an angle β can be defined between x_i and x_{i+1}, and the following constraint relationship holds:

$$\begin{Bmatrix} p_{i,x} \\ p_{i,y} \end{Bmatrix} = \begin{bmatrix} \cos\beta & \sin\beta \\ -\sin\beta & \cos\beta \end{bmatrix} \begin{Bmatrix} p_{i+1,x} \\ p_{i+1,y} \end{Bmatrix} \tag{D.12}$$

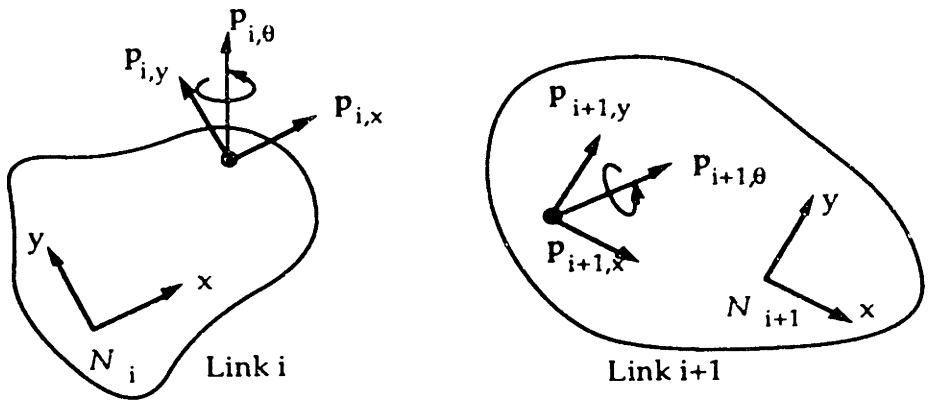

Figure D.1a. Reference frames, interface nodes and interface perturbations

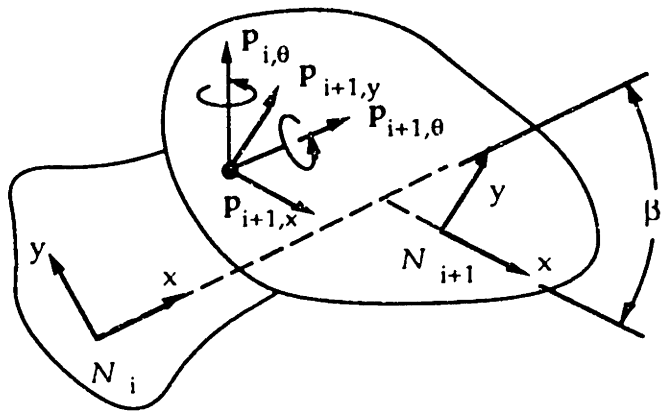

Figure D.1b. Links Joined by a Revolute Joint

The angular perturbations $p_{i,\theta}$ and $p_{i+1,\theta}$ remain independent because they are not constrained by the joint. To construct the $\mathbf{B}_i$ and $\mathbf{B}_{i+1}$ matrices, first choose either $p_{i,x}$ and $p_{i,y}$ or $p_{i+1,x}$, $p_{i+1,y}$ to appear as the independent coordinates in the $\mathbf{q}$ vector; the choice is arbitrary. For example, say that $p_{i+1,x}$, $p_{i+1,y}$ are chosen to be the independent coordinates. Then the portion of the $\mathbf{q}$ vector associated with these two interface points would be $\mathbf{q} = \{ p_{i+1,x} \;\; p_{i+1,y} \;\; p_{i,\theta} \;\; p_{i+1,\theta} \}^T$, and the two $\mathbf{B}$ matrices would be:

$$\mathbf{B}_i = \begin{bmatrix} \cos\beta & \sin\beta & 0 & 0 \\ -\sin\beta & \cos\beta & 0 & 0 \\ 0 & 0 & 1 & 0 \end{bmatrix}$$

$$\mathbf{B}_{i+1} = \begin{bmatrix} 1 & 1 & 0 & 0 \\ 1 & 1 & 0 & 0 \\ 0 & 0 & 0 & 1 \end{bmatrix} \qquad \text{(D.13)}$$

It is easy to verify that $\mathbf{a}_i = \{p_{i,x} \;\; p_{i,y} \;\; p_{i,\theta} \}^T = \mathbf{B}_i \, \mathbf{q}$, and that $\mathbf{a}_{i+1} = \{p_{i+1,x} \;\; p_{i+1,y} \;\; p_{i+1,\theta} \}^T = \mathbf{B}_{i+1} \, \mathbf{q}$. It should also be clear that this principle can be extended to other types of ideal joints that constrain different perturbation motions; for instance, a sliding joint would constrain the rotation perturbations and remove one independent degree of freedom from the translation perturbations. The principle can also be extended to reduced perturbation coordinate vectors $\mathbf{a}$ of arbitrary length, and to spatial systems, where there are six perturbation coordinates associated with each node point. Although internal forces do exist between the links, the ideal joint permits no relative displacements parallel to the lines of action of these internal forces. Therefore they can be shown to do zero work and they do not affect the link dynamic equations.

C. Global System Equations

Many steps are necessary to derive the equations of motion for an entire machine system, but in Appendix C and the preceding sections of Appendix D

they have all been introduced. This final section gives the big picture overview, showing how all of these steps are used to write a global equation of motion for the entire machine system.

Equation C.24 is the dynamic equation of motion for a finite element model of a machine system component in an accelerated reference frame, derived using the Lagrangian formulation of equations of motion. The difference between Equations C.24 and D.1 is that D.1 is valid only in a non accelerated reference frame, while C.24 includes the modifications required for an accelerated reference frame whose motion is described by the Hartenberg-Denavit variables of vector θ and its derivatives, with the specific link geometry expressed by the Hartenberg-Denavit T matrices explained in Appendix B.

After CMS has been performed for each link and the time varying dynamic matrices $\mathbf{M}_i^{dyn}$, $\mathbf{G}_i^{dyn}$ and $\mathbf{K}_i^{dyn}$ have been computed for each link as described in Appendix C, the dynamic matrices can be reduced using the CMS transformation defined in Equation D.4. Thus a reduced equation of motion for each link is produced:

$$\overline{\mathbf{M}}_i^{dyn}\,\ddot{\mathbf{a}}_i + \overline{\mathbf{G}}_i^{dyn}\,\mathbf{a} + \overline{\mathbf{K}}_i^{dyn}\,\mathbf{a}_i = \overline{\mathbf{f}}_i^{dyn} \tag{D.14}$$

where:

$$\overline{\mathbf{M}}_i^{dyn} = \mathbf{A}_i^T\,\mathbf{M}_i^{dyn}\,\mathbf{A}_i \tag{D.15}$$

$$\overline{\mathbf{G}}_i^{dyn} = \mathbf{A}_i^T\,\mathbf{G}_i^{dyn}\,\mathbf{A}_i + \mathbf{G}_i^{damp} \tag{D.16}$$

$$\overline{\mathbf{K}}_i^{dyn} = \mathbf{A}_i^T\,\mathbf{K}_i^{dyn}\,\mathbf{A}_i \tag{D.17}$$

$$\overline{\mathbf{f}}_i^{dyn} = \mathbf{A}_i^T\,\mathbf{f}_i \tag{D.18}$$

and the individual elements of the matrices $\mathbf{M}_i^{dyn}$, $\mathbf{G}_i^{dyn}$, $\mathbf{K}_i^{dyn}$ and $\overline{\mathbf{f}}_i^{dyn}$ are defined in Appendix C, Equations C.25 to C.28. In practice, the ASSET

software achieves an improvement in performance by splitting these calculations into time varying and time invariant portions, and performing the time invariant portions only once, before the beginning of the simulation. Equations D.15-D.18 define the CMS–reduced matrices in the equations of motion using the accelerated reference frame dynamics discussed in Appendix C. The accelerated dynamics are responsible for the introduction of Equation D.16, which has no parallel in the non accelerated reference frame. A viscous damping matrix is usually added to the system of equations to encourage numerical stability and to model natural dissipative phenomena. There are many methods for calculating such a matrix, but often the resu'· is small terms added to the diagonal elements of each link's $\overline{G}_i^{dyn}$ matrix, indicated by the term G_i^{damp} in Equation D.16.

Finally, the compatibility matrices and Equation D.11 are invoked to combine all of the Equations D.14, for i = 1 to NL, where NL is the number of links in the system, into a single system equation. Substituting D.11 and its derivatives into D.14 yields:

$$\mathbf{M}\,\ddot{\mathbf{q}} + \mathbf{G}\,\dot{\mathbf{q}} + \mathbf{K}\,\mathbf{q} = \mathbf{w} \tag{D.19}$$

where

$$\mathbf{M} = \sum_{i=1}^{NL} \mathbf{B}_i^T\, \overline{\mathbf{M}}_i^{dyn}\, \mathbf{B}_i \tag{D.20}$$

$$\mathbf{G} = \sum_{i=1}^{NL} \mathbf{B}_i^T \left(2\, \overline{\mathbf{M}}_i^{dyn}\, \dot{\mathbf{B}}_i + \overline{\mathbf{G}}_i^{dyn}\, \mathbf{B}_i\right) \tag{D.21}$$

$$\mathbf{K} = \sum_{i=1}^{NL} \mathbf{B}_i^T \left(\overline{\mathbf{M}}_i^{dyn}\, \ddot{\mathbf{B}}_i + \overline{\mathbf{G}}_i^{dyn}\, \dot{\mathbf{B}}_i + \overline{\mathbf{K}}_i^{dyn}\, \mathbf{B}_i\right) \tag{D.22}$$

$$\mathbf{w} = \sum_{i=1}^{NL} \mathbf{B}_i^T\, \mathbf{f}_i^{dyn} \tag{D.23}$$

and $\dot{\mathbf{B}}_i$, $\ddot{\mathbf{B}}_i$ denote the time derivatives of the compatibility matrices, defined by:

$$\dot{\mathbf{B}}_i = \sum_{j=1}^{i} \mathbf{B}_{ij} \frac{d\theta_j}{dt} \tag{D.24}$$

$$\ddot{\mathbf{B}}_i = 2 \sum_{j=1}^{i} \sum_{k=1}^{j-1} \mathbf{B}_{ijk} \frac{d\theta_j}{dt} \frac{d\theta_k}{dt} + \sum_{j=1}^{i} \left[\mathbf{B}_{ij} \frac{d^2\theta_j}{dt^2} + \mathbf{B}_{ijj} \left(\frac{d\theta_j}{dt} \right)^2 \right] \tag{D.25}$$

$$\mathbf{B}_{ij} = \frac{\partial \mathbf{B}_i}{\partial \theta_j} \tag{D.26}$$

$$\mathbf{B}_{ijk} = \frac{\partial^2 \mathbf{B}_i}{\partial \theta_j \partial \theta_k} \tag{D.27}$$

These equations comprise the global equation of motion for the entire machine system. Although the derivation in Appendices A-D has been directed toward machine systems with ideal non clearance joints, the same form of equations applies to systems with non ideal joints. The only difference between the ideal joint and non ideal joint cases is the definition of the compatibility matrices $\mathbf{B}_i$, due to the differing compatibility requirements.

Appendix E. Nominal Motion Equations for the Spatial Slider Crank

For brevity, a notation is used in this chapter in which, for instance, S_3 stands for $\sin(\theta_3)$, C_5 stands for $\cos(\theta_5)$, T_5 for $\tan(\theta_5)$, etc. Also, S_γ, C_γ and T_γ stand for the sin, cosine and tangent of γ, the motor angle defined in Figure 5.7. L_2, H_5 and H_6 are defined in the tabel of H-D parameters, Table 5.2. D_h, D_s and D_v are geometric constants in the experimental setup, see Figure 5.7. Other terms used do not always have simple physical interpretations but are used to permit compact expressions. The form "$\arctan\left(\frac{a}{b}\right)$" indicates that a four-quadrant arctangent function is required.

Definition of θ_2, motor angle and input variable:

$\theta_2 = \text{mod}(\Omega t, 2\pi)$ (mod() is the modulo function)

Position of the ball joint in the N_1 reference frame:

$x2 = L_2C_2$
$y2 = L_2S_2$
$z2 = 0$

Position of the slider shell in the N_1 reference frame, x_6, y_6, z_6:

$$L_v = \sqrt{H_5^2+H_6^2}$$

$y_6 = D_s - D_v$ (note that y_6 is constant)

$$a_l = \frac{T_\gamma D_h}{C_\gamma} - x_2$$

$$a_r = L_v^2 - y_6^2 - \left(\frac{D_h}{C_\gamma}\right)^2 - L_2^2 + 2y_6y_2$$

$$a_d = \sqrt{a_l^2+\frac{a_r}{C_\gamma^2}}$$

$$x_6 = C_\gamma^2(a_d - a_l)$$

$$z_6 = T_\gamma x_6 + \frac{D_h}{C_\gamma}$$

A vector pointing from N_6 to N_2 has components:

$$d_x = x_2 - x_6$$
$$d_y = y_2 - y_6$$
$$d_z = -z_6$$
$$r_{proj} = \sqrt{(d_x C_\gamma + d_z S_\gamma)^2 + d_y^2}$$

Definition of θ_7:

$$C_r = \frac{H_6}{r_{proj}}$$
$$S_a = \frac{d_y}{r_{proj}}$$
$$\theta_7 = \arccos(C_r) + \arcsin(S_a)$$

Definition of θ_4: $(0° \le \theta_4 \le 180°)$

$$C_4 = -\frac{(H_6 S_\gamma C_7 + d_z)}{H_5}$$
$$S_4 = \sqrt{1-C_4^2}$$
$$\theta_4 = \arctan\left(\frac{S_4}{C_4}\right)$$

Definition of θ_3:

$$r_a = H_6 C_7 C_\gamma + d_x$$
$$r_b = H_6 S_7 - d_y$$
$$C_3 = \frac{(-S_2 r_b + C_2 r_a)}{H_5 S_4}$$
$$S_3 = -\frac{(C_2 r_b + S_2 r_a)}{H_5 S_4}$$
$$\theta_3 = \arctan\left(\frac{S_3}{C_3}\right)$$

Definition of θ_5:

$$S_{23} = \sin(\theta_2+\theta_3)$$
$$C_{23} = \cos(\theta_2+\theta_3)$$
$$T_5 = \frac{T_\gamma S_{23}}{S_4 - T_\gamma C_4 C_{23}}$$
$$\left.\begin{aligned} C_5 &= \pm\sqrt{\frac{1}{1+T_5^2}} \\ S_5 &= C_5 T_5 \end{aligned}\right\}, \text{ choose sign of } C_5 \text{ such that } (C_4 S_5 S_{23} - C_5 C_{23}) > 0$$

$$\theta_5 = \arctan\left(\frac{S_5}{C_5}\right)$$

Definition of θ_6:

$$den_6 = C_4S_5S_{23} - C_5C_{23}$$

$$S_6 = \frac{-S_\gamma C_4 + C_\gamma S_4 C_{23}}{den_6}$$

$$C_6 = \frac{-S_\gamma S_4 C_5 + C_\gamma(-C_4C_5C_{23} + S_5S_{23})}{den_6}$$

$$\theta_6 = \arctan\left(\frac{S_6}{C_6}\right)$$

The simulation also requires the first and second time derivatives of θ_2–θ_7. The derivation of these from the above formulas is straightforward but lengthy and will not be repeated here. It may be noted that when the motor angle γ is zero, θ_4, θ_5 and θ_6 are constant and their derivatives are zero. This is difficult to show from the definitions above but is evident after considering the geometry of the SSC. It can also be demonstrated numerically by computing the above definitions for a variety of input angles θ_2.

Appendix F. Details of the ASSET models for the IBS and SSC

This appendix gives information about the numerical models of the IBS and SSC, in more detail than the discussions in the body of the thesis. As shown in Figure 3.1, the ASSET system uses a preprocessor program, which is called PHI3, to assemble together the finite element data from each link and perform CMS. PHI3 relies on the ADINA finite element program to generate FE mass and stiffness matrices, and a corresponding vector of eigenvalues and matrix of eigenvectors, for each link. PHI3 reads these ADINA output files, and, with additional input from the user, performs CMS, constructs the A_i matrix for each link, Equation 3.2, and computes the time-invariant portions of the $\overline{M}^i_{dyn}$ and $\overline{K}^i_{dyn}$ matrices, Equations D.15 and D.17.

A. The IBS Numerical Models

A.1. Finite element models of the IBS

Three numerical models for the distributed mass and stiffness of the IBS were developed. Refer to Figure 4.2 for identification of the part names used in this discussion.

The first model, the "rigid base model," suggested by Figure 4.6, assumes complete rigidity of the baseplate, force sensors and beam support post. The steel or aluminum beam is the only item with distributed mass and flexibility in the rigid base model, represented with a finite element (FE) model. The mass and suspension of the shaker's voice coil, and the mass of the connecting rod, are modeled by a lumped mass and external linear stiffness added at one FE node point on the beam. The compliance of the connecting rod is not included in this model. The clearance gap is modeled as a free-

flight, zero force zone when there is no contact between the beam and force sensor, and linearized Hertzian stiffness and damping when there is contact. As suggested by Figure 4.6, the contact stiffness and damping are modeled as being backed up by a rigid surface. Boundary conditions used in the rigid base model vary depending on whether the steel or aluminum beam is used, because of their different mounting arrangements. The aluminum beam is cantilevered from the support post. Therefore, the beam's FE node located at the support post is clamped, i.e. all six degrees of freedom at this node are set to zero. The steel beam is mounted using a flexure pivot, a small, thin strip of stainless steel. It is stiff except for vertical translations of the end of the beam, and beam rotation driven by the vertical motions of the shaker. Therefore, the boundary condition for the FE node at the supported end of the steel beam is fixed for four of the degrees of freedom, and compliant for the remaining two degrees of freedom. A high translational stiffness is used for the vertical direction and a very small rotational stiffness is used for the rotation driven by the shaker. The values used for these compliances come from analysis of the steel flexure pivot.

The second, the "flexible base model," suggested in Figure 4.7, includes FE representations of the beam support post, the baseplate, the yoke structure that holds the force sensors, the force sensors themselves, and the rod that connects the shaker and the beam. This model also includes lumped mass and external linear stiffness to model the shaker voice coil and suspension, added to a node at the end of the connecting rod. The clearance gap itself is modeled as in the rigid base model. However, in the flexible base model, contact forces are applied to node points at the ends of the force sensor FE models, and the motions of those node points are included in computations

of the clearance gap. Boundary conditions for the flexible base model are clamped for the FE nodes at the corners of the baseplate, and free for all other nodes on the edge of the baseplate. The flexure pivot is included as a beam element in the steel beam's flexible base FE model.

The third model, the "flexible base with cover model," is an adaptation of the flexible base model that includes a finite element model of the metal or fiberglass cover. Because of computer limitations encountered during the course of the research, the total number of finite element node points is approximately the same for the flexible base and flexible base with cover models. Therefore, the flexible base with cover model has a considerably coarser FE mesh than the flexible base model.

The flexible impact beam of the IBS is represented by a finite element model using two-node ADINA beam elements. Each node has six degrees of freedom. Section properties of the impact beams, and material properties for steel and aluminum, are listed in Table F.1. The simulations use the lbf-in-sec system of units, so consistent mass units are $\frac{\text{lbf}\cdot\text{sec}^2}{\text{in}}$. One $\frac{\text{lbf}\cdot\text{sec}^2}{\text{in}}$ is exactly equal to 12 slugs and approximately equal to 386 lbm or 175 kg.

Table F.1. Properties of the FE models of the IBS beams.

	Steel Beam	Aluminum Beam
cross section	0.75" x 0.25"	0.75" x 0.125"
area	0.188 in^2	9.38×10^{-2} in^2
moments of inertia: I_x	9.77×10^{-3} in^4	4.52×10^{-3} in^4
I_y	9.77×10^{-4} in^4	1.22×10^{-4} in^4
I_z	8.79×10^{-3} in^4	4.39×10^{-3} in^4
mass density	7.25×10^{-4} $\frac{\text{lbf}\cdot\text{sec}^2}{\text{in}^4}$	2.53×10^{-4} $\frac{\text{lbf}\cdot\text{sec}^2}{\text{in}^4}$

elastic modulus	$3.0 \times 10^7 \frac{\text{lbf}}{\text{in}^2}$	$1.06 \times 10^7 \frac{\text{lbf}}{\text{in}^2}$
Poisson's ratio	0.29	0.33

In all of the IBS numerical models, the x axis is parallel to the longest axis of the beam, the +z axis is vertically upward, and the y axis is crosswise to the long axis of the beam. In the rigid base model, the sense of +x is from the beam mount point toward the impact point and the coordinate origin is at the beam mount. In the flexible base and flexible base with covers models, the sense of +x is from the impact point toward the mount point and the coordinate origin is node 5, a corner of the baseplate.

In all the numerical models, the shaker's driving force is a calculated function of time applied at node 1. The shaker force calculation also accounts for the shaker's suspension spring, with a stiffness of 16.3 $\frac{\text{lbf}}{\text{in}}$. In the rigid base models, extra mass of $3.71 \times 10^{-4} \frac{\text{lbf} \cdot \text{sec}^2}{\text{in}^4}$ is applied at node 1 and included in the FE mass matrix to model the mass of the shaker's voice coil and the connecting rod. In the flexible base and flexible base with cover models, the connecting rod is part of the finite element model, and no extra mass needs to be included for it. The added mass of the shaker's voice coil is neglected in these models.

Impact forces are applied at node 2 in all models. In the rigid base models, the impact forces depend on the displacement and velocity of node 2. In the flexible base and flexible base with cover models, the impact forces depend on the relative displacements and velocities of nodes 2, 3 and 4. Node 3 in these models is the upper force transducer, and node 4 is the lower force transducer.

A.2. Rigid base models

The FE models of the steel and aluminum beam rigid base systems are alike in most respects. In either model, the endpoints of the beam are nodes 3 and 4. The interface nodes are nodes 1 and 2.

ADINA's 2-node, 6-degree-of-freedom-per-node beam elements are used in the aluminum and steel beam rigid base models to represent the impact beams. Each beam element requires two endpoint nodes and one auxiliary node. The auxiliary node has no effect on the dynamic properties of the element, but is needed to define the orientation of the local r-s-t coordinate frame associated with each element. For more details, refer to the ADINA documentation. There is one auxiliary node, node 5, in the steel and aluminum beam rigid base models.

The steel and aluminum beam models differ in a few details. The aluminum beam model has one more node and one additional beam element. The boundary conditions of the two models are different, corresponding to an idealized cantilever mount for the aluminum beam, and an idealized flexure pivot mount for the steel beam.

Table F.2 shows the coordinates of the node points used in the aluminum beam rigid base FE model.

Table F.2. Aluminum beam rigid base model.
FE node coordinates (inches).

NODE	X-coordinate	Y-coordinate	Z-coordinate
1	0.80000000E+01	0.00000000E+00	0.00000000E+00
2	0.10750000E+02	0.00000000E+00	0.00000000E+00
3	0.00000000E+00	0.00000000E+00	0.00000000E+00
4	0.11375000E+02	0.00000000E+00	0.00000000E+00

5	0.12000000E+02	0.00000000E+00	0.10000000E+01
6	0.30000000E+00	0.00000000E+00	0.00000000E+00
7	0.60000000E+00	0.00000000E+00	0.00000000E+00
8	0.90000000E+00	0.00000000E+00	0.00000000E+00
9	0.12000000E+01	0.00000000E+00	0.00000000E+00
10	0.15000000E+01	0.00000000E+00	0.00000000E+00
11	0.18000000E+01	0.00000000E+00	0.00000000E+00
12	0.21000000E+01	0.00000000E+00	0.00000000E+00
13	0.24000000E+01	0.00000000E+00	0.00000000E+00
14	0.27000000E+01	0.00000000E+00	0.00000000E+00
15	0.30000000E+01	0.00000000E+00	0.00000000E+00
16	0.33000000E+01	0.00000000E+00	0.00000000E+00
17	0.36000000E+01	0.00000000E+00	0.00000000E+00
18	0.39000000E+01	0.00000000E+00	0.00000000E+00
19	0.42000000E+01	0.00000000E+00	0.00000000E+00
20	0.45000000E+01	0.00000000E+00	0.00000000E+00
21	0.48000000E+01	0.00000000E+00	0.00000000E+00
22	0.51000000E+01	0.00000000E+00	0.00000000E+00
23	0.54000000E+01	0.00000000E+00	0.00000000E+00
24	0.57000000E+01	0.00000000E+00	0.00000000E+00
25	0.60000000E+01	0.00000000E+00	0.00000000E+00
26	0.63000000E+01	0.00000000E+00	0.00000000E+00
27	0.66000000E+01	0.00000000E+00	0.00000000E+00
28	0.69000000E+01	0.00000000E+00	0.00000000E+00
29	0.72000000E+01	0.00000000E+00	0.00000000E+00
30	0.75000000E+01	0.00000000E+00	0.00000000E+00
31	0.78000000E+01	0.00000000E+00	0.00000000E+00
32	0.84000000E+01	0.00000000E+00	0.00000000E+00
33	0.87000000E+01	0.00000000E+00	0.00000000E+00
34	0.90000000E+01	0.00000000E+00	0.00000000E+00
35	0.93000000E+01	0.00000000E+00	0.00000000E+00
36	0.96000000E+01	0.00000000E+00	0.00000000E+00
37	0.99000000E+01	0.00000000E+00	0.00000000E+00
38	0.10200000E+02	0.00000000E+00	0.00000000E+00
39	0.10500000E+02	0.00000000E+00	0.00000000E+00
40	0.11100000E+02	0.00000000E+00	0.00000000E+00
Boundary conditions, node 1: all DOF fixed			

Table F.3 shows the coordinates of the node points used in the steel beam rigid base FE model.

Table F.3. Steel beam rigid base model.
FE node coordinates (inches).

NODE	X-coordinate	Y-coordinate	Z-coordinate
1	0.80000000E+01	0.00000000E+00	0.00000000E+00
2	0.10750000E+02	0.00000000E+00	0.00000000E+00
3	0.15500000E+00	0.00000000E+00	0.00000000E+00
4	0.11155000E+02	0.00000000E+00	0.00000000E+00
5	0.12000000E+02	0.00000000E+00	0.10000000E+01
6	0.30000000E+00	0.00000000E+00	0.00000000E+00
7	0.60000000E+00	0.00000000E+00	0.00000000E+00
8	0.90000000E+00	0.00000000E+00	0.00000000E+00
9	0.12000000E+01	0.00000000E+00	0.00000000E+00
10	0.15000000E+01	0.00000000E+00	0.00000000E+00
11	0.18000000E+01	0.00000000E+00	0.00000000E+00
12	0.21000000E+01	0.00000000E+00	0.00000000E+00
13	0.24000000E+01	0.00000000E+00	0.00000000E+00
14	0.27000000E+01	0.00000000E+00	0.00000000E+00
15	0.30000000E+01	0.00000000E+00	0.00000000E+00
16	0.33000000E+01	0.00000000E+00	0.00000000E+00
17	0.36000000E+01	0.00000000E+00	0.00000000E+00
18	0.39000000E+01	0.00000000E+00	0.00000000E+00
19	0.42000000E+01	0.00000000E+00	0.00000000E+00
20	0.45000000E+01	0.00000000E+00	0.00000000E+00
21	0.48000000E+01	0.00000000E+00	0.00000000E+00
22	0.51000000E+01	0.00000000E+00	0.00000000E+00
23	0.54000000E+01	0.00000000E+00	0.00000000E+00
24	0.57000000E+01	0.00000000E+00	0.00000000E+00
25	0.60000000E+01	0.00000000E+00	0.00000000E+00
26	0.63000000E+01	0.00000000E+00	0.00000000E+00
27	0.66000000E+01	0.00000000E+00	0.00000000E+00
28	0.69000000E+01	0.00000000E+00	0.00000000E+00
29	0.72000000E+01	0.00000000E+00	0.00000000E+00
30	0.75000000E+01	0.00000000E+00	0.00000000E+00
31	0.78000000E+01	0.00000000E+00	0.00000000E+00

32	0.84000000E+01	0.00000000E+00	0.00000000E+00
33	0.87000000E+01	0.00000000E+00	0.00000000E+00
34	0.90000000E+01	0.00000000E+00	0.00000000E+00
35	0.93000000E+01	0.00000000E+00	0.00000000E+00
36	0.96000000E+01	0.00000000E+00	0.00000000E+00
37	0.99000000E+01	0.00000000E+00	0.00000000E+00
38	0.10200000E+02	0.00000000E+00	0.00000000E+00
39	0.10500000E+02	0.00000000E+00	0.00000000E+00
Boundary conditions, node 1: DOF 1,2,4,6 fixed, 204 lbf/in linear stiffness for DOF 3, 1.64 in·lbf/rad torsional stiffness for DOF 5.			

The boundary conditions shown at the end of Table F.3 for degrees of freedom (DOF) 3 and 5 at node 1 result from a separate finite element flexibility analysis of the flexure pivot. The fixed boundary condition used for the other DOF at node 1 is an idealization of the flexure pivot's much higher stiffness for motions in these directions. The flexure pivot is of stainless steel, measuring 0.005" in the z direction, 0.75" in the y direction and 0.155" in the x direction.

The ADINA beam elements are defined by the node point assignments shown in Table F.4 for the aluminum beam and steel beam rigid base models.

Table F.4. Beam element nodes for IBS rigid base models:

	aluminum beam				steel beam		
ELEMENT	Node 1	Node 2	Aux. Node	ELEMENT	Node 1	Node 2	Aux. Node
1	3	6	5	1	3	6	5
2	6	7	5	2	6	7	5
3	7	8	5	3	7	8	5
4	8	9	5	4	8	9	5
5	9	10	5	5	9	10	5
6	10	11	5	6	10	11	5
7	11	12	5	7	11	12	5
8	12	13	5	8	12	13	5

9	13	14	5	9	13	14	5
10	14	15	5	10	14	15	5
11	15	16	5	11	15	16	5
12	16	17	5	12	16	17	5
13	17	18	5	13	17	18	5
14	18	19	5	14	18	19	5
15	19	20	5	15	19	20	5
16	20	21	5	16	20	21	5
17	21	22	5	17	21	22	5
18	22	23	5	18	22	23	5
19	23	24	5	19	23	24	5
20	24	25	5	20	24	25	5
21	25	26	5	21	25	26	5
22	26	27	5	22	26	27	5
23	27	28	5	23	27	28	5
24	28	29	5	24	28	29	5
25	29	30	5	25	29	30	5
26	30	31	5	26	30	31	5
27	31	1	5	27	31	1	5
28	1	32	5	28	1	32	5
29	32	33	5	29	32	33	5
30	33	34	5	30	33	34	5
31	34	35	5	31	34	35	5
32	35	36	5	32	35	36	5
33	36	37	5	33	36	37	5
34	37	38	5	34	37	38	5
35	38	39	5	35	38	39	5
36	39	2	5	36	39	2	5
37	2	40	5	37	2	4	5
38	40	4	5				

The aluminum beam model has an extra node (node 40) and an extra beam element (element 38) that are not present in the steel beam model. These represent the slightly greater length of the aluminum beam from the impact point (node 2) to the end point (node 4).

A.3. Flexible base models

Tables F.5 and F.6 show the nodal coordinates for the aluminum beam and steel beam flexible base models of the IBS.

Table F.5. Flexible base aluminum beam model.
FE node coordinates (inches).

NODE	X-coordinate	Y-coordinate	Z-coordinate	Ident
1	0.48125000E+01	0.60000000E+01	-0.77500000E+01	Voice Coil
2	0.20625000E+01	0.60000000E+01	0.42500000E+01	Beam Impact Point
3	0.20625000E+01	0.60000000E+01	0.43750000E+01	Upper Force Sensor
4	0.20625000E+01	0.60000000E+01	0.41250000E+01	Lower Force Sensor
5	0.00000000E+00	0.00000000E+00	0.00000000E+00	Corner of Baseplate
6	0.15375000E+02	0.00000000E+00	0.00000000E+00	"
7	0.15375000E+02	0.12000000E+02	0.00000000E+00	"
8	0.00000000E+00	0.12000000E+02	0.00000000E+00	"
9	0.25625000E+01	0.00000000E+00	0.00000000E+00	Interior of Baseplate
10	0.51250000E+01	0.00000000E+00	0.00000000E+00	"
11	0.76875000E+01	0.00000000E+00	0.00000000E+00	"
12	0.10250000E+02	0.00000000E+00	0.00000000E+00	"
13	0.12812500E+02	0.00000000E+00	0.00000000E+00	"
14	0.12812500E+01	0.12000000E+01	0.00000000E+00	"
15	0.38437500E+01	0.12000000E+01	0.00000000E+00	"
16	0.64062500E+01	0.12000000E+01	0.00000000E+00	"
17	0.89687500E+01	0.12000000E+01	0.00000000E+00	"
18	0.11531250E+02	0.12000000E+01	0.00000000E+00	"
19	0.14093750E+02	0.12000000E+01	0.00000000E+00	"
20	0.00000000E+00	0.24000000E+01	0.00000000E+00	"
21	0.25625000E+01	0.24000000E+01	0.00000000E+00	"
22	0.51250000E+01	0.24000000E+01	0.00000000E+00	"
23	0.76875000E+01	0.24000000E+01	0.00000000E+00	"
24	0.10250000E+02	0.24000000E+01	0.00000000E+00	"
25	0.12812500E+02	0.24000000E+01	0.00000000E+00	"
26	0.15375000E+02	0.24000000E+01	0.00000000E+00	"

27	0.12812500E+01	0.36000000E+01	0.00000000E+00	"
28	0.38437500E+01	0.36000000E+01	0.00000000E+00	"
29	0.64062500E+01	0.36000000E+01	0.00000000E+00	"
30	0.89687500E+01	0.36000000E+01	0.00000000E+00	"
31	0.11531250E+02	0.36000000E+01	0.00000000E+00	"
32	0.14093750E+02	0.36000000E+01	0.00000000E+00	"
33	0.00000000E+00	0.48000000E+01	0.00000000E+00	"
34	0.25625000E+01	0.48000000E+01	0.00000000E+00	"
35	0.51250000E+01	0.48000000E+01	0.00000000E+00	"
36	0.76875000E+01	0.48000000E+01	0.00000000E+00	"
37	0.10250000E+02	0.48000000E+01	0.00000000E+00	"
38	0.12812500E+02	0.48000000E+01	0.00000000E+00	"
39	0.15375000E+02	0.48000000E+01	0.00000000E+00	"
40	0.20625000E+01	0.60000000E+01	0.00000000E+00	"
41	0.38437500E+01	0.60000000E+01	0.00000000E+00	"
42	0.64062500E+01	0.60000000E+01	0.00000000E+00	"
43	0.89687500E+01	0.60000000E+01	0.00000000E+00	"
44	0.11531250E+02	0.60000000E+01	0.00000000E+00	"
45	0.13312500E+02	0.60000000E+01	0.00000000E+00	"
46	0.00000000E+00	0.72000000E+01	0.00000000E+00	"
47	0.25625000E+01	0.72000000E+01	0.00000000E+00	"
48	0.51250000E+01	0.72000000E+01	0.00000000E+00	"
49	0.76875000E+01	0.72000000E+01	0.00000000E+00	"
50	0.10250000E+02	0.72000000E+01	0.00000000E+00	"
51	0.12812500E+02	0.72000000E+01	0.00000000E+00	"
52	0.15375000E+02	0.72000000E+01	0.00000000E+00	"
53	0.12812500E+01	0.84000000E+01	0.00000000E+00	"
54	0.38437500E+01	0.84000000E+01	0.00000000E+00	"
55	0.64062500E+01	0.84000000E+01	0.00000000E+00	"
56	0.89687500E+01	0.84000000E+01	0.00000000E+00	"
57	0.11531250E+02	0.84000000E+01	0.00000000E+00	"
58	0.14093750E+02	0.84000000E+01	0.00000000E+00	"
59	0.00000000E+00	0.96000000E+01	0.00000000E+00	"
60	0.25625000E+01	0.96000000E+01	0.00000000E+00	"
61	0.51250000E+01	0.96000000E+01	0.00000000E+00	"
62	0.76875000E+01	0.96000000E+01	0.00000000E+00	"
63	0.10250000E+02	0.96000000E+01	0.00000000E+00	"
64	0.12812500E+02	0.96000000E+01	0.00000000E+00	"

65	0.15375000E+02	0.96000000E+01	0.00000000E+00	"
66	0.12812500E+01	0.10800000E+02	0.00000000E+00	"
67	0.38437500E+01	0.10800000E+02	0.00000000E+00	"
68	0.64062500E+01	0.10800000E+02	0.00000000E+00	"
69	0.89687500E+01	0.10800000E+02	0.00000000E+00	"
70	0.11531250E+02	0.10800000E+02	0.00000000E+00	"
71	0.14093750E+02	0.10800000E+02	0.00000000E+00	"
72	0.25625000E+01	0.12000000E+02	0.00000000E+00	"
73	0.51250000E+01	0.12000000E+02	0.00000000E+00	"
74	0.76875000E+01	0.12000000E+02	0.00000000E+00	"
75	0.10250000E+02	0.12000000E+02	0.00000000E+00	"
76	0.12812500E+02	0.12000000E+02	0.00000000E+00	"
77	0.13312500E+02	0.60000000E+01	0.14166700E+01	Beam Support
78	0.13312500E+02	0.60000000E+01	0.28333300E+01	"
79	0.13312500E+02	0.60000000E+01	0.42500000E+01	"
80	0.12812500E+02	0.60000000E+01	0.42500000E+01	Impact Beam
81	0.11669643E+02	0.60000000E+01	0.42500000E+01	"
82	0.10526786E+02	0.60000000E+01	0.42500000E+01	"
83	0.93839286E+01	0.60000000E+01	0.42500000E+01	"
84	0.82410714E+01	0.60000000E+01	0.42500000E+01	"
85	0.70982143E+01	0.60000000E+01	0.42500000E+01	"
86	0.59553571E+01	0.60000000E+01	0.42500000E+01	"
87	0.48125000E+01	0.60000000E+01	0.42500000E+01	"
88	0.38125000E+01	0.60000000E+01	0.42500000E+01	"
89	0.28125000E+01	0.60000000E+01	0.42500000E+01	"
90	0.14375000E+01	0.60000000E+01	0.42500000E+01	"
91	0.20625000E+01	0.48750000E+01	0.55000000E+01	Yoke
92	0.20625000E+01	0.54375000E+01	0.55000000E+01	"
93	0.20625000E+01	0.60000000E+01	0.55000000E+01	"
94	0.20625000E+01	0.65625000E+01	0.55000000E+01	"
95	0.20625000E+01	0.71250000E+01	0.55000000E+01	"
96	0.20625000E+01	0.71250000E+01	0.48750000E+01	"
97	0.20625000E+01	0.71250000E+01	0.42500000E+01	"
98	0.20625000E+01	0.71250000E+01	0.36250000E+01	"
99	0.20625000E+01	0.71250000E+01	0.30000000E+01	"
100	0.20625000E+01	0.65625000E+01	0.30000000E+01	"
101	0.20625000E+01	0.60000000E+01	0.30000000E+01	"

102	0.20625000E+01	0.54375000E+01	0.30000000E+01	"
103	0.20625000E+01	0.48750000E+01	0.30000000E+01	"
104	0.20625000E+01	0.48750000E+01	0.36250000E+01	"
105	0.20625000E+01	0.48750000E+01	0.42500000E+01	"
106	0.20625000E+01	0.48750000E+01	0.48750000E+01	"
107	0.48125000E+01	0.60000000E+01	-0.57500000E+01	Connecting Rod
108	0.48125000E+01	0.60000000E+01	-0.37500000E+01	"
109	0.48125000E+01	0.60000000E+01	-0.17500000E+01	"
110	0.48125000E+01	0.60000000E+01	0.25000000E+00	"
111	0.48125000E+01	0.60000000E+01	0.22500000E+01	"
112	0.00000000E+00	0.60000000E+01	0.10000000E+02	Auxiliary
113	0.20625000E+01	0.00000000E+00	0.00000000E+00	Auxiliary
Boundary Conditions: Clamped at nodes 5, 6, 7 and 8. No DOF at nodes 112, 113.				

The flexible base steel beam model uses the same node locations, except for those listed in Table F.6. Node 114 is added at a location between nodes 79 and 80, and the location of node 80 is changed, to allow modeling the flexure pivot. The position of the end of the beam, node 90, is changed because the overall length of the steel beam is slightly different from that of the aluminum beam.

Table F.6. Flexible base steel beam model.
Coordinates of FE nodes differing from the al. beam model.

NODE	X-coordinate	Y-coordinate	Z-coordinate
80	0.12657500E+02	0.60000000E+01	0.42500000E+01
90	0.16575000E+01	0.60000000E+01	0.42500000E+01
114	0.12812500E+02	0.60000000E+01	0.42500000E+01

Table F.7 shows the node point assignments for the 120 3-node ADINA plate elements that are used to represent the baseplate. These node assignments are identical for the aluminum and steel beam versions of the IBS flexible baseplate model. Each element is of 1/2" thick aluminum. The material properties for aluminum are listed in Table F.1.

Table F.7. ADINA plate element node assignments, IBS flexible base models.

ELEMENT	Node 1	Node 2	Node 3	ELEMENT	Node 1	Node 2	Node 3
1	5	9	14	61	36	37	43
2	9	21	14	62	37	50	43
3	21	20	14	63	50	49	43
4	20	5	14	64	49	36	43
5	9	10	15	65	37	38	44
6	10	22	15	66	38	51	44
7	22	21	15	67	51	50	44
8	21	9	15	68	50	37	44
9	10	11	16	69	38	39	45
10	11	23	16	70	39	52	45
11	23	22	16	71	52	51	45
12	22	10	16	72	51	38	45
13	11	12	17	73	46	47	53
14	12	24	17	74	47	60	53
15	24	23	17	75	60	59	53
16	23	11	17	76	59	46	53
17	12	13	18	77	47	48	54
18	13	25	18	78	48	61	54
19	25	24	18	79	61	60	54
20	24	12	18	80	60	47	54
21	13	6	19	81	48	49	55
22	6	26	19	82	49	62	55
23	26	25	19	83	62	61	55
24	25	13	19	84	61	48	55
25	20	21	27	85	49	50	56
26	21	34	27	86	50	63	56
27	34	33	27	87	63	62	56
28	33	20	27	88	62	49	56
29	21	22	28	89	50	51	57
30	22	35	28	90	51	64	57
31	35	34	28	91	64	63	57
32	34	21	28	92	63	50	57
33	22	23	29	93	51	52	58
34	23	36	29	94	52	65	58

35	36	35	29	95	65	64	58
36	35	22	29	96	64	51	58
37	23	24	30	97	59	60	66
38	24	37	30	98	60	72	66
39	37	36	30	99	72	8	66
40	36	23	30	100	8	59	66
41	24	25	31	101	60	61	67
42	25	38	31	102	61	73	67
43	38	37	31	103	73	72	67
44	37	24	31	104	72	60	67
45	25	26	32	105	61	62	68
46	26	39	32	106	62	74	68
47	39	38	32	107	74	73	68
48	38	25	32	108	73	61	68
49	33	34	40	109	62	63	69
50	34	47	40	110	63	75	69
51	47	46	40	111	75	74	69
52	46	33	40	112	74	62	69
53	34	35	41	113	63	64	70
54	35	48	41	114	64	76	70
55	48	47	41	115	76	75	70
56	47	34	41	116	75	63	70
57	35	36	42	117	64	65	71
58	36	49	42	118	65	7	71
59	49	48	42	119	7	76	71
60	48	35	42	120	76	64	71

The flexible base and flexible base with cover models use ADINA 2-node beam elements to represent the impact beam, connecting rod, beam support, yoke and force transducer mounting studs (labeled "force sensor" in Table F.8). Section properties used for all of these except the impact beams are shown in Table F.8. Section properties for the impact beams are listed in Table F.1. Section properties I_r, I_s and I_t are the moments of inertia with respect the local r-s-t coordinate frame defined for each beam element. For details, see the ADINA documentation.

Table F.8. Section properties for additional ADINA beam elements in the IBS flexible base and flexible base with covers simulations.

	area (in^2)	I_r (in^4)	I_s (in^4)	I_t (in^4)
Yoke 1/2" square	0.25	1.04×10^{-2}	5.21×10^{-3}	5.21×10^{-3}
Beam Support Vert. 1" x 2"	2.0	0.833	0.667	0.167
Beam Support Horiz. 1" x 1/2"	1.0	0.354	0.333	2.08×10^{-2}
Conn. Rod Force Sensor 0.16" dia.	0.0201	6.43×10^{-5}	3.22×10^{-5}	3.22×10^{-5}
Yoke Support 1/2" dia.	0.196	6.14×10^{-3}	3.07×10^{-3}	3.07×10^{-3}
Flexure Pivot 0.75" x 0.005" (steel bm. only)	3.75×10^{-3}	1.76×10^{-4}	1.76×10^{-4}	7.82×10^{-9}

The nodes and section properties associated with each beam element are given in Tables F.9 and F.10. Table F.9 shows the element / node point assignments when the aluminum impact beam is used; Table F.10 shows the element / node point assignments when the steel impact beam is used. Note that Tables F.9 and F.10 are divided according to whether the ADINA beam elements use aluminum or steel material properties.

Table F.9. ADINA beam elements in the aluminum beam flexible base model.

	aluminum sections				steel sections			
ELE-MENT	Node 1	Node 2	Aux. node	Section	Node 1	Node 2	Aux. node	Section
1	45	77	112	Beam Support Vert.	3	93	112	Force Sensor
2	77	78	112	"	101	4	112	"
3	78	79	112	"	1	107	112	Conn. Rod
4	79	80	112	Impact Beam	107	108	112	"
5	80	81	112	"	108	109	112	"

6	81	82	112	"	109	110	112	"
7	82	83	112	"	110	111	112	"
8	83	84	112	"	111	87	112	"
9	84	85	112	"	40	101	112	Yoke Support
10	85	86	112	"				
11	86	87	112	"				
12	87	88	112	"				
13	88	89	112	"				
14	89	2	112	"				
15	2	90	112	"				
16	95	94	113	Yoke				
17	94	93	113	"				
18	93	92	113	"				
19	92	91	113	"				
20	95	96	113	"				
21	96	97	113	"				
22	97	98	113	"				
23	98	99	113	"				
24	99	100	113	"				
25	100	101	113	"				
26	101	102	113	"				
27	102	103	113	"				
28	91	106	113	"				
29	106	105	113	"				
30	105	104	113	"				
31	104	103	113	"				

Table F.10. ADINA beam elements in the steel beam flexible base model.

	aluminum sections				steel sections			
ELE-MENT	Node 1	Node 2	Aux. node	Section	Node 1	Node 2	Aux. node	Section
1	45	77	112	Beam Support Vert.	3	93	112	Force Sensor
2	77	78	112	"	101	4	112	"
3	78	79	112	"	1	107	112	Conn. Rod
4	95	94	113	Yoke	107	108	112	"
5	94	93	113	"	108	109	112	"

6	93	92	113	"	109	110	112	"
7	92	91	113	"	110	111	112	"
8	95	96	113	"	111	87	112	"
9	96	97	113	"	40	101	112	Yoke Support
10	97	98	113	"	80	81	112	Impact Beam
11	98	99	113	"	81	82	112	"
12	99	100	113	"	82	83	112	"
13	100	101	113	"	83	84	112	"
14	101	102	113	"	84	85	112	"
15	102	103	113	"	85	86	112	"
16	91	106	113	"	86	87	112	"
17	106	105	113	"	87	88	112	"
18	105	104	113	"	88	89	112	"
19	104	103	113	"	89	2	112	"
20	79	114	113	Beam Support Horiz.	2	90	112	"
21					114	80	112	Flexure Pivot

A.3. Flexible base with cover models

The flexible base with cover model was first implemented for the IBS with steel impact beam. Because of computer limitations, only a very crude model with a coarse finite element mesh could be implemented. Its performance was so poor that a model for the IBS with aluminum impact beam was not attempted. Therefore, in this section, only the finite element model for the steel impact beam is presented.

Node points and coordinates for the FE model are given in Table F.11.

Table F.11. Flexible base with cover model.
FE node coordinates (inches).

NODE	X-coordinate	Y-coordinate	Z-coordinate	Ident
1	0.48125000E+01	0.60000000E+01	-0.77500000E+01	Voice Coil

2	0.20625000E+01	0.60000000E+01	0.42500000E+01	Beam Impact Point
3	0.20625000E+01	0.60000000E+01	0.43750000E+01	Upper Force Sensor
4	0.20625000E+01	0.60000000E+01	0.41250000E+01	Lower Force Sensor
5	0.00000000E+00	0.00000000E+00	0.00000000E+00	Corner of Baseplate
6	0.15375000E+02	0.00000000E+00	0.00000000E+00	"
7	0.15375000E+02	0.12000000E+02	0.00000000E+00	"
8	0.00000000E+00	0.12000000E+02	0.00000000E+00	"
9	0.00000000E+00	0.00000000E+00	0.10200000E+02	Corner of Top Panel of Cover
10	0.15375000E+02	0.00000000E+00	0.10200000E+02	"
11	0.15375000E+02	0.12000000E+02	0.10200000E+02	"
12	0.00000000E+00	0.12000000E+02	0.10200000E+02	"
13	0.38437500E+01	0.00000000E+00	0.00000000E+00	Interior of Baseplate
14	0.76875000E+01	0.00000000E+00	0.00000000E+00	"
15	0.11531250E+02	0.00000000E+00	0.00000000E+00	"
16	0.19218750E+01	0.30000000E+01	0.00000000E+00	"
17	0.57656250E+01	0.30000000E+01	0.00000000E+00	"
18	0.96093750E+01	0.30000000E+01	0.00000000E+00	"
19	0.13453125E+02	0.30000000E+01	0.00000000E+00	"
20	0.00000000E+00	0.60000000E+01	0.00000000E+00	"
21	0.20625000E+01	0.60000000E+01	0.00000000E+00	"
22	0.76875000E+01	0.60000000E+01	0.00000000E+00	"
23	0.13312500E+02	0.60000000E+01	0.00000000E+00	"
24	0.15375000E+02	0.60000000E+01	0.00000000E+00	"
25	0.19218750E+01	0.90000000E+01	0.00000000E+00	"
26	0.57656250E+01	0.90000000E+01	0.00000000E+00	"
27	0.96093750E+01	0.90000000E+01	0.00000000E+00	"
28	0.13453125E+02	0.90000000E+01	0.00000000E+00	"
29	0.38437500E+01	0.12000000E+02	0.00000000E+00	"
30	0.76875000E+01	0.12000000E+02	0.00000000E+00	"
31	0.11531250E+02	0.12000000E+02	0.00000000E+00	"
32	0.19218750E+01	0.00000000E+00	0.25500000E+01	-y Panel of Cover
33	0.57656250E+01	0.00000000E+00	0.25500000E+01	"

34	0.96093750E+01	0.00000000E+00	0.25500000E+01	"
35	0.13453125E+02	0.00000000E+00	0.25500000E+01	"
36	0.00000000E+00	0.00000000E+00	0.51000000E+01	"
37	0.38437500E+01	0.00000000E+00	0.51000000E+01	"
38	0.76875000E+01	0.00000000E+00	0.51000000E+01	"
39	0.11531250E+02	0.00000000E+00	0.51000000E+01	"
40	0.15375000E+02	0.00000000E+00	0.51000000E+01	"
41	0.19218750E+01	0.00000000E+00	0.76500000E+01	"
42	0.57656250E+01	0.00000000E+00	0.76500000E+01	"
43	0.96093750E+01	0.00000000E+00	0.76500000E+01	"
44	0.13453125E+02	0.00000000E+00	0.76500000E+01	"
45	0.38437500E+01	0.00000000E+00	0.10200000E+02	"
46	0.76875000E+01	0.00000000E+00	0.10200000E+02	"
47	0.11531250E+02	0.00000000E+00	0.10200000E+02	"
48	0.19218750E+01	0.30000000E+01	0.10200000E+02	Top Panel of Cover
49	0.57656250E+01	0.30000000E+01	0.10200000E+02	"
50	0.96093750E+01	0.30000000E+01	0.10200000E+02	"
51	0.13453125E+02	0.30000000E+01	0.10200000E+02	"
52	0.00000000E+00	0.60000000E+01	0.10200000E+02	"
53	0.38437500E+01	0.60000000E+01	0.10200000E+02	"
54	0.76875000E+01	0.60000000E+01	0.10200000E+02	"
55	0.11531250E+02	0.60000000E+01	0.10200000E+02	"
56	0.15375000E+02	0.60000000E+01	0.10200000E+02	"
57	0.19218750E+01	0.90000000E+01	0.10200000E+02	"
58	0.57656250E+01	0.90000000E+01	0.10200000E+02	"
59	0.96093750E+01	0.90000000E+01	0.10200000E+02	"
60	0.13453125E+02	0.90000000E+01	0.10200000E+02	"
61	0.38437500E+01	0.12000000E+02	0.10200000E+02	"
62	0.76875000E+01	0.12000000E+02	0.10200000E+02	"
63	0.11531250E+02	0.12000000E+02	0.10200000E+02	"
64	0.19218750E+01	0.12000000E+02	0.76500000E+01	+y Panel of Cover
65	0.57656250E+01	0.12000000E+02	0.76500000E+01	"
66	0.96093750E+01	0.12000000E+02	0.76500000E+01	"
67	0.13453125E+02	0.12000000E+02	0.76500000E+01	"
68	0.00000000E+00	0.12000000E+02	0.51000000E+01	"
69	0.38437500E+01	0.12000000E+02	0.51000000E+01	"

70	0.76875000E+01	0.12000000E+02	0.51000000E+01	"
71	0.11531250E+02	0.12000000E+02	0.51000000E+01	"
72	0.15375000E+02	0.12000000E+02	0.51000000E+01	"
73	0.19218750E+01	0.12000000E+02	0.25500000E+01	"
74	0.57656250E+01	0.12000000E+02	0.25500000E+01	"
75	0.96093750E+01	0.12000000E+02	0.25500000E+01	"
76	0.13453125E+02	0.12000000E+02	0.25500000E+01	"
77	0.00000000E+00	0.90000000E+01	0.25500000E+01	-x Panel of Cover
78	0.00000000E+00	0.30000000E+01	0.25500000E+01	"
79	0.00000000E+00	0.60000000E+01	0.51000000E+01	"
80	0.00000000E+00	0.90000000E+01	0.76500000E+01	"
81	0.00000000E+00	0.30000000E+01	0.76500000E+01	"
82	0.15375000E+02	0.90000000E+01	0.25500000E+01	+x Panel of Cover
83	0.15375000E+02	0.30000000E+01	0.25500000E+01	"
84	0.15375000E+02	0.60000000E+01	0.51000000E+01	"
85	0.15375000E+02	0.90000000E+01	0.76500000E+01	"
86	0.15375000E+02	0.30000000E+01	0.76500000E+01	"
87	0.20625000E+01	0.48750000E+01	0.55000000E+01	Yoke
88	0.20625000E+01	0.60000000E+01	0.55000000E+01	"
89	0.20625000E+01	0.71250000E+01	0.55000000E+01	"
90	0.20625000E+01	0.71250000E+01	0.42500000E+01	"
91	0.20625000E+01	0.71250000E+01	0.30000000E+01	"
92	0.20625000E+01	0.60000000E+01	0.30000000E+01	"
93	0.20625000E+01	0.48750000E+01	0.30000000E+01	"
94	0.20625000E+01	0.48750000E+01	0.42500000E+01	"
95	0.13312500E+02	0.60000000E+01	0.14166667E+01	Beam Support
96	0.13312500E+02	0.60000000E+01	0.28333333E+01	"
97	0.13312500E+02	0.60000000E+01	0.42500000E+01	"
98	0.12812500E+02	0.60000000E+01	0.42500000E+01	Impact Beam
99	0.12657500E+02	0.60000000E+01	0.42500000E+01	"
100	0.10696250E+02	0.60000000E+01	0.42500000E+01	"
101	0.87350000E+01	0.60000000E+01	0.42500000E+01	"
102	0.67737500E+01	0.60000000E+01	0.42500000E+01	"
103	0.48125000E+01	0.60000000E+01	0.42500000E+01	"
104	0.34375000E+01	0.60000000E+01	0.42500000E+01	"

105	0.16575000E+01	0.60000000E+01	0.42500000E+01	"
106	0.48125000E+01	0.60000000E+01	-0.60357143E+01	Conn. Rod
107	0.48125000E+01	0.60000000E+01	-0.43214286E+01	"
108	0.48125000E+01	0.60000000E+01	-0.26071429E+01	"
109	0.48125000E+01	0.60000000E+01	-0.89285714E+00	"
110	0.48125000E+01	0.60000000E+01	0.82142857E+00	"
111	0.48125000E+01	0.60000000E+01	0.25357143E+01	"
112	0.00000000E+00	0.60000000E+01	0.10000000E+02	Auxiliary
113	0.20625000E+01	0.00000000E+00	0.00000000E+00	Auxiliary

ADINA 3-node plate elements are used to represent the baseplate and the panels of the covers of the flexible base with cover model of the IBS. Node assignments and locations of the plate elements are given in Table F.12.

Table F.12. ADINA plate element node assignments, IBS steel beam, flexible base with cover model.

ELE-MENT	Node 1	Node 2	Node 3	Location	ELE-MENT	Node 1	Node 2	Node 3	Location
1	5	13	16	Baseplate	81	52	53	57	Top Panel of Cover
2	13	21	16	"	82	53	61	57	"
3	21	20	16	"	83	61	12	57	"
4	20	5	16	"	84	12	52	57	"
5	13	14	17	"	85	53	54	58	"
6	14	22	17	"	86	54	62	58	"
7	22	21	17	"	87	62	61	58	"
8	21	13	17	"	88	61	53	58	"
9	14	15	18	"	89	54	55	59	"
10	15	23	18	"	90	55	63	59	"
11	23	22	18	"	91	63	62	59	"
12	22	14	18	"	92	62	54	59	"
13	15	6	19	"	93	55	56	60	"
14	6	24	19	"	94	56	11	60	"
15	24	23	19	"	95	11	63	60	"
16	23	15	19	"	96	63	55	60	"
17	20	21	25	"	97	12	61	64	+y Panel of Cover
18	21	29	25	"	98	61	69	64	"

19	29	8	25	"	99	69	68	64	"
20	8	20	25	"	100	68	12	64	"
21	21	22	26	"	101	61	62	65	"
22	22	30	26	"	102	62	70	65	"
23	30	29	26	"	103	70	69	65	"
24	29	21	26	"	104	69	61	65	"
25	22	23	27	"	105	62	63	66	"
26	23	31	27	"	106	63	71	66	"
27	31	30	27	"	107	71	70	66	"
28	30	22	27	"	108	70	62	66	"
29	23	24	28	"	109	63	11	67	"
30	24	7	28	"	110	11	72	67	"
31	7	31	28	"	111	72	71	67	"
32	31	23	28	"	112	71	63	67	"
33	5	13	32	-y Panel of Cover	113	68	69	73	"
34	13	37	32	"	114	69	29	73	"
35	37	36	32	"	115	29	8	73	"
36	36	5	32	"	116	8	68	73	"
37	13	14	33	"	117	69	70	74	"
38	14	38	33	"	118	70	30	74	"
39	38	37	33	"	119	30	29	74	"
40	37	13	33	"	120	29	69	74	"
41	14	15	34	"	121	70	71	75	"
42	15	39	34	"	122	71	31	75	"
43	39	38	34	"	123	31	30	75	"
44	38	14	34	"	124	30	70	75	"
45	15	6	35	"	125	71	72	76	"
46	6	40	35	"	126	72	7	76	"
47	40	39	35	"	127	7	31	76	"
48	39	15	35	"	128	31	71	76	"
49	36	37	41	"	129	8	20	77	-x Panel of Cover
50	37	45	41	"	130	20	79	77	"
51	45	9	41	"	131	79	68	77	"
52	9	36	41	"	132	68	8	77	"
53	37	38	42	"	133	20	5	78	"
54	38	46	42	"	134	5	36	78	"

55	46	45	42	"	135	36	79	78	"
56	45	37	42	"	136	79	20	78	"
57	38	39	43	"	137	68	79	80	"
58	39	47	43	"	138	79	52	80	"
59	47	46	43	"	139	52	12	80	"
60	46	38	43	"	140	12	68	80	"
61	39	40	44	"	141	79	36	81	"
62	40	10	44	"	142	36	9	81	"
63	10	47	44	"	143	9	52	81	"
64	47	39	44	"	144	52	79	81	"
65	9	45	48	Top Panel of Cover	145	7	24	82	+x Panel of Cover
66	45	53	48	"	146	24	84	82	"
67	53	52	48	"	147	84	72	82	"
68	52	9	48	"	148	72	7	82	"
69	45	46	49	"	149	24	6	83	"
70	46	54	49	"	150	6	40	83	"
71	54	53	49	"	151	40	84	83	"
72	53	45	49	"	152	84	24	83	"
73	46	47	50	"	153	72	84	85	"
74	47	55	50	"	154	84	56	85	"
75	55	54	50	"	155	56	11	85	"
76	54	46	50	"	156	11	72	85	"
77	47	10	51	"	157	84	40	86	"
78	10	56	51	"	158	40	10	86	"
79	56	55	51	"	159	10	56	86	"
80	55	47	51	"	160	56	84	86	"

The fiberglass and metal covers are represented by the same element topology, using different material properties for elements located on the panels of the cover. To model the metal cover, elements located on the panels of the cover use the material properties of aluminum, listed in Table F.1, and 1/16" thickness. To model the fiberglass cover, elements located on the panels of the cover use properties for fiberglass, listed in Table F.13, and 1/8" thickness.

Table F.13. Material properties of fiberglass.

mass density	$1.31 \times 10^{-4} \frac{lbf \cdot sec^2}{in^4}$
elastic modulus	$8.2 \times 10^5 \frac{lbf}{in^2}$
Poisson's ratio	0.32

The remaining elements of the IBS, namely, the yoke, beam support, force transducer studs, flexure pivot, and the impact beam itself, are represented by ADINA 2-node beam elements, as in the flexible base and rigid base models. Table F.14 lists the element and node point assignments for the ADINA beam elements. The section properties are listed in Table F.8.

Table F.14. ADINA beam elements in the steel beam flexible base with cover model.

	aluminum sections				steel sections			
ELE-MENT	Node 1	Node 2	Aux. node	Section	Node 1	Node 2	Aux. node	Section
1	89	88	113	Yoke	98	99	112	Flexure Pivot
2	88	87	113	"	99	100	112	Beam
3	87	94	113	"	100	101	112	"
4	94	93	113	"	101	102	112	"
5	89	90	113	"	102	103	112	"
6	90	91	113	"	103	104	112	"
7	91	92	113	"	104	2	112	"
8	92	93	113	"	2	105	112	"
9	23	95	112	Beam Support Vert.	92	4	112	Force Sensor
10	95	96	112	"	3	88	112	Force Sensor
11	96	97	112	"	1	106	112	Conn. Rod
12	97	98	112	Beam Support Horiz.	106	107	112	"
13					107	108	112	"

14					108	109	112	"
15					109	110	112	"
16					110	111	112	"
17					111	103	112	"
18					21	92	112	Yoke Support

Table F.14 completes the detailed description of the finite element models of the Impact Beam System.

B. Numerical Model of the SSC

B.1. Connecting rod finite element model

The ball joint-to-slider connecting rod is the only flexible body element in the numerical model of the spatial slider crank. It is link 5 in the kinematic model of the mechanism, discussed in section C.2 of Chapter 5. As shown in Figure 5.8, the z_5 and x_5 axes are perpendicular to the length of the connecting rod. Axis y_5 is not explicit in the figure. It lies along the length of the connecting rod. The sense of y_5 is from the ball joint toward the slider. The direction of z_5 is the pivot axis of the bearing on top of the slider yoke. This direction changes over time as the mechanism operates, and depends on the lengths of the links of the mechanism. With the link lengths given in Chapter 5, the direction of z_5 varies less than ±20° from vertical.

The finite element model for the connecting rod is presented in Tables F.15 through F.17. The connecting rod is made of steel, and uses the material properties shown in Table F.1. Two connecting rods were constructed for the SSC, differing only in their diameter. The larger one is 0.25" in diameter and the smaller is 0.125" diameter. Although results were presented in the body of the thesis only for the larger rod, numerical simulations for both of them

were constructed and exercised. The finite element models had identical topologies, differing only in the section properties. Section properties for the two connecting rods are shown in Table F.15.

Table F.15. Section properties for
ADINA beam elements in the SSC connecting rod models.

	area (in^2)	I_r (in^4)	I_s (in^4)	I_t (in^4)
Large rod 0.25" dia.	4.91×10^{-2}	3.83×10^{-4}	1.92×10^{-4}	1.92×10^{-4}
Small rod 0.125" dia.	1.23×10^{-2}	2.40×10^{-5}	1.20×10^{-5}	1.20×10^{-5}

Nodal coordinates for the ADINA models are shown in Table F.16. Node 1 is located at the ball joint end of the connecting rod, and node 2 is at the slider end.

Table F.16. SSC connecting rod.
FE node coordinates (inches) in reference frame N_5.

NODE	X-coordinate	Y-coordinate	Z-coordinate
1	0.00000000E+00	-0.90000000E+01	0.00000000E+00
2	0.00000000E+00	0.00000000E+00	0.00000000E+00
3	0.00000000E+00	-0.87500000E+01	0.00000000E+00
4	0.00000000E+00	-0.85000000E+01	0.00000000E+00
5	0.00000000E+00	-0.82500000E+01	0.00000000E+00
6	0.00000000E+00	-0.80000000E+01	0.00000000E+00
7	0.00000000E+00	-0.77500000E+01	0.00000000E+00
8	0.00000000E+00	-0.75000000E+01	0.00000000E+00
9	0.00000000E+00	-0.72500000E+01	0.00000000E+00
10	0.00000000E+00	-0.70000000E+01	0.00000000E+00
11	0.00000000E+00	-0.67500000E+01	0.00000000E+00
12	0.00000000E+00	-0.65000000E+01	0.00000000E+00
13	0.00000000E+00	-0.62500000E+01	0.00000000E+00
14	0.00000000E+00	-0.60000000E+01	0.00000000E+00
15	0.00000000E+00	-0.57500000E+01	0.00000000E+00
16	0.00000000E+00	-0.55000000E+01	0.00000000E+00
17	0.00000000E+00	-0.52500000E+01	0.00000000E+00

18	0.00000000E+00	-0.50000000E+01	0.00000000E+00
19	0.00000000E+00	-0.47500000E+01	0.00000000E+00
20	0.00000000E+00	-0.45000000E+01	0.00000000E+00
21	0.00000000E+00	-0.42500000E+01	0.00000000E+00
22	0.00000000E+00	-0.40000000E+01	0.00000000E+00
23	0.00000000E+00	-0.37500000E+01	0.00000000E+00
24	0.00000000E+00	-0.35000000E+01	0.00000000E+00
25	0.00000000E+00	-0.32500000E+01	0.00000000E+00
26	0.00000000E+00	-0.30000000E+01	0.00000000E+00
27	0.00000000E+00	-0.27500000E+01	0.00000000E+00
28	0.00000000E+00	-0.25000000E+01	0.00000000E+00
29	0.00000000E+00	-0.22500000E+01	0.00000000E+00
30	0.00000000E+00	-0.20000000E+01	0.00000000E+00
31	0.00000000E+00	-0.17500000E+01	0.00000000E+00
32	0.00000000E+00	-0.15000000E+01	0.00000000E+00
33	0.00000000E+00	-0.12500000E+01	0.00000000E+00
34	0.00000000E+00	-0.10000000E+01	0.00000000E+00
35	0.00000000E+00	-0.75000000E+00	0.00000000E+00
36	0.00000000E+00	-0.50000000E+00	0.00000000E+00
37	0.00000000E+00	-0.25000000E+00	0.00000000E+00
38	0.00000000E+00	0.10000000E+01	0.10000000E+01

Finite element node assignments are shown in Table F.17.

Table F.17. Beam element nodes for SSC connecting rod models.

ELE-MENT	Node 1	Node 2	Aux. Node	ELE-MENT	Node 1	Node 2	Aux. Node
1	1	3	38	19	20	21	38
2	3	4	38	20	21	22	38
3	4	5	38	21	22	23	38
4	5	6	38	22	23	24	38
5	6	7	38	23	24	25	38
6	7	8	38	24	25	26	38
7	8	9	38	25	26	27	38
8	9	10	38	26	27	28	38
9	10	11	38	27	28	29	38
10	11	12	38	28	29	30	38
11	12	13	38	29	30	31	38

12	13	14	38	30	31	32	38
13	14	15	38	31	32	33	38
14	15	16	38	32	33	34	38
15	16	17	38	33	34	35	38
16	17	18	38	34	35	36	38
17	18	19	38	35	36	37	38
18	19	20	38	36	37	2	38

Finally, extra mass of $4.0\text{x}10^{-4}$ $\frac{\text{lbf}\cdot\text{sec}}{\text{in}^2}$ is added at node 1 to account for the unmodeled mass of the ball joint housing.

B.2. Rigid body links

The yoke and slider shell appear as rigid body links in the numerical model of the SSC. Their mass properties are given in Table F.18. These properties are partly calculated and partly empirical. The masses result from weighing the parts on a balance. The center of mass and moments of inertia are calculated, based on the design geometry of the parts. Then, a correction factor derived from the difference between the calculated and measured masses of the parts is applied to the calculated moments of inertia to arrive at the values shown in the table and used in the simulation. Moments of inertia are referenced to N_6 for the yoke and to N_7 for the slider shell.

Table F.18. Rigid body link mass properties, SSC numerical model.

		Yoke	Slider Shell
mass $\left(\frac{\text{lbf}\cdot\text{sec}}{\text{in}^2}\right)$		$2.205\text{x}10^{-3}$	$6.380\text{x}10^{-4}$
moment of inertia (lbf·sec):	I_x	$3.209\text{x}10^{-3}$	$2.770\text{x}10^{-4}$
	I_y	$2.230\text{x}10^{-3}$	$2.770\text{x}10^{-4}$
	I_z	$1.430\text{x}10^{-3}$	$3.450\text{x}10^{-4}$
center of mass (in):	x	0.0	0.0
	y	-0.8560	0.0
	z	0.0	0.0

Table F.18 concludes the information presented for the SSC numerical model.

C. Bearing Contact Parameters

Calculation of the contact stiffness and damping parameters for the clearance joints of the IBS and SSC numerical models is considered in this section. In every case, contact stiffness is modeled using the formula for contact between two spheres, Equation 229 on page 412 of *Theory of Elasticity*, Third Edition, by Timoshenko and Goodier [107]. This formula is:

$$\alpha = \sqrt[3]{\frac{9\pi^2}{16}\frac{P^2(k_1+k_2)^2(R_1+R_2)}{R_1R_2}} \qquad \text{(F.1)}$$

where α is the displacement of the centers of the spheres due to deformation, R_1 and R_2 are the radii of the spheres, P is the load forcing the spheres together, and k_1 and k_2 depend on the material properties of the spheres:

$$k_n = \frac{1-\nu_n^2}{\pi E_n} \qquad n = 1,2 \qquad \text{(F.2)}$$

The values required for k are listed in Table F.19.

Table F.19. Material properties for contact models.

Material	Elastic constant, E	Poisson's ratio, ν	k
Steel	$3.0\text{x}10^7 \frac{\text{lbf}}{\text{in}^2}$	0.29	$9.72\text{x}10^{-9} \frac{\text{in}^2}{\text{lbf}}$
Aluminum	$1.06\text{x}10^7 \frac{\text{lbf}}{\text{in}^2}$	0.33	$2.68\text{x}10^{-8} \frac{\text{in}^2}{\text{lbf}}$
Brass	$1.59\text{x}10^7 \frac{\text{lbf}}{\text{in}^2}$	0.331	$1.78\text{x}10^{-8} \frac{\text{in}^2}{\text{lbf}}$

C.1. IBS contact parameters

The IBS force sensor tips are approximately hemispherical, 0.188" diameter, and made of steel. Because of an error made in the early phases of the modeling work of the IBS, a force sensor diameter of 0.25" was used to calculate the value of the contact stiffness. The force sensors come into contact with a flat beam, made of steel or aluminum. Therefore, to model the contact stiffness, $R_1 = 0.125"$ and $R_2 \rightarrow \infty$ are used in Equation F.1. Since the equation is nonlinear, a linearized stiffness is used, based on an estimated contact force magnitude. For the IBS, this estimated magnitude was 10 lbf. Therefore:

IBS steel beam contact stiffness:

$$\alpha\Big|_{10\ \text{lbf}}^{\text{steel}} = \sqrt[3]{\frac{9\pi^2}{16}\frac{10^2\,(9.72\text{x}10^{-9} + 9.72\text{x}10^{-9})^2}{0.125}} = 1.19\text{x}10^{-4}\ \text{in}$$

$$k\Big|_{\text{eff}}^{\text{steel}} = \frac{P}{\alpha} = 8.4\text{x}10^{4}\ \frac{\text{lbf}}{\text{in}} \qquad \text{(F.3)}$$

As noted, the value of 0.125" used for the radius of the force sensor tip is slightly in error. If the correct value $R_1 = 0.09375"$ is used, $k\Big|_{\text{eff}}^{\text{steel}}$ changes to $7.6\text{x}10^{-4}\ \frac{\text{lbf}}{\text{in}}$. This change of about 10% in the value of $k\Big|_{\text{eff}}^{\text{steel}}$ does not significantly affect the contact forces predicted by the simulation and, in any case, it is a small change compared with other uncertainties in the model. Therefore, the original value of $k\Big|_{\text{eff}}^{\text{steel}}$ was retained to maintain consistency between later and earlier parts of the research.

IBS aluminum beam contact stiffness:

$$\alpha\Big|_{10\ \text{lbf}}^{\text{al}} = \sqrt[3]{\frac{9\pi^2}{16}\frac{10^2\,(9.72\text{x}10^{-9} + 2.68\text{x}10^{-8})^2}{0.125}} = 1.81\text{x}10^{-4}\ \text{in}$$

$$k\Big|_{\text{eff}}^{\text{al}} = \frac{P}{\alpha} = 5.5\text{x}10^{4}\ \frac{\text{lbf}}{\text{in}} \qquad \text{(F.4)}$$

Using the correct value for R_1 changes $k|_{eff}^{al}$ to $5.0\text{x}10^4 \frac{\text{lbf}}{\text{in}}$, again considered to be an unimportant change.

Damping at the contact point was assumed to consist of a small amount of viscous damping. The amount of damping was characterized by the second order system damping ratio ζ, where $\zeta = \frac{b}{2\sqrt{km}}$. The mass was taken as the mass of the steel or aluminum beam. The mass of the steel beam is $1.50\text{x}10^{-3} \frac{\text{lbf}\cdot\text{sec}}{\text{in}^2}$ and the mass of the aluminum beam is $2.70\text{x}10^{-4} \frac{\text{lbf}\cdot\text{sec}}{\text{in}^2}$. Thus, for an assumed ζ of 0.5% or 0.005, damping constants are:

IBS steel beam contact damping:

$$b|_{eff}^{steel} = 2\zeta\sqrt{km} = 0.112 \left.\frac{\text{lbf}\cdot\text{sec}}{\text{in}}\right|_{\zeta=0.5\%} \tag{F.5}$$

IBS aluminum beam contact damping:

$$b|_{eff}^{al} = 2\zeta\sqrt{km} = 0.039 \left.\frac{\text{lbf}\cdot\text{sec}}{\text{in}}\right|_{\zeta=0.5\%} \tag{F.6}$$

C.2. SSC contact parameters

The force sensors used in the SSC's instrumented ball joint have flat steel tips. The ball that they come into contact with is steel, and is 0.625" in diameter. Therefore, for the ball joint, $R_1 \rightarrow \infty$, $R_2 = 0.3125$", and $k_1 = k_2 = k_{steel}$. Based on preliminary design studies [79], the maximum expected force is approximately 50 lbf. Therefore:

SSC ball joint contact stiffness:

$$\alpha|_{50\ \text{lbf}}^{\text{ball jt}} = \sqrt[3]{\frac{9\pi^2}{16}\frac{50^2\,(9.72\text{x}10^{-9} + 9.72\text{x}10^{-9})^2}{0.3125}} = 2.56\text{x}10^{-4}\ \text{in}$$

$$k|_{eff}^{\text{ball jt}} = \frac{P}{\alpha} = 2.0\text{x}10^5 \frac{\text{lbf}}{\text{in}} \tag{F.7}$$

The force sensors used in the sliding joint have hemispherical brass tips approximately 0.188" in diameter, which come into contact with a flat steel surface. Therefore, $R_1 = 0.09375$, $R_2 \rightarrow \infty$, $k_1 = k_{brass}$, $k_2 = k_{steel}$.

SSC sliding joint contact stiffness:

$$\alpha\Big|_{50\ lbf}^{slid\ jt} = \sqrt[3]{\frac{9\pi^2}{16}\frac{50^2\,(1.78\text{x}10^{-8} + 9.72\text{x}10^{-9})^2}{0.09375}} = 4.82\text{x}10^{-4}\ in$$

$$k\Big|_{eff}^{slid\ jt} = \frac{P}{\alpha} = 1.0\text{x}10^5\,\frac{lbf}{in} \qquad (F.8)$$

As in the IBS, contact damping was assumed to be viscous damping, determined from the formula $b = 2\zeta\sqrt{km}$ using an assumed value for ζ. The effective mass seen at the contact point is taken to be 1/2 the mass of the connecting rod plus the mass of the ball joint housing for contact in the ball joint, and 1/2 the mass of the connecting rod plus the mass of the yoke and slider for contact at the sliding joint. These masses are, respectively, $m\Big|_{eff}^{ball\ jt} = 4.51\text{x}10^{-4}\,\frac{lbf\cdot sec^2}{in}$ and $m\Big|_{eff}^{slid\ jt} = 7.71\text{x}10^{-4}\,\frac{lbf\cdot sec^2}{in}$. Therefore, assuming ζ = 1%:

SSC ball joint contact damping:

$$b\Big|_{eff}^{ball\ jt} = 2\zeta\sqrt{km} = 0.19\ \frac{lbf\cdot sec}{in}\Big|_{\zeta=1.0\%} \qquad (F.9)$$

and SSC sliding joint contact damping:

$$b\Big|_{eff}^{slid\ jt} = 2\zeta\sqrt{km} = 0.18\ \frac{lbf\cdot sec}{in}\Big|_{\zeta=1.0\%} \qquad (F.10)$$

This concludes the discussion of the details of the ASSET numerical models for the IBS and the SSC.